



# Study of the kinetics rates of low alkalinity cementitious materials carbonation: impact on the microstructure, the gas transport and the mechanical properties

Ekoé Kangni-Foli

## ► To cite this version:

Ekoé Kangni-Foli. Study of the kinetics rates of low alkalinity cementitious materials carbonation: impact on the microstructure, the gas transport and the mechanical properties. Theoretical and/or physical chemistry. Université Paris sciences et lettres, 2019. English. NNT : 2019PSLET056 . tel-02929257

**HAL Id: tel-02929257**

**<https://pastel.hal.science/tel-02929257>**

Submitted on 3 Sep 2020

**HAL** is a multi-disciplinary open access archive for the deposit and dissemination of scientific research documents, whether they are published or not. The documents may come from teaching and research institutions in France or abroad, or from public or private research centers.

L'archive ouverte pluridisciplinaire **HAL**, est destinée au dépôt et à la diffusion de documents scientifiques de niveau recherche, publiés ou non, émanant des établissements d'enseignement et de recherche français ou étrangers, des laboratoires publics ou privés.



**THÈSE DE DOCTORAT**  
**DE L'UNIVERSITÉ PSL**

Préparée à ESPCI Paris

(École supérieure de physique et de chimie industrielles de la ville de Paris)

**Apport de matériaux cimentaires modèles à la description des  
cinétiques de carbonatation de bétons bas-pH : conséquences  
sur la microstructure, le transfert de gaz et les déformations**

Soutenue par

**Ekoé KANGNI-FOLI**

*Le 27 septembre 2019*

Ecole doctorale n° 397

**Physique et Chimie des  
Matériaux**

Spécialité

**Physico-Chimie**



**Composition du jury :**

Barbara, LOTHEBACH Professeur, EMPA,	Présidente
Jørgen, SKIBSTED Professeur associé, Université d'Aarhus	Rapporteur
Véronique, BAROGHEL-BOUNY ITPE (divisionnaire), IFSTTAR	Examinatrice
Pierre, TOULHOAT Cadre scientifique des EPIC, BRGM	Examineur
Thibault, CHARPENTIER Directeur de recherche, CEA	Examineur
Jean-Baptiste, d'ESPINOSE de LACAILLERIE Professeur ESPCI Paris	Directeur de thèse



« L'amour ne se paie qu'avec l'amour ; et les œuvres avec des œuvres »

Fernando de Rojas

*Un grand merci à Stéphane POYET (CEA), à Alexandre DAUZERES (IRSN) et à Céline CAU-DIT-COUMES (CEA).*

*A toutes celles et ceux qui ont rendu ce travail possible.*



## **Carbonation of low-pH materials:**

*Consequences on the chemistry, mineralogy, microstructure,  
gas transport and deformation.*

## List of tables

### [FIRST PART](#)

Table 1: Compositions of the cementitious materials used for Industrial scales sealing projects (non exhaustive list). (in kg/m <sup>3</sup> )	5
Table 2: Composition of an anhydrous and hydrated OPC using cement nomenclature.	6
Table 3: Composition of developed Low-pH materials (not exhaustive list).	9
Table 4: Properties of crystalline calcium carbonates.	12
Table 5: Reported results from literature on calcium carbonate polymorphism and carbonation kinetics.	13
Table 6: Details of the formulation and some properties of the industrial LAC (50%CEM I + 50%SF)	20

### [SECOND PART](#)

#### [Chapter1](#)

Table 1: Composition of the model pastes for 1L	37
Table 2: Composition of the reference pastes for 1L	37
Table 3: Relative occurrence of silicate environments in synthetic and model pastes from <sup>29</sup> Si MAS-NMR.	43
Table 4: Mean value and standard deviation of the C/S ratio distribution of the model pastes	45
Table 5: Composition and properties of the synthetic and reference pastes obtained by TGA, $\mu$ CT and the buoyancy method. The C-S-H content was obtained following the method of Olson and Jennings [53]. (see Materials and method section)	46

#### [Chapter 2](#)

Table 1: Nominal composition of the C-(A-)S-H that were synthesized	69
Table 2: C-A-S-Hs <sup>27</sup> Al peak intensities, Al h refers to amorphous and ill-crystallized calcium aluminates hydrated potentially hydroxy-AFm, C <sub>3</sub> AH <sub>6</sub> , CAH <sub>10</sub> C <sub>2</sub> AH <sub>8</sub> , C <sub>4</sub> AH <sub>13-19</sub> .	74
Table 3: Comparison of Q <sup>3</sup> and Q <sup>4</sup> proportion for carbonated C(-A)-S-Hs	90

#### [Chapter 3](#)

Table 1: Composition of the model pastes for 1 L of paste	97
Table 2: Composition and main properties of the two model pastes	97
Table 3: Amount of calcium involved in the carbonation reaction	105
Table 4: Porosity and density of the carbonated pastes	106
Table 5: Volume and mass of the different phases of the non-carbonated paste (C/S = 1.4)	112

Table 6: Volume and mass of the different phases in the carbonated paste (C/S = 1.4)	112
Table 7: volume and mass of the different phases in the non-carbonated paste (C/S = 3.0)	113
Table 8: volume and mass of the different phases in the carbonated paste (C/S = 3.0)	113
Table 9: change in solid volume (cm <sup>3</sup> /mol) induced by the carbonation of C-S-H, according to E- 15	115
Table 10: Results of the carbonation shrinkage test	116
Table 11: Distribution of <sup>29</sup> Si MAS NMR between silicates environment of C-A-S-H and silicates in silica gel/ silica fume, based <sup>29</sup> Si MAS NMR spectra decomposition. C-A-S-H = (%Q <sup>1</sup> +%Q <sup>2b</sup> +%Q <sup>2p</sup> ), Silica gel/silica fume = (%Q <sup>3gel</sup> +%Q <sup>4gel</sup> ).	129
Table 12: Parameters used in the <sup>29</sup> Si MAS NMR spectra decomposition	130
Table 13: Details of shrinkage's contribution for the model pastes and the industrial LAC	133

# List of figures

## FIRST PART

Figure 1: Scheme of the French deep geological facility (Cigeo project). Reproduced from <a href="http://www.andra.fr">www.andra.fr</a> .....	1
Figure 2: Sealing concept proposed for ILW-LL (modified in [1] and extracted from <a href="http://www.andra.fr">www.andra.fr</a> ).....	2
Figure 3: Scheme of the Tunnel Sealing Experiment (From CEBAMA project Deliverable D 1.03 [5]).....	5
Figure 4: Scheme of the FSS experiment components [6]. ....	5
Figure 5: Cement paste equilibrium pH and associate C/S, redrawn from [8–19] and [20] is used as a model. ....	8
Figure 6: Equilibrium pH with respect to the silica content of a cement paste. (modified from[1]). ....	8
Figure 7: Molar fraction of $\text{H}_2\text{CO}_3$ , $\text{HCO}_3^-$ and $\text{CO}_3^{2-}$ according to the pH in water at 20°C at equilibrium, from [24]. Carbonates species' formation constant are extracted from [21,25]. ....	11
Figure 8: Scheme of the multi-technique approach. The different types of materials and the dedicated techniques are highlighted.....	17
Figure 9: Fabricated pastes C/S = 3: shrinkage samples ( $\varnothing = 14$ mm H= 90 mm) and remaining samples ( $\varnothing = 30$ mm H= 120 mm) cut to generate samples of different lengths for different carbonation terms.....	19
Figure 10: Pastes covered with adhesive aluminium foil after conditioning and prior to carbonation. ....	19
Figure 11: Comparison between the pore size distribution obtained by mercury intrusion porosimetry for the uncarbonated CEM I + SF (silica fume) and the model C-S-H paste C/S = 1.4 (3 samples were analysed for each formulation) .....	20
Figure 12: Example of a logistic function fit for the grey level transition area of C/S=1.4 carbonated sample. ....	23
Figure 13: Experimental set up in climatic chamber for shrinkage measurement. ....	26

## SECOND PART

### Chapter 1

Figure 1: XRD patterns of the synthetic pastes. As the C/S ratio decreases, Portlandite reflections progressively disappeared from the diffractogram. While still barely visible at C/S 1.4, they were absent for synthetic pastes of lower C/S ratios. C-S-H indexing was based on [64–66], ICDD files CH: 44-1481, $\text{C}_3\text{S}$ : 31-0301.....	40
Figure 2: DTA-DTG of the model pastes. Besides losses due the removal of water within C-S-H, the typical thermal loss of portlandite was massively observed in the $\text{C}_3\text{S}$ paste. In contrast, only a residual portlandite content was evidenced in the C/S = 1.40 paste, and it totally disappeared at lower C/S ratios.....	41
Figure 3: $^{29}\text{Si}$ MAS-NMR spectra of the series of model synthetic pastes with varying C/S ratios and of the reference pastes. Synthetic pastes of higher C/S ratio had lower proportion of $\text{Q}^2$ (middle chain) to $\text{Q}^1$ (end chain) silicate coordination evidencing the expected decrease in dreierketten chain length with increasing C/S ratios. The spectra of the end members of the synthetic series where very similar to the ones of the reference pastes. The reference CEM I and LAC pastes showed $\text{Q}^0$ and $\text{Q}^3/\text{Q}^4$ resonances due to unreacted calcium silicates and to unreacted silica fume or amorphous silica gel products respectively.....	42
Figure 4: SEM examination of the synthetic paste with a C/S ratio of 0.80. At the scale of the EDS mapping, the paste appeared very homogeneous in composition.....	43

Figure 5: Distribution of the CaO/SiO <sub>2</sub> ratio obtained using SEM-EDS for the C <sub>3</sub> S paste.....	44
Figure 6: Distribution of the CaO/SiO <sub>2</sub> ratios obtained using SEM-EDS for the synthetic pastes for C/S ≤ 1.40.....	44
Figure 7: pH of the poral solutions of the synthetic pastes measured using the ex-situ leaching method, redrawn from [12,73–83] along with the model proposed by Haas & Nonat [72]. The pH of the pore water of the synthetic pastes satisfactorily reproduced observation reported in the literature and conformed to the predictive model...45	
Figure 8: PSD from mercury intrusion porosimetry for reference (right) and synthetic pastes (left).The PSD of the high C/S ratio synthetic pastes conformed to the one of an OPC (CEM I) paste, and the one for the lower C/S ratios to the one of the LAC (CEMI+SF+FA) reference paste.....	47
Figure 9: X-ray μCT scans images of 3 samples of the synthetic pastes series. Significant cracking was observed in paste with lower C/S ratios.....	48
Figure 10: C-S-H mean chain length of the synthetic pastes (from <sup>29</sup> Si MAS NMR) along with literature data [12,40,74,75,88,90–93]. The MCL obtained for our model pastes correlated well with the MCL of the cementitious materials reported in the literature .....	49
Figure 11: Comparison of the bulk C/S ratios (excluding the silicon in the amorphous non C-S-H part of the sample, unreacted products or silica gels, estimated by <sup>29</sup> Si NMR) with the results of SEM-EDS and with the ones expected from modelling pH measurements (Haas and Nonat model) and NMR ones (Richardson model). .....	50

## [Chapter 2](#)

Figure 1: DTA of the C-S-Hs and C-A-S-Hs of Al/Si ratios of 0.05 and 0.1 Loss associated to C(-A)-S-H between 0-725°C, and wollastonite between 725-850°C. ....	71
Figure 2: <sup>29</sup> Si MAS NMR spectra of the C(-A)-S-Hs displayed from left to right with increasing Al/Si (0, 0.05, 0.1). 72	
Figure 3: <sup>27</sup> Al MAS-NMR of the C-A-S-Hs samples. Spectra's surface normalized to the same value in order to allow comparison. ....	73
Figure 4: C-S-H (left) and formation of C-A-S-H (right) by Al insertion in bridging silicates sites. The different silicates sites are highlighted, scheme adapted from [60].....	74
Figure 5: Al 3Q-MAS NMR spectra of (a) CA0.8-0.05 and (b) CA0.8-0.10. The contour lines (blue) are drawn from 10% to 100% of the maximum heights. The dotted lines represents the direction of broadening induced by an isotropic chemical shift (CS) and second-order quadrupolar induced shift (QIS) distribution.....	75
Figure 6: CA0.8-0.05 and CA0.8-0.10 simulated and experimental MQMAS NMR spectra (left panel) and distribution of δ <sub>iso</sub> plotted against C <sub>q</sub> (right panel) are shown on figure (a) and (b), respectively.....	76
Figure 7: <sup>27</sup> Al MQMAS NMR spectra of (a) CA0.95-0.1 (b) CA1.40-0.1.* spinning sideband.....	76
Figure 8: CA1.4-0.1 distribution of δ <sub>iso</sub> plotted against C <sub>q</sub> .....	77
Figure 9: <sup>27</sup> Al MAS NMR spectra from 2 months after synthesis to 6 months after synthesis for (a) CA1.2-0.05/0.1 (b) CA1.4-0.05/0.1 .....	78
Figure 10: X-ray diffractograms of C-S-Hs at C/S: 0.80 and 1.40. The pristine uncarbonated states are showed together with natural (after 17 days at P <sub>CO2</sub> : 0.04%) and accelerated (after 18 days at P <sub>CO2</sub> : 3%) carbonation products. The same polymorphs were yielded by the two types of carbonation. Regardless of the C/S ratios, carbonation was total after 18 days of accelerated carbonation .....	79
Figure 11: x-ray diffractograms of C-A-S-Hs (Al/Si = 0.1) at C/S of 0.80 and 1.40. The pristine uncarbonated states are showed together with natural (38 days at P <sub>CO2</sub> : 0.04%) and accelerated (34 days at P <sub>CO2</sub> : 3%) carbonation	

products. The same polymorphs are observed compared to C-S-Hs' carbonation (see Figure 10) but a slower carbonation kinetics is evidenced at high C/S ratio in presence of Al..... 79

Figure 12: Intensities of observed phases at different carbonation terms for CA0.8-0.05 and CA1.4-0.05. .... 80

Figure 13: DTG of the carbonated C-A-S-Hs Al/Si=0.05, partial carbonation for CA1.40-0.05 is evidenced by reduced loss centered at 625°C..... 81

Figure 14:  $^{29}\text{Si}$  MAS NMR spectra of non-carbonated (continued lines) and carbonated (dotted lines) (a) C-S-Hs at C/S ratios of 0.80 and 1.40 (b) C-A-S-Hs C/S: 0.80 and 1.20 at Al/Si: 0.1 and 0.05. .... 82

Figure 15: Comparison of  $\text{Q}^3$  and  $\text{Q}^4$  evolution for carbonated C(-A)-S-Hs..... 82

Figure 16:  $^{27}\text{Al}$  MAS NMR spectra of CA0.80-0.1 and CA1.20-0.05 sounds and carbonated state. .... 83

Figure 17: 2D  $^{27}\text{Al}$  MQMAS spectrum of carbonated CA0.8-0.05..... 83

Figure 18: 2D  $^{27}\text{Al}$  MQMAS spectrum of carbonated CA1.4-0.05..... 83

### [Chapter 3](#)

Figure 1: Principle of the gas diffusion test ..... 99

Figure 2: Diffractograms of the pastes at the end of accelerated carbonation (316 and 326 days for the C-S-H and  $\text{C}_3\text{S}$  pastes respectively) ..... 101

Figure 3: Evidence of the presence of silica gel in the carbonated zone of the C-S-H paste (C/S = 1.4) ..... 101

Figure 4: Mineralogical assemblage after accelerated carbonation (316 and 326 days for the C-S-H (top) and  $\text{C}_3\text{S}$  (bottom) pastes respectively) obtained using XRD ..... 102

Figure 5:  $\text{CaCO}_3$  polymorphic abundance (%wt) in the carbonated zone after accelerated carbonation (316 and 326 days for the C-S-H (top) and  $\text{C}_3\text{S}$  pastes (bottom) respectively) obtained using Rietveld refinement. The vertical bar stands for the uncertainty of the quantification using Rietveld refinement (evaluated to 5%). .... 103

Figure 6:  $^{29}\text{Si}$  NMR spectra of the C-S-H and  $\text{C}_3\text{S}$  pastes after accelerated carbonation (316 and 326 days for the C-S-H and  $\text{C}_3\text{S}$  pastes respectively)..... 104

Figure 7: Quantitative mineralogical profiles obtained using TGA after accelerated carbonation (316 and 326 days for the C-S-H and  $\text{C}_3\text{S}$  pastes respectively). The horizontal bar stands for the thickness of the disk that was sampled and tested using TGA. The vertical bar stands for the uncertainty of the measurement (evaluated to 5%) ..... 105

Figure 8: Pore size distribution obtained using MIP after accelerated carbonation ..... 106

Figure 9: Cracking pattern observed using X- $\mu\text{CT}$  after accelerated carbonation (316 and 326 days for the C-S-H and  $\text{C}_3\text{S}$  pastes respectively)..... 107

Figure 10: View of the four zones that were observed using X- $\mu\text{CT}$  in the C-S-H paste after carbonation (316 days) ..... 108

Figure 11: Close-up on the zone II of the C-S-H paste and view of the cracks and discrepancies in grey level..... 108

Figure 12: View of the three zones that were observed using X- $\mu\text{CT}$  in the  $\text{C}_3\text{S}$  paste after carbonation (326 days). The presence of some cracks was underlined using white dashed lines..... 109

Figure 13: Carbonation rates of the two pastes ..... 110

Figure 14: Effect of the carbonation on a C-S-H paste; the hydrates are fully carbonated and replaced by silica gel and calcium carbonate.....	111
Figure 15: Effect of the carbonation on a C-S-H + CH paste (C <sub>3</sub> S paste). The carbonation products and partially carbonated hydrated coexist.....	113
Figure 16: Length variation of the Ø14 mm cylinders exposed to drying (25°C 55% RH) and then accelerated carbonation (25°C, 55% RH and 3% CO <sub>2</sub> ).....	116
Figure 17: Comparison of the carbonation shrinkage results with the data of Chen et al. [76] .....	116
Figure 18: Shrinkage versus decalcification level $\Delta CS$ of high C/S C-S-H .....	117
Figure 19: Carbonated industrial LAC's XRD profiles, especially the diffractograms of uncarbonated area, carbonated front area and fully carbonated zone are showed. a: aragonite, v: vaterite, c: calcite, filled triangle: C-S-H. Carbonated zone (surface), carbonated front (15 mm), uncarbonated zone: pristine material. ....	127
Figure 20: Relative proportion of the different phases obtained by Rietveld analysis.....	128
Figure 21: Carbonation's profiles obtained by TGA analysis, the complementary to the calcium carbonates estimated by mass balance represents the hydrates of the CaO-SiO <sub>2</sub> -Al <sub>2</sub> O <sub>3</sub> -H <sub>2</sub> O quaternary system.....	128
Figure 22: <sup>29</sup> Si MAS NMR profiles of the carbonated industrial LAC.....	129
Figure 23: µCT of the industrial LAC at 50 days of accelerated carbonation at P <sub>CO2</sub> = 3% .....	130
Figure 24: Carbonation depth observed in the industrial LAC after 50 days of carbonation compared to the model pastes (C/S = 1.4 and 3.0).....	131
Figure 25: Individual linear shrinkage of the materials studied, from 0-195 days the drying shrinkage is acquired, then the materials were carbonated at P <sub>CO2</sub> = 3% .....	132
Figure 26: Extent of the carbonation shrinkage of the pastes associated to the C-S-H's C/S variation. The experimental results are compared to Chen <i>et al.</i> decalcification results [2] .....	132
Figure 27: µCT of a C/S = 0.95 sample carbonated during 50 days.....	134

## Table of contents

FIRST PART.....	1
I. INTRODUCTION.....	1
II. LITERATURE REVIEW.....	3
1.1 The large-scale frame of the Low-pH materials.....	3
1.2 The hydration of cementitious materials.....	6
1.3 Properties of low pH materials: .....	7
1.4 The reaction of carbonation .....	9
1.4.1 Mechanism of calcium carbonates formation.....	11
1.5 The carbonation reaction in cementitious materials.....	12
1.5.1 The carbonation of the CaO-H <sub>2</sub> O-SiO <sub>2</sub> system. ....	12
1.5.2 Studies on carbonation- carbonation mechanisms .....	13
1.5.3 Consequences of carbonation .....	14
1.5.3.1 Influence of the conditions .....	14
III. MATERIALS AND METHODS.....	16
1.1 Program and overall approach.....	16
1.2 Materials and methods.....	16
1.2.1 Materials .....	17
1.2.1.1 Powders .....	17
1.2.1.2 The pastes.....	18
1.2.2 Methods.....	21
1.3 Discussion on the methods used.....	26
IV. Bibliography.....	27
SECOND PART.....	33
CHAPTER 1: MODEL SYSTEM FOR CEMENTITIOUS MATERIALS.....	33
1.1 Abstract.....	34
1.2 Introduction.....	35
1.3 Materials and methods.....	36
1.4 Results.....	39



1.5	Discussion.....	48
1.6	Conclusion.....	50
1.7	Supplementary materials.....	57
CHAPTER 2: ROLE OF LOW Al CONTENT IN C-S-H STRUCTURE AND EVOLUTION IN PRESENCE AND IN ABSENCE OF CO <sub>2</sub> .....		65
1.1	Abstract.....	66
1.2	Introduction.....	67
1.3	Materials and methods.....	68
1.3.1	Materials .....	68
1.3.2	Methods.....	69
1.4	Results.....	70
1.4.1	Thermogravimetric behaviour before and after carbonation .....	70
1.4.2	MAS NMR studies of pristine samples .....	72
1.4.2.1	<sup>29</sup> Si MAS NMR of pristine.....	72
1.4.2.2	<sup>27</sup> Al MAS NMR.....	73
1.4.2.2.1	Al MQMAS NMR.....	75
1.4.2.2.1.1	Low C/S ratio: C/S = 0.80 & Al/Si = 0.05-0.1 .....	75
1.4.2.2.1.2	Samples at high C/S: the case of 0.95 and C/S > 0.95 .....	76
1.5	Evolution of the C-A-S-H.....	77
1.5.1	Aging of the pristine product in absence of CO <sub>2</sub> .....	77
1.5.2	Effect of the carbonation on C-A-S-H.....	78
1.5.2.1	Mineralogical properties of the pristine and the carbonated materials .....	78
1.5.2.2	DTG of carbonated product .....	80
1.5.2.3	<sup>29</sup> Si in the carbonated product.....	81
1.5.2.4	Al in the carbonated product (1D+2D).....	82
1.6	Discussion.....	83
1.7	Conclusion.....	85
1.8	Supplementary materials.....	90
CHAPTER 3: CARBONATION IN DIFFUSIVE SYSTEM: MODEL PASTES AND INDUSTRIAL Low alkalinity Cement ..		92
1.1	Introduction.....	95

1.1.1	Materials .....	96
1.1.2	Methods.....	98
1.1.3	Results.....	100
1.1.4	Discussion.....	117
1.1.5	Conclusion .....	119
1.2	Appendices.....	124
1.3	Carbonation of an industrial LAC .....	127
2.	CONCLUSIONS AND PROSPECTS .....	135
	<a href="#">SUMMARY IN FRENCH</a> .....	138

## **FIRST PART**

## I. INTRODUCTION

In France, the sustainable management of radioactive materials and waste is governed by the act n°2006-739 passed in 2006 and modified by the subsequent planning act, n°2016-1015 in 2016. A deep geological repository was chosen as a long-term solution for intermediate level long lived waste (ILW-LL) and high-level waste (HLW). Its development is conducted by the French public agency in charge of the radioactive waste management (Andra).

Following geological surveys, the Meuse/Haute-Marne site located in the eastern part of the Paris Basin was retained based on its stable geological formation. The surveyed environment made of limestone layers, marl and argillaceous rock, exhibits low seismicity and a lack of significant natural resources above the future disposal facility. Moreover, the confinement property of the geological formation especially the callovo-oxfordian (COX) clay, which is the argillaceous rock within which the repository is envisaged, is particularly favourable. The argillaceous rock has a homogeneous thickness (130-140 meters), a low permeability, a stable porosity, its diffusive properties coupled to stable mechanical properties, makes it an appropriate geological environment for the repository.

The foreseen industrial centre is named Cigeo. It consists in three surface's sites dedicated to the excavation work and to the waste package receipt and preparation; an underground facility dedicated for the repository; and the vertical shafts and access ramps that constitute the connection infrastructures' that join the underground facility to the surface sites.

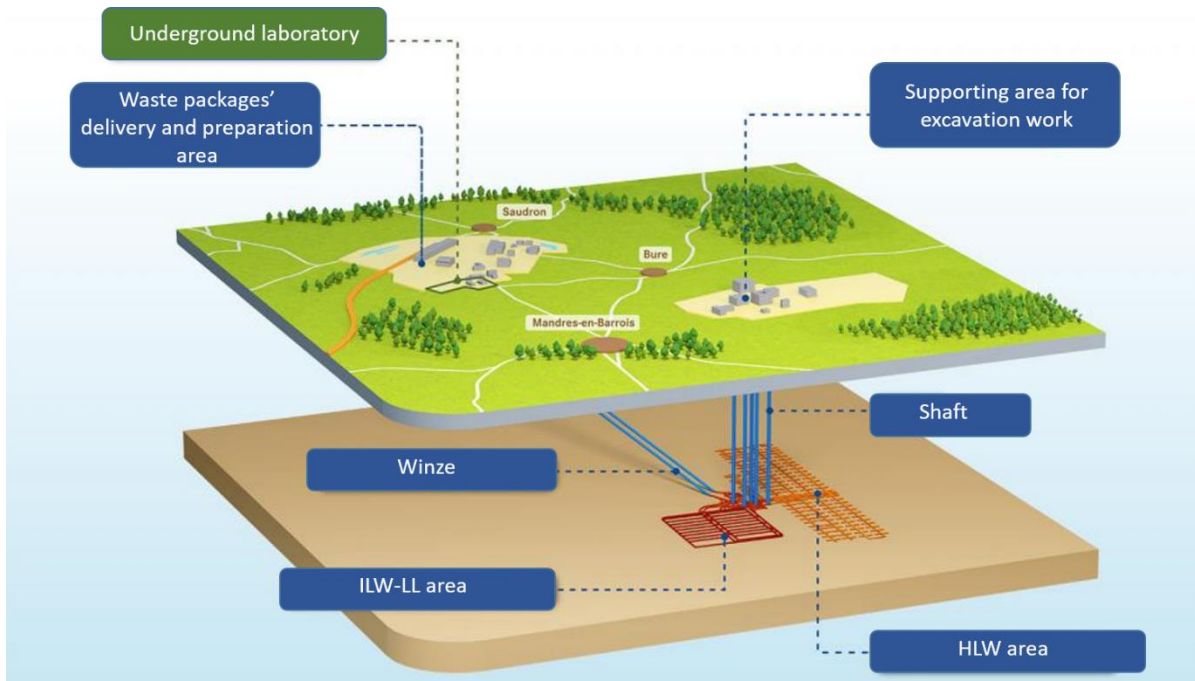
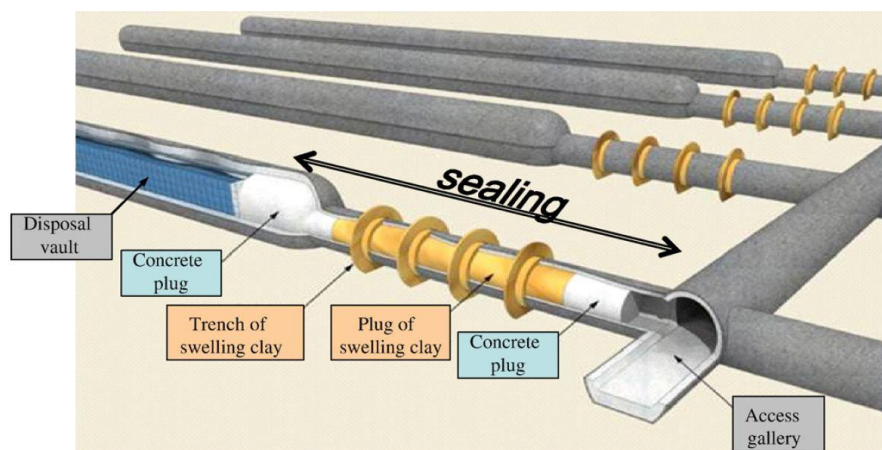


Figure 1: Scheme of the French deep geological facility (Cigeo project). Reproduced from [www.andra.fr](http://www.andra.fr).

Cementitious materials will be used as construction materials for the disposal facility. The resort to cementitious materials is justified by their mechanical properties, their low permeability and their radionuclides retention propensity. The concept retained by Andra for the closure of the disposal facility involves the plugging of the disposal cells by Low-pH concrete and swelling clay. The access drifts to the disposal cells are designed to be sealed with part of the excavated swelling clay, placed between two Low-pH concrete massive plugs (**Figure 2**). The first Low-pH plug is envisaged as a backfilling concrete structure located at one end of the disposal cells to ensure the closure of the disposal cells. The second Low-pH plug is planned to be located at the beginning of the access drift to maintain the swelling clay. The swelling clay once saturated, coupled to the Low-pH structures would guarantee the confinement. Several properties are expected from the Low-pH structure: (1) a lower hydration heat during the setting compared to OPC (ordinary Portland cement) to limit the temperature gradient in massive structure; (2) a reduced shrinkage to optimize the sealing; (3) and a pH value lower than 11 to minimize the chemical alteration (induced by the alkaline plume) likely deleterious to the bentonite swelling properties and thus to the confinement. Low-pH cementitious materials were formulated to meet these requirements [1–4]. Aside from the concrete plugs in the seals, low-alkalinity materials would be likely used for other structural applications such as vaults, linings or even waste package.



**Figure 2: Sealing concept proposed for ILW-LL (modified in [1] and extracted from [www.andra.fr](http://www.andra.fr)).**

Recent studies have highlighted an increased instability of the Low-pH cementitious materials with regard to the atmospheric carbonation [5,6]. The carbonation was related to a rise of the transport properties and the occurrence of cracks [6], phenomena that could strongly alter the durability of the cementitious materials, which would make the use of low-alkalinity concretes unsuitable for any other structural application. The underlying mechanisms of these phenomena have to be understood, for the purpose of an estimation of the structure's behavior and durability. This knowledge is required by IRSN for its evaluation of Andra's licence application for creating the disposal facility. The following research aims at obtaining a better understanding of the carbonation mechanisms of the Low-pH materials and providing more insight for the future IRSN's evaluation.

The approach followed in this thesis intends to highlight and to correlate the consequences of the carbonation of cementitious materials main building block, the calcium silicate hydrate (C-S-H), at several scales, from the microscale to the macroscale. From the C-S-H compositional and structural changes, to (for instance) the

deformation reflected by length variation on the overall material (the cement paste). A multi-technique approach was adopted to track the changes induced on:

- The microstructure, which includes the variation of the porosity, the nature of the porosity, the occurrence of cracks and the evolution of gas diffusivity, allowing the correlation between transport properties and pores network.
- The mineralogy and the chemistry since the initial phases are altered by the carbonation. Several uncertainties remain on the carbonation products: on the crystalline product, especially on the calcium carbonates polymorphism and on both the properties and the nature of the main amorphous phase formed, the silica gel. Moreover, the impact of the chemical composition of the C-S-H, *i.e.* the effect of the calcium and the aluminium content as well as the evolution of the carbonation kinetics was investigated.
- The overall structure at the macroscopic scale, knowing that the chemical and structural properties of (mainly) the C-S-H guarantee the mechanical integrity of the cementitious materials. The deformation induced by the changes in the chemistry and the effect of the carbonation on the overall material at a macroscopic scale is questionable and therefore explored through uniaxial length variation. The long-term shrinkage related to the drying and the carbonation was measured.

The following sections intend to describe the low-pH materials' framework, the realization at large scale and the nature of these projects. Thereafter, a literature review on carbonation's consequences is given. The approach adopted in this study, to allow a rigorous tracking of carbonation consequences, which comprises dedicated materials is then detailed.

The first chapter (2<sup>nd</sup> part of the manuscript) focuses on the synthesis and characterization of a model cementitious paste, with the aim of obtaining a model silicate subsystem of cementitious materials covering a large range of alkalinity. The second chapter (2<sup>nd</sup> part of the manuscript) deals with the effect of the chemistry of calcium silicate hydrate (C-S-H) on carbonation, more precisely the impact of the calcium content as well as the effect of the aluminium content on the calcium (alumino)silicate hydrate C(-A)-S-H structure and its carbonation's mechanisms. The structure of the cementitious material at atomic and molecular scale was investigated. For that second part of the study, the materials used were not pastes but synthesized pure C(-A)-S-H powders.

The third chapter (2<sup>nd</sup> part of the manuscript) is dedicated to the comparison of the carbonation mechanisms of pastes containing or not portlandite as a first step towards the comparison between low alkalinity and high alkalinity materials. Working with pastes, the carbonation's dependence and impact on diffusion can be examined. The carbonation is thus discussed considering all the changes detected in the chemistry, the mineralogy, the deformation observed at a macroscopic scale and finally the gas transport.

## **II. LITERATURE REVIEW**

### **1.1 The large-scale frame of the Low-pH materials**

Cementitious materials will be the main construction material for the repository. However, the properties demonstrated by usual cementitious materials are not directly fit to the confinement requirements for the sealing of the repository. Among the questions raised by the use of customary cementitious materials, one can consider: the difference of alkalinity between the construction material and the hydrogeological medium, the temperature's raise and variation during hydration and setting, the progress of the shrinkage and the cracking, and the time evolution of the transport properties.

Low-pH cementitious materials are expected to mitigate most of these effects and to date, the main application domain for Low-pH materials is indeed within the framework of deep geological repository which is the long-term solution adopted by many countries for nuclear waste storage. Consequently, programs aiming at the development of Low-pH materials and structures have been framed within numerous international collaboration involving countries such as Japan, Finland, the USA, Spain, Sweden, France, Canada, Switzerland and the UK. Numerous Low-pH formulations resulted from these collaborations and can be found in the literature [2–4]. Their output also included outstanding full-scale sealing projects for feasibility demonstration and bulkhead performance assessments. Some of these projects are described thereafter.

The first project, the TSX (Tunnel Sealing Experiment) took place in Canada from 1995 to 2008. The project involved countries such as Canada, France, the USA and Japan. Two bulkheads were placed 420 m below the surface. The first one was made of mixed sand and bentonite blocks (a swelling clay), the second of a Low Heat High performance concrete (LH-HPC) (**Figure 3**). A pore pressure was generated by a pressurized chamber placed between the two bulkheads. The experiments steps involved the heating (at 65°C), the cooling and the depressurizing of the bulkheads. The sealing properties were measured through seepage and transport measurements. The capability of the bulkheads to limit a unidirectional water flow was assessed. A compressive resistance of  $76 \pm 14$  MPa and a Young modulus of  $36.6 \pm 4.8$  GPa were obtained.

The ESDRED project (Engineering Studies and Demonstration of Repository Design) concerned the feasibility of sealing plugs and rock support thanks to shotcrete techniques. Its implementation took place from 2004 to 2009. The project involved the following countries: Spain, Germany, Sweden, Netherlands, the UK, Belgium, France, Finland and Switzerland. A short plug, and a long plug loaded using bentonite blocks swelling pressure were fabricated.

The Demonstration of Plugs And Seals (DOPAS) was an European project which involved countries such as Switzerland, France, Czech Republic, Sweden, Finland, the UK, and Germany. Within the DOPAS project, the Full Scale Sealing experiment comprised the design and the construction of a bentonite core placed between two concrete plugs (**Figure 4**). The full length of the structure was 35 meters, with an internal diameter of 7.6 meters. It included among others a pre cast Low-pH wall of 2 m thick and a Low-pH cast concrete of 5 meters thick. The temperature variation in the plugs did not exceed 15°C and after 3 months the pH was below 11. A compressive resistance around 51 MPa and a Young modulus of 28 GPa for the self-compacting concrete was obtained.

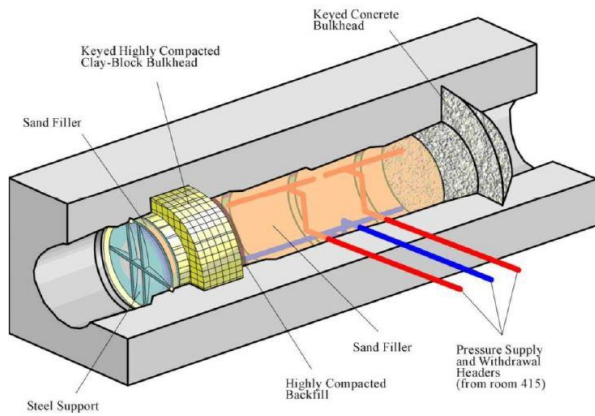


**Figure 3: Scheme of the Tunnel Sealing Experiment**  
(From CEBAMA project Deliverable D 1.03 [5]).

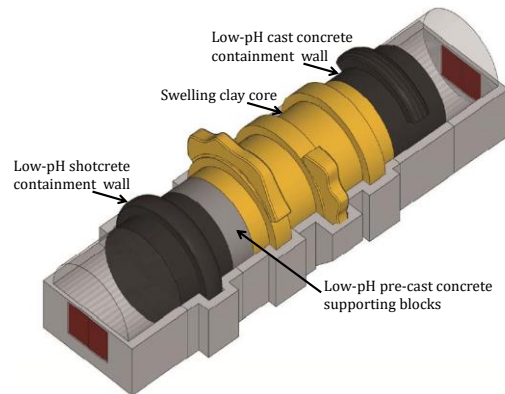


**Figure 4: Scheme of the FSS experiment components [6].**

**Table 1: Compositions of the cementitious materials used for Industrial scales sealing projects (non exhaustive list). (in kg/m<sup>3</sup>)**

	ESDRED		FSS		TSX	POPLUG
	Short plug	Long plug	Self compacting concrete	Shotcrete concrete	LH-HPC	Binary mix
Water	277.2	230	204	200	97	125
CEM I/ Cement	184.3	165	130	190	97	120
Aggregate	1633.4	1635	682	408	1040	1805
Silica fume	122.9	110	130	190	97	80
Superplasticizer	5.5	2.8	14.7	14	10.3	
Accelerant	18.5	16.5		2.7		
Air entrapper	0.6					
Filler		70	408.4			256
Sand			699	1347	895	
Silica flour					194	

Posiva, a Finnish's expert organization in nuclear waste management designed an end tunnel plug in the project POPLUG. A structure of 6 m length with a diameter between 4.35 m and 6.35 m was built. A compressive strength exceeding 50 MPa, a temperature increase of 5°C and a pH lower than 11 were achieved.

The formulation used during the TSX, ESDRED, DOPAS projects and one of the two formulations used in the POPLUG project are detailed in Table 1.



The Low pH materials are formulated to essentially meet two requirements, a reduced alkalinity, a lower pH and a lower hydration heat. Depending on the nature of the materials, grouts [7] or concrete, for instance shotcrete, several other requirements have to be met in term of penetration ability, fluidity, bleeding, and workability.

## 1.2 The hydration of cementitious materials

Carbonation is the main focus of this thesis. However, as carbonation affects mainly the hydrated phases yielded by the hydration of anhydrous phases present in the cement, the hydration mechanisms of cementitious materials (regardless of its alkalinity) is detailed thereafter.

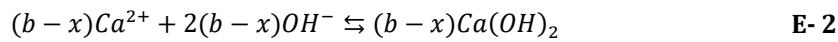
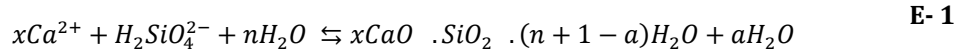
The partial fusion of limestone and clay at about 1450°C forms the clinker. In order to control the (future) setting rate of the clinker's hydrates, gypsum or anhydrite is added. The obtained powder is a hydraulic binders also called Portland cement. Cements gain their mechanical properties through hydration. The anhydrous cement powder contains several mineral phases which following the addition of water form a paste which harden. The different cement used by the cement industry are subdivided in 5 types, CEM I the Portland cement, CEM II called the Portland composite cement which is made of clinker, pozzolanic and hydraulic compounds, CEM III which is a mix of Portland cement and slag (also called ground granulated blast furnace slag), CEM IV which is a pozzolanic cement, and CEM V a composed cement. The development of these cements fits into several frameworks including the development of building materials for the construction but also ecological and sustainable development in order to reduce carbon emissions. The most usual cement encountered is the Portland cement also called ordinary Portland cement (OPC). Its main phases are Alite (tricalcium silicate), Belite (dicalcium silicate), aluminate phases (mainly tricalcium aluminate) and a ferrite phase (tetracalcium aluminoferrite). Their main crystal structures (specified in brackets) are modified by foreign ions present in the ores used to generate the cement. The proportion of the minerals constituting the major phases, are detailed in Table 2

**Table 2: Composition of an anhydrous and hydrated OPC using cement nomenclature.**

Main phases' content and proportion (wt %)	Chemical formula	Cement nomenclature	Hydrated phase
Dicalcium silicate (20-25)	2CaO, SiO <sub>2</sub>	C <sub>2</sub> S	C-S-H; CH
Tricalcium silicate (60-65)	3CaO, SiO <sub>2</sub>	C <sub>3</sub> S	C-S-H; CH
Tricalcium aluminate (8-12)	3CaO, Al <sub>2</sub> O <sub>3</sub>	C <sub>3</sub> A	C <sub>4</sub> AH <sub>13</sub> ; C <sub>3</sub> AH <sub>6</sub> ; C <sub>2</sub> AH <sub>8</sub> ; C <sub>3</sub> A.3C $\bar{S}$ .H <sub>32</sub> ; CAH <sub>10</sub> ; C <sub>3</sub> A.C $\bar{S}$ .H <sub>12</sub>
Tetracalcium aluminoferrite (8-10)	4CaO, Al <sub>2</sub> O <sub>3</sub> , Fe <sub>2</sub> O <sub>3</sub>	C <sub>4</sub> AF	C <sub>4</sub> (A,F)H <sub>13</sub> ; C <sub>3</sub> (A,F)H <sub>6</sub> C <sub>3</sub> (A,F).3C $\bar{S}$ .H <sub>32</sub> ; C <sub>3</sub> (A,F).C $\bar{S}$ .H <sub>12</sub>
H <sub>2</sub> O: H, CaO: C, SiO <sub>2</sub> : S, Al <sub>2</sub> O <sub>3</sub> : A, Fe <sub>2</sub> O <sub>3</sub> : F, CO <sub>2</sub> : $\bar{C}$ , $\bar{S}$ : SO <sub>3</sub> (sulfates are from gypsum, anhydrite...)			

The main hydration products' from anhydrous cement phases are detailed thereafter. Anhydrous phases of the CaO-SiO<sub>2</sub> system, yield hydrates called calcium silicate hydrates (C-S-H) (E- 1), the main hydrates of the cement paste,

and portlandite a calcium hydroxide (CH) (E- 2). For C-S-H, at equilibrium, the molar ratio of C/S expressed as x (E- 1) ranges between 0.67 which is considered to be the lower limit to the existence of C-S-H and 1.7 [8,9] or 2.0 [10] the upper limit of C-S-H obtained without the presence of detected portlandite. The C/S ratio measured from chemical analysis of hydrated Portland cement ranges between 1.2-2.2. 1.7 is considered as the mean value of the C/S ratio for Portland cement and C<sub>3</sub>S paste [11–13]. In equation E- 2, b is the total calcium content available in the silicate phases. In the case of tricalcium silicate's (C<sub>3</sub>S) hydration, a commonly accepted value for x is 1.7 and (b-x) is equal to 1.3.



The aluminate phase, C<sub>3</sub>A is a highly reactive phase: it leads to a rapid setting accompanied by a significant heat release. In absence of setting regulating-addition a flash setting occurs. The consequences are the lack of workability and mechanical resistance, high thermal expansion, and limitation of the hydration of calcium silicates phases. Calcium sulfate is thus added (gypsum, anhydrite) to regulate the setting. This explains the presence of sulfate in hydrated aluminate phases formed such as ettringite (C<sub>3</sub>A.3C<sub>2</sub>S.H<sub>32</sub>) a tri-sulfoaluminate (AFt). Ettringite tends to dissolve into a monosulfoaluminate (AFm) phase when the concentration of sulphate decreases.

Hydration of the ferrite phase yields the same phases as the aluminate phase, due to Al and Fe solid solution.

### 1.3 Properties of low pH materials:

To decrease the pH, the alkalinity of the basic hydrates has first to be lowered. This is obtained by dilution of sodium and potassium hydroxides and reduced overall calcium content. The lower hydration heat is obtained by the decrease of the cement content.

To attain the Low-pH materials properties, a decrease of the clinker content is necessary. Only substitutive reactive materials that lead to a lower alkalinity can be used. Lowering the alkalinity implies the decrease of the calcium to silica ratio (C/S) to values lower than 1.0 (Figure 5).

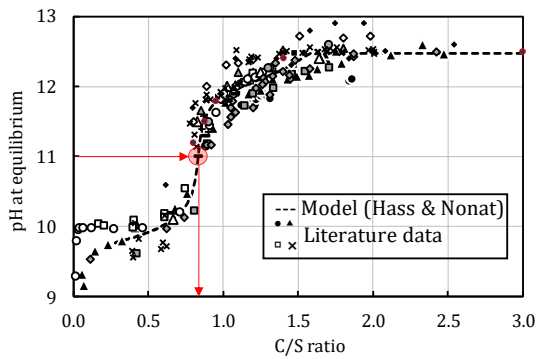


**Figure 5: Cement paste equilibrium pH and associate C/S, redrawn from [8–19] and [20] is used as a model.**

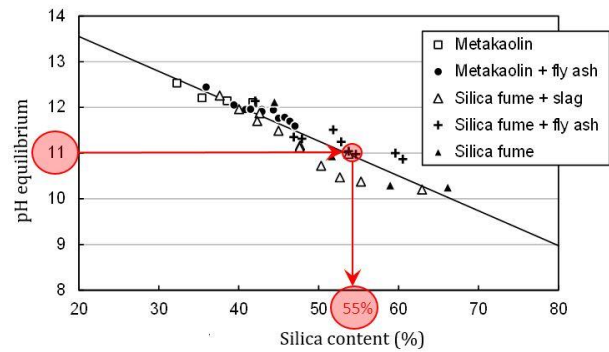


**Figure 6: Equilibrium pH with respect to the silica content of a cement paste. (modified from[1]).**

In this respect, pozzolanic and hydraulic compounds were found to be adequate substitutes to clinker. These replacement materials encompass fly ashes, silica fume, metakaolin and blast furnace slag. The key aspects are the silica content and the availability of the silica within the supplementary materials. It has been shown that due to its high silica content ( $\approx 95\%$ ) and the reactivity of its silica, which is available in an amorphous form, silica fumes represent the most effective pH lowering supplementary materials. A pH value of 11 is often targeted for low pH materials. This implies a minimal silica incorporation of 55% by mass to reach a pH value of 11 (Figure 6). The downside of the incorporation of such high amounts of silica is the decrease of the mix's workability. Ternary formulations (Table 3) made of CEM I, silica fume and fly ash remediated this pitfall. By blending the mix with supplementary material of lower silica content (fly ash) a paste with a reduced viscosity is obtained.

The development of Low-pH materials and the study of their durability have been closely related. This prevails for the materials detailed previously and used in industrials scale construction projects. Among the durability studies, in France, Codina [2,14] worked on binary, ternary and quaternary mixes in order to formulate, characterize and discriminate the most appropriate Low-pH material to be used in the French context. Her studies comprised the acquisition of chemical and physical parameters. In her durability study, she assessed the extent of leaching induced by water, the mechanical resistance, the porosity, and the chlorides' ion diffusion. Her work highlighted for the five blends studied (three ternary, one quaternary and one binary) a reduced hydration heat, a refined porosity despite a higher overall porosity, and a pores solution pH between values of 11.7-12.4. The leaching by water, yielded a minor rate of decalcification (4 times lower than the CEM I). The following works include at least one of the ternary Codina's mix, which was retained as a reference Low-pH. Dauzères' work [15] was focused on the interaction between developed cementitious materials and the clayey environment and the evolution of the cementitious materials itself upon leaching of the geological aqueous environment [15]. The monitoring of the chemical and the physical properties including aqueous species diffusion evidenced two different mechanisms occurring at the interface of Low-pH material and the COX clay and between a CEM I and the COX clay. It was observed, a reduced alteration of the clay in contact with the Low-pH materials but an intensive degradation induced by the geological water ( $< 1.5$  mm degraded at 5 months) leaching. Contrarily, the CEM I was found to intensively alter the clay by inducing illitisation, but the effect of the leaching was negligible due to calcite formation at the CEM I cement paste's surface. Following Dauzères studies [15], Drouet's work [16] was focused on the effect of the relative

humidity (RH) and the temperature on the carbonation mechanism. Drouet's studies [16] evidenced a higher carbonation depth with the raise of the temperature, a control by both the solubility of the reactive phases involved and the hydric properties of the cementitious material. Drouet's work put forward the relation between RH associated with the beginning of the capillary condensation and the highest rate of carbonation observed for all materials. Later, Auroy's work [17] on the mineralogical and the microstructural properties of carbonated materials revealed the major changes induced by the carbonation. A higher diffusivity and cracking rate was observed in low pH materials while CEM I materials demonstrated a decreased diffusivity after carbonation due to the clogging and the lower cracking's rate. This last study brought questions about the durability of blended cementitious materials upon carbonation since Low pH materials are highly blended materials with a long-term durability requirement in the deep geological framework.

**Table 3: Composition of developed Low-pH materials (not exhaustive list).**

	Materials	Composition
Binary	Grouts [18], Shotcrete	CEM I 60%+SF 40%
	Shotcrete [3] Self-compacting concrete [19]	CEM I 50%+SF 50%
Ternary	Shotcrete[3]	CEM I 35%+SF 35%+FA 30%
	High performance concrete [2]	CEM I 37.5%+SF 32.5%+FA 30.0% CEM I 20.0%+SF 32.5%+BFS 47.5%
Binary	Cement [4]	CEM III/B 90%+Nanosilica 10%
Quaternary	High strength concrete & grout [20]	CEM I 40%+BFS 30%+FA 25%+SF 5%
	Cement [2,14]	CEM I 33%+BFS 13.5%+FA 13.5%+SF 40%

Further studies are thus required to identify, understand and confirm the underlying mechanisms that control the durability of low-pH materials in atmospheric carbonation conditions, and to estimate the extent of the consequences of the carbonation, since carbonation is the major chemical alteration expected during the disposal operating phase.

The next section will detail the mechanisms of carbonation and its consequences on the cementitious materials' hydrates.

#### **1.4 The reaction of carbonation**

Cracks are one of the numerous consequences of the carbonation. Besides the weakening of the cementitious materials induced by the cracks, they aggravate the corrosion of the steel reinforcement. The carbonation induces an acidification of the pore solution, which tends to unpassivate the steels. Furthermore, cracks are preferential ways for amplified air supply, which promotes an increased corrosion rate. This phenomenon leads to highly fragilized structures. The carbonation of cementitious materials could be defined as the reaction of the Ca from Ca-bearing phases with dissolved CO<sub>2</sub> into the pores solution (E- 3)



In the following, the general carbonation process will be presented before addressing the case of the cementitious materials.

The carbonation process requires the prior dissolution of CO<sub>2</sub> into an aqueous medium. The three predominant dissolved species of CO<sub>2</sub> are the carbonic acid (H<sub>2</sub>CO<sub>3</sub>), the bicarbonate (HCO<sub>3</sub><sup>-</sup>), and the carbonate ion (CO<sub>3</sub><sup>2-</sup>). The concentration of dissolved CO<sub>2</sub> in aqueous solution at equilibrium (E- 5) is given based on the relation between CO<sub>2</sub> pressure and its concentration (E- 4) and Henry's law [21]. The concentration of CO<sub>2(g)</sub> is expressed in mol.L<sup>-1</sup>,  $H$  is the constant of Henry's law for CO<sub>2</sub> (in mol.L<sup>-1</sup>.Pa<sup>-1</sup>);  $\alpha_{\text{CO}_{2g}}$  is the volume fraction of CO<sub>2</sub> in the gas in equilibrium with the aqueous phase,  $R$  is the perfect gas constant (8.32 J.mol<sup>-1</sup>.K<sup>-1</sup>) and  $T$  the temperature (in K).  $H$  is proven to be close to  $H_0$  the constant of Henry's law for H<sub>2</sub>O in diluted solution. The relation between the concentration of CO<sub>2</sub> in air and its dissolved concentration in aqueous medium is given by the E- 6 [22].

$$[\text{CO}_{2(g)}] = \alpha_{\text{CO}_{2(g)}} \cdot \frac{P_{\text{gas}}}{RT} = \frac{P_{\text{CO}_{2(g)}}}{RT} \quad \text{E- 4}$$

$$[\text{H}_2\text{CO}_{3(aq)}] = H \cdot P_{\text{CO}_{2(g)}} \quad \text{E- 5}$$

$$[\text{H}_2\text{CO}_{3(aq)}] = RT \cdot H_0 [\text{CO}_{2(g)}] \quad \text{E- 6}$$

At CO<sub>2</sub> pressure below 10<sup>5</sup> Pa, the activities of CO<sub>2</sub> dissolved species could be simplified and expressed as their concentrations. The dissolved species encountered for the CO<sub>2</sub> are governed by several equilibria (from **E- 7** to **E- 10**). Equation **E- 7** has a finite reaction rate, as CO<sub>2</sub> structural modification is involved. On the contrary, the reactions of Equations **E- 8** and **E- 9** can be considered as instantaneous since only a proton exchange occurs [23]. The pH of the pores solution plays a key role in carbonation since the pH defines the predominant CO<sub>2</sub> dissolved species as evidenced from **E- 7** to **E- 9**. The dissolution of CO<sub>2</sub>, leads to an acidification of the reaction medium (Figure 7).

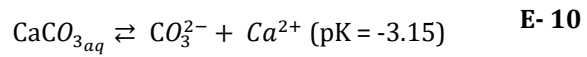
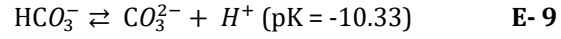
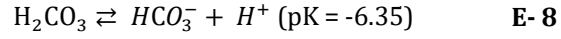
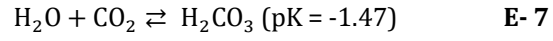
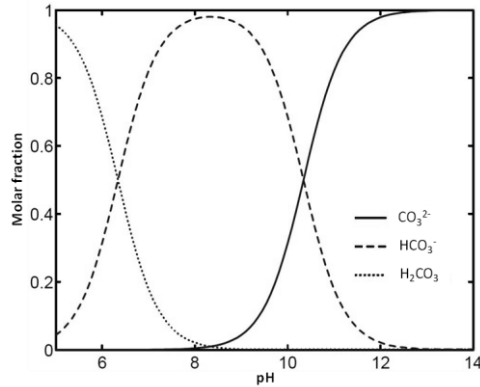


**Figure 7: Molar fraction of  $\text{H}_2\text{CO}_3$ ,  $\text{HCO}_3^-$  and  $\text{CO}_3^{2-}$  according to the pH in water at 20°C at equilibrium, from [24]. Carbonates species' formation constant are extracted from [21,25].**

#### 1.4.1 Mechanism of calcium carbonates formation

Calcium carbonates are generated by the reaction of carbonate ions with  $\text{Ca}^{2+}$ . Pre-nucleation clusters (PNCs) [26–29] are assumed to be the first (stable) structure formed [30]. PNCs are presumed to transform into amorphous calcium carbonates likely by a non-classical nucleation pathway: a solid state transition [31]. However, the dissolution and precipitation crystallization remain the main mechanism as reported by Nielsen *et al.* [32]. Despite uncertainties on the structure of the clusters, a growth mechanism based on aggregation followed by dehydration was proposed. The transformation of highly hydrated calcium carbonate amorphous phase into an ordered structure is suggested to strongly depends on the dynamics of the water constituting the cluster [33], their electrostatic interaction with  $\text{Ca}^{2+}$ , and the H-bond formed with  $\text{CO}_3^{2-}$  [34]. The H bond of  $\text{CO}_3^{2-}$  are thought to generate a network, which contains loosely bond  $\text{H}_2\text{O}$ . Stable ordered structures (crystalline polymorphs) are thought to emanate from amorphous systems which hold less loosely bonded  $\text{H}_2\text{O}$  [33]. Characteristics short-range order was observed in amorphous calcium carbonates, this phenomenon is called polyamorphism. Gebauer *et al.* [35] and Fernandez-Martinez *et al.* [36] evidenced several short order domains characteristic of calcite, vaterite and aragonite, in amorphous calcium carbonates.

The hydrated amorphous calcium carbonates could persist several months at room temperature, while anhydrous amorphous species directly transform into one of the crystalline polymorphs. Those polymorphs are the monohydrocalcite, ikaite, calcite, aragonite, and vaterite. The three later are the more recurrent in cementitious materials and their structural properties are listed in Table 4.

**Table 4: Properties of crystalline calcium carbonates.**

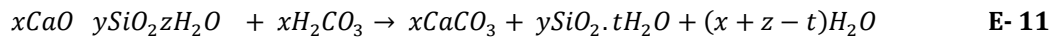
	Calcite	Vaterite	Aragonite
Lattice system	Rhombohedral	hexagonal	orthorhombic
Lattice parameters	a = 4.989 b = 17.062	a = 7.135 c = 16.98	a = 4.959 b = 7.968 c = 5.741
Molar volume (cm <sup>3</sup> /mol)	35	38	34
Density (g/cm <sup>3</sup> )	2.76	2.68	3.01

Recent studies highlighted the existence of several structures for a polymorph such as vaterite, which advocate variations in the structural organization (bond length and angle); this polymorphism is explained by the narrow thermal range (room temperature) in which falls the free energy of several of the stable structures [37].

## 1.5 The carbonation reaction in cementitious materials

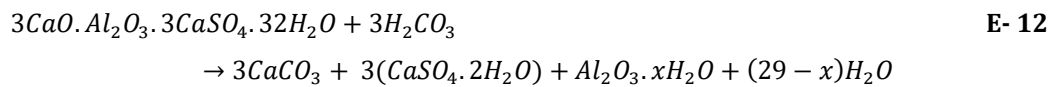
### 1.5.1 The carbonation of the CaO-H<sub>2</sub>O-SiO<sub>2</sub> system.

Calcium silicate hydrates are subjected to carbonation due to their calcium content. The ultimate decalcification state leads to a fully degraded C-S-H. The hydrated silica polymerizes to form silica gel made of silicates unit with incorporated water in the network. The mechanism proposed detailed a mobilization of the calcium into carbonates phases (E- 11).



The products yielded by the carbonation were reported by several studies. Trimethylsilylation experiments [38] gave insight on the silica gel formation. High molecular weight ( $Si_6O_{19}^{14-}$ ) transient product were evidenced during the formation of the silica gel. The amorphous nature of the silica gel yields a diffuse background observed between 20-30°(2θ) in X-ray diffractograms obtained with Cu K<sub>α</sub> source [39]. The nature of the gel could only be adequately characterized by spectroscopy techniques such as IR, Raman, or magnetic resonance. No detailed carbonation mechanism is reported in the case of Al incorporation in C-S-H.

Aluminates species are the other hydrates impacted by the carbonation. Hydrogrossular and calcium aluminates carbonation are known to generate alumina gel, water and calcium carbonates. Sulphates aluminates such as Aft and AFm are expected to form gypsum, alumina gel, water and calcium. The carbonation of ettringite is described below in E- 12:



### 1.5.2 Studies on carbonation- carbonation mechanisms

The carbonation also occurs for anhydrous calcium silicates phases in presence of an adequate relative humidity as observed by [40]. Ill-crystallize calcium carbonate and the three crystalline forms of calcium carbonate are detected.

**Table 5** gathers results and observations from carbonation studies.

Black *et al.* [29] observed the formation of aragonite which they explained by the presence of silica gel or low C/S ratio C-S-H during the carbonation. Considering Sauman *et al.* [41] and Anstices *et al.* [42] results, Black *et al.* [29] explanation could justify the presence of aragonite. Nonetheless, in the case of C<sub>3</sub>S paste carbonation at low and high  $P_{CO_2}$  [43] no aragonite was observed.

**Table 5: Reported results from literature on calcium carbonate polymorphism and carbonation kinetics.**

		Kinetics	Polymorphism					
			High CO <sub>2</sub>			Low CO <sub>2</sub>		
			Low RH	50-76%	RH100%	Low RH	High RH< 100%	RH100%
Sauman <i>et al.</i> [41]		(2)		10%CO2  Calcite vaterite aragonite	30%CO2  calcite		Calcite Vaterite Aragonite	calcite
Dunster <i>et al.</i> [38]		(1)						
Morandeau <i>et al.</i> [44]								
Hunt & Tomes [45]								
Groves <i>et al.</i> [43]				Calcite vaterite			Calcite vaterite	
			Shorter silicate chains but highly polymerized			Longer silicate chains less crosslinked		
Black <i>et al.</i> [29]	C/S>0.67	(3)					Aragonite vaterite	
	C/S<0.67						aragonite	
Anstice <i>et al.</i> [42]				Calcite vaterite Aragonite*			Calcite vaterite Aragonite	
*low abundance or not detected								
(1) simultaneous carbonation of C-S-H and CH								
(2) observed kinetics correlate with the Ca content								
(3) observed kinetics does not correlate with the Ca content								



Moreover calcite was not observed in the case of natural carbonation even in presence of portlandite. These results show a discrepancy among the reported polymorphic distribution. Similar polymorphic distribution was observed for  $C_3S$  at both high and low  $P_{CO_2}$  but the properties of the silica gel obtained in each case are different. A lower silicate chain length and higher crosslinking was observed at high  $CO_2$  pressure. Consequently, the analysis of the reaction products cannot be limited to the polymorphic distribution alone. The nature of both the calcium carbonates formed and the silica gel should be considered. Besides the polymorphic abundance, the relative kinetics of the carbonation of the calcium bearing hydrates holds uncertainties. It was first described a mechanism involving solely portlandite carbonation. Then further studies reported the simultaneous carbonation of portlandite and C-S-H. Finally, Parrot and Killoh studies [46] outlined, in a 39 years old carbonated concrete, fully carbonated C-S-H in presence of portlandite.

### **1.5.3 Consequences of carbonation**

#### **1.5.3.1 Influence of the conditions**

Impact of relative humidity:

To take place, carbonation requires both the carbon dioxide and the calcium to be in aqueous phase but diffusion is much faster in gaseous than in aqueous phase. The higher carbonation kinetics is thus obtained between 40-60% RH [24,47–49]. Drouet's conclusion on high alkalinity and LAC [16] study is that a RH corresponding to the triggering point of the capillary condensation is the optimum for the carbonation of each material considered. The hydric condition of the environment surrounding the materials controls the carbonation rate due to the dependency between the materials' saturation and the external RH. The RH of the environment along with the microstructure impose the degree of saturation of the material. A fully saturated material carbonates slower than a partially saturated one. Indeed, carbonation will then be limited by the diffusion of  $CO_2$ , that is  $10^4$  times lower in water compared to air [50]. Oppositely, the carbonation rate is also decreased when the saturation of the cement pore structure is too low (typically RH domain lower than 40%) to allow optimum  $CO_2$  dissolution in water. The polymorphism is also influenced by RH. Calcite is the polymorph obtained during carbonation in fully saturated medium and at high RH  $\approx 80\%$ . Drouet's work [16] has shown a predominant proportion of metastable calcium carbonates phases during carbonation at low relative humidity [16]. This was confirmed by the study of the carbonation at increasing RH from other materials than cementitious materials', such as calcium hydroxide nanoparticles [51]. The transformation from metastable phases to a more stable phase is thought to be limited at low RH, which would explain the absence of significant conversion to stable phases [52].

Impact of temperature and pH:

Temperature and pH strongly influence the polymorphs obtained. Tai and Chens [53] investigation on calcium carbonates yielded at 24 and 58°C shows a dependency with respect to both the temperature and the pH. They highlight several tendencies. At 58°C, above pH 11, the main polymorph found is calcite, while below a pH value of 10.5, aragonite is the predominant calcium carbonate. At a lower temperature, 24°C, three domains are observed, calcite is the main polymorph above a pH value of 12, between 12 and 11 aragonite is predominant, and below 10 vaterite is the main polymorph. The tendency is clear at high pH, irrespective of the temperature calcite seems to

be the predominant polymorph and at high temperature and low pH, aragonite is the predominant species. However, at lower temperature a more contrasted behaviour is observed since aragonite is found within a medium pH range (10-12) and vaterite is the main species at lower pH values.

Impact of w/b and curing period:

The curing period allows the hydration to extend in time, which is beneficial for LAC that have longer hydration period than high alkalinity materials [4]. That hydration is closely related to the mechanical resistance of the material, given the higher proportion of C-S-H yielded. A higher curing period is observed to induce both a more refined porosity due to the formation of C-S-H but also a porosity which is less connected [17], the latter impacts the microstructure therefore the progress of the carbonation. The same tendency is evidenced during natural carbonation of OPC at different w/b = 0.30 and 0.50, namely the decrease in total porosity and the clogging of porosity between 100 and 10 nm.

Representativeness of the carbonation pressure:

The effect of the concentration of CO<sub>2</sub> raises the question of the representativeness between accelerated carbonation and natural carbonation. The aim of an accelerated carbonation is to access advanced carbonation states that are indicative of a natural progress of the chemical, the mineralogical, and the microstructural properties. Studies at several CO<sub>2</sub> concentration from 1% to 100% [5,6,54–59] are available. They reveal that several modifications are closely related to the exposure at high CO<sub>2</sub> concentration, namely the change in microstructure and the carbonation kinetics reflected through the carbonation depth. The carbonation depth tends to increase when the CO<sub>2</sub> concentration is increased, from 0 to 50% of CO<sub>2</sub> in volume [60]. The alteration of pores of diameter less than 10 nm was shown to be greater during high concentration carbonation. Those pores were reduced from 11.7 to 1.85% at 20% CO<sub>2</sub> and only to an extent of 5% when the CO<sub>2</sub> concentration was set to 3%. Literature seems to agree on the use of low concentration during carbonation without a consensus on the most appropriate concentration to use. Several studies have proposed 3% to be an adequate concentration [5,59].

Consequences on microstructure and the transport:

Cui *et al.* [57] studies on Portland cement concrete on carbonation report a higher carbonation depth at  $P_{CO_2}$  ranging between 2 and 20% compared to a  $P_{CO_2}$  of 50%. SEM analysis unveils a denser microstructure, due to calcite clogging. A higher reactivity induced by a higher  $P_{CO_2}$ , is responsible for a greater extent of clogging. A deepened CO<sub>2</sub> access to the pores network is limited by the obstructed pores present in the first millimetres of the materials and this explains the lower carbonation depth in presence of high  $P_{CO_2}$ . The calcium carbonates formed within the porosity generate denser materials in OPC type material [61] especially at low w/b ratio [62]. The alteration of the microstructure affects the gas diffusion and the hydric state and therefore the carbonation which depends both on the microstructure (pores network, gas diffusion) and the materials' chemistry. Despite few results evidencing in high alkalinity paste a coarsening of the pore structure such as an increase of pores with diameter higher than 100 nm [63], the predominant mechanism at high alkalinity is the porosity clogging, with an overall decrease of the porosity. The contribution of micro-cracking might explain the apparition of this porosity [6].

## Particularity of blended cementitious materials-effect of the composition

The LAC are characterized by both a finer and a higher porosity due to their greater C-S-H content. The blended cementitious materials exhibit different behaviour compared to high alkalinity materials in carbonation condition representative to natural carbonation. The low alkalinity materials overall resistance to carbonation is assumed to be minored due to their lower calcium content [58]. Nonetheless, among LAC, the type of porosity is expected to plays a key role on the carbonation resistance, as a refined and less connected porosity is appropriate for a higher resistance. Indeed, a decrease of the pore diameter induces a higher saturation, which lowers the diffusion of CO<sub>2</sub>.

### III. MATERIALS AND METHODS

#### 1.1 Program and overall approach

This work aims to identify the main chemical and physical mechanisms and parameters related to the changes generated by carbonation in Low-pH materials. The focus was therefore on the chemical evolutions, the changes in the mineralogy, the microstructure, and the kinetics of carbonation. The timeframe of the studies imposed the resort to an accelerated carbonation, which had to be representative of natural carbonation, therefore the representativeness of the carbonation implemented was questioned.

Cementitious materials are complex composite materials with an organizational range, extended from the nanoscale to the macroscale. Mortars, incorporate cement, sand, water, and in the case of concretes, aggregates are also added. The binder, which results from cement hydration represents itself a multiphasic system (Table 2). This organizational complexity, could prevent deciphering the mechanisms of interest and their consequences on specific phases. Considering the case of carbonation, the binder deserves a particular attention as, through the calcium silicate hydrate, it represents the main calcium-bearing phase, while being responsible of the mechanical and the cohesive properties.

With regard to the complexity of the carbonation mechanism, the experimental system requires: (1) a decrease in compositional complexity (compared to cementitious binder) to allow access to mechanisms at molecular level; (2) a tailored chemistry to permit an understanding of the impact of the chemical parameters such as C/S and Al/Si ratios; and (3) the coupling between the chemistry (microscale) and the transport (macroscale).

#### 1.2 Materials and methods

We've adopted a "model material" approach, *i.e.* the use of materials of controlled mineralogical and chemical compositions, constituted of pure phases. The study of the consistency of the accelerated carbonation conditions used, imposed the recourse to two types of materials: paste and powders. Since, the carbonation in porous system is diffusion dependant; the kinetics of the carbonation of a paste is substantially slowed down and dependant on the microstructure. However, to access the ultimate state of carbonation and the properties of the products yielded we also considered the study of powders of pure phases.

We selected two types of material which includes, powders based on quaternary system (CaO-SiO<sub>2</sub>-H<sub>2</sub>O-Al<sub>2</sub>O<sub>3</sub>) and pastes based on ternary system (CaO-SiO<sub>2</sub>-H<sub>2</sub>O). This approach constitutes a first step avoiding issues related to the complexity associated with a true multiphasic cement paste but it presents the advantage of allowing a rigorous

mass balance after carbonation of the silicate phase. The overall approaches including the materials used are schematically described in **Figure 8**.

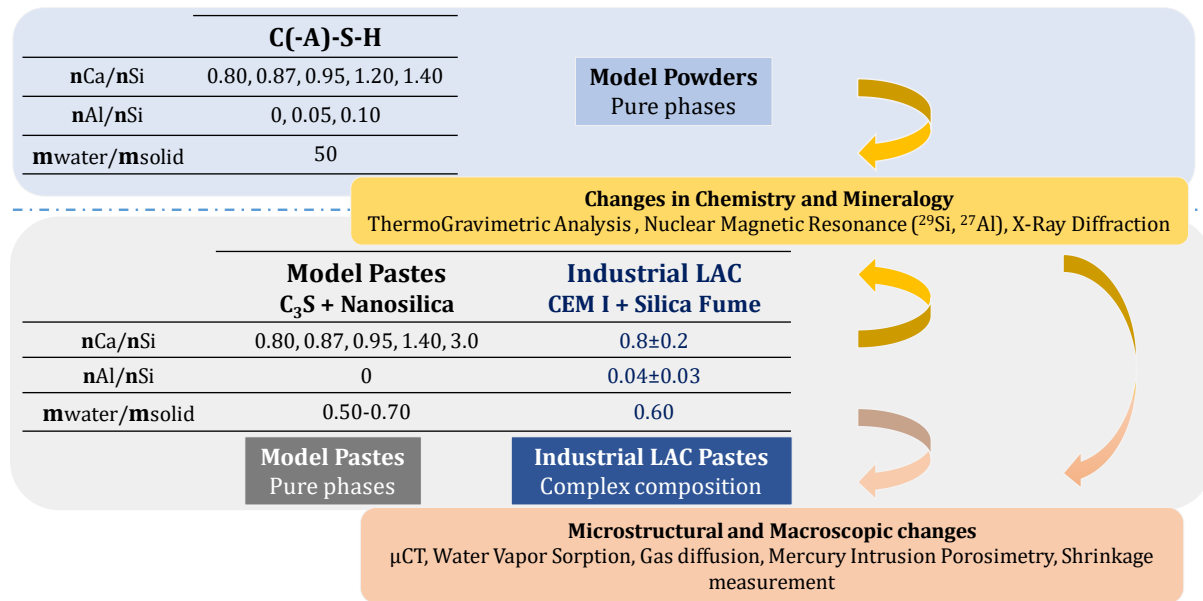


**Figure 8: Scheme of the multi-technique approach. The different types of materials and the dedicated techniques are highlighted.**

## 1.2.1 Materials

### 1.2.1.1 Powders

The powders were made of calcium (alumino)silicate hydrates with an increased content on aluminium and calcium. The incorporation of aluminium aimed at being representative of C-S-H occurring in cementitious gels. The content on Al was limited to an Al/Si=0.1 in order to focus on behaviour at low Al content. Several methods allow the obtention of C-A-S-H powders. The first, the double decomposition synthesis route, consists in the use of calcium nitrate and sodium silicate mixed in water. The main drawback of this approach is the necessary recourse to washing, which tends to be partially efficient if only water is used. As sodium becomes a compensating charge in the calcium silicate structure [64], even washing with basic solutions does not prevent a persistent alkali content [8]. The second, the silica lime route consists in the use of calcium oxide and silica. Two pathways are used, the first one is the three steps synthesis: firstly, calcium oxide and silica are mixed in ultrapure water to obtain the C-S-H, secondly the aluminium source are prepared, and thirdly the C-S-H and the aluminium source are mixed [65,66]. Several aluminium sources are available, Faucon *et al.* [67] used aluminium nitrate, but this route always requires the synthesis product's washing by sodium hydroxide. An alternative aluminium source to nitrate aluminium could be a solution of hydrated tricalcium aluminate. In this case, once the C-S-H obtained, the adequate amount of the filtrated solution of tricalcium aluminate is added to the C-S-H powder. Another approach consists in a one-step synthesis based on a silica lime reaction. The C-A-S-H powders can be obtained through a one pot synthesis, by mixing the powders of the reactants with an ultrapure water [68–70]. C<sub>3</sub>S or calcium oxide could be used as calcium

sources. A variant method, the mechanochemically synthesis route involves the recourse to intermittent milling in devices such as roller mill pot during the synthesis time [29,71].

To control the C/S ratio, Lecoq and Nonat developed a synthesis method, which allowed the synthesis of high C/S ratio C-S-H of controlled C/S, based on the conductivity's evolution during the synthesis [72]. A continuous monitoring system by conductimetry, which according to the evolution of the calcium concentration in the synthesis suspension, the targeted calcium concentration is maintained by replacing an adequate volume of the solution by a volume of water. C<sub>3</sub>S was used as a precursor, C-S-H with C/S ratio neighbouring 1.8 was obtained. Usually at C/S > 1.5 portlandite is currently produced in the synthesis. Chen *et al.* [8] reported the synthesis of C-S-H at C/S = 1.7 obtained by C<sub>3</sub>S hydration and a (6M) ammonium nitrate leaching.

We made the choice of a one pot synthesis for the C(-A)-S-Hs, powders using:

- Fumed silica aerosil 200 provided by Evonik industries 99.8% purity,  $\approx 200 \text{ m}^2.\text{g}^{-1}$
- CaO Alfa Aesar 99.95%
- CaOAl<sub>2</sub>O<sub>3</sub> Alfa Aesar 99.95%
- Ultrapure water Milli-Q (18.2M $\Omega$ .cm, 25°C)
- High-density polyethylene bottle sealed with polytetrafluoroethylene and parafilm

The syntheses were performed in a CO<sub>2</sub>-free glovebox, the powders were mixed and the water added thereafter. Once sealed the syntheses were kept agitated by rotation at 15 rpm and maintained at 22 C  $\pm$  2°C during 6 months.

The choice of the reactant was motivated by the absence of polluting elements that could alter the purity of the synthesis, which might be the case in the double decomposition method. Nonat & Lecoq's method was not required since the C/S ratios targeted for the powders were below 1.4. We've resorted to the one pot synthesis method, since it has not proven any consistent drawback related to the quality of the synthesis' product [68,69].

### 1.2.1.2 The pastes

The requirement of model materials in the form of pastes is essential to take into account the contribution of the gas diffusion during the carbonation and the contribution of the microstructure and medium [73] on the carbonation reaction.

Different ways to obtain monolithic cementitious materials have been documented [8,70,74]. Several works relied on compacted powders. Ensuring first a minimal water content by imposing a certain RH to the powders (obtained by one of the synthesis methods detailed previously in the powder obtention part), the powders are then pressed together. This approach does not allow however for the full range of durability study methods. For instance, leaching studies involve the immersion of the compacted powders in suspension. This was reported to induce disintegration.

It is thus preferable to work on true pastes obtained by hydration of anhydrous cement. Recent studies reported the fabrication of pastes using calcium oxide and silica gel [74].

We aimed at model pastes that cover the full range of cementitious material alkalinity including Low-pH ones. The requirement of Low-pH model pastes implied the incorporation of high amount of reactive silica in the pastes. We made the choice of a suspension of dispersed nanosilica with 50 wt% of water. Silica fine particles are adequate for

a high reaction rate which shortens the time period to reach the highest reactivity. The calcium source was chosen to be a pure phase of usual cement anhydrous phase, the  $C_3S$  found in alite. The choice of an anhydrous cement phase is justified by the will to generate paste with microstructure generated by hydration as it is the case in cementitious materials. The synthesis route retained involves as calcium source the  $C_3S$  and a suspension of nanosilica as silica source. The components of the pastes are listed thereafter:

- $C_3S$  (Mineral Research Processing) produced in France
- Rheomac AS 150, provided by BASF
- Superplasticiser (MasterGlenium Sky 537 from BASF)
- Water

The content of silica was adjusted to obtain pastes of  $C/S = 0.80, 0.87, 0.95, 1.40$  and  $3.00$ . An increased viscosity was evidenced by the pastes with decreasing  $C/S$ . The use of a high surface silica induced a high-water demand and an increase of viscosity of the fresh mix. The viscosity increase was overcome using polycarboxylate superplasticizer. The superplasticizer content was increased empirically to ensure the continuous mobilization of the fresh mix without the formation of segregated silica gel during the fabrication. The water demand imposed paste with high water/ binder ( $C_3S$ +Silica) ratio ( $0.5$ - $0.8$ ). The detail of the fabrication of the pastes is the focus of the first chapter (2<sup>nd</sup> part of the manuscript), which is dedicated to the model pastes.

Two samples sizes were fabricated using two different moulds size. The first type was dedicated to chemical and microstructural analyses ( $\varnothing = 30$  mm  $H = 120$  mm), the second sample's type was devoted to shrinkage measurement ( $\varnothing = 14$  mm  $H = 90$  mm). The pastes were cured first in their mould for 1 month, unmolded then placed in curing water for two months ( $\approx 25^\circ C$ ). The leaching of the samples was limited by using a curing water containing grounded samples in deionized water for  $C/S < 3.0$  pastes.  $C_3S$  pastes curing solution was fabricated adding calcium oxide to deionized water.



**Figure 9: Fabricated pastes  $C/S = 3$ : shrinkage samples ( $\varnothing = 14$  mm  $H = 90$  mm) and remaining samples ( $\varnothing = 30$  mm  $H = 120$  mm) cut to generate samples of different lengths for different carbonation terms.**



**Figure 10: Pastes covered with adhesive aluminium foil after conditioning and prior to carbonation.**

In addition to the model materials one of the full scale sealing project's low-pH formulation was fabricated, the latter is part of the retained materials in the French disposal framework. The formulation was based on equal wt% content on cement and silica fume (**Table 6**).

**Table 6: Details of the formulation and some properties of the industrial LAC (50%CEM I + 50%SF)**

Industrial material	LAC
Cement (g)	714.6
Silica fume (g)	714.6
Added water (g)	857.6
w/b ratio	0.6
Superplasticiser (wt. % of binder)	0.9
Batching time (min)	5
C/S atomic ratio (mean/median/ $\sigma$ )	0.84/0.88/0.2
Al/Si atomic ratio (mean/median/ $\sigma$ )	0.04/0.04/0.03
Porosity (80°C-105°C)	52-55%

The cement a CEM I 52.5 N from Lafarge, Le Teil (France), (composition detailed in appendix D in the first chapter) and a mechanically densified silica fume provided by Condensil (S95 DM) were used. The workability of the fresh mix was adjusted by a superplasticiser a MasterGlenium Sky 537 provided by BASF. The same curing period was retained all pastes (models pastes and industrial LAC). The curing solution was obtained by crushing some samples in deionized water to limit eventual leaching. The evolution of the properties of this material is discussed in the third chapter, which focuses on the carbonation of model materials.

Figure 11 displays the pore size distribution for two uncarbonated pastes the LAC and the model C-S-H paste C/S = 1.4). Despite a similar total porosity obtained by water gravimetry and oven drying for both pastes (52% at 80°C and 56% at 105°C for C/S = 1.4), the industrial LAC demonstrated a broad distribution including a refined porosity with a critical pore entry diameter around 4 nm against 20 nm for the C-S-H paste. The industrial LAC's and the C-S-H pastes' pore entry diameter threshold is nonetheless observed at similar values, around 30 nm.

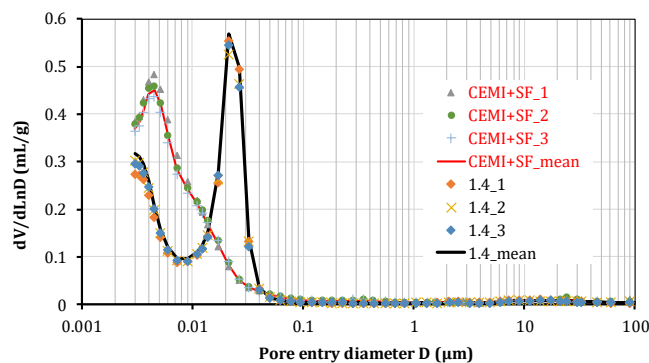


**Figure 11: Comparison between the pore size distribution obtained by mercury intrusion porosimetry for the uncarbonated CEM I + SF (silica fume) and the model C-S-H paste C/S = 1.4 (3 samples were analysed for each formulation)**

### 1.2.2 Methods

#### Carbonation device

Prior to carbonation the samples were maintained in desiccator equipped with fans to avoid humidity gradient, the desiccator's RH was maintained by saturated solution of  $\text{Mg}(\text{NO}_3)_2$  salt which generates a RH of 54% at 20°C. The desiccator's room temperature was at  $21^\circ\text{C} \pm 2^\circ\text{C}$ . Once the sample reached a weight loss which correlates with the water loss expected on desorption isotherm. The samples were covered with an aluminium adhesive foil to allow unidirectional carbonation through one of the cylinders' end face. The accelerated carbonation was implemented in an experimental set-up developed by Drouet [16], which includes a climatic chamber and a control system for  $\text{CO}_2$  partial pressure. The carbonation conditions were set to  $25^\circ\text{C} \pm 0.2^\circ\text{C}$ ,  $P_{\text{CO}_2}$ :  $3.0\% \pm 0.2\%$ , and 55% RH.

#### X-Ray Diffraction

X ray diffraction allows the characterization of the materials' long-range order, so to say their crystallinity. Bragg's law expresses the condition of wave diffraction on ordered atomic planes.

$$n\lambda = 2d_{(hkl)} \sin(\theta) \quad \text{E- 13}$$

where  $\lambda$  is the wavelength of the diffracted intensity,  $d_{(hkl)}$  the distance between two diffraction planes of the same family identified by hkl Miller index,  $\theta$  the angle between two reflection planes (of the same hkl family) and the incident and diffracted beams.

The qualitative approach aimed at the control of the powders' syntheses, the verification of the absence of undesired phases, the presence of expected phases (C-S-Hs, CH, the calcium carbonates). The diffractograms obtained are compared to reference phases' diffractograms in the ICDD database.

Several quantitative approaches exist based on the use of an internal/ external standard, or the Rietveld method. An adequate quantification is hard to obtain in cementitious materials due to the multiphasic contain and especially the presence of nano-crystalline phase such as C(-A)-S-H and unreacted amorphous silica. The use of a significant amount of internal standard is required but this led to a dilution of the specimen. We thus preferred to conduct a Rietveld analysis despite its weaknesses. For example, the lack of a model structure that fully describes the C-A-S-H phase limits the accuracy of the phase quantification. We resorted to Richardson' files [75] because, although not allowing a perfect consideration of C-A-S-Hs' structural features, they proved to be satisfactory in our Rietveld analyses ran through HighScore Plus software.

Data were acquired on a PANalytical X'Pert device equipped with a copper source (45 kV, 40 mA) and using copper  $K\alpha$  radiation ( $\lambda = 1.54 \text{ \AA}$ ). Acquisitions were made with a Bragg-Brentano geometry and in a  $\theta$ - $\theta$  configuration. The detector used an X'Celerator, allowed a wide-angle scan ( $5^\circ$  to  $55^\circ$ ) with an angular step of  $0.017^\circ$  in less than 20 minutes.

#### Water vapour sorption

The C-S-H content is determined following a method derived from the one proposed by Olson and Jennings [13] and relying on water vapour sorption obtained on a DVS Advantage device. Acquisitions were run at  $25^\circ\text{C} \pm 0.1^\circ\text{C}$ , and



the automatic 'dm/dt' mode was set for the relative humidity (RH) decrease. Prior to analysis the pastes were crushed and sieved in a CO<sub>2</sub>-free glove box. Particles exceeding 150 µm were eliminated by sieving and the powders saturated using deionized water. More details can be found in [76]. Olson and Jennings [13] assumed a constant specific surface irrespective of the C/S ratio, and that the amount of adsorbed water at 20% RH correlates linearly with the C-S-H surface. They consequently associate a quantity of adsorbed water to an amount of C-S-H with a calibration on a system where the amount of C-S-H can be obtained independently by mass balance (namely a C<sub>3</sub>S paste). In our case, the adsorbed water at 20% RH, estimated by an isotherm sorption, is compared to the data of Olson and Jennings to obtain the C-S-H content in mol per Litre of paste. Despite relying on numerous hypotheses, this method provides consistent trends when comparing cementitious materials with increasing content on supplementary materials [6].

### Water gravimetry

The samples' saturated density ( $d_{sat}$ ) were measured by hydrostatic weighing (E- 14). They were considered as saturated once a constant weigh was obtained. Their saturated weigh, in air ( $m_{air}$ ) and in water ( $m_w$ ) were measured. Part of the saturated samples were then dried at 80 and 105°C (to allow comparison with literature) and weight ( $m_{T^{\circ}C}$ ) to estimate their porosity  $\phi$  (E- 15).

$$d_{sat} = \frac{m_{air}}{m_{air} - m_w} \quad \text{E- 14}$$

$$\phi = \frac{m_{air} - m_{T^{\circ}C}}{m_{air} - m_w} \quad \text{E- 15}$$

### X-Ray micro computed tomography µ-CT:

An acquisition of radiograph on 0-360° domain is obtained during the rotation of the sample. The radiographs are obtained by processing the attenuated intensity by the sample using Beer-Lambert law. The attenuation of the incident beam by the sample is relative to the density of the phases on the beam path, are accounted the mean atomic number and the energy beam which affect the phase absorption coefficient. 3D representation of the lineic absorption coefficient allows the reconstruction of the studied sample. Analyses were run on a Skyscan 1173 device with a flat detector. The conditions were set as follow: the angular step was defined to 0.4°, the operating voltage ranged between 115-130 kV, an exposure time of 1100 ms was chosen, as well as an averaging frame between 8-10. An images pixel size of 16.8 µm was acquired.

Properties such as the homogeneity of the pastes (distribution of phases, bubbles), the presence of crack and their propagation or the position of carbonation front were accessed. The limitation is mainly the resolution and the contrast in term of grey level which allows to differentiate one feature to its surroundings. The approach adopted to delimit the front area is based on the logistic function detailed thereafter.

$$\text{Logistic function used} = A + \frac{B}{(1 + Ce^{(-D+F)^2})} \quad \text{E- 16}$$

**A:** sigmoid lower y-axis value, **B:** difference between the sigmoid higher y-axis value and its lower y-axis value, **C:** random factor, **D:** grey level value associated to the position fitted, **F:** sigmoid midpoint

In **Figure 12** the beginning of the front is taken as  $1.04A$  and the end of the front as  $0.996(A+B)$ . The reciprocal of the logistic function yields the position associated to the beginning and the end of the front.

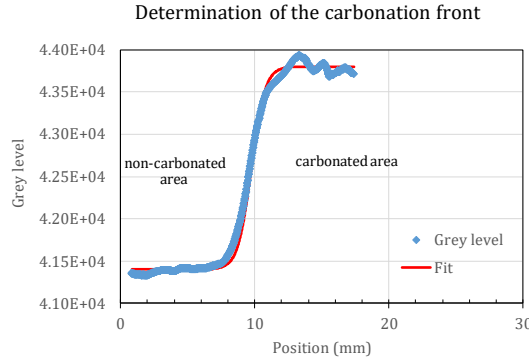


**Figure 12: Example of a logistic function fit for the grey level transition area of C/S=1.4 carbonated sample.**

The carbonation of the pastes led to a densified carbonated area with a higher grey level value. The grey level values extracted correspond to the mean grey value per slice 2 voxels thick.

### Mercury intrusion Porosimetry

The method is based on the application of an external mercury pressure. Mercury is a non-wetting liquid, which contact angle is higher than  $90^\circ$ . Its penetration is thus not favoured due to its surface tension. The pressure applied is the mean to control the intrusion (E- 17). The simplification of E- 17 gives E- 18 from which the distribution of pore size openings can be obtained from the cumulative amount of intruded mercury at a given pressure.

$$-P_c = \gamma \left( \frac{1}{r_m} + \frac{1}{r_{m'}} \right) \quad \text{E- 17}$$

$$P = - \frac{4\gamma \cos(\theta)}{d} \quad \text{E- 18}$$

where  $P_c$  is the capillary pressure,  $P$  the mercury pressure applied,  $\gamma$  the Hg surface tension at  $25^\circ\text{C}$  in the void ( $0.485 \text{ N/m}$ ),  $r_m$  and  $r_{m'}$  the meniscus curvature radii,  $\theta$  contact angle  $\approx 140^\circ$ , and  $d$  is the diameter.

The geometrical approach does not consider several experimental aspects such as the modification of the contact angle during the analysis due the changes in chemistry and the contamination of the surfaces. Furthermore, a unique pore shape is assumed. The method masks topological characteristics of the pore network such as its roughness (influence on the surface/volume ratio), tortuosity, and interconnection rate. An important bias encountered is the probable alteration of the material during the analysis since the unfilled part of the material is under vacuum, and the part filled is undergoing localized pressure; this obviously generates a field constraint with strong gradients. Nevertheless, experiences on brittle porous medium such as silica aerogel hasn't shown destruction of the porous

media over applied pressure [77]. Knowing the bias of the methods, only tendencies are extracted, presuming that those discrepancies are similarly expressed on all the samples. The samples were crushed then immersed into liquid nitrogen before 24 hours freeze-drying. Acquisitions were made on a Micromeritics Autopore IV.

## NMR

Each type of NMR experiment is specifically described in the concerned chapter (see the 2<sup>nd</sup> part), only the general principle of  $^{29}\text{Si}$ ,  $^{27}\text{Al}$  MAS NMR need to be introduced in this section.

The nuclear magnetic resonance analysis of solids informs on the chemical environment of the nucleus probed, such as the coordination and the type of nuclei interacting. The interaction between a non-zero spin isotope and an external magnetic field ( $B_0$ ) generates at equilibrium a diamagnetic spin magnetization aligned with the external magnetic field. When put out of equilibrium, the coupling between this spin magnetization and the external field induces a precession at the frequency  $\omega_0$  called the Larmor frequency. This precession is proportional to the gyromagnetic ratio ( $\gamma$ ) of the nucleus and the intensity of the magnetic field:

$$\omega_0 = -\gamma B_0 \quad \text{E- 19}$$

The presence of electrons in the environment of the nuclei induces a shielding of the magnetic field. This phenomenon is observed through a shift in the precession frequency of the considered nucleus (E- 20).

$$\omega_{cs} = -\gamma(1 - \alpha)B_0 \quad \text{E- 20}$$

The chemical shift is expressed in proportion of the Larmor frequency in ppm:

$$\delta_{cs} (ppm) = \frac{\omega_{cs}}{\omega_0} \times 10^6 \quad \text{E- 21}$$

The shielding observed depends on the relative orientation of the field with the principal axis of the considered interaction (for example the chemical shift). Within a powder there is a distribution of the molecular orientation, which generates a distribution of the chemical shift due to the anisotropy of the system. In order to limit the broadening of the resonances, the powders are spun at an angle corresponding to the diagonal of a cube with respect to the direction of the field. This method is called magic angle spinning (MAS). The aim is the access to the isotropic component of the chemical shift.

## TGA

Thermogravimetric analysis is run on a Netzsch STA 409 PC Luxx apparatus for the quantification of the different hydrated phases present in the cementitious materials. The calcium carbonates formed by the carbonation as well could be identified and quantified. The domains associated to the different losses are thereafter specified, one can see the overlapping of several domains [78]:

- 110-130°C: degradation of the C-S-H and the Aft, the water loss associated to the C-S-H is extended until 550°C
- 170-190°C: AFm degradation
- 230-240°C: decomposition of the gypsum
- 300-450°C: katoite dehydroxylation
- 350-450°C: brucite decomposition
- 400-600°C: portlandite dehydroxylation

- 575-579°C: transformation of  $\alpha$ -quartz into  $\beta$ -quartz
- 600-900°C: decarbonation
- 780-800°C: decomposition of the magnesian part of the dolomite
- 800-1200°C: transformation of the C-S-H into  $\alpha$  and  $\beta$  wollastonite

The multiphasic composition of the cementitious materials prevents an accurate quantification of each phase, therefore the tracking of the evolution of a specific component. However, in our case, due to the relatively simple chemistry (C-S-H, portlandite, carbonates and amorphous silica), the identification, the quantification and the tracking of the evolution on content of specific phases was possible. A STA 409 PC Luxx device was used, the loss associated to 120 mg of powder was recorded under a nitrogen flow of 80 ml/min, and a heating rate of 10°C/min between 25°C and 1150°C.

### **SEM-EDS**

Scanning electron microscopy allowed the investigation on the texture of our samples. Analysis on secondary electron (SE) mode and on the backscattered electron (BSE) mode inform on the morphology and the chemical contrast respectively. The latter mode was used combined with energy dispersive X ray analysis (EDS) which allowed the elemental chemical analysis. Analyses were performed on a ZEISS EVO MA15 microscope equipped with a Quantax detector for chemical mapping. The samples were freeze dried and mounted using epoxy resin prior to the polishing with an alcohol-based diamond suspension. Data were acquired at 15 kV and 1 nA, a grid of 609 points, and recorded at 200 $\times$  magnification.

### **Gas diffusion**

We resorted to through diffusion experiment on discs ( $\varnothing = 30.0$  mm H = 8 mm), to estimate the gas diffusion coefficient. The discs were placed between an upstream chamber filled with synthetic air (20% O<sub>2</sub> and 80% N<sub>2</sub>) and a downstream chamber filled with 100% N<sub>2</sub>.

### **Shrinkage measurement**

The length variation associated to drying and carbonation were measured by linear variable differential transformer (LVDT sensors) manufactured by Solartron Metrology. The analysis set up included the sensors equipped with a control module, an electrical supply module and a data acquisition computer. For the purpose of this study, dedicated samples with smaller diameter were fabricated ( $\varnothing = 14$  mm H = 90 mm), in order to minimize the drying period.



**Figure 13: Experimental set up in climatic chamber for shrinkage measurement.**

### 1.3 Discussion on the methods used

#### Chemistry and mineralogy

Some properties related to durability such as the mechanical behaviour result from the chemical properties of the materials. The multiscale organization of the materials requires different probes to unveil the materials properties. Methods such as pH measurement reflect the interaction between dissolved species in the porous structure and the solid, which is an average picture of the alkalinity developed within the materials. The chemical elemental composition analysis, which lies at a reduced scale compared to pH measurement, is obtained by running SEM-EDS analysis, the latter allows a spatial discrimination based on the composition. A  $\mu\text{m}^3$  resolution is both approached and limited by the electron-matter interaction. To reach information at the nanometer scale we made use of NMR. The latter informs both on the chemical composition and the structural organization of the C(-A)-S-H, based on nuclei endowed with a spin. In the framework of this study  $^{27}\text{Al}$  and  $^{29}\text{Si}$  environment were probed, properties such as silicates mean chain length, aluminium incorporation and chemical composition defined as C/S and Al/Si ratios. Moreover, the detection of residual content on amorphous or nanocrystalline phases such as silica gel or calcium aluminates phases were accessible.

#### Microstructure and gas transport:

Cementitious materials' microstructures are strongly affected by the carbonation since changes in hydric properties, clogging, and coarsening happen at different extent according to the chemistry and the initial microstructure. The microstructural properties such as the porosity were probed with complementary techniques to follow up the changes induced by carbonation. An estimation of the total porosity is accessible thanks to oven drying and water gravimetry but the distribution of the pores volume is only accessible with MIP. Since the porosities below 3 nm are not probed by MIP, the combination of those methods allows access to the full range of porosity demonstrated by the materials. The recourse to  $\mu\text{CT}$  allows at a higher scale ( $\approx 16 \mu\text{m}$  considering our sample size) the access to features such as cracks, inhomogeneity including the presence of bubbles or unreacted materials. Information related to the texture by an imaging technique at higher resolution was assessed thanks to scanning electron microscopy. However contrarily to the 3D imaging yielded by  $\mu\text{CT}$ , the information obtained by SEM mapping is limited to the surface. Gas diffusion experiment informs on the nature and the evolution of the

pores network especially in the case of carbonation where phenomena such as clogging, pore coarsening and cracking are expected.

#### IV. BIBLIOGRAPHY

- [1] C. Cau Dit Coumes, S. Courtois, D. Nectoux, S. Leclercq, X. Bourbon, Formulating a low-alkalinity, high-resistance and low-heat concrete for radioactive waste repositories, *Cem. Concr. Res.* 36 (2006) 2152–2163. doi:10.1016/j.cemconres.2006.10.005.
- [2] M. Codina, C. Cau-dit-Coumes, P. Le Bescop, J. Verdier, J.P. Ollivier, Design and characterization of low-heat and low-alkalinity cements, *Cem. Concr. Res.* 38 (2008) 437–448. doi:10.1016/j.cemconres.2007.12.002.
- [3] J.L. García Calvo, A. Hidalgo, C. Alonso, L. Fernández Luco, Development of low-pH cementitious materials for HLRW repositories, *Cem. Concr. Res.* 40 (2010) 1290–1297. doi:10.1016/j.cemconres.2009.11.008.
- [4] B. Lothenbach, G. Le Saout, M. Ben Haha, R. Figi, E. Wieland, Hydration of a low-alkali CEM III/B–SiO<sub>2</sub> cement (LAC), *Cem. Concr. Res.* 42 (2012) 410–423. doi:10.1016/j.cemconres.2011.11.008.
- [5] M. Auroy, S. Poyet, P. Le, J.-M. Torrenti, U. Paris-est, D. Matériaux, B. Newton, P. Le Bescop, J.-M. Torrenti, T. Charpentier, M. Moskura, X. Bourbon, Comparison between natural and accelerated carbonation (3% CO<sub>2</sub>): Impact on mineralogy, microstructure, water retention and cracking, *Cem. Concr. Res.* 109 (2018) 64–80. doi:10.1016/j.cemconres.2018.04.012.
- [6] M. Auroy, S. Poyet, P. Le Bescop, J.M. Torrenti, T. Charpentier, M. Moskura, X. Bourbon, Impact of carbonation on unsaturated water transport properties of cement-based materials, *Cem. Concr. Res.* 74 (2015) 44–58. doi:10.1016/j.cemconres.2015.04.002.
- [7] A. Kronlöf, Injection grout for deep repositories-Low pH cementitious grout for larger fractures: Testing technical performance of materials, Posiva Oy, Olkiluoto, Finland. Posiva Work. Rep. 45 (2004).
- [8] J.J. Chen, J.J. Thomas, H.F.W. Taylor, H.M. Jennings, Solubility and structure of calcium silicate hydrate, *Cem. Concr. Res.* 34 (2004) 1499–1519. doi:10.1016/j.cemconres.2004.04.034.
- [9] E. Tajuelo Rodriguez, I.G. Richardson, L. Black, E. Boehm-Courjault, A. Nonat, J. Skibsted, Composition, silicate anion structure and morphology of calcium silicate hydrates (C-S-H) synthesised by silica-lime reaction and by controlled hydration of tricalcium silicate (C<sub>3</sub>S), *Adv. Appl. Ceram.* 114 (2015) 362–371. doi:10.1179/1743676115Y.0000000038.
- [10] A. Nonat, X. Lecoq, The Structure, Stoichiometry and Properties of C-S-H Prepared by C3S Hydration Under Controlled Condition, in: P. Colombet, A.-R. Grimmer, H. Zanni, P. Sozzani (Eds.), *Nucl. Magn. Reson. Spectrosc. Cem. Mater.*, Springer, 1998: pp. 197–207. doi:10.1007/978-3-642-80432-8\_14.
- [11] H.F.W. Taylor, *Cement chemistry*, Limited, Academic press, 1990.
- [12] H.M. Jennings, A model for the microstructure of calcium silicate hydrate in cement paste, *Cem. Concr. Res.* 30 (2000) 101–116. doi:10.1016/S0008-8846(99)00209-4.
- [13] R.A. Olson, H.M. Jennings, Estimation of C-S-H content in a blended cement paste using water adsorption, *Cem. Concr. Res.* 31 (2001) 351–356. doi:10.1016/S0008-8846(01)00454-9.
- [14] M. Codina, C. Cau-dit-Coumes, J. Verdier, P. Le Bescop, Formulation et caractérisation de bétons bas pH, *Rev. Eur. Génie Civ.* 11 (2007) 423–435. doi:10.1080/17747120.2007.9692937.
- [15] A. Dauzères, Etude expérimentale et modélisation des mécanismes physico-chimiques des interactions béton-argile dans le contexte du stockage géologique des déchets radioactifs (in French), Ph.D. Thesis, University of Poitiers, 2010.
- [16] E. Drouet, Impact de la température sur la carbonatation des matériaux cimentaires - prise en compte des transferts hydriques (in French), Ph.D. Thesis, Ecole Normale Supérieure de Cachan (France), 2010. <http://hal.archives-ouvertes.fr/tel-00618092/>.

- [17] M. Auroy, Impact de la carbonatation Sur les proprietes de transport d'eau des matériaux cimentaires (in French), Ph.D. Thesis, Université Paris-Est, 2014.
- [18] E. Holt, M. Leivo, T. Vehmas, Low-pH Concrete Developed for Tunnel End Plugs Used in nuclear waste containment, in: *Concr. Innov. Conf. 2014*, 2014: pp. 1–8.
- [19] S. Poyet, P. Le Bescop, C. Cau Dit Coumes, G. Touzé, J. Moth, Formulating a low-alkalinity and self-consolidating concrete for the DOPAS-FSS experiment, *Nuwcem* 2014. (2014) 1–16.
- [20] R. Dole, Leslie, C.H. Mattus, Low-pH concrete for use in the us high-level waste repository: part I overview, *Work. R&D Low-PH Cem. a Geol. Repos.* (2007) 31–39.
- [21] H.S. Harned, R. Davis, The Ionization Constant of Carbonic Acid in Water and the Solubility of Carbon Dioxide in Water and Aqueous Salt Solutions from 0 to 50°, *J. Am. Chem. Soc.* 65 (1943) 2030–2037. doi:10.1021/ja01250a059.
- [22] P.V. Danckwerts, *Gas-Liquid Reactions*, McGraw-Hill Book Company, 1970.
- [23] R. Segev, D. Hasson, R. Semiat, Rigorous modeling of the kinetics of calcium carbonate deposit formation - CO<sub>2</sub> effect, *AIChE J.* 58 (2012) 2286–2289. doi:10.1002/aic.12730.
- [24] M. Thiery, Modélisation de la carbonatation atmosphérique des matériaux cimentaires : Prise en compte des effets cinétiques et des modifications microstructurales et hydriques (in French), Ph.D. thesis, Ecole Nationale des Ponts et Chaussées, 2005. papers2://publication/uuid/F46A9B50-F797-4267-B6E6-FC248C0E9F75.
- [25] M.M. Reddy, L.N. Plummer, E. Busenberg, Crystal growth of calcite from calcium bicarbonate solutions at constant PCO<sub>2</sub> and 25°C: a test of a calcite dissolution model, *Geochim. Cosmochim. Acta.* 45 (1981) 1281–1289. doi:10.1016/0016-7037(81)90222-2.
- [26] T.M. Stawski, T. Roncal-Herrero, A. Fernandez-Martinez, A. Matamoros-Veloza, R. Kröger, L.G. Benning, “on demand” triggered crystallization of CaCO<sub>3</sub> from solute precursor species stabilized by the water-in-oil microemulsion, *Phys. Chem. Chem. Phys.* 20 (2018) 13825–13835. doi:10.1039/c8cp00540k.
- [27] H. Imai, T. Terada, T. Miura, S. Yamabi, Self-organized formation of porous aragonite with silicate, *J. Cryst. Growth.* 244 (2002) 200–205. doi:10.1016/S0022-0248(02)01616-0.
- [28] C. Rodriguez-Navarro, K. Kudłacz, Ö. Cizer, E. Ruiz-Agudo, Formation of amorphous calcium carbonate and its transformation into mesostructured calcite, *CrystEngComm.* 17 (2015) 58–72. doi:10.1039/C4CE01562B.
- [29] L. Black, C. Breen, J. Yarwood, K. Garbev, P. Stemmermann, B. Gasharova, Structural Features of C-S-H(I) and Its Carbonation in Air-A Raman Spectroscopic Study. Part II: Carbonated Phases, *J. Am. Ceram. Soc.* 90 (2007) 908–917. doi:10.1111/j.1551-2916.2006.01429.x.
- [30] D. Gebauer, A. Verch, H.G. Börner, H. Cölfen, Influence of selected artificial peptides on calcium carbonate precipitation - A quantitative study, *Cryst. Growth Des.* 9 (2009) 2398–2403. doi:10.1021/cg801292p.
- [31] P. Raiteri, J.D. Gale, Water Is the Key to Nonclassical Nucleation of Amorphous Calcium Carbonate, *J. Am. Chem. Soc.* 132 (2010) 17623–17634. doi:10.1021/ja108508k.
- [32] M.H. Nielsen, S. Aloni, J.J. De Yoreo, In situ TEM imaging of CaCO<sub>3</sub> nucleation reveals coexistence of direct and indirect pathways, *Science* (80-. ). 345 (2014) 1158–1162. doi:10.1126/science.1254051.
- [33] R. Innocenti Malini, Y.G. Bushuev, S.A. Hall, C.L. Freeman, P.M. Rodger, J.H. Harding, Using simulation to understand the structure and properties of hydrated amorphous calcium carbonate, *CrystEngComm.* 18 (2016) 92–101. doi:10.1039/C5CE01536G.
- [34] M. Saharay, R.J. Kirkpatrick, Water dynamics in hydrated amorphous materials: a molecular dynamics study of the effects of dehydration in amorphous calcium carbonate, *Phys. Chem. Chem. Phys.* 19 (2017) 29594–29600. doi:10.1039/C7CP04683A.
- [35] D. Gebauer, P.N. Gunawidjaja, J.Y.P. Ko, Z. Bacsik, B. Aziz, L. Liu, Y. Hu, L. Bergström, C.W. Tai, T.K. Sham, M. Edén, N. Hedin, Proto-calcite and proto-vaterite in amorphous calcium carbonates, *Angew. Chemie - Int. Ed.*

49 (2010) 8889–8891. doi:10.1002/anie.201003220.

- [36] A. Fernandez-Martinez, B. Kalkan, S.M. Clark, G.A. Waychunas, Pressure-induced polyamorphism and formation of “aragonitic” amorphous calcium carbonate, *Angew. Chemie - Int. Ed.* 52 (2013) 8354–8357. doi:10.1002/anie.201302974.
- [37] R. Demichelis, P. Raiteri, J.D. Gale, R. Dovesi, A new structural model for disorder in vaterite from first-principles calculations, *CrystEngComm.* 14 (2012) 44–47. doi:10.1039/C1CE05976A.
- [38] A.M. Dunster, An investigation of the carbonation of cement paste using trimethylsilylation, *Adv. Cem. Res.* 2 (1989) 99–106. doi:10.1680/adcr.1989.2.7.99.
- [39] Y. Fang, J. Chang, Microstructure changes of waste hydrated cement paste induced by accelerated carbonation, *Constr. Build. Mater.* 76 (2015) 360–365. doi:10.1016/j.conbuildmat.2014.12.017.
- [40] C.J. Goodbrake, J.F. Young, R.L. Berger, Reaction of beta-dicalcium silicate and tricalcium silicate with carbon dioxide and water vapor, *J. Am. Ceram. Soc.* 62 (1979) 168–171. doi:10.1111/j.1151-2916.1979.tb19046.x.
- [41] Z. Šauman, Carbonization of porous concrete and its main binding components, *Cem. Concr. Res.* 1 (1971) 645–662. doi:10.1016/0008-8846(71)90019-6.
- [42] D.J. Anstice, C.L. Page, M.M. Page, The pore solution phase of carbonated cement pastes, *Cem. Concr. Res.* 35 (2005) 377–383. doi:10.1016/j.cemconres.2004.06.041.
- [43] G.W. Groves, A. Brough, I.G. Richardson, C.M. Dobson, Progressive changes in the structure of hardened C3S cement pastes due to carbonation, *J. Am. Ceram. Soc.* 74 (1991) 2891–2896.
- [44] A. Morandea, M. Thiéry, P. Dangla, Investigation of the carbonation mechanism of CH and C-S-H in terms of kinetics, microstructure changes and moisture properties, *Cem. Concr. Res.* 56 (2014) 153–170. doi:10.1016/j.cemconres.2013.11.015.
- [45] C.M. Hunt, L.A. Tomes, Reaction of hardened portland cement paste with carbon dioxide, *J. Res. Natl. Bur. Stand. Sect. A Phys. Chem.* 66A (1962) 9. doi:10.6028/jres.066a.048.
- [46] L.J. Parrott, D.C. Kiloh, Carbonation in a 36 year old, in-situ concrete, *Cem. Concr. Res.* 19 (1989) 649–656. doi:10.1016/0008-8846(89)90017-3.
- [47] V.G. Papadakis, C.G. Vayenas, M.N. Fardis, Fundamental modeling and experimental investigation of concrete carbonation, *ACI Mater. J.* 88 (1991) 363–373. doi:10.14359/1863.
- [48] G.J. Verbeck, Carbonation of hydrated portland cement, *ASTM Spec. Tech. Publ.* 205 (1958) 17–36. doi:10.1520/STP39460S.
- [49] S.K. Roy, K.B. Poh, D. o. Northwood, Durability of concrete—accelerated carbonation and weathering studies, *Build. Environ.* 34 (1999) 597–606. doi:10.1016/S0360-1323(98)00042-0.
- [50] Y.F. Houst, F.H. Wittmann, Influence of porosity and water content on the diffusivity of CO<sub>2</sub> and O<sub>2</sub> through hydrated cement paste, *Cem. Concr. Res.* 24 (1994) 1165–1176. doi:10.1016/0008-8846(94)90040-X.
- [51] P. López-Arce, L.S. Gómez-Villalba, S. Martínez-Ramírez, M. Álvarez de Buergo, R. Fort, Influence of relative humidity on the carbonation of calcium hydroxide nanoparticles and the formation of calcium carbonate polymorphs, *Powder Technol.* 205 (2011) 263–269. doi:10.1016/j.powtec.2010.09.026.
- [52] S. Goñi, M.T. Gaztañaga, A. Guerrero, Role of cement type on carbonation attack, *J. Mater. Res.* 17 (2002) 1834–1842. doi:10.1557/JMR.2002.0271.
- [53] C.Y. Tai, F.-B. Chen, Polymorphism of CaCO<sub>3</sub>, precipitated in a constant-composition environment, *AIChE J.* 44 (1998) 1790–1798. doi:10.1002/aic.690440810.
- [54] A. Leemann, F. Moro, Carbonation of concrete: the role of CO<sub>2</sub> concentration, relative humidity and CO<sub>2</sub> buffer capacity, *Mater. Struct.* 50 (2017) 2–14. doi:10.1617/s11527-016-0917-2.
- [55] E. Drouet, S. Poyet, P. Le Bescop, J.-M. Torrenti, X. Bourbon, Carbonation of hardened cement pastes: Influence of temperature, *Cem. Concr. Res.* 115 (2019) 445–459. doi:10.1016/j.cemconres.2018.09.019.



- [56] Q. Shen, G. Pan, B. Bao, A method for calculating the carbonation degree of calcium-silicate-hydrate, *Adv. Cem. Res.* 30 (2018) 427–436. doi:10.1680/jadcr.16.00086.
- [57] H. Cui, W. Tang, W. Liu, Z. Dong, F. Xing, Experimental study on effects of CO<sub>2</sub> concentrations on concrete carbonation and diffusion mechanisms, *Constr. Build. Mater.* 93 (2015) 522–527. doi:10.1016/j.conbuildmat.2015.06.007.
- [58] Z. Shi, B. Lothenbach, M.R. Geiker, J. Kaufmann, A. Leemann, S. Ferreiro, J. Skibsted, Experimental studies and thermodynamic modeling of the carbonation of Portland cement, metakaolin and limestone mortars, *Cem. Concr. Res.* 88 (2016) 60–72. doi:10.1016/j.cemconres.2016.06.006.
- [59] M. Castellote, L. Fernandez, C. Andrade, C. Alonso, Chemical changes and phase analysis of OPC pastes carbonated at different CO<sub>2</sub> concentrations, *Mater. Struct.* 42 (2009) 515–525. doi:10.1617/s11527-008-9399-1.
- [60] G. Pan, Q. Shen, J. Li, Microstructure of cement paste at different carbon dioxide concentrations, *Mag. Concr. Res.* 70 (2018) 154–162. doi:10.1680/jmacr.17.00106.
- [61] V.T. Ngala, C.L. Page, Effects of carbonation on pore structure and diffusional properties of hydrated cement pastes, *Cem. Concr. Res.* 27 (1997) 995–1007.
- [62] M. Thiéry, P. Faure, A. Morandeau, G. Platret, J.-F. Bouteloup, P. Dangla, V. Baroghel-Bouny, Effect of carbonation on the microstructure and the moisture properties of cement-based materials, in: *Int. Conf. Durab. Build. Mater. Componets*, Porto (Portugal), 2011: pp. 1–8.
- [63] S.E. Pihlajavaara, Some results of the effect of carbonation on the porosity and pore size distribution of cement paste, *Matériaux Constr.* 1 (1968) 521–527. doi:10.1007/BF02473640.
- [64] G.K. Sun, J.F. Young, R.J. Kirkpatrick, The role of Al in C-S-H: NMR, XRD, and compositional results for precipitated samples, *Cem. Concr. Res.* 36 (2006) 18–29. doi:10.1016/j.cemconres.2005.03.002.
- [65] X. Pardal, I. Pochard, A. Nonat, Experimental study of Si-Al substitution in calcium-silicate-hydrate (C-S-H) prepared under equilibrium conditions, *Cem. Concr. Res.* 39 (2009) 637–643. doi:10.1016/j.cemconres.2009.05.001.
- [66] J. Haas, A. Nonat, From C-S-H to C-A-S-H: Experimental study and thermodynamic modelling, *Cem. Concr. Res.* 68 (2015) 124–138. doi:10.1016/j.cemconres.2014.10.020.
- [67] P. Faucon, J.C. Petit, T. Charpentier, J.F. Jacquinot, F. Adenot, Silicon substitution for aluminum in calcium silicate hydrates, *J. Am. Ceram. Soc.* 82 (1999) 1307–1312. doi:10.1111/j.1151-2916.1999.tb01912.x.
- [68] E. L'Hôpital, B. Lothenbach, G. Le Saout, D. Kulik, K. Scrivener, Incorporation of aluminium in calcium-silicate-hydrates, *Cem. Concr. Res.* 75 (2015) 91–103. doi:10.1016/j.cemconres.2015.04.007.
- [69] E. L'Hôpital, B. Lothenbach, D.A. Kulik, K. Scrivener, Influence of calcium to silica ratio on aluminium uptake in calcium silicate hydrate, *Cem. Concr. Res.* 85 (2016) 111–121. doi:10.1016/j.cemconres.2016.01.014.
- [70] J.J. Beaudoin, B. Patarachao, L. Raki, J. Margeson, R. Alizadeh, Length change of C-S-H of variable composition immersed in aqueous solutions, *Adv. Cem. Res.* 22 (2010) 15–20. doi:10.1680/adcr.2008.22.1.15.
- [71] K. Garbev, M. Bornefeld, G. Beuchle, P. Stemmermann, Cell dimensions and composition of nanocrystalline calcium silicate hydrate solid solutions. Part 2: X-ray and thermogravimetry study, *J. Am. Ceram. Soc.* 91 (2008) 3015–3023. doi:10.1111/j.1551-2916.2008.02601.x.
- [72] A. Nonat, X. Lecoq, The structure, stoichiometry and properties of CSH prepared by C3S hydration under controlled conditions, *Nucl. Magn. Reson. Spectrosc. Cem. Mater.* Springer, Berlin. (1998) 197–207. doi:10.1007/978-3-642-80432-8\_14.
- [73] M. Dietzsch, I. Andrusenko, R. Branscheid, F. Emmerling, U. Kolb, W. Tremel, Snapshots of calcium carbonate formation - A step by step analysis, *Zeitschrift Fur Krist. - Cryst. Mater.* 232 (2017) 255–265. doi:10.1515/zkri-2016-1973.
- [74] W. Kunther, S. Ferreiro, J. Skibsted, Influence of the Ca/Si ratio on the compressive strength of cementitious calcium-silicate-hydrate binders, *J. Mater. Chem. A* 5 (2017) 17401–17412. doi:10.1039/c7ta06104h.

- [75] I.G. Richardson, Model structures for C-(A)-S-H(I), *Acta Crystallogr. Sect. B Struct. Sci. Cryst. Eng. Mater.* 70 (2014) 903–923. doi:10.1107/S2052520614021982.
- [76] S. Poyet, K. Trentin, E. Amblard, The use of sorption balance for the characterization of the water retention curve of cement-cased materials, *J. Adv. Concr. Technol.* 14 (2016) 354–367. doi:10.3151/jact.14.354.
- [77] G.W. Scherer, D.M. Smith, D. Stein, Deformation of aerogels during characterization, *J. Non. Cryst. Solids.* 186 (1995) 309–315. doi:10.1016/0022-3093(95)00058-5.
- [78] V. Baroghel-Bouny, T. Chaussadent, G. Croquette, L. Divet, J. Gawsewitch, J. Godin, Méthode d’essai n°58: Caractéristiques microstructurales et propriétés relatives à la durabilité des bétons, (in French), Laboratoire Centrale des Ponts et Chaussées, 2002.

## **SECOND PART**

## **CHAPTER 1: MODEL SYSTEM FOR CEMENTITIOUS MATERIALS**

The first chapter presents our approach to obtain model cementitious material with controlled chemistry and mineralogy, in the form of pastes. A broad range of alkalinity was targeted to cover the domain of alkalinity encountered in cementitious materials with a peculiar effort on the obtention of low alkalinity materials, which was the main challenge due to the high silica content required. The properties of the fabricated are detailed and discussed. The features of the obtained materials are compared to industrial's one. The work presented in this part, especially the representativeness of the model system proposed was the prerequisite for the third chapter, which deals with the carbonation of model pastes.

It takes the form of an article submitted to *Cement and Concrete Research* currently under review

# Model synthetic pastes for low alkalinity cements

Kangni-Foli E.<sup>1,2</sup>, Poyet S.<sup>3</sup>, Le Bescop P.<sup>3</sup>, Charpentier T.<sup>4</sup>, Bernachy-Barbé F.<sup>3</sup>, Dauzères A.<sup>1</sup>, L'Hôpital E.<sup>1</sup>, Neji M.<sup>1</sup>, d'Espinose de Lacaillerie J.-B.<sup>2</sup>

(1) IRSN, Institute of Radiation Protection and Nuclear Safety, PSE-ENV/SEDRE/ LETIS, BP 17, F-92262 Fontenay Aux Roses, France

(2) Soft Matter Science and Engineering, UMR CNRS 7615, ESPCI Paris, Université PSL, 10 rue Vauquelin, 75005 Paris, France

(3) Den-Service d'Etude du Comportement des Radionucléides (SECR), CEA, Université de Paris-Saclay, F-91191, France

(4) NIMBE, CEA, CNRS, Université Paris-Saclay, CEA Saclay, F-91191 Gif-sur-Yvette Cedex, France

**Corresponding author:** Stéphane POYET

- Postal address: CEA Saclay, DEN/DANS/DPC/SECR/LECBA, B158 PC25, F-91191 Gif-sur-Yvette cedex, France.
- Email: [stephane.poyet@cea.fr](mailto:stephane.poyet@cea.fr)

**Declarations of interest:** none

## 1.1 Abstract

New cementitious materials with low calcium contents and pHs are being currently developed. To assess their durability with respect to Ordinary Portland cement, model synthetic pastes were designed. The goal is to obtain a simplified silica system that could be used in durability studies on materials with low calcium-to-silica ratios. To be as representative as possible, particular care was taken not only to formulate synthetic pastes with controlled and tailored chemistry, but also to examine their porous structures in comparison to cement pastes. The synthetic pastes made use of the well-known pozzolanic reaction between tricalcium silicate ( $C_3S$ ) and nanosilica, covering calcium-to-silica ratios ( $CaO/SiO_2$  or  $C/S$ ) from 0.8 to 3.0. The pure  $C_3S$  paste ( $C/S = 3.0$ ) contained C-S-H and portlandite, while pastes with  $C/S < 1.4$  only included C-S-H. The pore solution pH directly correlated with the  $C/S$  ratio. The pastes demonstrated a mineralogy, a C-S-H structure, a mean chain length (MCL) and poral network features that were similar to ordinary Portland cement (OPC) and low-alkalinity cementitious materials, depending on their  $C/S$  ratios. The main shortcoming was the necessity to use a high water-to-binder ratio and high superplasticizer dosage to maintain the workability of the synthetic pastes of high  $C/S$  ratios. This resulted in a higher pore volume for the synthetic pastes compared to low-alkalinity cement pastes.

**Keywords:** Calcium-Silicate-Hydrate (C-S-H) – Model pastes – Microstructure – Mineralogy

## 1.2 Introduction

Despite its crucial societal importance, the chemical durability of concrete structures is difficult to predict. This is largely due to the conjunction of a metastable phase assembly in the binder with a multiscale mechanical and porous structure. Correctly predicting crack propagation or reactive transport for example, needs a thorough understanding of the governing phenomena across several length scales [1]: the cement paste at the nano and meso scale [2], the aggregate and the interfacial transition zone at the meso scale [3,4], and finally the structure itself at the macroscale [5]. An unavoidable prelude to multiscale numerical modelling, thermodynamical or mechanical, is thus the understanding of the material at each scale taken separately.

Along this line, a lot of progress has been obtained in the last decades by focusing on concrete at the smallest scale: the mineralogical assembly of the cement paste [6–11]. An ordinary Portland cement (OPC) paste is in itself a highly complex heterogeneous system made of empty pores, water saturated pores, calcium silicate and aluminate oxides and carbonates. This has led researchers to further simplify the system by restricting the chemistry to the hydration products of calcium tri- ( $C_3S$ ) or di- ( $\beta$ - $C_2S$ ) silicates [12–19]. It was thus possible to deconvolute the impact of silicates and aluminates chemistry and successfully rationalize non trivial behaviour such as induction and creep [2,19]. However, new needs in term of reduction of  $CO_2$  emission or radioactive waste management has led to the development of low calcium cement formulation and in particular of the so-called low-alkalinity cements (LAC). Just as for OPC, the long-term prediction of the durability of LAC requires the design of a model chemical system reproducing the LAC main characteristics in terms of mineralogy and porosity.

For OPC, the paste formed by hydration of  $C_3S$  or  $\beta$ - $C_2S$  constitutes a relevant model of the calcium silicate sub-system since it leads to the precipitation of the two main calcium-bearing hydrates of Portland cements, namely calcium-silicate hydrate (C-S-H) and portlandite (calcium hydroxide CH). While C-S-H is largely responsible for the mechanical properties of the pastes, portlandite is a key component as it buffers the pH value at 12.5 (at 25°C). This latter fact is not true however for LACs which have very different specificities when compared to OPCs, the main one being a much smaller amount of portlandite and a pH of the poral solution (around 11) that is 1 to 3 points lower than in usual cements ( $\approx 13.5$ ) [20–24]. Such low pH values are commonly achieved by adding significant amounts of secondary cementing materials poor in calcium [25]. As a result, the C/S ratio of the paste is much lower than usual and the development of another chemical model is needed. This is particularly important since the long-term durability of LAC is still an open question, especially with respect to carbonation which is highly pH dependent. Consequently, the aim of this paper is to synthesize and describe model synthetic low-alkalinity porous systems representative of LAC pastes.

Several attempts have already been presented in the literature. Firstly, Chen *et al.* [26] exposed  $C_3S$  hardened pastes to ammonium nitrate (6M) in order to dissolve portlandite and lower the  $CaO/SiO_2$  ratio of the C-S-H. Alternatively, other authors created porous compacts of C-S-H powders obtained by aqueous mineral synthesis in excess water [27–36]. These methods demonstrated each, one main drawback inherent to their fabrication methods, *i.e.* the chemical attack or the mechanical compaction may induce a dissimilarity in the porous medium with regard to that generated by hydration. The chemical attack alters both the hydrates [37] and the pore network [38]. For compacts, comparison with hardened cement pastes does not provide strong evidence of their full representativeness [39]. In addition, compact disintegration subsequent to water immersion has already been observed, which makes them

unsuitable for transport modelling [29]. More recently, another approach was proposed by Kunther *et al.* [40] while studying the influence of the C/S ratio on the mechanical properties of C-S-H. It consists in using a combination of calcium oxide and amorphous silica mixed with water in presence of a superplasticiser (SP) to produce pastes with adjustable average C/S ratios. However, the chemical analysis of paste obtained in that manner reveals highly scattered C/S ratios. For instance, in [40], the paste with an average C/S ratio of 1.25 includes areas with C/S ratios of 0.80 and others with C/S of 1.50. This could be the expression of a limited control of the pastes' local chemistry. Moreover, the use of calcium oxide instead of C<sub>3</sub>S might have produced a microstructure not representative of a cement paste. Indeed, the hydration kinetics of cement pastes are largely controlled by the dissolution rate of C<sub>3</sub>S [41–43] which thus indirectly affects the development of hydrate microstructures [44–46]. Consequently, the use of calcium oxide instead of C<sub>3</sub>S, as in the study of Kunther *et al.* [40], induces different hydration kinetics and might lead to a paste model system not fully representative of usual LAC pastes.

In this study, keeping the idea of Kunther *et al.* [40] for obtaining pastes by exploiting the pozzolanic reaction of nanosilica but replacing CaO by C<sub>3</sub>S, we synthesized a series of model pastes of controlled chemistry, that is narrowly distributed C/S ratios of means between 0.8 and 3.0. We describe the methodology used to obtain the model pastes and detail their chemical, mineralogical, microstructural properties. Finally, we discuss their relevance as model subsystems for real LAC pastes.

### 1.3 Materials and methods.

#### *Synthesis of the model synthetic pastes.*

The pastes were prepared using stoichiometric amounts of finely ground C<sub>3</sub>S and amorphous nanosilica (SiO<sub>2</sub>) [47] in order to maximise the hydration rate. Triclinic C<sub>3</sub>S was provided by Mineral Research Processing (Meyzieu, France) and presented a specific area of 4600 cm<sup>2</sup>/g. The nanosilica was Rheomac AS 150, provided by BASF in the form of an aqueous suspension (50 wt%) with a median diameter D<sub>50</sub> equal to 100 nm. The workability of the fresh mix was adjusted using a commercial polycarboxylate superplasticiser (MasterGlenium Sky 537 from BASF). The pastes were prepared in batches of 1.40 L using a planetary mixer. Before using expensive C<sub>3</sub>S, tests were conducted using OPC with a similar specific surface to that of C<sub>3</sub>S. The tests aimed at determining the most appropriate batching sequence, water-to-binder ratio (w/b) and superplasticiser dosage. The resulting compositions were then tested using C<sub>3</sub>S and modified accordingly. The pastes incorporated significant amounts of nanosilica (up to 42 wt% for C/S = 0.80, see Table ); this induced two major issues: (1) the high water demand of nanosilica [48,49], and (2) the significant flocculation of nanosilica in the presence of calcium ions [50]. Consequently, the w/b ratio and the SP dosage had to be increased when the C/S decreased. In the case of the paste with a C/S ratio of 0.80, the w/b ratio and SP dosage reached high values, i.e. 0.78 and 8.0% respectively. Table 1 gives the formulation of the pastes that we were able to produce. The exact batching sequence is provided in the Supplementary materials section.

**Table 1: Composition of the model pastes for 1L**

<b>C/S ratio</b>	<b>3.00</b>	<b>1.40</b>	<b>0.95</b>	<b>0.87</b>	<b>0.80</b>
C <sub>3</sub> S (g)	1218.8	791.7	586.0	563.9	506.2
Colloidal silica slurry (g)	0.0	475.8	664.5	726.3	734.3
Added water (g)	609.4	379.9	264.1	239.3	244.5
w/b ratio	0.50	0.63	0.73	0.72	0.78
Superplasticiser (wt% of binder)	0.0	3.0	8.0	7.0	8.0
Batching time (min)	5	8	15	17	20

*Reference cement pastes.*

To assess the representativity of the synthetic pastes, two cement pastes based on CEM I were prepared: an OPC paste (CEM I) and a reference LAC, namely the T<sub>1</sub> blend (CEM I + SF + FA) proposed by Codina *et al.* [20] and studied later by Auroy *et al.* [23] (Table 2). The pastes components chemical analyses are reproduced from [20] in the Supplementary materials section.

**Table 2: Composition of the reference pastes for 1L**

<b>Reference materials</b>	<b>LAC (CEM I + SF + FA)</b>	<b>CEM I</b>
C/S ratio	0.53	3.3
Cement (g)	470.4	1396.7
Fly ash (g)	378.2	-
Silica fume (g)	406.8	-
Added water (g)	502.2	558.0
w/b ratio	0.40	0.40
Superplasticiser (wt. % of binder)	1.0	0.0
Batching time (min)	5	5

The SP dosage of the model synthetic pastes - especially for the lower C/S ratios (0.95, 0.87 and 0.80) - was quite high compared to the reference cement pastes. It should be pointed out that nanosilica was incorporated in the model paste, whereas silica fume and fly ash were used in the reference paste. This is why the SP dosage had to be increased to partially offset the water demand of the fine nanosilica particles.

*Mineralogical and chemical characterisation.*

The pH of the poral solution was measured using the *ex situ* leaching (ESL) method [51–53]. Owing to the absence of alkalis in the binders, ESL is known to yield similar results with respect to the reference method (extraction).



Thermogravimetric analysis (TGA) was performed using a Netzsch STA 409 PC Luxx apparatus. Analyses were run under a constant N<sub>2</sub> flowrate (80 ml/min). The weight losses were recorded from 25°C to 1150°C with a heating rate of 10°C/min. The quantification of portlandite (using tangential method), expressed in mol/l is obtained by considering the weight loss (between 420-580°C) associated to 120 mg of powdered sample of each model paste and their saturated volumes and apparent densities [54].

Powder X-ray diffraction (XRD) patterns were collected using an XPD PANalytical X'Pert diffractometer with a Bragg-Brentano geometry in an  $\theta$ - $\theta$  configuration and a Cu K $\alpha$  radiation source (45 kV, 40 mA). The use of an X'Celerator detector made possible to scan a 2 $\theta$  angular area ranging from 5° to 55° with an angular step of 0.017° in less than 20 minutes.

Silicon magic-angle spinning nuclear magnetic resonance (<sup>29</sup>Si MAS NMR) single-pulse data was collected using a Bruker Avance III 500 spectrometer operating at the Larmor frequency resonance of 99.3 MHz. Conditions were set to  $\pi/2$  pulses of 3.5  $\mu$ s, recycle delays of 20 s, spinning in 7 mm zirconia rotor at 5.5 kHz, and a minimum of 4000 scans for each spectrum. Tetramethylsilane was used as an external standard (0 ppm) to report the chemical shifts. The <sup>29</sup>Si MAS NMR results were processed using an internally developed software [55,56]. The spectra were fitted using gaussio-lorentzian line shapes with chemical shifts and widths kept identical for all pastes (Table 3 and appendix).

A ZEISS EVO MA15 scanning electron microscope (SEM) equipped with a Quantax detector for energy-dispersive spectrometry (EDS) was used for chemical mapping together with backscattered electrons (BSE) imaging. Acquisitions were collected at 15 kV and 1 nA. Pastes were freeze-dried, mounted using epoxy resin, and then polished using an alcohol-based diamond suspension. Grids of 609 points recorded at 200 $\times$  magnification were acquired for each sample. Due to the working voltage used, an electron-matter interaction depth of about 1-10  $\mu$ m within the material was generated.

#### *Microstructure characterisation.*

Microtomographic projections were acquired on a Bruker SkyScan1173 device equipped with a flat detector (2240  $\times$  2240 pixel) using the following operating conditions: 115-130 kV and 61-69  $\mu$ A. We obtained 360° scans with a rotational step of 0.3°, exposure time of 1100 ms, a frame averaging from 8 to 10, and images with a pixel size of 16.8  $\mu$ m.

The porosity and density of the pastes were obtained using the buoyancy method. Firstly, cylinders were re-saturated under vacuum and water [57], and their volume and weight were measured. They were then dried at 80°C in the presence of CaCl<sub>2</sub> and 105°C until constant weight was reached in order to compute porosity.

The pore entry size distribution (PSD) of the pastes was characterised using mercury intrusion porosimetry (MIP) with a Micromeritics Autopore IV. Prior to the tests, the specimens were crushed into centimetric pieces that were immersed in liquid nitrogen and then freeze-dried for 24 hours.

The C-S-H content of the pastes was estimated using the method proposed by Olson and Jennings [58] based on the quantification of the water content at 20% RH. Here we did not strictly follow the protocol recommended by Olson and Jennings. Rather we estimated the water content at 20% RH using a desorption experiment and a sorption balance (DVS Advantage). Acquisitions were run at  $25^{\circ}\text{C} \pm 0.1^{\circ}\text{C}$ , and the automatic 'dm/dt' mode was set for the relative humidity (RH) decrease. Prior to analysis the pastes were crushed and sieved in a  $\text{CO}_2$ -free glove box. Particles exceeding  $150\text{ }\mu\text{m}$  were eliminated by sieving and the powders saturated using deionized water. More details can be found in [59]. Such an approach offered a very significant gain of time but might have overestimated the C-S-H content due to the hysteresis between the adsorption and desorption path. The reader should also be aware that the method of Olson and Jennings assumes that the C/S ratio of the C-S-H is equal to 1.7 that is well suited for the  $\text{C}_3\text{S}$  and CEM I pastes but not for the others. This might have also induced uncertainties in the C-S-H quantification process. This point would require more attention.

## 1.4 Results

### *Reference cement pastes*

The characteristics of reference cement pastes, OPC or LAC were fully in line with what was expected from the literature and need not to be extensively reported here (see later the NMR spectra in Figure 3, the MIP in Figure 7, and XRD as Supplementary materials). The main difference in terms of mineralogy for the LAC compared to OPC is the absence of portlandite and the presence of calcium-bearing amorphous silica (unreacted product or silica gel). Furthermore, the low C/S ratio resulted in longer dreierketten chains in the C-S-H of the LAC cement paste. The porosity of the LAC paste presented a more refined pore structures with a closure of the porosity in the 10 to 100 nm range due to pore filling by precipitation of pozzolanic C-S-H.

### *Mineralogy of the model synthetic pastes*

X-ray diffractograms of the model pastes with C/S ratios from 0.80 to 3.00 are shown in Figure 1. The paste with a C/S ratio of 3.00 corresponds to the sample prepared without silica and, logically, its diffractogram corresponded to what was expected from the hydration of pure  $\text{C}_3\text{S}$ , *i.e.* it mainly showed diffraction peaks of the portlandite and C-S-H patterns [60–63]. Only traces of reflections corresponding to remaining  $\text{C}_3\text{S}$  were detected, indicating that hydration was almost complete [18]. Pastes with C/S ratios of 1.40 mainly displayed C-S-H signals and traces of portlandite and unreacted  $\text{C}_3\text{S}$ . Finally, for C/S ratios lower than 1.40, the diffractograms only exhibited the C-S-H diffraction pattern.

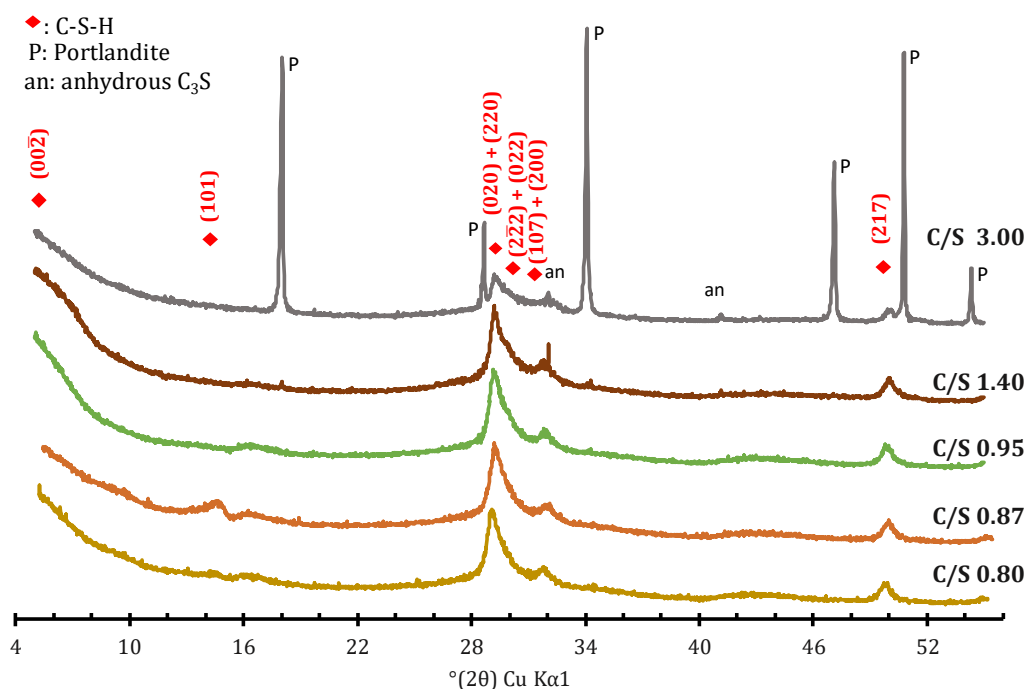


**Figure 1: XRD patterns of the synthetic pastes. As the C/S ratio decreases, Portlandite reflections progressively disappeared from the diffractogram. While still barely visible at C/S 1.4, they were absent for synthetic pastes of lower C/S ratios. C-S-H indexing was based on [64–66], ICDD files CH: 44-1481, C<sub>3</sub>S: 31-0301**

TGA confirmed the results obtained using XRD. The portlandite content measured in the C<sub>3</sub>S paste (7.3 mol/L of paste, cf. Table 5) was very close to that of a fully hydrated C<sub>3</sub>S paste (7.0 mol/L of paste with C-S-H with C/S = 1.70). For C/S ratios of 1.40, losses associated with C-S-H and traces of portlandite were observed (Figure 2). For C/S ratios lower than 1.40, the thermograms only exhibited signals related to C-S-H (see the thermogram of the C/S = 0.80 in Figure 2).

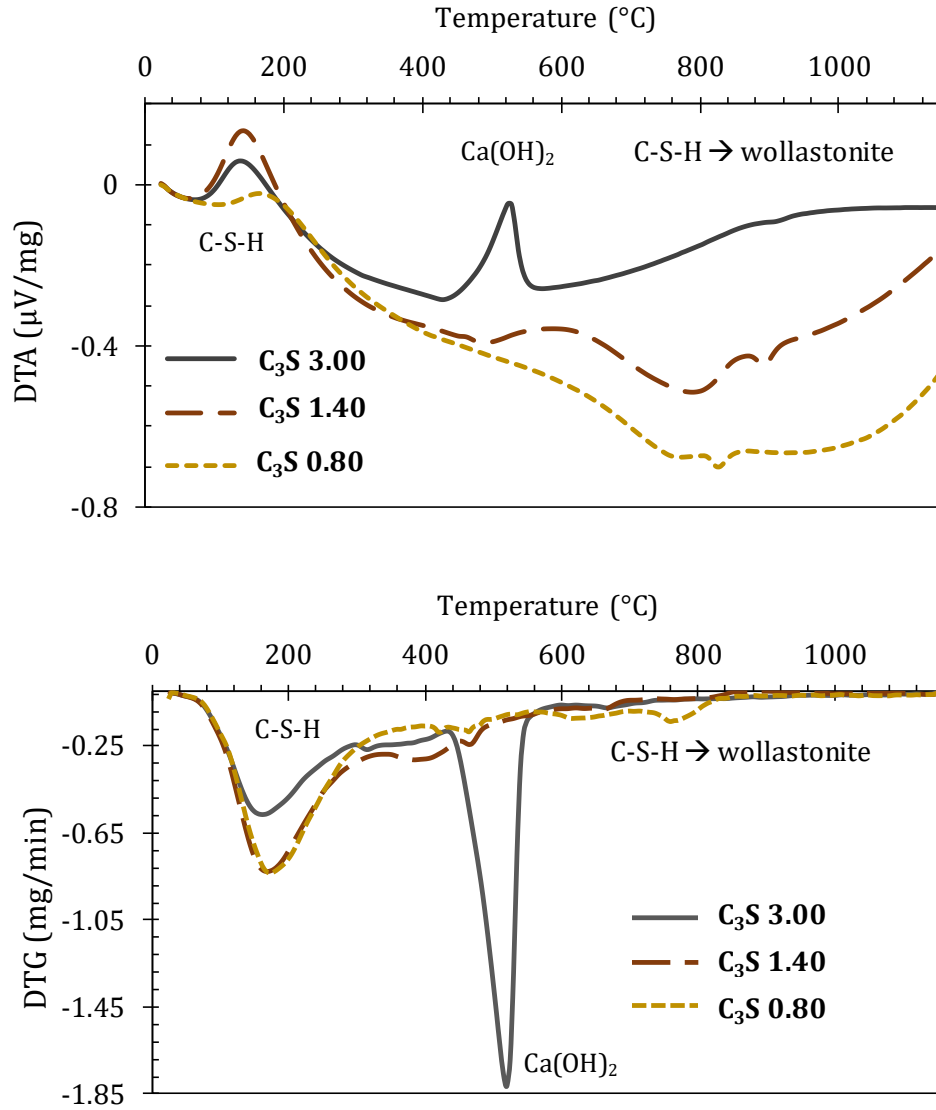


**Figure 2: DTA-DTG of the model pastes. Besides losses due the removal of water within C-S-H, the typical thermal loss of portlandite was massively observed in the  $C_3S$  paste. In contrast, only a residual portlandite content was evidenced in the  $C/S = 1.40$  paste, and it totally disappeared at lower  $C/S$  ratios.**

The  $^{29}\text{Si}$  MAS-NMR spectra of the pastes are shown in Figure 3. The spectra of the higher  $C/S$  ratios (3.00 and 1.40) samples exhibited the usual resonances attributed to silica tetrahedra sharing one ( $Q^1$ ) or two ( $Q^2$ ) oxygen atoms with another tetrahedra at -79.19 ppm and between -83 and -86 ppm respectively [40,67]. As expected, the decrease in the  $C/S$  ratio resulted in a relative increase in the  $Q^2$  contribution reflecting the increase of the length of the dreierketten chains of the C-S-H. The spectra of pastes with  $C/S$  ratios lower than 1.40 predominantly showed  $Q^2$  silicate tetrahedra. In that case, the bridging and the paired tetrahedra of the dreierketten chains of C-S-H ( $Q^{2b}$ ,  $Q^{2p}$ ) could also be distinguished. According to the literature, they occur at -83.13 ppm and -85.38 ppm [68]. A broad contribution in the frequency range of  $Q^3$  tetrahedra (-90 to -100 ppm) was detected in samples with  $C/S$  below 0.95.  $Q^3$  coordination has been proposed in C-S-H of low  $C/S$  ratios but are expected to be a minor occurrence in the

absence of aluminium [69]. Without further evidence, and considering its breadth, it was thus preferred to attribute tentatively this resonance to the occurrence of an amorphous silica ( $Q^3_{\text{gel}}$ ). The distribution of the silicate tetrahedra environment as a function of the C/S ratio was obtained by decomposition of the  $^{29}\text{Si}$  resonances and reported in Table 3. Details of the decomposition procedure and results are provided as Supplementary materials.

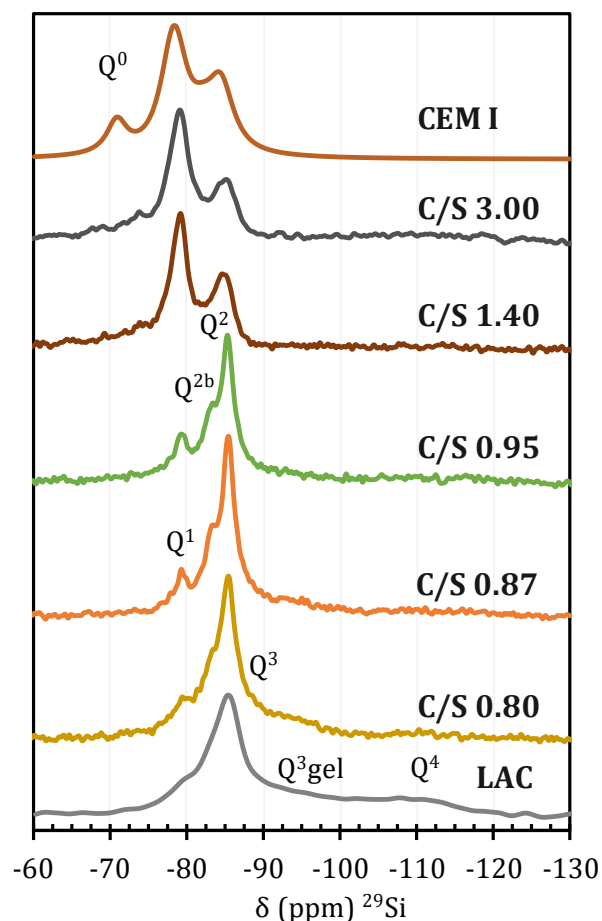
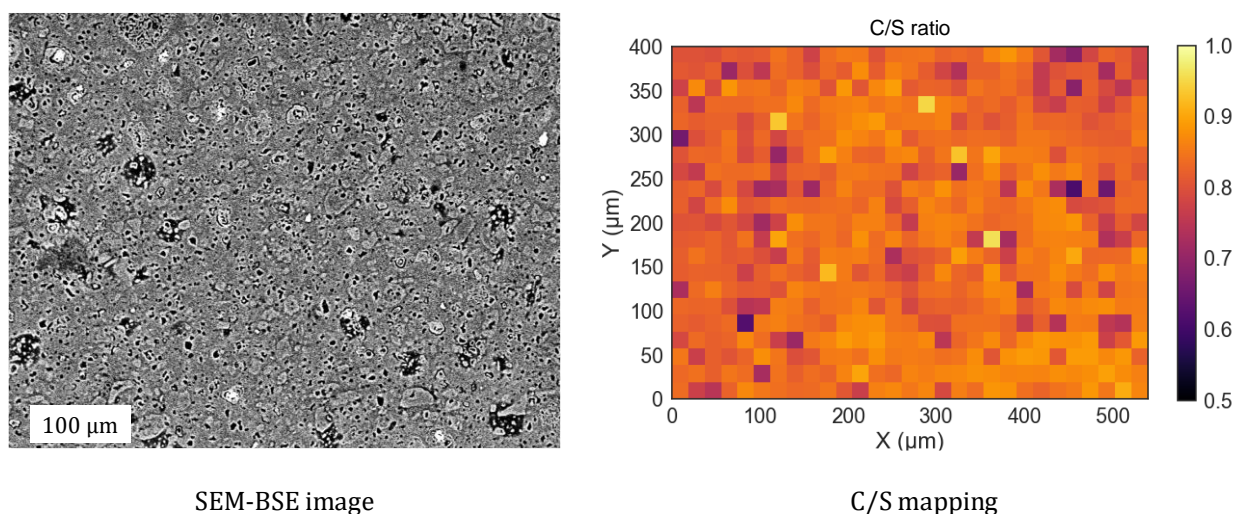


**Figure 3:**  $^{29}\text{Si}$  MAS-NMR spectra of the series of model synthetic pastes with varying C/S ratios and of the reference pastes. Synthetic pastes of higher C/S ratio had lower proportion of  $Q^2$  (middle chain) to  $Q^1$  (end chain) silicate coordination evidencing the expected decrease in dreierketten chain length with increasing C/S ratios. The spectra of the end members of the synthetic series were very similar to the ones of the reference pastes. The reference CEM I and LAC pastes showed  $Q^0$  and  $Q^3/Q^4$  resonances due to unreacted calcium silicates and to unreacted silica fume or amorphous silica gel products respectively.

**Table 3: Relative occurrence of silicate environments in synthetic and model pastes from  $^{29}\text{Si}$  MAS-NMR.**

Paste		$Q^0$	$Q^1$	$Q^{2b}$	$Q^{2p}$	$Q^3$	$Q^4$
$\delta$ (ppm)		-71.6	-79.2	-83.1	-85.4	-92.0	-110.0
Model pastes	0.80	-	10%	21%	43%	26%	-
	0.87	-	14%	25%	50%	11%	-
	0.95	-	16%	25%	51%	8%	-
	1.40	-	52%	13%	25%	5%	-
	3.00	-	68%	11%	21%	-	-
Reference pastes	CEM I	11%	56%	11%	22%	-	-
	LAC	-	7%	15%	30%	37%	11%

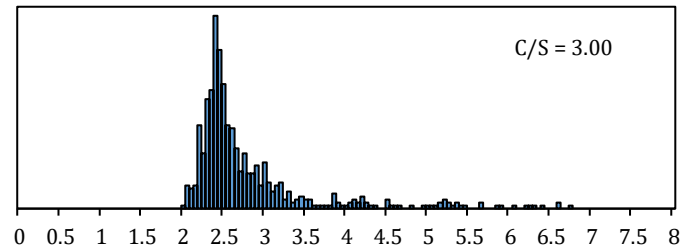
Figure 4 shows the chemical analysis (SEM) results obtained for the model synthetic paste with the lowest (0.80) C/S ratio. A typical electron density contrast image given by BSE mapping is shown in Figure 4(a) and the subsequent mapping of the C/S ratio distribution obtained using EDS on a  $400 \times 550 \mu\text{m}^2$  ( $21 \times 29$  points) subzone is displayed in Figure 4 (b). These results revealed an almost homogeneous distribution of the C/S ratio at the scale of EDS sampling ( $20 \times 20 \mu\text{m}^2$  surface with an analysis depth of  $\sim 1\text{-}10 \mu\text{m}$ ) with a limited standard deviation (coefficient of variation CV = 5%).



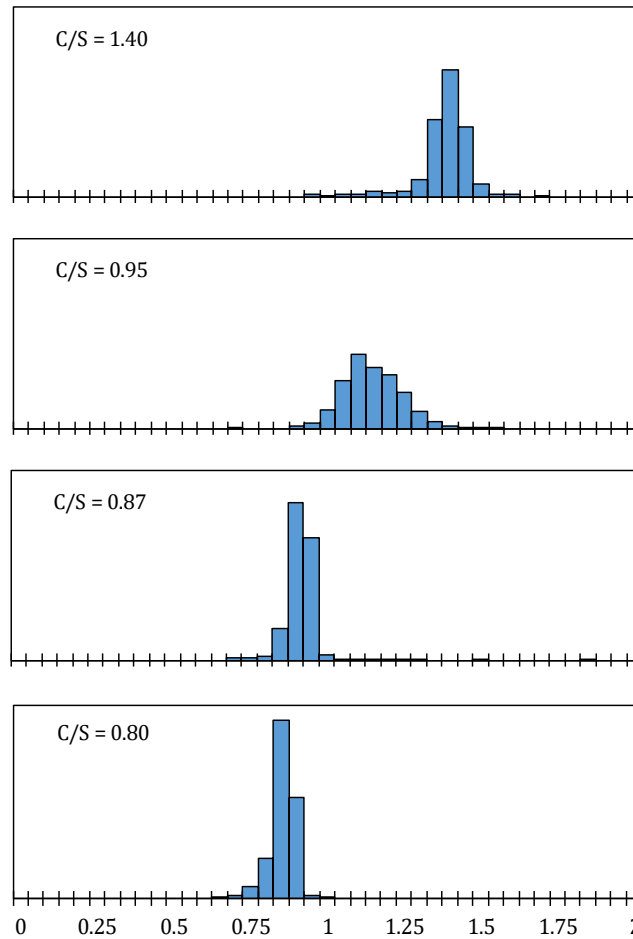
**Figure 4: SEM examination of the synthetic paste with a C/S ratio of 0.80. At the scale of the EDS mapping, the paste appeared very homogeneous in composition.**

Figure 5 and Figure 6: show the C/S ratio occurrence in each model synthetic pastes. All the samples presented average C/S ratios that were very close to the targets except the  $\text{C}_3\text{S}$  paste results that were scattered over a wider range probably due to the expected precipitation of portlandite crystals. In contrast, the other samples were

narrowly distributed with a CV between 5% and 6%, with the exception of the paste with a C/S ratio of 0.95 with a CV of 12% (Table 4).



**Figure 5: Distribution of the CaO/SiO<sub>2</sub> ratio obtained using SEM-EDS for the C<sub>3</sub>S paste**



**Figure 6: Distribution of the CaO/SiO<sub>2</sub> ratios obtained using SEM-EDS for the synthetic pastes for C/S ≤ 1.40**

**Table 4: Mean value and standard deviation of the C/S ratio distribution of the model pastes**

Target C/S	0.80	0.87	0.95	1.40	3.00
Average C/S value	0.83	0.89	1.06	1.36	2.53
Standard deviation	0.04	0.05	0.10	0.08	0.31
Coefficient of variation (CV)	5%	6%	9%	6%	12%

*Representativity of the chemistry and mineralogy of the model synthetic pastes.*

XRD and TGA proved that the pastes with C/S ratios lower than 1.40 contained C-S-H only, whereas the paste based on pure  $C_3S$  showed the concomitant precipitation of portlandite. This is in line with what is expected from a LAC and a CEM I paste respectively.  $^{29}Si$  MAS-NMR analysis of the pastes evidenced C-S-H silicates environment distribution evolving continuously with the C/S ratio between what is observed in a LAC and in a CEM I paste. Furthermore, EDS chemical analysis highlighted the relative homogeneity of the C-S-H pastes with actually an even narrower scatter in the C/S ratios, compared to those usually observed in cementitious materials but in line with what is observed in pure calcium silicate hydrate pastes [70,71]. In that respect, the synthetic pastes formed a representative model of the silicates mineralogical assembly found in LAC pastes.

The pH values of the poral solutions obtained using the ESL method are given in Figure 7. For the purpose of comparison, the values are plotted together with literature data and with the model proposed by Haas & Nonat [72]. The pH of the synthetic pastes poral solution (measurement made at  $20 \pm 2^\circ C$ , with temperature compensation) demonstrated a decrease while the target C/S ratios were lowered. Our data falls within the variance shown by literature data and confirmed that the model synthetic pastes also successfully reproduced the low alkalinity character of LAC pastes.

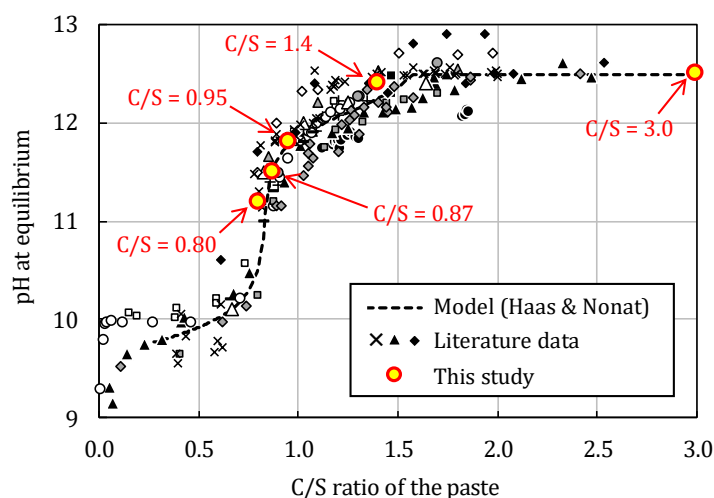


**Figure 7: pH of the poral solutions of the synthetic pastes measured using the ex-situ leaching method, redrawn from [12,73–83] along with the model proposed by Haas & Nonat [72]. The pH of the pore water**



of the synthetic pastes satisfactorily reproduced observation reported in the literature and conformed to the predictive model.

#### *Microstructure of the model synthetic pastes.*

The saturated density, porosity and chemical composition (C-S-H and CH contents) are reported in Table 5. The estimated C-S-H content was higher for the pastes with C/S ratios lower than 3.00: this was in line with the expected formation of extra C-S-H from silica through pozzolanic reactions. The paste porosity increased and the density decreased when the target C/S ratio decreased. However, as the C/S ratio was decreased by addition of nanosilica, a concomitant increase of the w/b ratio was needed to maintain the workability of the synthetic pastes. The variations in porosity and density was thus probably more associated to the water content than to a change of chemistry.

**Table 5: Composition and properties of the synthetic and reference pastes obtained by TGA,  $\mu$ CT and the buoyancy method. The C-S-H content was obtained following the method of Olson and Jennings [53]. (see Materials and method section)**

Model pastes						Reference pastes	
C/S ratio	3.00	1.40	0.95	0.87	0.80	CEM I	CEMI+SF+FA
C/S of the C-S-H	1.70	1.40	0.95-1.10	0.87-1.00	0.80-1.00	1.70	[0.8-1.1]*
Porosity (80°C)	38%	52%	57%	57%	58%	36%#°	41%#°
Porosity (105°C)	41%	56%	61%	61%	62%	38%#°	43%#°-46%*°
Saturated density	1.89	1.76	1.68	1.67	1.63	2.04*-2.05#	1.73*-1.77#
C-S-H (mol/L of paste)	5.6	7.0	6.7	7.0	6.3	5.1*-5.2°	7.4*-7.6°
CH (mol/L of paste)	7.3	0.0	0.0	0.0	0.0	5.6*-5.3#	0.0*#
Cracking (μCT)	-	-	+	++	++	-	-
- no crack observed	+ few small cracks		++ several extended cracks				
data from *[84], °[23], *[20], #[85] *°[86]							

**Figure 8** illustrates the PSD of the synthetic pastes obtained by MIP. For sake of comparison, the cement pastes are also presented. While the PSD of the pastes with C/S ratios of 3.00 and 1.40 revealed the expected presence of the C-S-H gel porosity in the 10 nm range, the pore structure was considerably refined for the lower C/S ratio. Again, this could be related to the filling effect induced by the precipitation of pozzolanic C-S-H. The increase of the porous volume on the other hand was probably related to the increased w/b ratios of the synthetic pastes.

### Representativity of the microstructure of the model synthetic pastes.

The synthetic pastes had a narrower PSD and a higher pore volume than the one of the reference LAC paste, again due to the w/b ratio needed for their mixing as previously stated in the Materials and methods section. However, the PSD of the low C/S synthetic pastes had no pores with critical entry diameter above 10 nm (Figure 8). This was reminiscent of what is observed in LAC pastes where the C-S-H gel porosity is considerably reduced by the pozzolanic reaction.

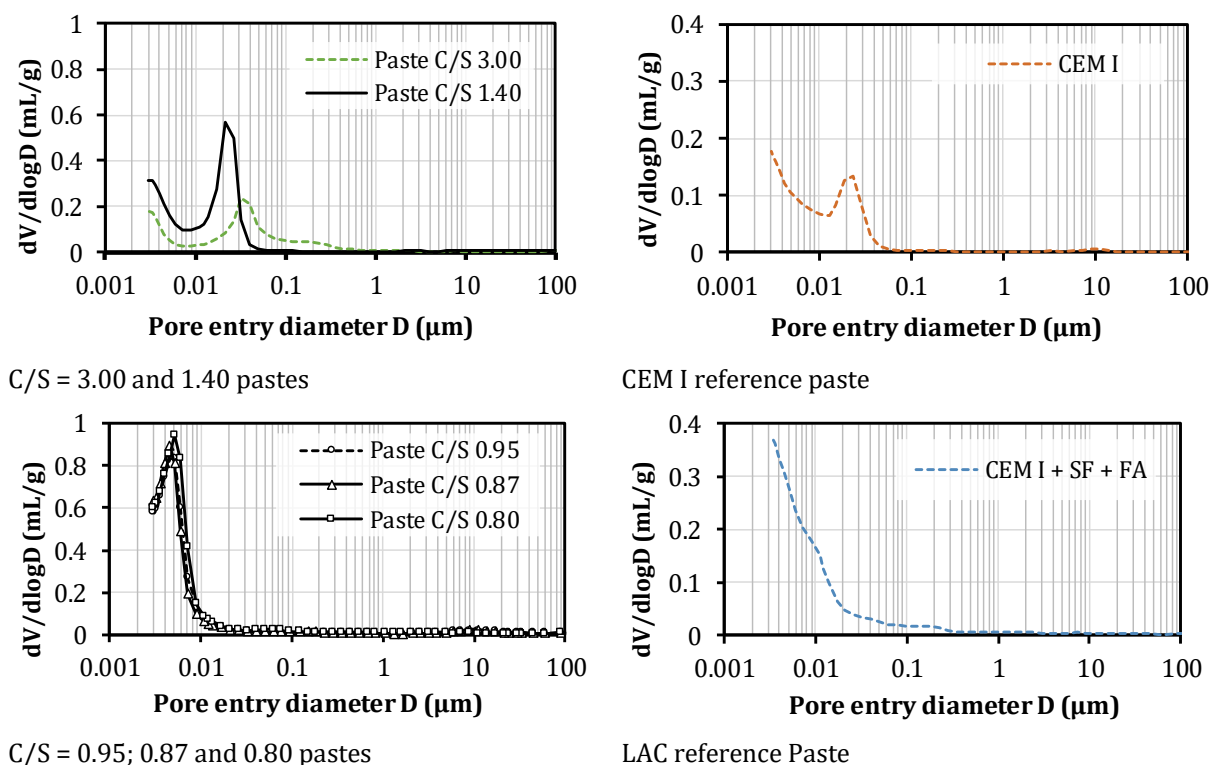


**Figure 8: PSD from mercury intrusion porosimetry for reference (right) and synthetic pastes (left). The PSD of the high C/S ratio synthetic pastes conformed to the one of an OPC (CEM I) paste, and the one for the lower C/S ratios to the one of the LAC (CEMI+SF+FA) reference paste.**

X- $\mu$ CT scans of samples with C/S ratios of 1.40, 0.87 and 0.80 are shown in Figure 9. The C/S ratio of 1.40 showed a homogenous matrix, almost exempt of bubbles. No cracks were observed in the pastes with the higher C/S ratios (3.00 and 1.40) (image a). The pastes with lower C/S ratios of 0.87 and 0.80 exhibited more contrasted features with darker spots observed in the matrix; these areas could be attributed to silica-enriched areas, thus supporting the NMR observation of a small amount of unreacted silica. These pastes also contained several bubbles due to reduced workability induced by the high amount of nanosilica in their formulations. Furthermore, they had an extended crack network (images b, c). The cracks made the samples very brittle and it was necessary to be extremely careful when handling the low C/S synthetic pastes and they proved to be very difficult (almost impossible) to cut without breaking. This was believed to be due to the polymerisation of the silica chains of the C-

S-H induced by the incorporation of silica in the C-S-H, which is known to generate significant volume changes and might result in densification and internal stress during maturation [87] of the lower C/S pastes.

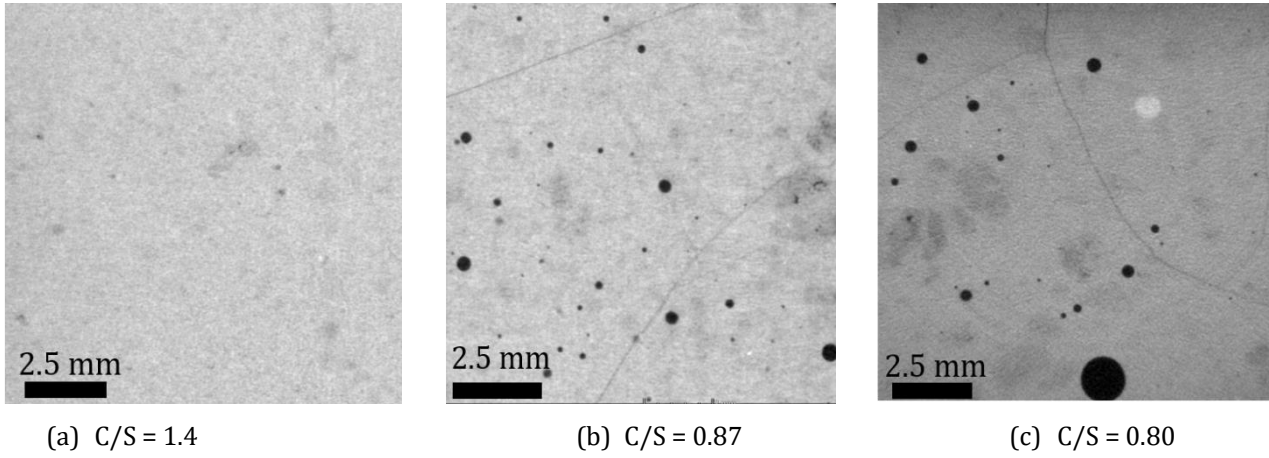


**Figure 9: X-ray  $\mu$ CT scans images of 3 samples of the synthetic pastes series. Significant cracking was observed in paste with lower C/S ratios**

### 1.5 Discussion

At first sight and as exposed in the results section, the mineralogical assembly of the model synthetic pastes seemed to correctly represent the one expected from LAC pastes. To examine further this issue, the atomic and molecular structure of their C-S-H, as revealed by NMR, was examined in details and compared to the ones of cement pastes.

It is common practice to estimate the mean chain length (MCL) of the C-S-H dreierketten silicate chains from the distribution of the silicate environment obtained by  $^{29}\text{Si}$  MAS-NMR. Accordingly, the MCL was obtained in the synthetic pastes using the C-S-H crystal chemical model of Richardson [88]. Indeed, the following simplified expression (Equation 1) relates the MCL to the NMR relative intensities of the  $Q^1$  and  $Q^2$  ( $Q^{2b}$  and  $Q^{2p}$ ) environments:

$$\text{MCL} = 2 \left( \frac{Q^1 + Q^{2b} + Q^{2p}}{Q^1} \right) \quad \text{Equation 1}$$

Figure 10 shows the C-S-H MCL of the pastes depending on their targeted C/S, along with predictions from the Richardson tobermoritic model and some data from literature. In the higher C/S range (above 1.5), the C-S-H of the pastes demonstrated a chain length variation that was not fully described by the simple tobermoritic model. This behaviour is similar to what is commonly observed in cement paste and is rationalized through an additional charge compensation mechanism, which involved calcium insertion in interlayers [88,89]. However, within the lower C/S domain ( $C/S \leq 1.0$ ), the mean chain length of the C-S-H in the synthetic pastes followed reasonably well the prediction of a tobermoritic behaviour.

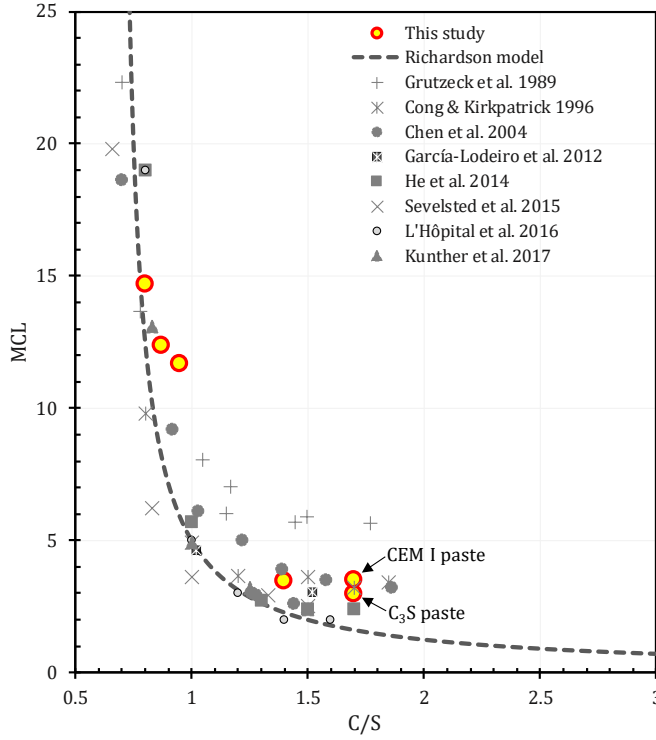


**Figure 10: C-S-H mean chain length of the synthetic pastes (from  $^{29}\text{Si}$  MAS NMR) along with literature data [12,40,74,75,88,90–93]. The MCL obtained for our model pastes correlated well with the MCL of the cementitious materials reported in the literature**

In the crystal-chemical structure provided by Richardson [88], the C-S-H gel is considered as a structurally defective form of tobermorite. The structural model describes the C-S-H structure (MCL, C/S ratio) based on the rate of occupancy of the vacant sites. Adopting this structural model, one can in principle back-calculate the C/S ratio of the C-S-H from the NMR spectrum. Practically speaking, following Richardson [88] the C/S ratio (Equation 2) and the mean chain length (MCL) were calculated using:

$$\text{MCL} = \frac{1 - v}{v} \quad \text{and} \quad \frac{C}{S} = \frac{\frac{2}{3} + v}{1 - v} \quad \text{Equation 2}$$

where the fraction of vacant sites  $v$  (Equation 3) within the C-S-H structure was evaluated by decomposition of the NMR contributions:

$$v = \frac{\frac{1}{2}Q^1}{\frac{3}{2}Q^1 + Q^2 + Q^3} \quad \text{Equation 3}$$

Excluding the  $Q^3$  resonance attributed to a silica gel, the C/S ratio predicted from the Richardson defective tobermoritic model agreed reasonably well with the bulk C/S ratio of the pastes (Figure 11). This meant not only that the paste were indeed devoid of portlandite, as seen by XRD and TGA, but also that their C-S-Hs' structure behaved identically to the ones encountered in real (LAC) cement paste where the defective tobermorite structural model is now well established [94]. This confirmed the representativity of the mineralogy of synthetic pastes silicate with respect to the one of LAC paste of identical C/S.

Finally, it might be useful to stress the fundamental difference between the C/S pertaining to NMR on the one hand and to SEM-EDS analyses and to the pH of the poral solutions on the other hand (Figure 11). NMR analyses account for properties at the molecular scale and thus reflects the local availability of Ca and Si at the C-S-H scale. In contrast pH is a macroscopic property reflecting phase equilibria within the sample, namely C-S-H and portlandite. Lastly, SEM-EDS probes the sample at the micro scale and its mean value is thus expected to reproduce the bulk composition of the paste within experimental errors. These considerations are illustrated in Figure 11 where C/S ratios obtained by SEM-EDS and by modelling the  $^{29}\text{Si}$  NMR spectra as well as the pH are compared to the bulk C/S ratio recalculated excluding the silicon incorporated in amorphous silica (estimated from the  $^{29}\text{Si}$  NMR spectra). The latter C/S ratio was taken as being the one of the C-S-H/portlandite assemblage.

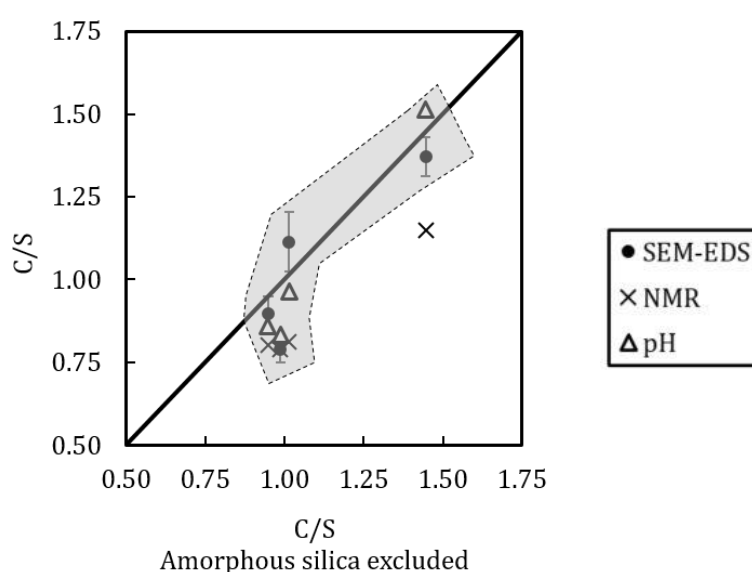


**Figure 11: Comparison of the bulk C/S ratios (excluding the silicon in the amorphous non C-S-H part of the sample, unreacted products or silica gels, estimated by  $^{29}\text{Si}$  NMR) with the results of SEM-EDS and with the ones expected from modelling pH measurements (Haas and Nonat model) and NMR ones (Richardson model).**

## 1.6 Conclusion

In this study we synthesized a series of synthetic pastes with C/S ratios between 0.80 and 3.0 and evaluated its potential as a model silicate subsystems for LAC pastes. From a chemical and mineralogical standpoint, the synthetic pastes appeared as good models, reproducing satisfactorily the mineralogical assemblage. The structure of the C-S-H and the amount of portlandite formed, or not, followed what was expected from a LAC paste. Furthermore, the pH of the poral solutions also conformed very well to predictions with respect to the C/S ratios. This objective was met by choosing  $\text{C}_3\text{S}$  and nanosilica with the appropriate dosage. However, the use of nanosilica induced a high-water demand and the formulation had to be optimized through an increased w/b ratio and high superplasticiser dosage. Consequently, the synthetic pastes had a higher pore volume. All the while, the evolution of the PSDs of the synthetic pastes with the C/S ratio was similar to those of the reference pastes. The protocol proposed in the present

work thus constituted an interesting route to design synthetic pastes to model the silica subsystem of LAC pastes. This might be particularly useful to model experimentally complex reactive transport within low-alkalinity cements, such as carbonation. In addition, since a narrow variation of C/S ratios was obtained for each targeted value, this series could be suitable for studying the influence of the C/S ratio on various properties of cementitious materials, such as the C-S-H gel mechanical properties. Such studies will have to factor in however, the fact that the pore volume of the model pastes was much higher than those usually encountered in real cement pastes

Finally, to be complete, it must be emphasised that one of the main shortcomings of these model synthetic pastes was their tendency to crack; the density of cracks increased when the C/S ratio decreased. This could be hypothesized to be an intrinsic property due to the polymerisation of the C-S-H induced by incorporation of silicate in the C-S-H during the pozzolanic reaction. Indeed, chain length variation is known to generate change in volume [26]. Shaping test samples for transport studies will thus require particular care.

### Acknowledgments

The financial support provided by IRSN and the CEA is gratefully acknowledged.

### References

- [1] N. Seigneur, É. Kangni-foli, V. Lagneau, A. Dauzères, S. Poyet, P. Le Bescop, E. L'Hôpital, J.B. d'Espinose de Lacaille, Understanding the effects of the atmospheric carbonation of cementitious materials using reactive transport modelling, *Submitt. to Cem. Concr. Res.* (2019).
- [2] K. Ioannidou, K.J. Krakowiak, M. Bauchy, C.G. Hoover, E. Masoero, S. Yip, F.-J. Ulm, P. Levitz, R.J.-M. Pellenq, E. Del Gado, Mesoscale texture of cement hydrates, *Proc. Natl. Acad. Sci.* 113 (2016) 2029–2034. doi:10.1073/pnas.1520487113.
- [3] J. Ollivier, J. Torrenti, La structure poreuse des bétons et les propriétés de transfert, *La Durabilité Des Bétons.* (2008) 51–133.
- [4] K.L. Scrivener, A.K. Crumbie, P. Laugesen, The Interfacial Transition Zone (ITZ) Between Cement Paste and Aggregate in Concrete, *Interface Sci.* 12 (2004) 411–421. doi:10.1023/B:INTS.0000042339.92990.4c.
- [5] J.S. Dolado, K. van Breugel, Recent advances in modeling for cementitious materials, *Cem. Concr. Res.* 41 (2011) 711–726. doi:10.1016/j.cemconres.2011.03.014.
- [6] A. Dauzères, P. Le Bescop, P. Sardini, C. Cau Dit Coumes, Physico-chemical investigation of clayey/cement-based materials interaction in the context of geological waste disposal: Experimental approach and results, *Cem. Concr. Res.* 40 (2010) 1327–1340. doi:10.1016/j.cemconres.2010.03.015.
- [7] P. Lalan, A. Dauzères, L. De Windt, J. Sammaljärvi, D. Bartier, I. Techer, V. Detilleux, M. Siitari-Kauppi, Mineralogical and microstructural evolution of Portland cement paste/argillite interfaces at 70 °C – Considerations for diffusion and porosity properties, *Cem. Concr. Res.* 115 (2019) 414–425. doi:10.1016/j.cemconres.2018.09.018.
- [8] C. Carde, R. François, J.-M. Torrenti, Leaching of both calcium hydroxide and C-S-H from cement paste: Modeling the mechanical behavior, *Cem. Concr. Res.* 26 (1996) 1257–1268. doi:10.1016/0008-8846(96)00095-6.
- [9] C. Carde, R. François, Effect of the leaching of calcium hydroxide from cement paste on mechanical and physical properties, *Cem. Concr. Res.* 27 (1997) 539–550. doi:10.1016/S0008-8846(97)00042-2.
- [10] E. Drouet, S. Poyet, P. Le Bescop, J.-M. Torrenti, X. Bourbon, Carbonation of hardened cement pastes:

Influence of temperature, *Cem. Concr. Res.* 115 (2019) 445–459. doi:10.1016/j.cemconres.2018.09.019.

- [11] D. Planel, J. Sercombe, P. Le Bescop, F. Adenot, J.M. Torrenti, Long-term performance of cement paste during combined calcium leaching-sulfate attack: Kinetics and size effect, *Cem. Concr. Res.* 36 (2006) 137–143. doi:10.1016/j.cemconres.2004.07.039.
- [12] X. Cong, R.J. Kirkpatrick, <sup>29</sup>Si MAS NMR study of the structure of calcium silicate hydrate, *Adv. Cem. Based Mater.* 3 (1996) 144–156. doi:10.1016/S1065-7355(96)90046-2.
- [13] A. Nonat, X. Lecoq, The Structure, Stoichiometry and Properties of C-S-H Prepared by C3S Hydration Under Controlled Condition, in: P. Colombet, A.-R. Grimmer, H. Zanni, P. Sozzani (Eds.), *Nucl. Magn. Reson. Spectrosc. Cem. Mater.*, Springer, 1998: pp. 197–207. doi:10.1007/978-3-642-80432-8\_14.
- [14] I.F. Sáez Del Bosque, M. Martín-Pastor, I. Sobrados, S. Martínez-Ramírez, M.T. Blanco-Varela, Quantitative analysis of pure triclinic tricalcium silicate and C-S-H gels by <sup>29</sup>Si NMR longitudinal relaxation time, *Constr. Build. Mater.* 107 (2016) 52–57. doi:10.1016/j.conbuildmat.2015.12.146.
- [15] K.O. Kjellsen, H. Justnes, Revisiting the microstructure of hydrated tricalcium silicate—a comparison to Portland cement, *Cem. Concr. Compos.* 26 (2004) 947–956. doi:10.1016/j.cemconcomp.2004.02.030.
- [16] A. Helmuth, H. Turk, Elastic Moduli of Hardened Portland Cement and Tricalcium Silicate Pastes : Effect of Porosity, *Portl. Cem. Assoc R D Lab Bull.* 144 (1966) 135–144. <http://onlinepubs.trb.org/Onlinepubs/sr/sr90/90-012.pdf>.
- [17] J. Hagymassy, I. Odler, M. Yudenfreund, J. Skalny, S. Brunauer, Pore structure analysis by water vapor adsorption. III. Analysis of hydrated calcium silicates and portland cements, *J. Colloid Interface Sci.* 38 (1972) 20–34. doi:10.1016/0021-9797(72)90215-9.
- [18] G. Geng, R. Taylor, S. Bae, D. Hernández-Cruz, D.A. Kilcoyne, A.-H. Emwas, P.J.M. Monteiro, Atomic and nano-scale characterization of a 50-year-old hydrated C3S paste, *Cem. Concr. Res.* 77 (2015) 36–46. doi:10.1016/j.cemconres.2015.06.010.
- [19] E. Pustovgar, R.P. Sangodkar, A.S. Andreev, M. Palacios, B.F. Chmelka, R.J. Flatt, J.-B. d’Espinoise de Lacaille, Understanding silicate hydration from quantitative analyses of hydrating tricalcium silicates, *Nat. Commun.* 7 (2016) 10952. doi:10.1038/ncomms10952.
- [20] M. Codina, C. Cau-dit-Coumes, P. Le Bescop, J. Verdier, J.P. Ollivier, Design and characterization of low-heat and low-alkalinity cements, *Cem. Concr. Res.* 38 (2008) 437–448. doi:10.1016/j.cemconres.2007.12.002.
- [21] H. Sakamoto, K. Haga, H. Fujita, K. Ishizaki, H. Amano, M. Hironaga, S. Nagasaki, S. Tanaka, pH Behavior of Hydrated Low-Alkalinity Cement, *J. Nucl. Fuel Cycle Environ.* 5 (1999) 37–42. doi:10.3327/jnuce.5.37.
- [22] B. Lothenbach, G. Le Saout, M. Ben Haha, R. Figi, E. Wieland, Hydration of a low-alkali CEM III/B-SiO<sub>2</sub> cement (LAC), *Cem. Concr. Res.* 42 (2012) 410–423. doi:10.1016/j.cemconres.2011.11.008.
- [23] M. Auroy, S. Poyet, P. Le Bescop, J.M. Torrenti, T. Charpentier, M. Moskura, X. Bourbon, Impact of carbonation on unsaturated water transport properties of cement-based materials, *Cem. Concr. Res.* 74 (2015) 44–58. doi:10.1016/j.cemconres.2015.04.002.
- [24] K. Iriya, A. Matsui, M. Mihara, Study on applicability of HFSC for radioactive waste repositories, in: ASME (Ed.), *ASME Conf., Nagoya (Japan)*, 1999. doi:10.1081/E-EEE2-120046011.
- [25] C. Cau Dit Coumes, S. Courtois, D. Nectoux, S. Leclercq, X. Bourbon, Formulating a low-alkalinity, high-resistance and low-heat concrete for radioactive waste repositories, *Cem. Concr. Res.* 36 (2006) 2152–2163. doi:10.1016/j.cemconres.2006.10.005.
- [26] J.J. Thomas, J.J. Chen, A.J. Allen, H.M. Jennings, Effects of decalcification on the microstructure and surface area of cement and tricalcium silicate pastes, *Cem. Concr. Res.* 34 (2004) 2297–2307. doi:10.1016/j.cemconres.2004.04.007.
- [27] J.J. Beaudoin, B. Patarachao, L. Raki, J. Margeson, R. Alizadeh, Length change of C–S–H of variable composition immersed in aqueous solutions, *Adv. Cem. Res.* 22 (2010) 15–20. doi:10.1680/adcr.2008.22.1.15.
- [28] R.F. Feldman, Factors affecting young’s modulus — Porosity relation of hydrated portland cement compacts,

Cem. Concr. Res. 2 (1972) 375–386. doi:10.1016/0008-8846(72)90054-3.

- [29] P.J. Sereda, R.F. Feldman, Compacts of powdered material as porous bodies for use in sorption studies, *J. Appl. Chem.* 13 (2007) 150–158. doi:10.1002/jctb.5010130402.
- [30] Y. Wang, Q. Yuan, D. Deng, T. Ye, L. Fang, Measuring the pore structure of cement asphalt mortar by nuclear magnetic resonance, *Constr. Build. Mater.* 137 (2017) 450–458. doi:10.1016/j.conbuildmat.2017.01.109.
- [31] W.A. Gutteridge, L.J. Parrott, A study of the changes in weight, length and interplanar spacing induced by drying and rewetting synthetic CSH (I), *Cem. Concr. Res.* 6 (1976) 357–366. doi:10.1016/0008-8846(76)90098-3.
- [32] E.M. Foley, J.J. Kim, M.M. Reda Taha, Synthesis and nano-mechanical characterization of calcium-silicate-hydrate (C-S-H) made with 1.5 CaO/SiO<sub>2</sub> mixture, *Cem. Concr. Res.* 42 (2012) 1225–1232. doi:10.1016/j.cemconres.2012.05.014.
- [33] P. Pourbeik, J.J. Beaudoin, R. Alizadeh, L. Raki, Correlation between dynamic mechanical thermo-analysis and composition-based models for C-S-H in hydrated portland cement paste, *Mater. Struct.* 48 (2015) 2447–2454. doi:10.1617/s11527-014-0330-7.
- [34] R. Khoshnazar, J.J. Beaudoin, L. Raki, R. Alizadeh, Durability and mechanical properties of C-S-H/nitrobenzoic acid composite systems, *Mater. Struct.* 49 (2016) 5315–5325. doi:10.1617/s11527-016-0862-0.
- [35] E. Bernard, B. Lothenbach, C. Cau-Dit-Coumes, C. Chlique, A. Dauzères, I. Pochard, Magnesium and calcium silicate hydrates, Part I: Investigation of the possible magnesium incorporation in calcium silicate hydrate (C-S-H) and of the calcium in magnesium silicate hydrate (M-S-H), *Appl. Geochemistry*. 89 (2018) 229–242. doi:10.1016/j.apgeochem.2017.12.005.
- [36] E. Bernard, B. Lothenbach, F. Le Goff, I. Pochard, A. Dauzères, Effect of magnesium on calcium silicate hydrate (C-S-H), *Cem. Concr. Res.* 97 (2017) 61–72. doi:10.1016/j.cemconres.2017.03.012.
- [37] H. Yang, Y. Che, F. Leng, Calcium leaching behavior of cementitious materials in hydrochloric acid solution, *Sci. Rep.* 8 (2018) 1–9. doi:10.1038/s41598-018-27255-x.
- [38] Y.S. Choi, E.I. Yang, Effect of calcium leaching on the pore structure, strength, and chloride penetration resistance in concrete specimens, *Nucl. Eng. Des.* 259 (2013) 126–136. doi:10.1016/j.nucengdes.2013.02.049.
- [39] P.J. Sereda, R.F. Feldman, E.G. Swenson, Effect of sorbed water on some mechanical properties of hydrated Portland cement pastes and compacts, 1967.
- [40] W. Kunther, S. Ferreira, J. Skibsted, Influence of the Ca/Si ratio on the compressive strength of cementitious calcium-silicate-hydrate binders, *J. Mater. Chem. A* 5 (2017) 17401–17412. doi:10.1039/c7ta06104h.
- [41] L. Nicoleau, A. Nonat, D. Perrey, The di- and tricalcium silicate dissolutions, *Cem. Concr. Res.* 47 (2013) 14–30. doi:10.1016/j.cemconres.2013.01.017.
- [42] S. Garrault, Study of C-S-H growth on C3S surface during its early hydration, *Mater. Struct.* 38 (2005) 435–442. doi:10.1617/14343.
- [43] H.F.W. Taylor, *Cement chemistry*, Limited, Academic press, 1990.
- [44] C. Rößler, F. Steiniger, H.-M. Ludwig, Characterization of C-S-H and C-A-S-H phases by electron microscopy imaging, diffraction, and energy dispersive X-ray spectroscopy, *J. Am. Ceram. Soc.* 100 (2017) 1733–1742. doi:10.1111/jace.14729.
- [45] Z.-Q. Wu, J.F. Young, The hydration of tricalcium silicate in the presence of colloidal silica, *J. Mater. Sci.* 19 (1984) 3477–3486. doi:10.1007/BF02396922.
- [46] K.O. Kjellsen, B. Lagerblad, Microstructure of tricalcium silicate and Portland cement systems at middle periods of hydration-development of Hadley grains, *Cem. Concr. Res.* 37 (2007) 13–20. doi:10.1016/j.cemconres.2006.09.008.



- [47] K. Baltakys, R. Jauberthie, R. Jauberthie, R. Siauciunas, R. Kaminskas, Influence of modification of SiO<sub>2</sub> on the formation of calcium silicate hydrate, *Mater. Sci.* 25 (2007) 663–670.
- [48] G. Quercia, G. Hüsken, H.J.H. Brouwers, Water demand of amorphous nano silica and its impact on the workability of cement paste, *Cem. Concr. Res.* 42 (2012) 344–357. doi:10.1016/j.cemconres.2011.10.008.
- [49] S. Abd.ElAleem, M. Heikal, W.M. Morsi, Hydration characteristic, thermal expansion and microstructure of cement containing nano-silica, *Constr. Build. Mater.* 59 (2014) 151–160. doi:10.1016/j.conbuildmat.2014.02.039.
- [50] E.A. Gorrepati, P. Wongthahan, S. Raha, H.S. Fogler, Silica precipitation in acidic solutions: Mechanism, pH effect, and salt effect, *Langmuir*. 26 (2010) 10467–10474. doi:10.1021/la904685x.
- [51] M.C. Alonso, J.L. García Calvo, S. Petterson, I. Puigdomenech, M.A. Cunado, M. Vuorio, H. Weber, H. Ueda, M. Naito, C. Walker, Y. Takeshi, C. Cau Dit Coumes, Round Robin test for define an accurate protocol to measure the pore fluid pH of low-pH cementitious materials, in: SFEN (Ed.), *Proc. 2nd Int. Symp. Cem. Mater. Nucl. Wastes*, SFEN, Avignon, France, 2014: pp. 1–10.
- [52] A. Behnood, K. van Tittelboom, N. de Belie, Methods for measuring pH in concrete : A review, *Constr. Build. Mater.* 105 (2016) 176–188. doi:10.1016/j.conbuildmat.2015.12.032.
- [53] G. Plusquellec, M.R. Geiker, J. Lindgård, J. Duchesne, B. Fournier, K. De Weerd, Determination of the pH and the free alkali metal content in the pore solution of concrete: Review and experimental comparison, *Cem. Concr. Res.* 96 (2017) 13–26. doi:10.1016/j.cemconres.2017.03.002.
- [54] G. Villain, M. Thiery, G. Platret, Measurement methods of carbonation profiles in concrete: Thermogravimetry, chemical analysis and gammadensimetry, *Cem. Concr. Res.* 37 (2007) 1182–1192. doi:10.1016/j.cemconres.2007.04.015.
- [55] F. Angeli, M. Gaillard, P. Jollivet, T. Charpentier, Contribution of <sup>43</sup>Ca MAS NMR for probing the structural configuration of calcium in glass, *Chem. Phys. Lett.* 440 (2007) 324–328. doi:10.1016/j.cplett.2007.04.036.
- [56] T. Charpentier, Résonance magnétique nucléaire haute-résolution des noyaux quadripolaires dans les solides. PhD thesis, (in French), University Paris IX Orsay, 1998.
- [57] AFNOR, Essai pour béton durci : essai de porosité et de masse volumique (in French), *Stand. NF P18-459*. (2010) 9p.
- [58] R.A. Olson, H.M. Jennings, Estimation of C-S-H content in a blended cement paste using water adsorption, *Cem. Concr. Res.* 31 (2001) 351–356. doi:10.1016/S0008-8846(01)00454-9.
- [59] S. Poyet, K. Trentin, E. Amblard, The use of sorption balance for the characterization of the water retention curve of cement-cased materials, *J. Adv. Concr. Technol.* 14 (2016) 354–367. doi:10.3151/jact.14.354.
- [60] G.W. Groves, A. Brough, I.G. Richardson, C.M. Dobson, Progressive changes in the structure of hardened C3S cement pastes due to carbonation, *J. Am. Ceram. Soc.* 74 (1991) 2891–2896.
- [61] I.G. Richardson, G.W. Groves, Models for the composition and structure of calcium silicate hydrate (CSH) gel in hardened tricalcium silicate pastes, *Cem. Concr. Res.* 22 (1992) 1001–1010. doi:10.1016/0008-8846(92)90030-Y.
- [62] J.W. Bullard, J. Hagedorn, T.M. Ley, Q. Hu, W. Griffin, J.E. Terrill, A critical comparison of 3D experiments and simulations of tricalcium silicate hydration, *J. Am. Ceram. Soc.* 101 (2018) 1453–1470. doi:10.1111/jace.15323.
- [63] Z. Xu, Z. Zhou, P. Du, X. Cheng, Effects of nano-silica on hydration properties of tricalcium silicate, *Constr. Build. Mater. J.* 125 (2016) 1169–1177. doi:10.1016/j.conbuildmat.2016.09.003.
- [64] S. Grangeon, F. Claret, Y. Linard, C. Chiaberge, X-ray diffraction: A powerful tool to probe and understand the structure of nanocrystalline calcium silicate hydrates, *Acta Crystallogr. Sect. B Struct. Sci. Cryst. Eng. Mater.* 69 (2013) 465–473. doi:10.1107/S2052519213021155.
- [65] S. Merlino, E. Bonaccorsi, T. Armbruster, The real structure of tobermorite 11A: normal and anomalous forms, OD character and polytypic modifications, *Eur. J. Mineral.* 13 (2001) 577–590. doi:10.1127/0935-

- [66] E. Bonaccorsi, S. Merlino, H.F.W. Taylor, The crystal structure of jennite,  $\text{Ca}_9\text{Si}_6\text{O}_{18}(\text{OH})_6 \cdot 8\text{H}_2\text{O}$ , *Cem. Concr. Res.* 34 (2004) 1481–1488. doi:10.1016/j.cemconres.2003.12.033.
- [67] I. Klur, B. Pollet, J. Virlet, A. Nonat, C-S-H Structure Evolution with Calcium Content by Multinuclear NMR, in: *Nucl. Magn. Reson. Spectrosc. Cem. Mater.*, Springer Berlin Heidelberg, Berlin, Heidelberg, 1998: pp. 119–141. doi:10.1007/978-3-642-80432-8\_8.
- [68] I. Klur, J.-F. Jacquinet, F. Brunet, T. Charpentier, J. Virlet, C. Schneider, P. Tekely, NMR Cross-Polarization when  $T_{\text{IS}} > T_{\text{1}\rho}$ ; Examples from Silica Gel and Calcium Silicate Hydrates, *J. Phys. Chem. B.* 104 (2000) 10162–10167. doi:10.1021/jp001342u.
- [69] S. Grangeon, F. Claret, C. Roosz, T. Sato, S. Gaboreau, Y. Linard, Structure of nanocrystalline calcium silicate hydrates: Insights from X-ray diffraction, synchrotron X-ray absorption and nuclear magnetic resonance, *J. Appl. Crystallogr.* 49 (2016) 771–783. doi:10.1107/S1600576716003885.
- [70] I.G. Richardson, G.W. Groves, Microstructure and microanalysis of hardened ordinary Portland cement pastes, *J. Mater. Sci.* 28 (1993) 265–277. doi:10.1007/BF00349061.
- [71] J.E. Rossen, B. Lothenbach, K.L. Scrivener, Composition of C-S-H in pastes with increasing levels of silica fume addition, *Cem. Concr. Res.* 75 (2015) 14–22. doi:10.1016/j.cemconres.2015.04.016.
- [72] J. Haas, A. Nonat, From C-S-H to C-A-S-H: Experimental study and thermodynamic modelling, *Cem. Concr. Res.* 68 (2015) 124–138. doi:10.1016/j.cemconres.2014.10.020.
- [73] E.P. Flint, L.S. Wells, Study of the system  $\text{CaO-SiO}_2\text{-H}_2\text{O}$  at 30 C and of the reaction of water on the anhydrous calcium silicates, *Bur. Stand. J. Res.* 12 (1934) 33. doi:10.6028/jres.012.060.
- [74] S.A. Greenberg, T.N. Chang, Investigation of the Colloidal Hydrated Calcium Silicates. II. Solubility Relationships in the Calcium Oxide-Silica-Water System at 25°, *J. Phys. Chem.* 69 (1965) 182–188. doi:10.1021/j100885a027.
- [75] K. Suzuki, T. Nishikawa, S. Ito, Formation and carbonation of C-S-H in water, *Cem. Concr. Res.* 15 (1985) 213–224. doi:10.1016/0008-8846(85)90032-8.
- [76] A. Atkinson, J.A. Hearne, C.F. Knights, Aqueous chemistry and thermodynamic modelling of  $\text{CaO-SiO}_2\text{-H}_2\text{O}$  gels, *J. Chem. Soc., Dalt. Trans.* 0 (1989) 2371–2379. doi:10.1039/DT9890002371.
- [77] M. Atkins, F.P. Glasser, A. Kindness, Cement hydrate phase: Solubility at 25°C, *Cem. Concr. Res.* 22 (1992) 241–246. doi:10.1016/0008-8846(92)90062-Z.
- [78] A. Harris, M. Manning, W. Tearle, C. Tweed, Testing of models of the dissolution of cements—leaching of synthetic CSH gels, *Cem. Concr. Res.* 32 (2002) 731–746. doi:10.1016/S0008-8846(01)00748-7.
- [79] J. Hill, A.W. Harris, M. Manning, A. Chambers, S.W. Swanton, The effect of sodium chloride on the dissolution of calcium silicate hydrate gels, *Waste Manag.* 26 (2006) 758–768. doi:https://doi.org/10.1016/j.wasman.2006.01.022.
- [80] C.S. Walker, D. Savage, M. Tyrer, K.V. Ragnarsdottir, Non-ideal solid solution aqueous solution modeling of synthetic calcium silicate hydrate, *Cem. Concr. Res.* 37 (2007) 502–511. doi:10.1016/j.cemconres.2006.12.002.
- [81] D. Sugiyama, Chemical alteration of calcium silicate hydrate (C-S-H) in sodium chloride solution, *Cem. Concr. Res.* 38 (2008) 1270–1275. doi:10.1016/j.cemconres.2008.06.002.
- [82] M. Grutzeck, A. Benesi, B. Fanning, Silicon-29 Magic Angle Spinning Nuclear Magnetic Resonance Study of Calcium Silicate Hydrates, *J. Am. Ceram. Soc.* 72 (1989) 665–668. doi:10.1111/j.1151-2916.1989.tb06192.x.
- [83] J.J. Chen, J.J. Thomas, H.F.W. Taylor, H.M. Jennings, Solubility and structure of calcium silicate hydrate, *Cem. Concr. Res.* 34 (2004) 1499–1519. doi:10.1016/j.cemconres.2004.04.034.
- [84] A. Dauzères, Etude expérimentale et modélisation des mécanismes physico-chimiques des interactions béton-argile dans le contexte du stockage géologique des déchets radioactifs (in French), Ph.D. Thesis,

University of Poitiers, 2010.

- [85] M. Auroy, Impact de la carbonatation Sur les proprietes de transport d'eau des matériaux cimentaires (in French), Ph.D. Thesis, Université Paris-Est, 2014.
- [86] E. Drouet, S. Poyet, J.-M. Torrenti, Temperature influence on water transport in hardened cement pastes, *Cem. Concr. Res.* 76 (2015) 37–50. doi:10.1016/j.cemconres.2015.05.002.
- [87] J.J. Chen, J.J. Thomas, H.M. Jennings, Decalcification shrinkage of cement paste, *Cem. Concr. Res.* 36 (2006) 801–809. doi:10.1016/j.cemconres.2005.11.003.
- [88] I.G. Richardson, Model structures for C-(A)-S-H(I), *Acta Crystallogr. Sect. B Struct. Sci. Cryst. Eng. Mater.* 70 (2014) 903–923. doi:10.1107/S2052520614021982.
- [89] A. Nonat, The structure and stoichiometry of C-S-H, *Cem. Concr. Res.* 34 (2004) 1521–1528. doi:10.1016/j.cemconres.2004.04.035.
- [90] I. García-Lodeiro, A. Fernández-Jiménez, I. Sobrados, J. Sanz, A. Palomo, C-S-H gels: Interpretation of <sup>29</sup>Si MAS-NMR spectra, *J. Am. Ceram. Soc.* 95 (2012) 1440–1446. doi:10.1111/j.1551-2916.2012.05091.x.
- [91] Y. He, L. Lu, L.J. Struble, J.L. Rapp, P. Mondal, S. Hu, Effect of calcium–silicon ratio on microstructure and nanostructure of calcium silicate hydrate synthesized by reaction of fumed silica and calcium oxide at room temperature, *Mater. Struct.* 47 (2014) 311–322. doi:10.1617/s11527-013-0062-0.
- [92] T.F. Sevelsted, J. Skibsted, Carbonation of C-S-H and C-A-S-H samples studied by <sup>13</sup>C, <sup>27</sup>Al and <sup>29</sup>Si MAS NMR spectroscopy, *Cem. Concr. Res.* 71 (2015) 56–65. doi:10.1016/j.cemconres.2015.01.019.
- [93] E. L'Hôpital, B. Lothenbach, D.A. Kulik, K. Scrivener, Influence of calcium to silica ratio on aluminium uptake in calcium silicate hydrate, *Cem. Concr. Res.* 85 (2016) 111–121. doi:10.1016/j.cemconres.2016.01.014.
- [94] R.J. Myers, S.A. Bernal, R. San Nicolas, J.L. Provis, Generalized structural description of calcium-sodium aluminosilicate hydrate gels: The cross-linked substituted tobermorite model, *Langmuir.* 29 (2013) 5294–5306. doi:10.1021/la4000473.

## 1.7 Supplementary materials

### Appendix A: details of the batching sequence.

The final batching sequence obtained for the model pastes including nanosilica was as follows:

1. Addition of C<sub>3</sub>S in the planetary mixer (mixing speed at 95 rpm).
2. Addition of all the water, including half of the total amount of SP.
3. Mixing at 250 rpm for 30 s.
4. Slow incorporation of nanosilica (at 400 rpm) while monitoring the fresh mix rheology to avoid flocculation and a viscosity increase that could eventually make it irreversibly unworkable. Addition of SP to maintain the workability of the fresh mix. The duration of this step depended on the amount of nanosilica added (Table 1).
5. Preparation of the test specimens: the paste was poured into polytetrafluoroethylene (PTFE) moulds (Ø30 × H110 mm) and vibrated. This phase proved complicated due to the strong thixotropic behaviour of the fresh mix, which worsened when the silica content was increased.
6. The specimens were kept one month in their sealed moulds at ambient temperature. After unmoulding, they were cured for two more months under a batch of water to which small amounts of crushed samples were added to ensure that chemical equilibrium was reached in the curing solution.

## Appendix B: decomposition of NMR spectra.

Figure S1: Examples of decompositions of the  $^{29}\text{Si}$  NMR spectra.

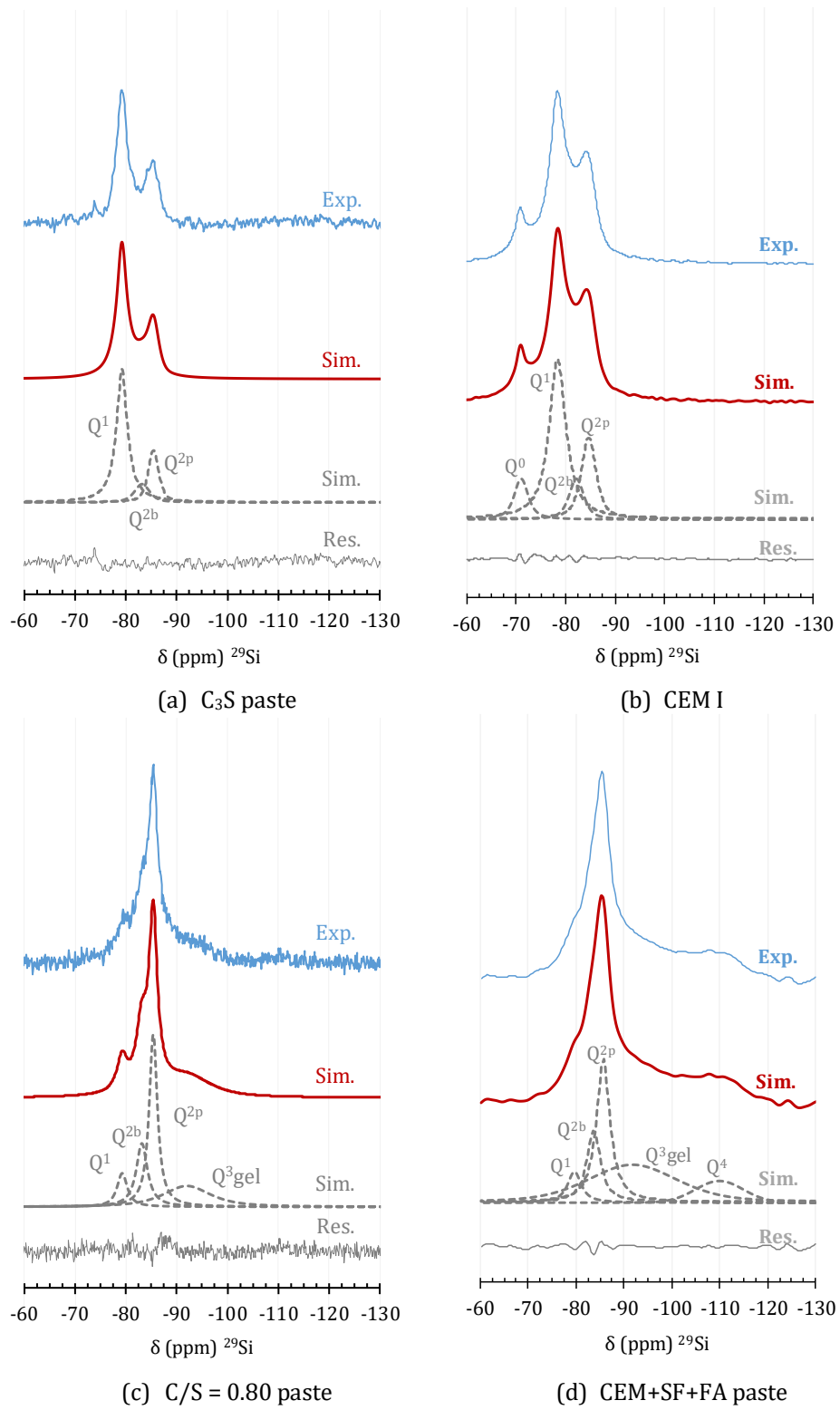


Table SI: Parameters of the decomposition of the  $^{29}\text{Si}$  NMR spectra of the synthetic pastes. No  $Q^0$  peak was considered for the  $C_3S$  paste as its contribution was of the order of the noise.

C/S ratio		0.8-3.00	
Q <sup>1</sup>	δ (ppm)	-79.2	
	FWHM (ppm)	2.9	
	xG+(1-x)L	0.05	
	GB	1.02	
Q <sup>2<sub>b</sub></sup>	δ (ppm)	-83.1	
	FWHM (ppm)	2.9	
	xG+(1-x)L	0.05	
	GB	1.1	
Q <sup>2<sub>p</sub></sup>	δ (ppm)	-85.4	
	FWHM (ppm)	2.21	
	xG+(1-x)L	0.01	
	GB	0.8	
Q <sup>3</sup> +Q <sup>3<sub>gel</sub></sup>	δ (ppm)	-92	
	FWHM (ppm)	11.3	
	xG+(1-x)L	0.2	
	GB (ppm)	4.7	
G: Gaussian, L: Lorentzian, GB: Gaussian enhancement			

## Appendix C: diffractograms of the reference system

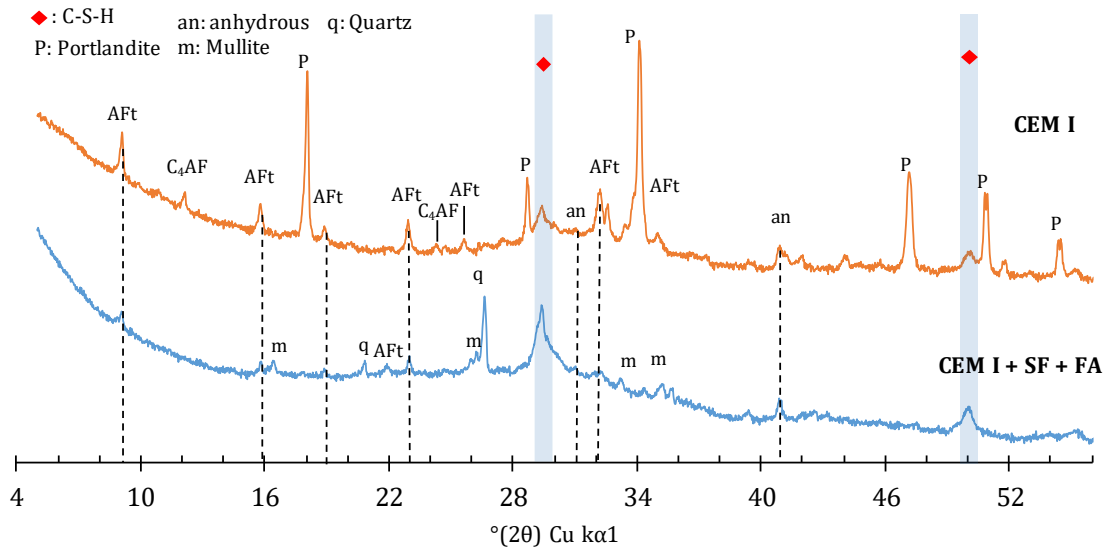


Figure S2: Diffractograms of the reference pastes. For the OPC (CEM I) paste, besides aluminates, C-S-H and portlandite signals were observed. No portlandite reflections were present in the LAC (CEM I + SF + FA) paste. Besides the C-S-H signal, an intense diffuse background located between 20-28  $^{\circ}(2\theta)$  typical of unreacted silica and small reflections of quartz occurred. ICDD CH: 44-1481, AFt:41-1451, mullite: 15-0776,  $C_4AF$ : 30-0226, an:31-0301/31-0302 ( $C_3S/C_2S$ )

**Appendix D: Chemical composition of the reference pastes' components, reproduced from [2] and along with the composition of the synthetic pastes components.**

	wt% of the components				wt % of the blend
	CEM I	Silica Fume	Fly Ash	C <sub>3</sub> S	LAC
CaO	67.41	0.40	5.52	73.68	27.0
SiO <sub>2</sub>	22.84	95.00	49.48	26.32	54.3
Al <sub>2</sub> O <sub>3</sub>	2.70	0.60	29.17		10.0
Fe <sub>2</sub> O <sub>3</sub>	1.84	<0.05	6.23		2.6
MgO	0.81	0.30	2.08		1.0
MnO	-	-	0.08		-
Na <sub>2</sub> O	0.14	<0.20	0.58		0.3
K <sub>2</sub> O	0.23	0.29	1.22		0.5
SO <sub>3</sub>	2.23	<0.20	0.64		1.1
S <sup>2-</sup>	<0.01	<0.10	-		
P <sub>2</sub> O <sub>5</sub>	-	-	0.70		
TiO <sub>2</sub>	-	-	1.61		
Loss of ignition (1000°C)	1.72	3.10	2.20		
CEM (Lafarge, Le Teil), densified silica fume (ChrysoSilica), Fly Ash (EDF), -:not measured					

Rheomac AS 150 (colloidal silica):

$\sigma$  (g.cm<sup>-3</sup>): 1.40 ± 0.02; pH: 10 ± 1.5; Cl: <0.1 wt%; Na<sub>2</sub>O eq: < 1.0 wt%



**Summary of the first chapter:**

Based on the results presented in the first chapter, the fabricated pastes' chemical, mineralogical and microstructural features confidently allow to consider them as model system for cementitious material especially in the case of studies related to C-S-H and CH. Their simplified chemistry was designed to permit a carbonation study, which includes a volume and a mass balance. The main weakness of the fabricated pastes lies in the cracking observed at lower C/S ratio. This aspect is obviously deleterious in studies of mechanisms strongly dependent on gas transfer, since cracks offer preferential pathway for gas transfer. More mechanical characterization such as creep and compressive strength need to be assessed to fully understand the materials developed, the hydration mechanisms as well have to be investigated with regard to the C/S ratios.

## **CHAPTER 2: ROLE OF LOW AL CONTENT IN C-S-H STRUCTURE AND EVOLUTION IN PRESENCE AND IN ABSENCE OF CO<sub>2</sub>**

The second chapter focuses on the model powders synthesized. Contrarily to the first chapter, this chapter deals exclusively with the structural and chemical properties of synthetic C-S-H and low Al/Si C(-A)-S-H powders. The evolution of their properties in presence and in absence of CO<sub>2</sub> is also addressed. The effect of an increasing Al and Ca content is explored. Dealing with powders instead of pastes gives access to the ultimate carbonation state. It allows discussing the representativity of the carbonation condition employed as well as the durability of the materials. The diffusive contribution of the microstructure is lost when working with powders but it allows comparison with observations made on pastes as will be done in chapter 3. Specifically, this second chapter aims to unveil the impact of Al chemistry in the quaternary system CaO-Al<sub>2</sub>O<sub>3</sub>-SiO<sub>2</sub>-H<sub>2</sub>O. NMR experiment and modelling were used as the main tool to detect atomic and molecular configuration and environment changes.

This work takes the form of a manuscript in preparation for submission to *Inorganic Chemistry*

# Impact of Al on the reactivity of calcium silicate hydrates

Kangni-Foli E. <sup>1,2</sup>, Charpentier T. <sup>4</sup>, Poyet S. <sup>3</sup>, Le Bescop P. <sup>3</sup>, Dauzères A. <sup>1</sup>, L'Hôpital E. <sup>1</sup>, d'Espinose de Lacaillerie J.-B. <sup>2</sup>

(1) IRSN, Institute of Radiation Protection and Nuclear Safety, PSE-ENV/SEDRE/ LETIS, BP 17, F-92262 Fontenay Aux Roses, France

(2) Soft Matter Science and Engineering, UMR CNRS 7615, ESPCI Paris, Université PSL, 10 rue Vauquelin, 75005 Paris, France

(3) Den-Service d'Etude du Comportement des Radionucléides (SECR), CEA, Université de Paris-Saclay, F-91191, France

(4) NIMBE, CEA, CNRS, Université Paris-Saclay, CEA Saclay, F-91191 Gif-sur-Yvette Cedex, France

**Corresponding authors:** Stéphane POYET; Thibault CHARPENTIER

- Postal address: CEA Saclay, DEN/DANS/DPC/SECR/LECBA, B158 PC25, F-91191 Gif-sur-Yvette cedex, France.
- NIMBE UMR 3685, CEA, CNRS, Université Paris-Saclay, CEA Saclay
- Emails: [stephane.poyet@cea.fr](mailto:stephane.poyet@cea.fr) ; [thibault.charpentier@cea.fr](mailto:thibault.charpentier@cea.fr)

**Declarations of interest:** none

## 1.1 Abstract

The structural modifications associated with the carbonation of synthetic C-(A-)S-Hs at low Al/Si ratios (from 0 to 0.1) were characterized, focusing on low calcium to silica ratio (C/S) but exploring a large C/S domain (from 0.80 to 1.40). The method of choice was <sup>27</sup>Al, <sup>29</sup>Si magic angle nuclear magnetic resonance (MAS NMR), one-pulse and multiple-quantum (MQ) MAS NMR. Moreover, X-ray diffraction and conventional thermogravimetric techniques were also used. First, the structure of the pristine C-(A-)S-Hs was investigated. <sup>27</sup>Al MQMAS NMR revealed a distorted aluminium tetrahedral site in the C-A-S-Hs at low C/S (0.80) and two tetrahedral environments at high C/S (0.95, 1.20, 1.40). These results suggest the incorporation of Al in bridging and pairing positions, at high C/S. Furthermore, in this C/S range, the structure of the pristine C-A-S-Hs was observed to evolve substantially upon aging. This change involved the mobilization of part of the TAH and of the pentahedral aluminium into C-A-S-Hs' tetrahedral environment. It occurred during the 6 months following the synthesis. The synthetic C-(A-)S-Hs were

submitted to accelerated carbonation which was showed to be representative of the natural carbonation by the nature of the products generated, especially by the calcium carbonates polymorphic distribution (vaterite + aragonite). MAS NMR showed that the carbonation of all the studied C-(A-)S-H yielded identical hydrated aluminosilicate gel, independently of the C/S ratios and the Al content: a novel tetrahedral aluminium environment is formed embedded in a polymerized network comprising mainly Q<sup>3</sup> and Q<sup>4</sup> silicate units. The presence of TAH and pentahedral aluminium is observed to induce a slower carbonation kinetics which supports the assumption that TAH and pentahedral Al species are in vicinity of C-A-S-H phases and limit therefore the CO<sub>2</sub> diffusion by their presence both at the surface and within the C-A-S-Hs' interlayer.

## 1.2 Introduction

Calcium Silicate Hydrates (C-S-H) is the main binding phase of Ordinary Portland Cement (OPC), by large the most manufactured inorganic material in the world today. As the crystal chemistry of C-S-H largely dictates the mechanical properties of the bulk material, an accurate understanding of the C-S-H's molecular properties is of great importance for the prediction of concrete structure's design and concrete durability assessment. Consequently, the C-S-H phase has been the focus of several structural studies for almost 70 years. Bernal *et al.* in 1952 proposed a C-S-H with an infinite silicates chain as found in tobermorite, a natural crystalline calcium silicate hydrate. Numerous models also based on naturally occurring minerals' structure have been proposed. For instance, Taylor's model relied on jennite and 14 Å tobermorite structures and Richardson & Groves model's [1] was based on portlandite and jennite. An improved version of the latter, advanced by Richardson in 2008 [2], took into consideration the variable degree of silicates polymerization. Those models have been essential for understanding the structure and the reactivity of the C-S-Hs.

In industrial materials, C-S-Hs form by hydration of anhydrous phases containing various metals and alkali-metals such as Mg, Na, K, and Al. Some of these species are ultimately incorporated within the C-S-H structure and can potentially modify its reactivity. Aluminium noticeably substitutes for silicon within the C-S-H [3]. The hydrate is then called a calcium-aluminium-silicon hydrate and noted C-A-S-H. Numerous studies can now be found on C-A-S-H properties such as the solubility and ion exchange behaviour [4–6], the effect of Al incorporation on the mechanical properties [7–9], the morphological and microstructural changes related to C-A-S-H compositions [2,10,11] as well as the mechanisms of silicates' substitution by Al [9,12–17].

Studies on C-A-S-H structure and the nature of Al environment are thereafter detailed. Al-substituted tobermorite evidences tetrahedral and octahedral environments. Kalousek *et al.* [18] suggested C-A-S-H and C-S-H as a solid solution and proposed that aluminium substitutes silicon in the C-S-H tetrahedral sites. The possibility of tetrahedral Al substitution in tobermorite was also established by Kormaneni *et al.* [19]. Similar incorporation was proposed by Richardson *et al.* [20] in cementitious materials and the bridging site of the C-S-H dreierketten chain was proposed to be the unique Al incorporation site. The same authors also proved the occurrence of octahedral Al environments but their exact nature remained an open question. Faucon *et al.* [21] also supported the insertion of Al in C-A-S-H tetrahedral site but proposed that isomorphic substitution, while favoured in the bridging sites, could occur in addition at the pairing site. Concerning the observation of pentahedral and octahedral sites, the octahedral ones were assumed to be induced by Ca substitution by Al in the C-A-S-H's main CaO layer. Andersen *et al.* [22] proposed from an array of evidences mainly based on magic angle nuclear magnetic resonance (MAS NMR) that

part of the octahedrally coordinated environment with a NMR resonance at 5 ppm be associated to aluminate moieties on the C-A-S-H's surfaces (the so-called third aluminate hydrate, or TAH). The pentahedral species detected along with TAH had been previously proposed by Faucon *et al.* [21] to compensate the tetrahedral aluminium charge deficit. Based on crystal chemical considerations, Andersen *et al.* [22] concluded instead that aluminium for calcium substitution in the main calcium oxide layer was unlikely. It is thus apparent that despite the number of available studies on C(-A)-S-H structural properties, several aspects still require a deeper understanding. Tetrahedral Si for Al substitution in C(-A)-S-H is well established but details on the exact Al location are still debated (occurrence or not in pairing sites, oxygen sharing between adjacent chains). More importantly, the nature and properties of TAH and pentahedral Al remains to be clarified. This knowledge is however essential to understand the changes generated in cementitious materials under aggressive conditions.

Numerous studies on cementitious materials durability particularly on their carbonation [23–38] were made these last years and the topic is still the focus of current studies [39–41]. This is justified by the high degree of alteration that originates from the carbonation and its deleterious consequences on the materials durability. Carbonation initiates favourable conditions for an active corrosion of steel reinforcement. For now, several aspects such as the kinetics of carbonation and the structure and properties of the carbonated products remain only partially understood, mainly due to the focus on the evolution of the overall cementitious material, at the expense of the observation of mechanisms that occur at the microscale.

In this study we aimed an understanding the role of aluminium at low Al content ( $\text{Al/Si} = 0.05$  and  $0.1$ ) in the carbonation mechanisms at a molecular and atomic level. We synthesized C(-A)-S-Hs with increasing C/S ratios between  $0.80$  and  $1.40$ , at three Al/Si ratios  $0.0$ ,  $0.05$  and  $0.1$ . These samples were submitted to an accelerated ( $P_{\text{CO}_2} = 3\%$ ) and a natural ( $P_{\text{CO}_2} = 0.04\%$ ) carbonation. The environments of the incorporated Al within the C-A-S-H structure were probed by  $^{27}\text{Al}$  multiple quantum (MQ) MAS NMR. The representativeness between the two types of carbonation was assessed as well as the progress of the carbonation and the mechanisms involved. We focused on the consequences of carbonation at a molecular scale, by investigating the nature of the product yielded by C(-A)-S-Hs' ultimate state of carbonation and the influence of Al on the carbonation kinetics.

### **1.3 Materials and methods**

#### **1.3.1 Materials**

The C(-A)-S-Hs powders were synthesized from ultrapure water (Milli-Q,  $18.2 \text{ M}\Omega\cdot\text{cm}$ ), calcium oxide powder calcium aluminate provided by Alfa Aesar, and fumed silica (Aerosil 200) from Evonik industries. A water/solid weight ratio of  $50$  was used for all syntheses. The C-A-S-Hs were obtained following a one-step synthesis: the stoichiometric amount of powders and water were mixed in HDPE bottles to ensure the compositions displayed in Table 1. The bottles were rotated at  $15 \text{ rpm}$  and kept at  $22 \text{ C} \pm 2^\circ\text{C}$  during 6 months.

**Table 1: Nominal composition of the C-(A-)S-H that were synthesized**

<b>C-A-S-H</b>	CA1.4-0.10	CA1.2-0.10	CA0.95-0.10	CA0.8-0.10
Target C/S-Al/Si	1.40-0.10	1.20-0.10	0.95-0.10	0.80-0.10
Synthesis C/S-Al/Si	1.40-0.10	1.23-0.10	0.96-0.10	0.84-0.10
C/(Al+Si)	1.27	1.12	0.87	0.76
Al/(Al+Si)	0.09	0.09	0.09	0.09

<b>C-A-S-H</b>	CA1.4-0.05	CA1.2-0.05	CA0.95-0.05	CA0.8-0.05
Target C/S-Al/Si	1.40-0.05	1.20-0.05	0.95-0.05	0.8-0.05
Synthesis C/S-Al/Si	1.39-0.05	1.20-0.05	0.95-0.05	0.8-0.05
C/(Al+Si)	1.32	1.14	0.90	0.77
Al/(Al+Si)	0.05	0.05	0.05	0.05

<b>C-S-H</b>	C1.40	C1.20	C0.95	C0.80
Target C/S	1.40	1.20	0.95	0.8
Synthesis C/S	1.38	1.22	0.97	0.78

Following the hydration time, the solutions were filtrated and the obtained pastes were dried to yield the C-A-S-H powders. The whole process, mixing, synthesis and handling, was performed under N<sub>2</sub> atmosphere to avoid undesired carbonation.

### 1.3.2 Methods

Thermogravimetric analysis (TGA) presented in the form of the differential of the thermogravimetric analysis (DTG) profiles were acquired using a Netzsch STA 409 PC Luxx apparatus. A constant N<sub>2</sub> flowrate (80 ml/min) as well as a heating rate of 10 °C/min were ensured during the acquisition. The weigh losses associated to the temperature range from 25°C to 1150°C were recorded.

C-A-S-Hs' mineralogical characteristics were investigated by powder X-ray diffraction (XRD). The data were collected using an XPD PANalytical X'Pert diffractometer operated at 45 kV and 40 mA. Acquisition were made on a Bragg-Brentano geometry, in a  $\theta$ - $\theta$  configuration, and using Cu K $\alpha$  radiation as a light source.

#### Nuclear Magnetic Resonance spectroscopy

MAS NMR data were collected at ambient temperature, on a Bruker 500WB Avance II spectrometer (11.72 T) operating at a Larmor frequency resonance of 99.3 MHz and 130.06 MHz, for <sup>29</sup>Si and <sup>27</sup>Al respectively. A Bruker 4 mm (outer diameter of the zirconia rotor) CPMAS probe was used at a spinning frequency of 12.5 kHz.

For C(-A)-S-H samples,  $^{29}\text{Si}$  MAS NMR spectra were acquired following a  $90^\circ$  single pulse excitation after a pre-saturation period (made of a train of 20  $90^\circ$  pulses, in order to allow quantitative analysis of the spectra) followed by a recovery delay of 20 s. No variation in the line shape was observed for longer recovery delays. For  $^{27}\text{Al}$  MAS NMR spectra, a short single pulse of 1  $\mu\text{s}$  (tip angle of about  $\pi/8$  to ensure a quantitative response) and a recycle delay of 2 s were used. Typically, 2000-4000 scans were acquired. Chemical shifts were referenced to an external samples 1M  $\text{AlCl}_3$  aqueous solution (0 ppm) and powder tetrakis(trimethyl)silane (TKS) with the highest intensity peak situated at -9.9 ppm (from that of tetramethylsilane) for  $^{27}\text{Al}$  and  $^{29}\text{Si}$ , respectively.

$^{27}\text{Al}$  MQMAS NMR experiments were performed in order to obtain a higher resolution of the various peaks observed under MAS and a better determination of the NMR parameters. Indeed, these two-dimensional experiments provide a first dimension free of the second-order quadrupolar (SOQ) broadening, correlated to the standard MAS NMR (second) dimension which is impacted by the SOQ broadening. Additionally, such experiments allow one to separate the broadening induced by the distribution of the isotropic chemical shift and the quadrupolar interaction parameter. Such distributions of the NMR parameters are inherent to disordered materials such as C-A-S-H, as clearly shown here. They often result in strong overlapping featureless peaks in (one-dimensional) MAS NMR spectra making their analysis rather difficult. In this work, when necessary, models of NMR parameter distribution were used as introduced in previous works [42–44] and employed routinely in analysis of aluminosilicate glasses [45–47]. NMR data were processed and fitted using an in-house software [44]. Parameters are given as mean values that also correspond to the most probable values associated to the detected distribution. This choice is explained by the disordered nature of the environments.

For analysis of the NMR data, the tobermoritic structure model was adopted which implies the distinction of the different sites within the C(-A)-S-H silicates chains according to the dreierketten pattern: paired tetrahedral, noted  $\text{Q}^{2p}$  and forming dimers, and bridging tetrahedron, noted  $\text{Q}^{2b}$ , linking the pairs. The number of bridging tetrahedra ( $\text{Q}^{2b}$ ) was therefore defined as half of the population of the pairing tetrahedra ( $\text{Q}^{2p}$ ) *i.e.*:  $\text{Q}^{2p} = 2\text{Q}^{2b}$ . Silicates end chain unit connected only once, to one other silicate, are noted  $\text{Q}^1$ .

Natural and accelerated carbonation of the powders were realized in climatic chambers at  $25^\circ\text{C}$ , under the following conditions: 55% of relative humidity,  $\text{P}_{\text{CO}_2}$  of 0.04% and 3% for natural and accelerated carbonation, respectively.

## 1.4 Results

### 1.4.1 Thermogravimetric behaviour before and after carbonation

The Differential of the thermogravimetric profiles (Figure 1) mainly exhibited the typical C(-A)-S-H's weight loss, which persisted until  $850^\circ\text{C}$ . Nonetheless, two domains could be distinguished, the first from 0 to  $725^\circ\text{C}$  and the second which spread from 725 to  $850^\circ\text{C}$ . The loss exhibited in the first domain was attributed to C(-A)-S-H's dehydroxylation and water loss (peak with minima at  $180^\circ\text{C}$ ). C-A-S-Hs demonstrated a more pronounced weight loss in the 300 to  $525^\circ\text{C}$  domain compared to C-S-Hs (Figure b,c). This weight loss could be imputed to the presence of minor phases such as hydrated calcium aluminate not detected by XRD due to their minor content and their lack of crystallinity. Those species could not be quantified since their weight loss is not resolved from the one of the

C-A-S-H. The loss observed in the second domain (from 725 to 850°C) was associated to the formation of wollastonite [48].

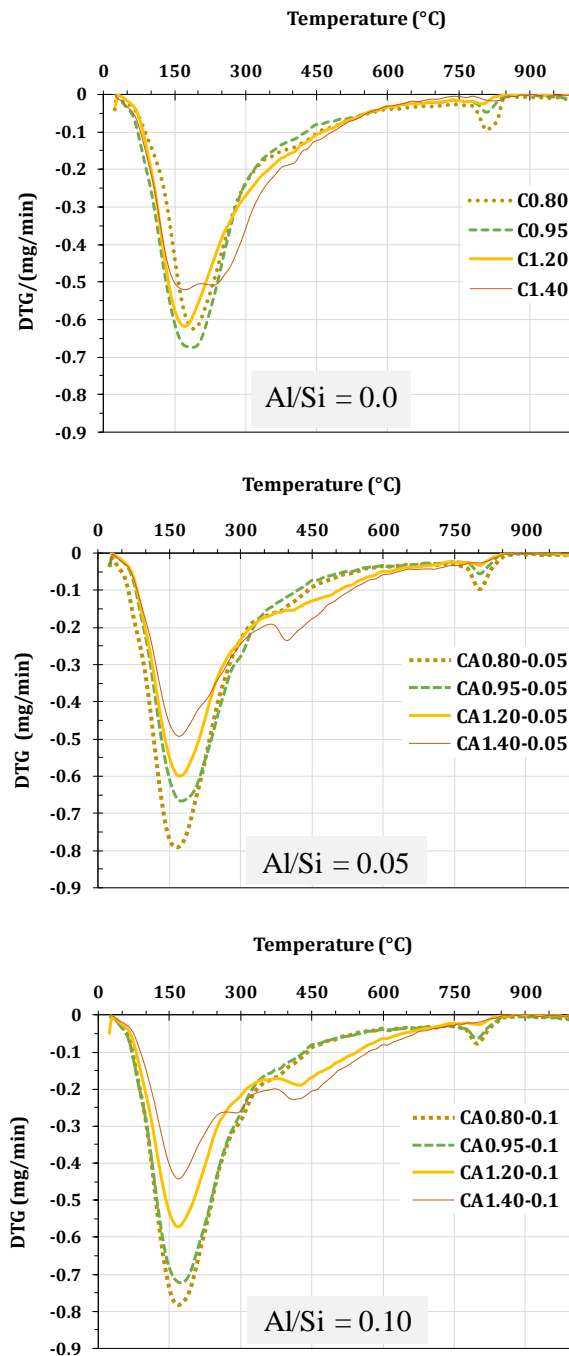


**Figure 1: DTA of the C-S-Hs and C-A-S-Hs of Al/Si ratios of 0.05 and 0.1 Loss associated to C(-A)-S-H between 0-725°C, and wollastonite between 725-850°C.**



## 1.4.2 MAS NMR studies of pristine samples

### 1.4.2.1 $^{29}\text{Si}$ MAS NMR of pristine

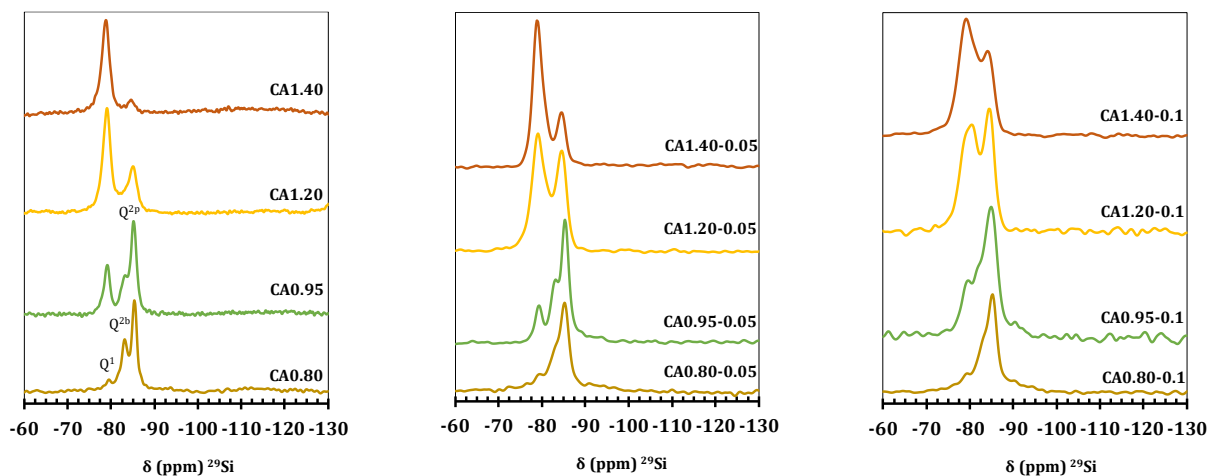


**Figure 2:**  $^{29}\text{Si}$  MAS NMR spectra of the C(-A)-S-Hs displayed from left to right with increasing Al/Si (0, 0.05, 0.1).

$^{29}\text{Si}$  MAS NMR spectra of C-S-H and C-A-S-H samples are displayed on Figure 2. Al-free C-S-H showed the typical C-S-H resonances: the  $\text{Q}^1$  environment (associated to silicates tetrahedra linked to a single silicate tetrahedral) is detected at -79.2 ppm,  $\text{Q}^2$  environments (associated to silicates tetrahedra connected to two others silicates tetrahedral) are detected between -83 and -86 ppm. Two environments are generally defined as  $\text{Q}^2$  environments: the  $\text{Q}^{2b}$  and  $\text{Q}^{2p}$ , observed at -83.1 and -85.4 ppm respectively [49,50].  $\text{Q}^{2b}$  and  $\text{Q}^{2p}$  correspond to the bridging and the pairing silicates tetrahedra of the dreierketten pattern.

The incorporation of Al within C-S-Hs produced a wider distribution of silicon environments as evidenced by the broadening of the resonances which was more pronounced with the increase of Al content (Figure 2). The silicon isotropic chemical shift is known to increase by 3-5 ppm [45] when connected to one aluminium atom (*i.e.*  $\text{Si}^*\text{-O-Al}$  versus  $\text{Si}^*\text{-O-Si}$ ) so that incorporation of Al is expected to lead to a higher dispersion of the chemical shifts. Unfortunately, the resolution of  $^{29}\text{Si}$  MAS NMR spectra resonances of new Al environments were hardly distinguished, especially at low Al/Si.

A general increase of mean chains length (MCL) and degree of the polymerization degree was suggested by both the moderate growth of intensity related to  $\text{Q}^3$  environment (the tail around -90 ppm) at low C/S ratios (0.80, 0.95) and the substantial increase of the intensity of  $\text{Q}^2$  silicates. Both the broadening of the resonances and the increase of connectivity relates coherently with the effective and homogenous (no clusterization) insertion of Al in C-S-Hs. The broadening observed at high Al content and high C/S ratios brought out resonance around -76 ppm which could be explained by the presence of Al in non-bridging position generating thus  $\text{Q}^1(1\text{Al})$  units [51].

#### 1.4.2.2 $^{27}\text{Al}$ MAS NMR

The  $^{27}\text{Al}$  MAS NMR spectra displayed in Figure 3 shows the typical environments of aluminium in the C-A-S-Hs: octahedral (Al(VI)) units from 0 to 20 ppm, pentahedral (Al(V)) units from 30 to 50 ppm and tetrahedral Al(IV) units from 55 to 80 ppm. One can notice the changes induced by both the C/S ratios and the Al content on the Al environments. An increase of octahedral [52] and pentahedral units at higher C/S ratios was observed. At C/S = 0.80, the aluminium was mainly found in tetrahedral environments in the silicate chains and to a smaller extent in an octahedral coordination state related to the formation of calcium aluminates hydrate phases. At higher C/S ratios, the pentahedral Al species and third aluminate hydrates (TAH) constituted the major phases for a C/S ratio higher or equal to 1.2. Tetrahedral units were characterized by a broad asymmetric peak and a global increase of the chemical shift was observed with increasing C/S ratio. A resolved peak at around 66 ppm can be ascribed to a calcium aluminate species the strätlingite [53] (not observed in XRD), however its octahedral resonance could not be discriminated and was assumed to lie in the octahedral band associate to calcium aluminates resonances. The content on strätlingite barely exceeded 2% of the total Al content. Its presence was detected in samples with Al/Si: 0.1 at C/S = 0.80 and 0.95.

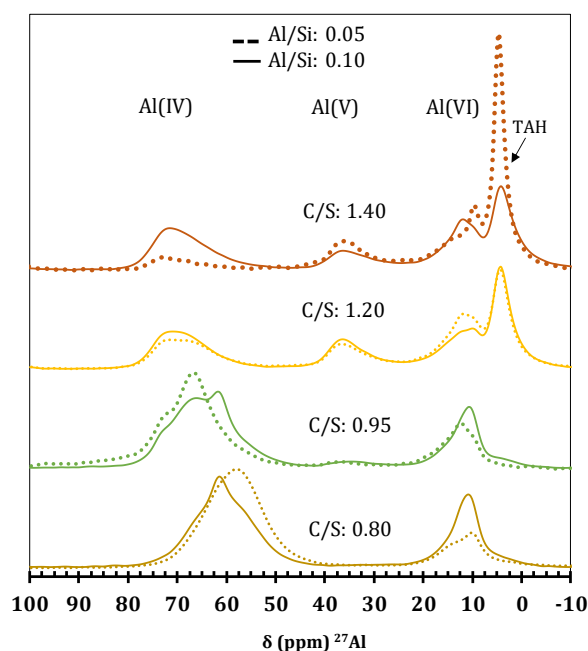


**Figure 3:  $^{27}\text{Al}$  MAS-NMR of the C-A-S-Hs samples. Spectra's surface normalized to the same value in order to allow comparison.**

The proportion of Al detected in tetrahedral environments (determined by fitting the  $^{27}\text{Al}$  MAS NMR spectra as detailed in the supplementary materials (Table S1), see also below the NMR parameters determined from the MQMAS spectra) was retained as the effective C-A-S-H's Al/Si ratio, considering thus, only the Al inserted in silicates chains as part of the C-A-S-H. The higher Al incorporation rate was observed at low C/S ratios (0.80 and 0.95) and high Al/Si ratio (0.1). This behaviour is in agreement with previous studies [9,15,51,54–59]. C-S-Hs of low C/S are

known to have higher silicate MCL, allowing thus in the dreierketten pattern, a higher rate of bridging silicates' substitution by aluminates tetrahedra (Figure 4).

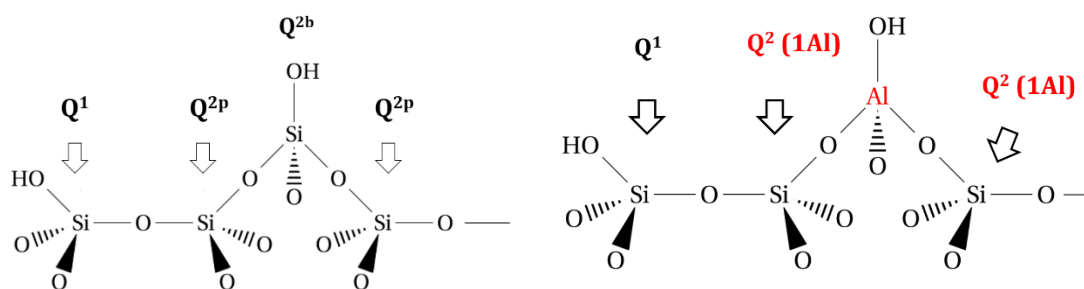


**Figure 4: C-S-H (left) and formation of C-A-S-H (right) by Al insertion in bridging silicates sites. The different silicates sites are highlighted, scheme adapted from [60]**

The aluminium was also found in several octahedral species. Except TAH, calcium aluminium hydrates represented 24-45% of the total Al content. Due the reduced initial Al amount and their poor crystallinity, those phases were neither detected in XRD and ATG nor distinctly identified in one pulse NMR. The broad resonance displayed in 1D <sup>27</sup>Al at 10 ppm is typical of species such as hydroxy-AFm [61], C<sub>3</sub>AH<sub>6</sub>, and non-equilibrium phases such as CAH<sub>10</sub> C<sub>2</sub>AH<sub>8</sub>, C<sub>4</sub>AH<sub>13-19</sub>, (see Table 2)

**Table 2: C-A-S-Hs <sup>27</sup>Al peak intensities, Al h refers to amorphous and ill-crystallized calcium aluminates hydrated potentially hydroxy-AFm, C<sub>3</sub>AH<sub>6</sub>, CAH<sub>10</sub> C<sub>2</sub>AH<sub>8</sub>, C<sub>4</sub>AH<sub>13-19</sub>.**

Target C/S-Al/Si	Al/Si (from <sup>27</sup> Al NMR)	% Al incorporated in C-S-H as Al(IV)	%Al (V)	%Al (VI)	
				%Al h	%TAH
0.80-0.05	0.04	75	0	23	2
0.95-0.05	0.03	65	5	27	3
1.20-0.05	0.01	27	14	35	24
1.40-0.05	<0.01	11	17	27	45
0.80-0.10*	0.06	58	0	38	2
0.95-0.10*	0.06	62	5	24	7
1.20-0.10	0.04	39	12	39	10
1.40-0.10	0.03	31	11	45	13
* Samples with ≈2% of Al in strätlingite phase					

### 1.4.2.2.1 Al MQMAS NMR

#### 1.4.2.2.1.1 Low C/S ratio: C/S = 0.80 & Al/Si = 0.05-0.1

The 2D MQMAS spectra of CA0.8-0.05 and CA0.8-0.1 are displayed on Figure 6a, b respectively. It is important to note that because of the non-homogeneous excitation of sites with respect to their quadrupolar interaction, the MQMAS spectroscopy is non quantitative and sites with small (or vanishing) quadrupolar interactions can appear with a reduced intensity (the same is true of sites with too large quadrupolar interaction), contrarily to the quantitative MAS NMR spectra [62]. In this work, the experimental conditions (RF pulse lengths) have been experimentally optimized for the observation of the tetrahedral sites.

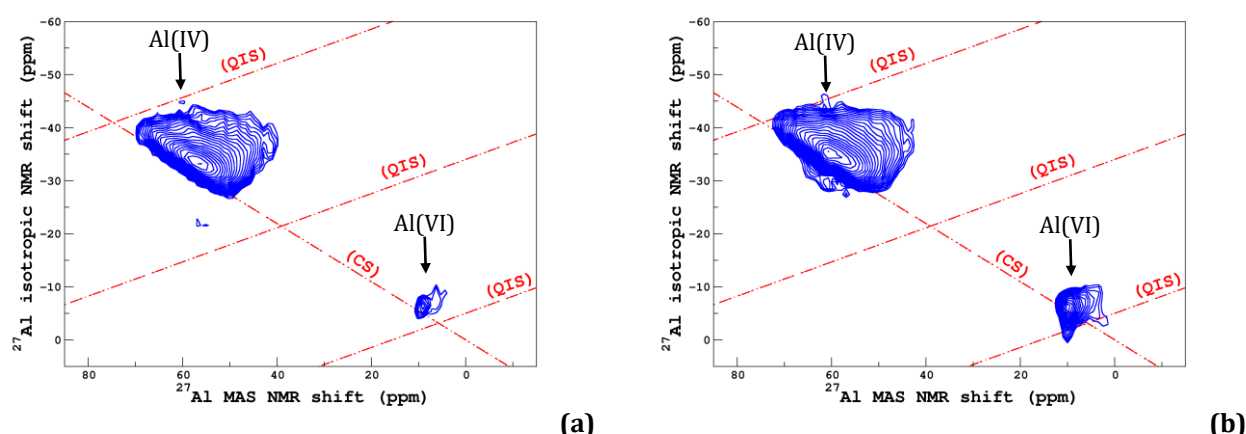


**Figure 5: Al 3Q-MAS NMR spectra of (a) CA0.8-0.05 and (b) CA0.8-0.10. The contour lines (blue) are drawn from 10% to 100% of the maximum heights. The dotted lines represent the direction of broadening induced by an isotropic chemical shift (CS) and second-order quadrupolar induced shift (QIS) distribution.**

In the CA0.8 MQMAS NMR spectra (Figure 5), the broad tetrahedral peak was dominant. In contrast, the octahedral peak was narrower along both directions of broadening (dashed lines), *i.e.* by a distribution of the isotropic chemical shift and of the quadrupolar coupling constant  $C_Q$ . The shape of the tetrahedral peak in the MQMAS spectra for CA0.8-0.05 and CA0.8-0.1 is a typical line shape reflective of a disordered environment and is similar to the one observed in aluminosilicate glasses [45]. A slight variation in the tetrahedral peak shape and position was observed when the Al content increased (see Table S1). This peak could be well fitted using a model of NMR distribution as introduced for aluminosilicate glasses [45,47], as shown in Figure 6. A second resonance in the tetrahedral domain was observed for CA0.8-0.1 (Figure 6b) which was attributed to strätlingite since its isotropic shift  $\delta_{iso}$  was similar to the one reported by Kwan *et al.* [53]. Moreover, this environment exhibited a lower mean quadrupolar constant and a smaller chemical shift distribution compared to the tetrahedral environment originated from Al incorporation in C-A-S-H. Kwan *et al.* [53] reports as well an octahedral resonance for strätlingite at 9.7 ppm, which was presumed to be part of the calcium aluminates resonance observed around 10 ppm. The broadening of the  $^{29}\text{Si}$  spectra and the low content on strätlingite did not permit to discriminate strätlingite signal on  $^{29}\text{Si}$  MAS-NMR.

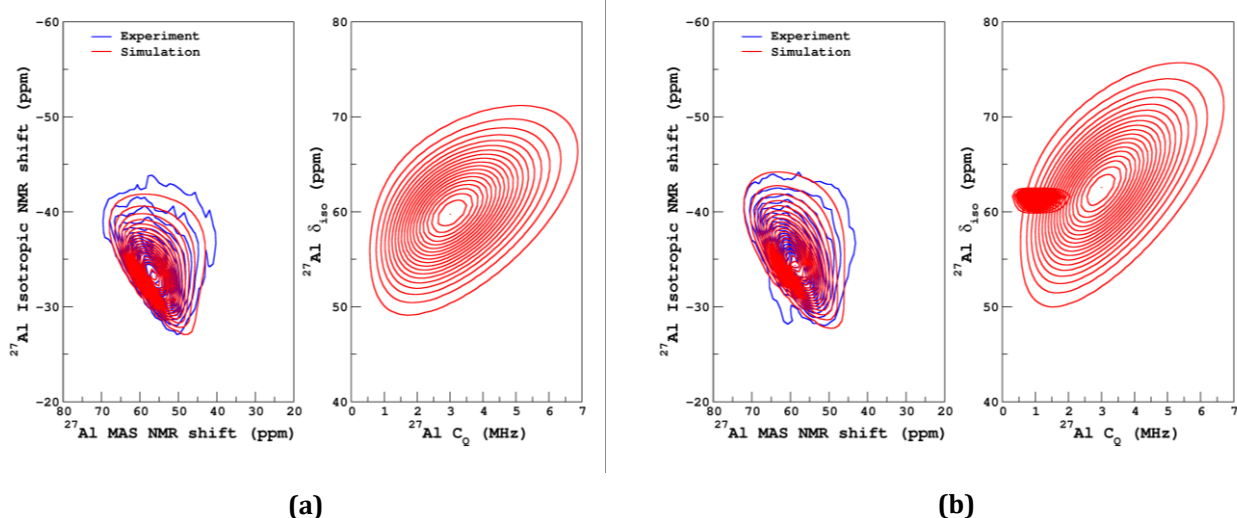


Figure 6: CA0.8-0.05 and CA0.8-0.10 simulated and experimental MQMAS NMR spectra (left panel) and distribution of  $\delta_{\text{iso}}$  plotted against  $C_Q$  (right panel) are shown on figure (a) and (b), respectively.

#### 1.4.2.2.1.2 Samples at high C/S: the case of 0.95 and $C/S > 0.95$

The increase of the calcium content from a C/S ratio of 0.8 to 0.95 resulted in different Al environments in the C-A-S-Hs. Similarly, to  $C/S = 0.80$ , a broadened tetrahedral environment was observed. However, the corresponding isotropic chemical shift in C-A-S-Hs at  $C/S = 0.95$  as revealed by MQMAS NMR unambiguously differentiated their tetrahedral environments from the ones observed at lower C/S ratios (see Figure 7a and Table S1 for the (mean) values of the parameters). The pentahedral environment not observed at lower C/S ratio (0.80) appeared for a C/S of 0.95 at around 37 ppm. A broad octahedral resonance of weak intensity appeared at high Al content at a chemical shift of 6.4 ppm. This environment has been referred to as the third aluminate hydrate (TAH) in previous work [22]. The C-A-S-H (CA0.95-0.1) with higher Al content exhibited residual contents of strätlingite.

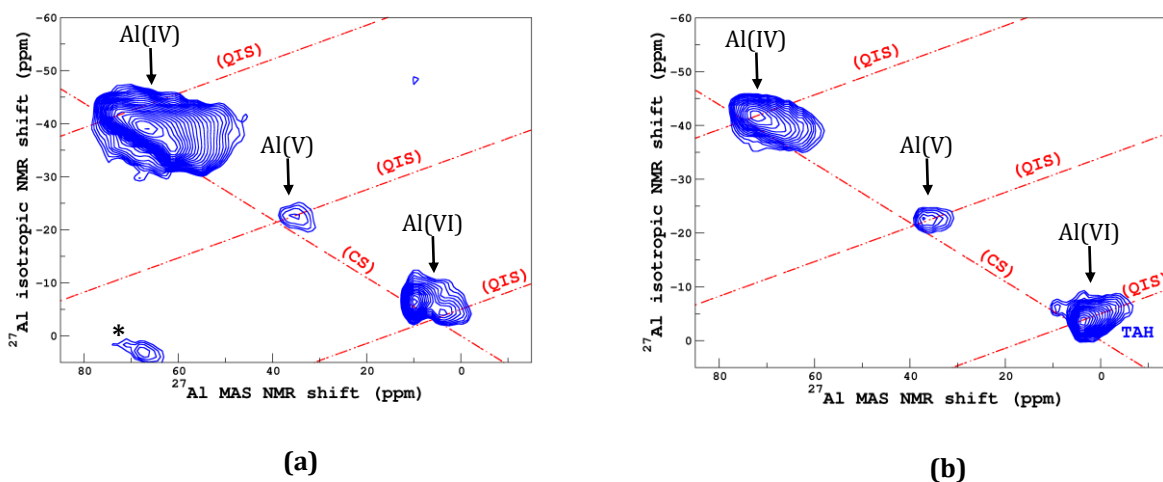
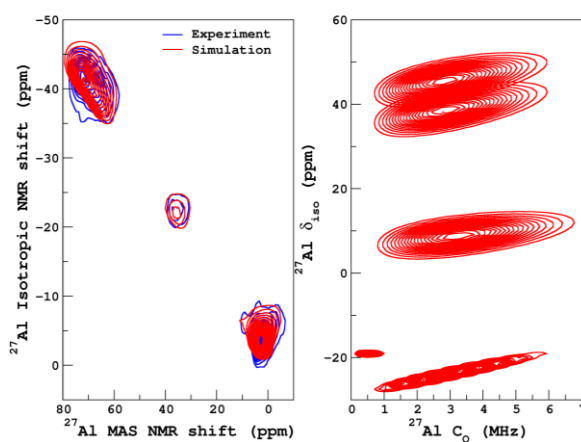


Figure 7:  $^{27}\text{Al}$  MQMAS NMR spectra of (a) CA0.95-0.1 (b) CA1.40-0.1.\*spinning sideband.

The MAS NMR spectra of C-A-S-Hs at C/S ratio of 0.95 and higher showed the same tetrahedral environment associated to Al incorporation in C-A-S-H (Figure 7b), however, they exhibited a narrower distribution of the quadrupolar parameters and the chemical shift compared to lower C/S ratio (0.80). The pentahedral environment detected was similar for all C/S ratios, higher or equal than 0.95. The TAH and the calcium aluminium hydrate at around 10 ppm signal were the dominant octahedral environments. Figure 8 shows the simulation of the MQMAS NMR spectra for CA0.95-0.1 and CA1.40-0.1, along with the isotropic chemical shift and the quadrupolar NMR parameter distribution related to each environment. Two environments were found necessary for the simulation of the tetrahedral aluminium peak (the requirement of the two environments used were distinctly evidenced by MQMAS spectrum of partially carbonated samples, see Figure 18).



**Figure 8: CA1.4-0.1 distribution of  $\delta_{\text{iso}}$  plotted against  $C_Q$**

## 1.5 Evolution of the C-A-S-H

### 1.5.1 Aging of the pristine product in absence of $\text{CO}_2$

Over a period of 12 months, we observed that the TAH content evolved in the high C/S (1.2, 1.4) samples as shown in Figure 9. The decrease of TAH was found to be concomitant with the decrease of Al (V) and the increase of Al(IV). This suggests that Al migrated with time from pentahedral and octahedral environment to tetrahedral sites, and that Al(V) and TAH species were correlated species. This phenomenon appeared to be more pronounced at lower Al/Si and no further change was observed 1 year later.

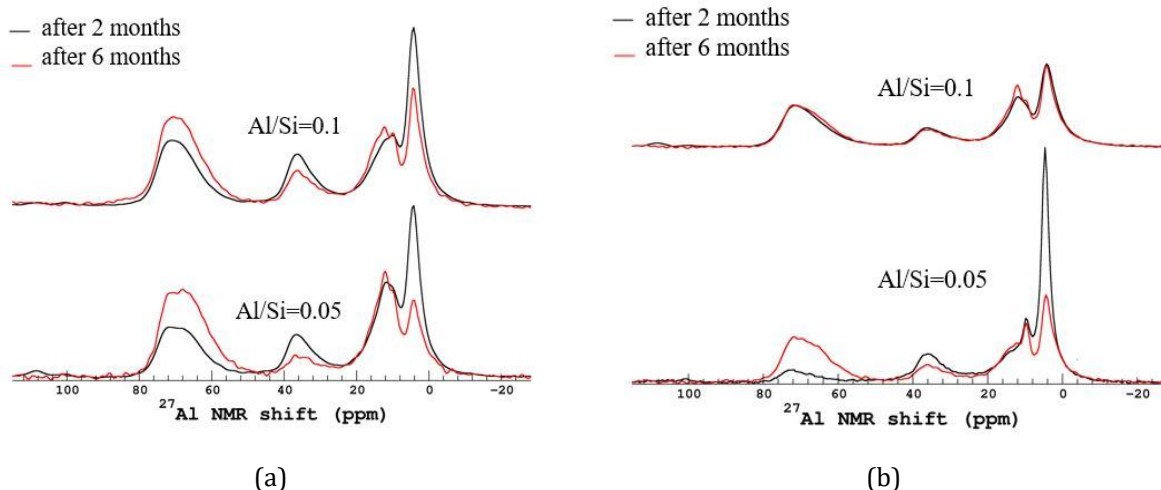


**Figure 9:  $^{27}\text{Al}$  MAS NMR spectra from 2 months after synthesis to 6 months after synthesis for (a) CA1.2-0.05/0.1 (b) CA1.4-0.05/0.1**

## 1.5.2 Effect of the carbonation on C-A-S-H

### 1.5.2.1 Mineralogical properties of the pristine and the carbonated materials

The X-ray diffractograms of the natural and the accelerated C-S-Hs' carbonation ( $\text{C/S} = 0.80$  and  $1.40$ ) are presented along with the sound materials in Figure 10. The pristine materials only exhibited the typical C-S-H pattern (black diamond). The carbonation, either accelerated or natural, generated the same calcium carbonate polymorphs, mainly vaterite and marginally aragonite. From the standpoint of XRD, accelerated ( $\text{P}_{\text{CO}_2}$ : 3%) and natural carbonation ( $\text{P}_{\text{CO}_2}$ : 0.04%) appeared identical in their consequences, which suggest the representativeness of the accelerated condition used compared to the natural carbonation. After less than 20 days of accelerated carbonation, one could see the extinction of the diffraction's signal from C-S-H at  $\approx 29.1^\circ(2\theta)$ , extinction associated to the degradation of the main CaO layer, and this independently of the C/S ratio. The same could be said of the basal reflection at low angle, related to the C-A-S-H interlayers distance and interstratification.

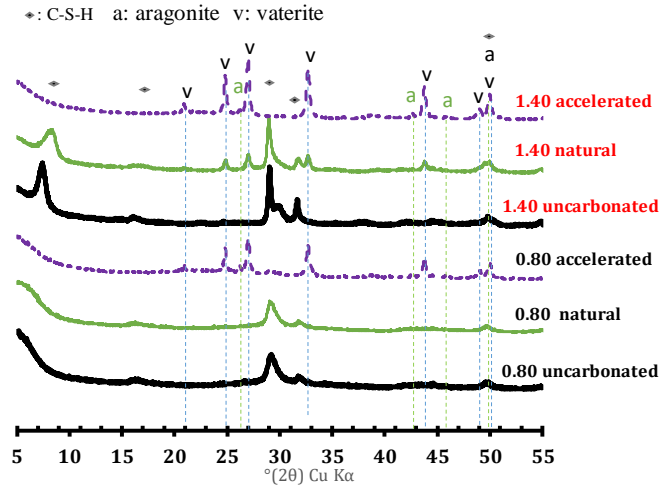


**Figure 10: X-ray diffractograms of C-S-Hs at C/S: 0.80 and 1.40. The pristine uncarbonated states are showed together with natural (after 17 days at  $P_{CO_2}$ : 0.04%) and accelerated (after 18 days at  $P_{CO_2}$ : 3%) carbonation products. The same polymorphs were yielded by the two types of carbonation. Regardless of the C/S ratios, carbonation was total after 18 days of accelerated carbonation**

Only characteristic C-S-H's signal was observed from the pristine C-A-S-Hs, this highlighted a solid solution between C-S-H and C-A-S-H (at least at low Al/Si) and the absence of detectable crystalline impurities in the syntheses. The carbonated C-A-S-Hs demonstrated the same polymorphic orientation as the C-S-Hs during natural and accelerated carbonation (essentially vaterite, and aragonite as a minor phase). The main difference appeared in the kinetics of carbonation. After 34 days of accelerated carbonation, the ultimate carbonation state was not reached for the higher C/S samples, as indicated by the C-A-S-H's peak around  $29.1^\circ(2\theta)$  and the presence of a reflection at low angle ( $7.4^\circ(2\theta)$ ) characteristic of the basal distance. The C-A-S-Hs of higher C/S ratios (1.4, 1.2) and higher aluminium content (Al/Si = 0.1) presented the slower carbonation kinetic.

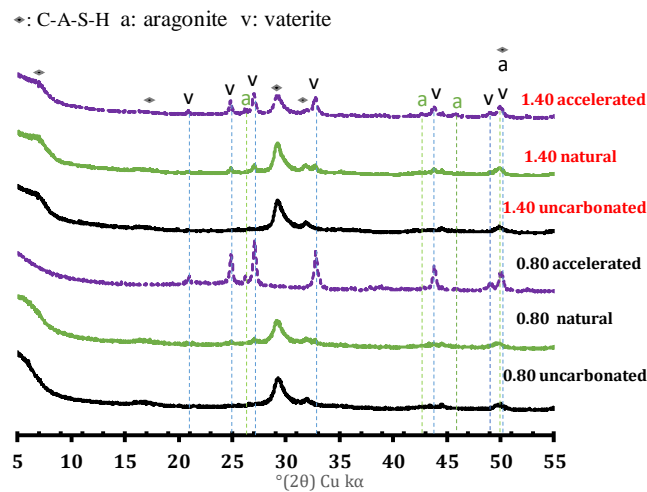


**Figure 11: x-ray diffractograms of C-A-S-Hs (Al/Si = 0.1) at C/S of 0.80 and 1.40. The pristine uncarbonated states are showed together with natural (38 days at  $P_{CO_2}$ : 0.04%) and accelerated (34 days at  $P_{CO_2}$ : 3%) carbonation products. The same polymorphs are observed compared to C-S-Hs' carbonation (see Figure 10) but a slower carbonation kinetics is evidenced at high C/S ratio in presence of Al.**



To highlight the progress of the carbonation, the evolution of the calcium carbonate phases (vaterite, aragonite) and of the C-A-S-H diffracted intensities related to the CaO main layer are represented in Figure 12 with respect to the duration of the carbonation for C/S ratios of 0.8 and 1.4 and for an Al/Si: 0.05 and 0.1. The contrast of the carbonation's speed highlighted the effect of the calcium content. The C-A-S-Hs with the higher C/S ratios required longer time to attain the steady calcium carbonate diffracted intensity typical of the fully carbonated state. An incomplete carbonation after 145 days was observed at the highest C/S ratio and Al content. The progress of the carbonation seemed to be controlled by the calcium content but also the Al content of the overall system. Comparing CA1.40-0.05 and CA1.40-0.1 the sample with the higher Al content demonstrated the slower carbonation rate.

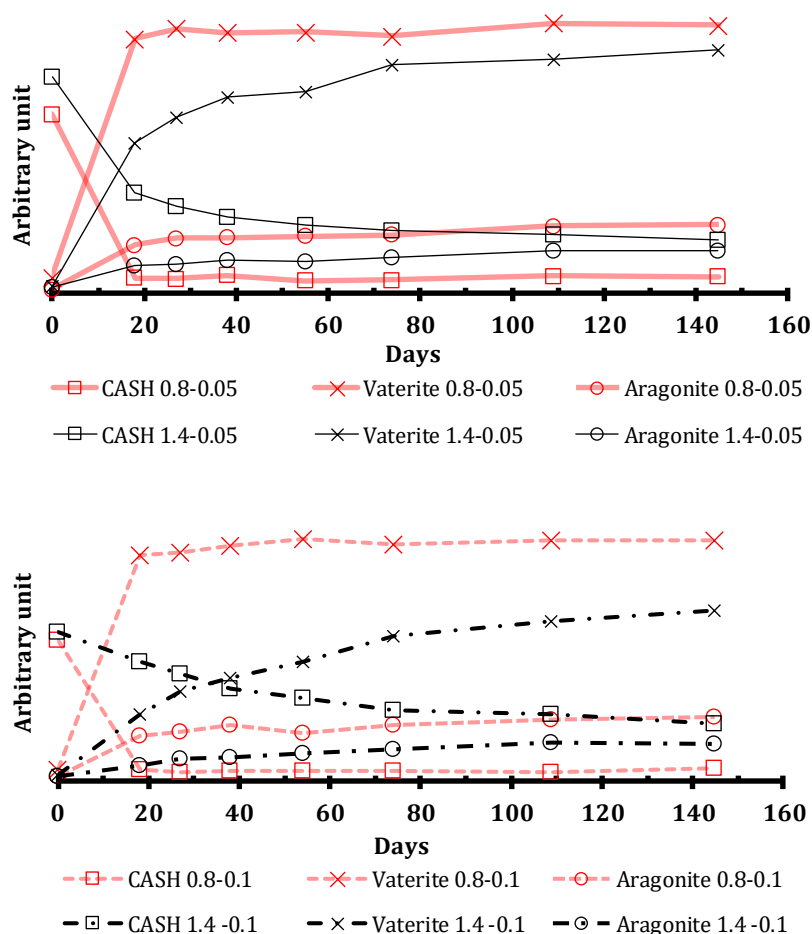


**Figure 12: Intensities of observed phases at different carbonation terms for CA0.8-0.05 and CA1.4-0.05.**

### 1.5.2.2 DTG of carbonated product

The thermal analyses of the carbonated products (Figure 13) demonstrated a loss centered at 120°C and at 650°C (Figure 13). The first loss was related to the water loss of non-carbonated C-A-S-H and the silica gel formed after carbonation. The loss centered at 625°C and limited to 780°C was known to be the domain of degradation of calcium carbonates such as aragonite and vaterite [32,63].

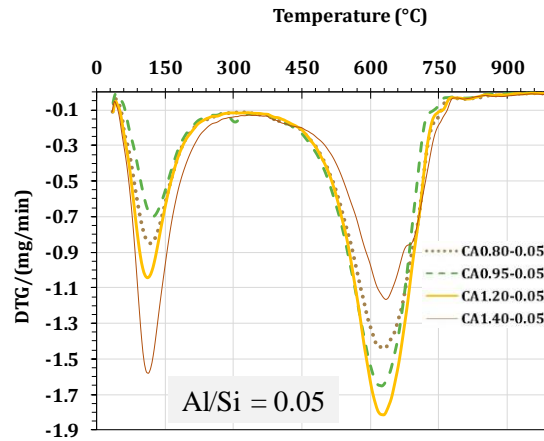


**Figure 13: DTG of the carbonated C-A-S-Hs Al/Si=0.05, partial carbonation for CA1.40-0.05 is evidenced by reduced loss centered at 625°C.**

This domain was narrower than usually observed, due to the absence of calcite, which is usually indicated by losses between 800 and 900°C. Our results evidenced through the carbonates' losses exhibited below 800°C the presence of metastable carbonates, due to the carbonates' losses exhibited below 800°C, which correlates with the phases evidenced by XRD (aragonite and vaterite). Partial carbonation is demonstrated by the sample with the higher C/S ratio CA1.40-0.05, as supported by a reduced loss seen in the calcium carbonates region (loss centered at 625°C) and a higher weight loss centered at 120°C associated to C-A-S-Hs' water loss (compared to fully carbonated samples).

### 1.5.2.3 <sup>29</sup>Si in the carbonated product

The significant impact of the degradation induced by accelerated carbonation on silicates environments is illustrated in Figure 14 for C0.80, C1.20, CA1.2-0.05 and CA0.80-0.1 in the pristine and carbonated state. The Al content did not seem to affect the type of products obtained; silicon atoms were dominantly in Q<sup>3</sup> and Q<sup>4</sup> units forming network typical of silica gel. However, the silica gel yielded by C-S-Hs' carbonation had a higher degree of polymerization (Figure 15 & Table S2).

The polymerization of the gel increased with the C-S-H's calcium content. A strong decrease of the polymerization of the silica gel is observed in presence of aluminium reflected through a higher Q<sup>3</sup> content (Figure 14) as shown by Gambuzzi *et al.* [45].

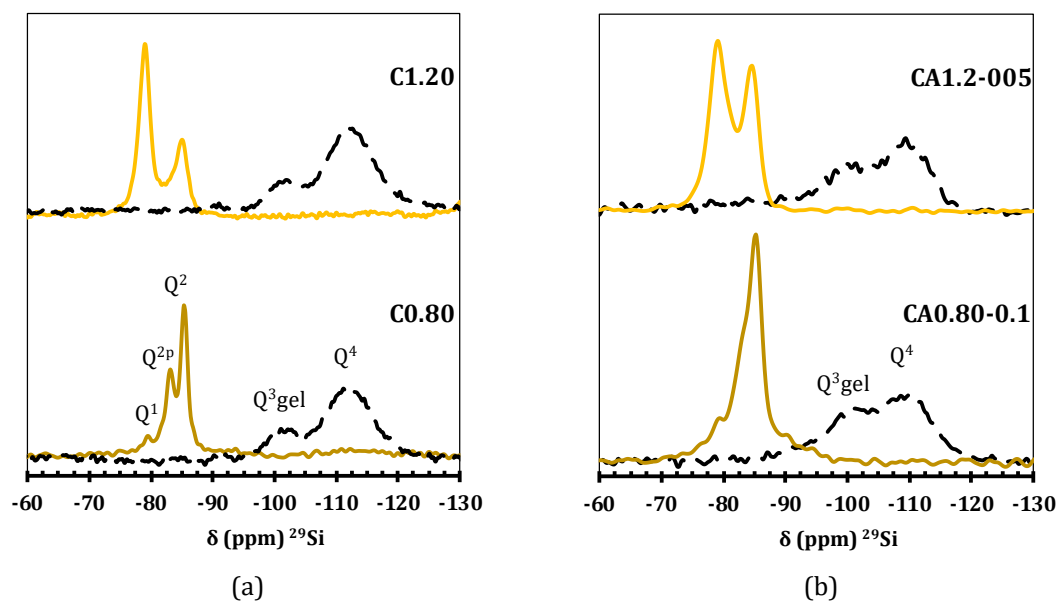


**Figure 14:**  $^{29}\text{Si}$  MAS NMR spectra of non-carbonated (continued lines) and carbonated (dotted lines) (a) C-S-Hs at C/S ratios of 0.80 and 1.40 (b) C-A-S-Hs C/S: 0.80 and 1.20 at Al/Si: 0.1 and 0.05.

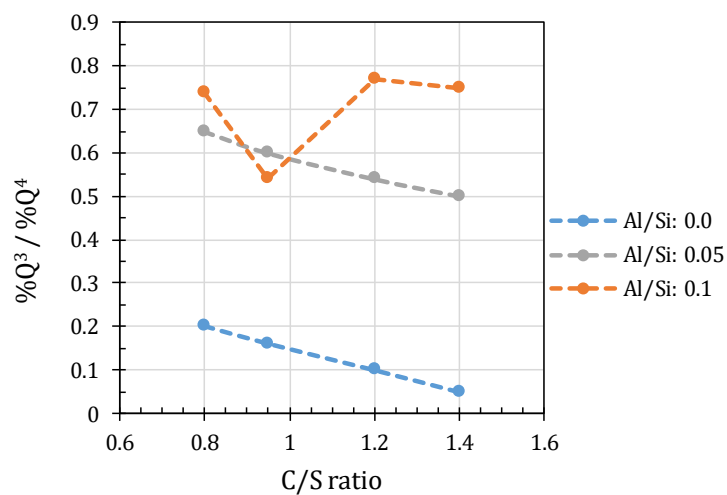


**Figure 15:** Comparison of  $Q^3$  and  $Q^4$  evolution for carbonated C(-A)-S-Hs.

#### 1.5.2.4 Al in the carbonated product (1D+2D)

The  $^{27}\text{Al}$  MAS NMR spectra of carbonated samples highlighted a well resolved Al environment for fully carbonated C-A-S-Hs (Table S1 & Figure 16). Only part of the hydrated calcium aluminate signal in octahedral domain was affected by carbonation. No signals of TAH and Al (V) were detected.

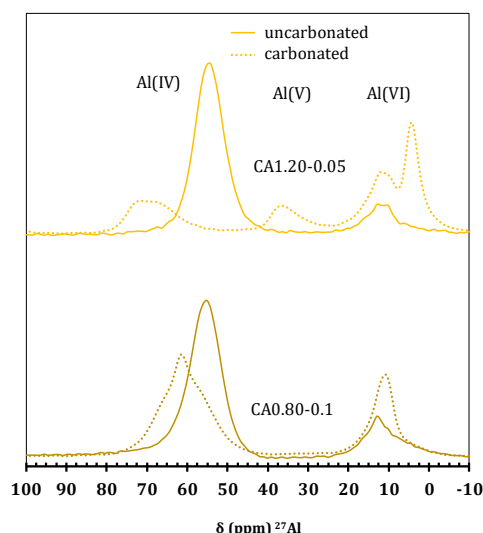


**Figure 16:**  $^{27}\text{Al}$  MAS NMR spectra of CA0.80-0.1 and CA1.20-0.05 sounds and carbonated state.

The 2D 3QMAS spectrum of CA0.8-0.05's carbonated product, displayed in Figure 17, confirmed the formation of a novel carbonated environment for Al. This environment was more easily discernible from an uncarbonated environment for CA1.40-0.05 sample as shown in Figure 18. The two tetrahedral sites highlighted at high C/S ratio in pristine samples were clearly still visible along with the carbonated environment, which was found to be identical for all studied samples.

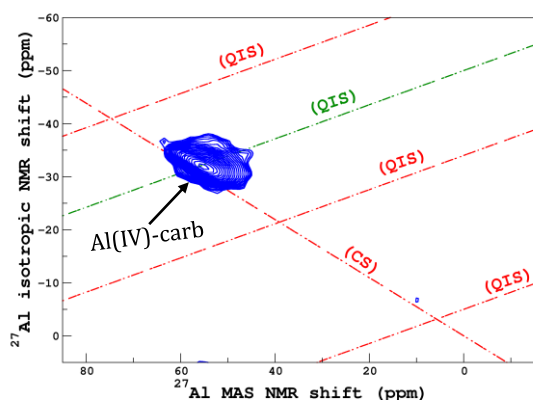


**Figure 17:** 2D  $^{27}\text{Al}$  MQMAS spectrum of carbonated CA0.8-0.05.

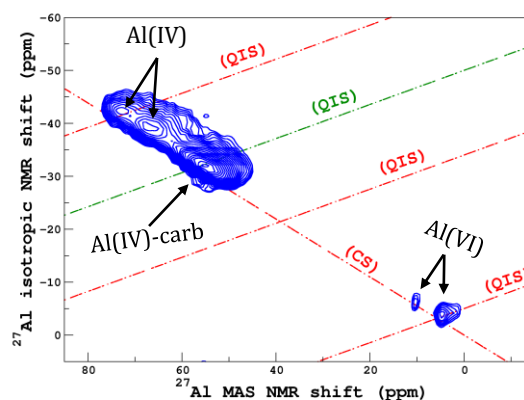


**Figure 18:** 2D  $^{27}\text{Al}$  MQMAS spectrum of carbonated CA1.4-0.05.

## 1.6 Discussion

NMR Investigation on C-S-Hs structural properties, at low Al/Si, unveiled two different structural features according to the calcium content. At low C/S ratio (0.80), the MQMAS spectra revealed a broad resonance with a mean isotropic chemical shifts ranging from 60 ppm at Al/Si = 0.05 to 63.0 ppm at Al/Si = 0.10 (see Figure 5a and b respectively). This range of resonances was previously assigned in tobermorite and C-A-S-Hs as  $\text{Q}^2(1\text{Al})$  and  $\text{Q}^3(1\text{Al})$  for Al in bridging position (64 ppm) in a single chain and for Al in crosslinking position (57 ppm) on the dreierketten

double chains [19,64–66]. The same attributions can be made here. The  $^{29}\text{Si}$  resonance at -92 ppm (Figure 2b,c) suggested the appearance of crosslinked chains, which confirmed the presence of  $\text{Q}^3(1\text{Al})$  environment.

The increase of the C/S ratio from 0.80 to 0.95 manifested itself by strong changes in the  $^{27}\text{Al}$  tetrahedral resonances. Except the maintained  $\text{Q}^3$  feature seen in the  $^{29}\text{Si}$  spectra, the  $^{27}\text{Al}$  MQMAS spectra exhibited two new environments located around 70 and 76 ppm. For the resonance at 70 ppm, we suggest at higher C/S ratio the presence of the same bridging tetrahedra observed at C/S = 0.80 but in an environment with modified geometry and charge distribution (a smaller mean quadrupolar coupling constant was measured, see Table S1) due to an increased calcium shielding. This would explain the difference of chemical shift of 4 ppm, from 66 to 70 ppm [67,68]. This attribution seemed reasonable given the concomitant chemical shift increase with the C/S ratio, and the presence of bridging tetrahedra despite the shortening of the chains at high C/S ratio.

We propose the environment observed at 76 ppm to result from the insertion of Al in pairing position. The increase of the C/S ratio is known to induce shorten chains such as dimers, allowing thus the possible insertion of aluminium in others available position such as pairing position [17]. Furthermore, the presence of Al in non-bridging position is supported by the presence of minor  $\text{Q}^1(1\text{Al})$  unit exhibited in  $^{29}\text{Si}$  spectra at high C/S ratio (1.2, 1.4)  $\approx$  -76 ppm.

The resonance at 76 ppm is proposed in [22,64,65] to correspond to tetrahedral Al in bridging position. In the literature, this aluminium environment is suggested to be the signature of tetrahedral aluminium compensated by pentahedral and octahedral Al species located in C-A-S-Hs' interlayer and surfaces. This is supported both by the commonly accepted higher stability of the substitution on the bridging site over the pairing position, and the recurrence of the maximum silicon substitution rate usually reported close to 0.3, [5,64,69]. Therefore, the high chemical shift observed is proposed to be explained by the vicinity between the TAH and the pentahedral species, and the inserted Al in C-A-S-H's bridging silicate chains.

Considering the tetrahedral environment at 76 ppm, charge compensated by Al (V, VI) as proposed by the literature, the decrease of the content of pentahedral and octahedral species (observed in this work following the synthesis) should lead to a strong modification of the properties of the tetrahedral environment. The modification of those compensating charges should induce a change in the chemical shift and in the quadrupolar parameter. However, despite the conversion of TAH and pentahedral environment into tetrahedral Al, no change was observed in the parameters related to the tetrahedral environment. The vicinity of TAH and pentahedral Al to C-A-S-H, as suggested by Andersen *et al.* [22], is supported by the mobilization of Al in C-A-S-H but it seemed that the charge compensation mechanism might not be sufficient to explain the higher chemical shift observed with the increase of the C/S ratio. Following our observations, a more plausible answer to the high chemical shift demonstrated would be the higher Ca shielding combined to the presence of Al in pairing position in shorten chains which both might affect structural features such as the bond distance, angles and the geometry, thus the chemical shift [68].

The accelerated carbonation of the C(-A)-S-Hs yielded aluminosilica gel and calcium carbonates as expected. The same calcium carbonates polymorphic abundance was observed during accelerated and natural carbonation, which supports the representativeness of the accelerated carbonation implemented with compared to the natural carbonation. The presence and the nature of Al insertion in C-A-S-H, did not influence the formation of the carbonated products. However, the C-A-S-Hs of high C/S ratios 1.2 and 1.4 were observed to carbonate slower than

the C-A-S-Hs of low C/S. This might be explained by both the high calcium content and the presence of Al not incorporated in C-A-S-H responsible of the formation of distinct phases, (nonetheless in vicinity of the C-A-S-H) such as TAH and Al(V). The carbonation of C-A-S-Hs of high C/S was characterized by a slower rate of degradation attributed to the presence of TAH and pentahedral Al at the surface and within C-A-S-H interlayers.

## 1.7 Conclusion

The effect of Al incorporation and the evolution in presence and in absence of CO<sub>2</sub> of C(-A)-S-H of C/S ratios from 0.80 to 1.40, at low Al/Si (0, 0.05, 0.1) were investigated by XRD, <sup>29</sup>Si and <sup>27</sup>Al NMR spectroscopy, and TGA. At low C/S, similarly to previous findings, Al was found to be mainly incorporated in tetrahedral bridging positions that are the bridging position of dreierketten pattern in single silicate chain, and in silicates crosslinked chains. However, these two environments could not be resolved. At higher C/S ratios, Al was detected in two distinctly resolved tetrahedral positions, which are suggested to correspond to aluminates in substitution of bridging silicates, and pairing silicates in single chain. The incorporation of Al in pairing position was confirmed by resonance at <sup>29</sup>Si frequencies higher than -80 ppm (Q<sup>1</sup>(1Al) species) and the broadening of <sup>29</sup>Si spectra towards lower fields. All C/S ratios evidenced octahedral environment that was attributed to calcium aluminates hydrates. The increase of C/S ratios from 0.80-0.95 induced the concomitant formation of pentahedral species and a second type of octahedral site, generally referred to as TAH. Previous works proposed the compensation of inserted Al in tetrahedral position by TAH and pentahedral Al as an explanation of the simultaneous increase of Al frequency with the C/S. Our observations invalidate this hypothesis since we noticed unchanged (tetrahedral) NMR parameter upon the disappearance of pentahedral species and TAH. Instead, we observed the transformation of pentahedral and TAH aluminium within C-A-S-H into tetrahedral environment, the resonances of the latter despite the degradation of Al (V) and TAH were maintained.

The effect of the carbonation led to the formation of a calcium aluminosilicate gel and carbonates. The gel was characterized by a single Al environment, independent of the initial composition, distinguishable from both C-A-S-Hs' high and low C/S tetrahedral environments. The carbonation kinetics was found to depend on TAH and pentahedral Al species. The incorporation of Al in tetrahedral position and the presence of calcium aluminates hydrate except pentahedral species and TAH, did not demonstrate a strong influence on the carbonation kinetics, since all C-S-Hs and C-A-S-Hs at low C/S ratio showed the similar rate of degradation. The formation of aluminates species typical of high C/S (TAH and Al (V)), which were found to be intimately related to the C-A-S-Hs structures induced a slower rate of carbonation. We believe that those species reduce the CO<sub>2</sub> access to C-A-S-Hs

## Acknowledgements

The financial support from IRSN and CEA is gratefully acknowledged.

## References

- [1] I.G. Richardson, G.W. Groves, Models for the composition and structure of calcium silicate hydrate (CSH) gel in hardened tricalcium silicate pastes, *Cem. Concr. Res.* 22 (1992) 1001–1010. doi:10.1016/0008-8846(92)90030-Y.
- [2] I.G. Richardson, The calcium silicate hydrates, *Cem. Concr. Res.* 38 (2008) 137–158. doi:10.1016/j.cemconres.2007.11.005.

- [3] M.D. Andersen, H.J. Jakobsen, J. Skibsted, Characterization of white Portland cement hydration and the C-S-H structure in the presence of sodium aluminate by  $^{27}\text{Al}$  and  $^{29}\text{Si}$  MAS NMR spectroscopy, *Cem. Concr. Res.* 34 (2004) 857–868. doi:10.1016/j.cemconres.2003.10.009.
- [4] J. Haas, A. Nonat, From C-S-H to C-A-S-H: Experimental study and thermodynamic modelling, *Cem. Concr. Res.* 68 (2015) 124–138. doi:10.1016/j.cemconres.2014.10.020.
- [5] E. L'Hôpital, B. Lothenbach, G. Le Saout, D. Kulik, K. Scrivener, Incorporation of aluminium in calcium-silicate-hydrates, *Cem. Concr. Res.* 75 (2015) 91–103. doi:10.1016/j.cemconres.2015.04.007.
- [6] E. L'Hôpital, B. Lothenbach, D.A. Kulik, K. Scrivener, Influence of calcium to silica ratio on aluminium uptake in calcium silicate hydrate, *Cem. Concr. Res.* 85 (2016) 111–121. doi:10.1016/j.cemconres.2016.01.014.
- [7] G. Geng, R.J. Myers, J. Li, R. Maboudian, C. Carraro, D.A. Shapiro, P.J.M. Monteiro, Aluminum-induced dreierketten chain cross-links increase the mechanical properties of nanocrystalline calcium aluminosilicate hydrate, *Sci. Rep.* 7 (2017). doi:10.1038/srep44032.
- [8] C.C. Dharmawardhana, A. Misra, S. Aryal, P. Rulis, W.Y. Ching, Cement and Concrete Research Role of interatomic bonding in the mechanical anisotropy and interlayer cohesion of CSH crystals, *Cem. Concr. Res.* 52 (2013) 123–130. doi:10.1016/j.cemconres.2013.05.009.
- [9] F. Puertas, M. Palacios, H. Manzano, J.S. Dolado, A. Rico, J. Rodríguez, A model for the C-A-S-H gel formed in alkali-activated slag cements, *J. Eur. Ceram. Soc.* 31 (2011) 2043–2056. doi:10.1016/j.jeurceramsoc.2011.04.036.
- [10] C. Rößler, F. Steiniger, H.-M. Ludwig, Characterization of C-S-H and C-A-S-H phases by electron microscopy imaging, diffraction, and energy dispersive X-ray spectroscopy, *J. Am. Ceram. Soc.* 100 (2017) 1733–1742. doi:10.1111/jace.14729.
- [11] E. Kapeluszna, Ł. Kotwica, A. Różycka, Ł. Gołek, Incorporation of Al in C-A-S-H gels with various Ca/Si and Al/Si ratio: Microstructural and structural characteristics with DTA/TG, XRD, FTIR and TEM analysis, *Constr. Build. Mater.* 155 (2017) 643–653. doi:10.1016/j.conbuildmat.2017.08.091.
- [12] S. V. Churakov, C. Labbez, Thermodynamics and Molecular Mechanism of Al Incorporation in Calcium Silicate Hydrates, *J. Phys. Chem. C* 121 (2017) 4412–4419. doi:10.1021/acs.jpcc.6b12850.
- [13] G. Renaudin, J. Russias, F. Leroux, C. Cau-dit-Coumes, F. Frizon, Structural characterization of C-S-H and C-A-S-H samples-Part II: Local environment investigated by spectroscopic analyses, *J. Solid State Chem.* 182 (2009) 3320–3329. doi:10.1016/j.jssc.2009.09.024.
- [14] M.J. Abdolhosseini Qomi, F.-J. Ulm, R.J.M. Pellenq, Evidence on the Dual Nature of Aluminum in the Calcium-Silicate-Hydrates Based on Atomistic Simulations, *J. Am. Ceram. Soc.* 95 (2012) n/a-n/a. doi:10.1111/j.1551-2916.2011.05058.x.
- [15] M.J. Abdolhosseini Qomi, K.J. Krakowiak, M. Bauchy, K.L. Stewart, R. Shahsavari, D. Jagannathan, D.B. Brommer, A. Baronnet, M.J. Buehler, S. Yip, F.-J. Ulm, K.J. Van Vliet, R.-. M. Pellenq, Combinatorial molecular optimization of cement hydrates, *Nat. Commun.* 5 (2014) 4960. doi:10.1038/ncomms5960.
- [16] L. Pegado, C. Labbez, S. V. Churakov, Mechanism of aluminium incorporation into C-S-H from ab initio calculations, *J. Mater. Chem. A* 2 (2014) 3477–3483. doi:10.1039/C3TA14597B.
- [17] H. Manzano, J.S. Dolado, A. Ayuela, Aluminum Incorporation to Dreierketten Silicate Chains, *J. Phys. Chem. B* 113 (2009) 2832–2839. doi:10.1021/jp804867u.
- [18] G.L. Kalousek, R. Rustum, *Crystal Chemistry of Hydrous Calcium Silicates*, 40 (1957) 74–80.
- [19] S. Komarneni, R. Roy, D.M. Roy, C.A. Fyfe, G.J. Kennedy, A.A. Bothner-By, J. Dadok, A.S. Chesnick,  $^{27}\text{Al}$  and  $^{29}\text{Si}$  magic angle spinning nuclear magnetic resonance spectroscopy of Al-substituted tobermorites, *J. Mater. Sci.* 20 (1985) 4209–4214. doi:10.1007/BF00552416.
- [20] I.G. Richardson, A.R. Brough, G.W. Groves, C.M. Dobson, The characterization of hardened alkali-activated blast-furnace slag pastes and the nature of the calcium silicate hydrate (C-S-H) phase, *Cem. Concr. Res.* 24 (1994) 813–829. doi:10.1016/0008-8846(94)90002-7.

- [21] P. Faucon, T. Charpentier, A. Nonat, J.C. Petit, Triple-Quantum Two-Dimensional  $^{27}\text{Al}$  Magic Angle Nuclear Magnetic Resonance Study of the Aluminum Incorporation in Calcium Silicate Hydrates, *J. Am. Chem. Soc.* 120 (1998) 12075–12082. doi:10.1021/ja9806940.
- [22] M.D. Andersen, H.J. Jakobsen, J. Skibsted, A new aluminium-hydrate species in hydrated Portland cements characterized by  $^{27}\text{Al}$  and  $^{29}\text{Si}$  MAS NMR spectroscopy, *Cem. Concr. Res.* 36 (2006) 3–17. doi:10.1016/j.cemconres.2005.04.010.
- [23] S. Goñi, M.T. Gaztañaga, A. Guerrero, Role of cement type on carbonation attack, *J. Mater. Res.* 17 (2002) 1834–1842. doi:10.1557/JMR.2002.0271.
- [24] V.T. Ngala, C.L. Page, Effects of carbonation on pore structure and diffusional properties of hydrated cement pastes, *Cem. Concr. Res.* 27 (1997) 995–1007.
- [25] M. Auroy, S. Poyet, P. Le Bescop, J.M. Torrenti, T. Charpentier, M. Moskura, X. Bourbon, Impact of carbonation on unsaturated water transport properties of cement-based materials, *Cem. Concr. Res.* 74 (2015) 44–58. doi:10.1016/j.cemconres.2015.04.002.
- [26] G.W. Groves, D.I. Rodway, I.G. Richardson, The carbonation of hardened cement pastes, *Adv. Cem. Res.* 3 (1990) 117–125.
- [27] G.W. Groves, A. Brough, I.G. Richardson, C.M. Dobson, Progressive changes in the structure of hardened C3S cement pastes due to carbonation, *J. Am. Ceram. Soc.* 74 (1991) 2891–2896.
- [28] A. Silva, R. Neves, J. De Brito, Statistical modelling of carbonation in reinforced concrete, *Cem. Concr. Compos.* 50 (2014) 73–81. doi:10.1016/j.cemconcomp.2013.12.001.
- [29] J. Chang, Y. Fang, Quantitative analysis of accelerated carbonation products of the synthetic calcium silicate hydrate(C-S-H) by QXRD and TG/MS, *J. Therm. Anal. Calorim.* 119 (2015) 57–62. doi:10.1007/s10973-014-4093-8.
- [30] A. Dauzeres, P. Le Bescop, P. Sardini, C. Cau Dit Coumes, Physico-chemical investigation of clayey/cement-based materials interaction in the context of geological waste disposal: Experimental approach and results, *Cem. Concr. Res.* 40 (2010) 1327–1340. doi:10.1016/j.cemconres.2010.03.015.
- [31] Y.F. Houst, Y.F. Houst, F.H. Wittmann, F.H. Wittmann, Depth profiles of carbonates formed during natural carbonation, *Cem. Concr. Res.* 32 (2002) 1923–1930. doi:10.1016/s0008-8846(02)00908-0.
- [32] M. Thiery, G. Villain, P. Dangla, G. Platret, Investigation of the carbonation front shape on cementitious materials: Effects of the chemical kinetics, *Cem. Concr. Res.* 37 (2007) 1047–1058. doi:10.1016/j.cemconres.2007.04.002.
- [33] I. Monteiro, F.A. Branco, J. De Brito, R. Neves, Statistical analysis of the carbonation coefficient in open air concrete structures, *Constr. Build. Mater.* 29 (2012) 263–269. doi:10.1016/j.conbuildmat.2011.10.028.
- [34] F. Claret, S. Grangeon, A. Loschetter, C. Tournassat, W. De Nolf, N. Harker, F. Boulahya, S. Gaboreau, Y. Linard, X. Bourbon, A. Fernandez-Martinez, J. Wright, Deciphering mineralogical changes and carbonation development during hydration and ageing of a consolidated ternary blended cement paste, *IUCrJ.* 5 (2018) 150–157. doi:10.1107/S205225251701836X.
- [35] L. Black, C. Breen, J. Yarwood, K. Garbev, P. Stemmermann, B. Gasharova, Structural Features of C-S-H(I) and Its Carbonation in Air-A Raman Spectroscopic Study. Part II: Carbonated Phases, *J. Am. Ceram. Soc.* 90 (2007) 908–917. doi:10.1111/j.1551-2916.2006.01429.x.
- [36] E.G. Swenson, P.J. Sereda, Mechanism of the carbonation shrinkage of lime and hydrated cement, *J. Appl. Chem.* 18 (2007) 111–117. doi:10.1002/jctb.5010180404.
- [37] K. Kamimura, P.J. Sereda, E.G. Swenson, Changes in weight and dimensions in the drying and carbonation of Portland cement mortars, *Mag. Concr. Res.* 17 (1965) 5–14.
- [38] E.G. Swenson, P.J. Sereda, Mechanism of the carbonation shrinkage of lime and hydrated cement, *J. Appl. Chem.* 18 (1968) 111–117.
- [39] M. Auroy, S. Poyet, P. Le, J.-M. Torrenti, U. Paris-est, D. Matériaux, B. Newton, P. Le Bescop, J.-M. Torrenti, T.



- Charpentier, M. Moskura, X. Bourbon, Comparison between natural and accelerated carbonation (3% CO<sub>2</sub>): Impact on mineralogy, microstructure, water retention and cracking, *Cem. Concr. Res.* 109 (2018) 64–80. doi:10.1016/j.cemconres.2018.04.012.
- [40] E. Drouet, S. Poyet, P. Le Bescop, J.-M. Torrenti, X. Bourbon, Carbonation of hardened cement pastes: Influence of temperature, *Cem. Concr. Res.* 115 (2019) 445–459. doi:10.1016/j.cemconres.2018.09.019.
- [41] V. Shah, K. Scrivener, B. Bhattacharjee, S. Bishnoi, Changes in microstructure characteristics of cement paste on carbonation, *Cem. Concr. Res.* 109 (2018) 184–197. doi:10.1016/j.cemconres.2018.04.016.
- [42] X. Pardal, I. Pochard, A. Nonat, Experimental study of Si-Al substitution in calcium-silicate-hydrate (C-S-H) prepared under equilibrium conditions, *Cem. Concr. Res.* 39 (2009) 637–643. doi:10.1016/j.cemconres.2009.05.001.
- [43] A.S. Andreev, S.F. Tikhov, A.N. Salanov, S. V. Cherepanova, O.B. Lapina, V.A. Bolotov, Y.Y. Tanashev, J.B. d’Espinose de Lacaillerie, V.A. Sadykov, Design of Al<sub>2</sub>O<sub>3</sub>/CoAlO/CoAl Porous Ceramometal for Multiple Applications as Catalytic Supports, *Adv. Mater. Res.* 702 (2013) 79–87. doi:10.4028/www.scientific.net/AMR.702.79.
- [44] F. Brunet, P. Bertani, T. Charpentier, A. Nonat, J. Virlet, Application of <sup>29</sup>Si Homonuclear and <sup>1</sup>H-<sup>29</sup>Si Heteronuclear NMR Correlation to Structural Studies of Calcium Silicate Hydrates, *J. Phys. Chem. B* 108 (2004) 15494–15502. doi:10.1021/jp031174g.
- [45] E. Gambuzzi, A. Pedone, M.C. Menziani, F. Angeli, D. Caurant, T. Charpentier, Probing silicon and aluminium chemical environments in silicate and aluminosilicate glasses by solid state NMR spectroscopy and accurate first-principles calculations, *Geochim. Cosmochim. Acta.* 125 (2014) 170–185. doi:10.1016/j.gca.2013.10.025.
- [46] E. Gambuzzi, T. Charpentier, M.C. Menziani, A. Pedone, Computational interpretation of <sup>23</sup>Na MQMAS NMR spectra: A comprehensive investigation of the Na environment in silicate glasses, *Chem. Phys. Lett.* 612 (2014) 56–61. doi:10.1016/j.cplett.2014.08.004.
- [47] F. Angeli, M. Gaillard, P. Jollivet, T. Charpentier, Contribution of <sup>43</sup>Ca MAS NMR for probing the structural configuration of calcium in glass, *Chem. Phys. Lett.* 440 (2007) 324–328. doi:10.1016/j.cplett.2007.04.036.
- [48] E. Tajuelo Rodriguez, K. Garbev, D. Merz, L. Black, I.G. Richardson, Thermal stability of C-S-H phases and applicability of Richardson and Groves’ and Richardson C-(A)-S-H(I) models to synthetic C-S-H, *Cem. Concr. Res.* 93 (2017) 45–56. doi:10.1016/j.cemconres.2016.12.005.
- [49] I. Klur, B. Pollet, J. Virlet, A. Nonat, C-S-H Structure Evolution with Calcium Content by Multinuclear NMR, in: *Nucl. Magn. Reson. Spectrosc. Cem. Mater.*, Springer Berlin Heidelberg, Berlin, Heidelberg, 1998: pp. 119–141. doi:10.1007/978-3-642-80432-8\_8.
- [50] W. Kunther, S. Ferreiro, J. Skibsted, Influence of the Ca/Si ratio on the compressive strength of cementitious calcium-silicate-hydrate binders, *J. Mater. Chem. A* 5 (2017) 17401–17412. doi:10.1039/c7ta06104h.
- [51] I.G. Richardson, A.R. Brough, R. Brydson, G.W. Groves, C.M. Dobson, Location of Aluminum in Substituted Calcium Silicate Hydrate (C-S-H) Gels as Determined by <sup>29</sup>Si and <sup>27</sup>Al NMR and EELS, *J. Am. Ceram. Soc.* 76 (1993) 2285–2288. doi:10.1111/j.1151-2916.1993.tb07765.x.
- [52] H. Stade, D. Müller, On the coordination of al in ill-crystallized C-S-H phases formed by hydration of tricalcium silicate and by precipitation reactions at ambient temperature, 17 (1987) 553–561.
- [53] S. Kwan, J. LaRosa, M.W. Grutzeck, <sup>29</sup>Si and <sup>27</sup>Al MASNMR Study of Stratlingite, *J. Am. Ceram. Soc.* 78 (1995) 1921–1926. doi:10.1111/j.1151-2916.1995.tb08910.x.
- [54] G. Pérez, A. Guerrero, J.J. Gaitero, S. Goñi, Structural characterization of C-S-H gel through an improved deconvolution analysis of NMR spectra, *J. Mater. Sci.* 49 (2014) 142–152. doi:10.1007/s10853-013-7688-8.
- [55] A.F. Jamsheer, K. Kupwade-Patil, O. Büyükoztürk, A. Bumajdad, Analysis of engineered cement paste using silica nanoparticles and metakaolin using <sup>29</sup>Si NMR, water adsorption and synchrotron X-ray Diffraction, *Constr. Build. Mater.* 180 (2018) 698–709. doi:10.1016/j.conbuildmat.2018.05.272.
- [56] I.G. Richardson, Model structures for C-(A)-S-H(I), *Acta Crystallogr. Sect. B Struct. Sci. Cryst. Eng. Mater.* 70

(2014) 903–923. doi:10.1107/S2052520614021982.

- [57] J.J. Thomas, J.J. Chen, A.J. Allen, H.M. Jennings, Effects of decalcification on the microstructure and surface area of cement and tricalcium silicate pastes, *Cem. Concr. Res.* 34 (2004) 2297–2307. doi:10.1016/j.cemconres.2004.04.007.
- [58] S. Grangeon, F. Claret, C. Roos, T. Sato, S. Gaboreau, Y. Linard, Structure of nanocrystalline calcium silicate hydrates: Insights from X-ray diffraction, synchrotron X-ray absorption and nuclear magnetic resonance, *J. Appl. Crystallogr.* 49 (2016) 771–783. doi:10.1107/S1600576716003885.
- [59] B. Walkley, R. San Nicolas, M.-A. Sani, G.J. Rees, J. V. Hanna, J.S.J. van Deventer, J.L. Provis, Phase evolution of C-(N)-A-S-H/N-A-S-H gel blends investigated via alkali-activation of synthetic calcium aluminosilicate precursors, *Cem. Concr. Res.* 89 (2016) 120–135. doi:10.1016/j.cemconres.2016.08.010.
- [60] Roos, Propriétés thermodynamiques des phases cimentaires hydratées : C-S-H, C-A-S-H et M-S-H. Ph.D thesis, (in French), Université de Poitiers, 2016.
- [61] T.F. Sevelsted, J. Skibsted, Carbonation of C-S-H and C-A-S-H samples studied by  $^{13}\text{C}$ ,  $^{27}\text{Al}$  and  $^{29}\text{Si}$  MAS NMR spectroscopy, *Cem. Concr. Res.* 71 (2015) 56–65. doi:10.1016/j.cemconres.2015.01.019.
- [62] F. Angeli, T. Charpentier, P. Faucon, J.-C. Petit, Structural Characterization of Glass from the Inversion of  $^{23}\text{Na}$  and  $^{27}\text{Al}$  3Q-MAS NMR Spectra, *J. Phys. Chem. B.* 103 (1999) 10356–10364. doi:10.1021/jp9910035.
- [63] A. Morandeau, M. Thiéry, P. Dangla, Investigation of the carbonation mechanism of CH and C-S-H in terms of kinetics, microstructure changes and moisture properties, *Cem. Concr. Res.* 56 (2014) 153–170. doi:10.1016/j.cemconres.2013.11.015.
- [64] G.K. Sun, J.F. Young, R.J. Kirkpatrick, The role of Al in C-S-H: NMR, XRD, and compositional results for precipitated samples, *Cem. Concr. Res.* 36 (2006) 18–29. doi:10.1016/j.cemconres.2005.03.002.
- [65] T.F. Sevelsted, J. Skibsted, Carbonation of C-S-H and C-A-S-H samples studied by  $^{13}\text{C}$ ,  $^{27}\text{Al}$  and  $^{29}\text{Si}$  MAS NMR spectroscopy, *Cem. Concr. Res.* 71 (2015) 56–65. doi:10.1016/j.cemconres.2015.01.019.
- [66] I.G. Richardson, G.W. Groves, Microstructure and microanalysis of hardened ordinary Portland cement pastes, *J. Mater. Sci.* 28 (1993) 265–277. doi:10.1007/BF00349061.
- [67] J.C.C. Chan, M. Bertmer, H. Eckert, Site connectivities in amorphous materials studied by double-resonance NMR-of quadrupolar nuclei: High-resolution  $^{11}\text{B}$  mutually implies  $^{27}\text{Al}$  spectroscopy of aluminoborate glasses, *J. Am. Chem. Soc.* 121 (1999) 5238–5248. doi:10.1021/ja983385i.
- [68] E. Lam, A. Comas-Vives, C. Copéret, Role of Coordination Number, Geometry, and Local Disorder on  $^{27}\text{Al}$  NMR Chemical Shifts and Quadrupolar Coupling Constants: Case Study with Aluminosilicates, *J. Phys. Chem. C.* 121 (2017) 19946–19957. doi:10.1021/acs.jpcc.7b07872.
- [69] P. Faucon, J.C. Petit, T. Charpentier, J.F. Jacquinot, F. Adenot, Silicon substitution for aluminum in calcium silicate hydrates, *J. Am. Ceram. Soc.* 82 (1999) 1307–1312. doi:10.1111/j.1151-2916.1999.tb01912.x.

## 1.8 Supplementary materials

### Appendix A

**Table S1: Mean value of  $^{27}\text{Al}$  NMR parameters as determined from the MQMAS NMR spectra of the environments observed in the studied C-A-S-H samples (\*samples containing strätlingite). In brackets are given the standard deviation of the NMR parameter distribution. Only species detected in MQMAS NMR spectra are given.  $\eta_q$  is taken as  $0.7 \pm 0.3$ .**

C/S-Al/Si	Al <sup>IV</sup>		Al <sup>V</sup>		Al <sup>VI</sup>	
	$\delta_{iso}$ (ppm)	$C_Q$ (MHz)	$\delta_{iso}$ (ppm)	$C_Q$ (MHz)	$\delta_{iso}$ (ppm)	$C_Q$ (MHz)
0.80-0.05	60 (5)	3.4 (1.3)				
0.8-0.10*	63 (5)	3.2 (1.3)				
0.95-0.05	69 (3)	3.1 (1.2)			TAH	
0.95-0.10*			40 (3)	3.6 (1.4)	6 (2)	3.1 (1.2)
1.20-0.05/0.1 1.40-0.05/0.10					Hydrated calcium aluminate	
		11 (1)			0.5 (0.2)	
strätlingite	63 (3)	3.5 (1.4)				
carbonated environment	57 (3)	2.6 (1)				

### Appendix B

**Table 3: Comparison of  $\text{Q}^3$  and  $\text{Q}^4$  proportion for carbonated C(-A)-S-Hs**

C/S-Al/Si	% $\text{Q}^3\text{gel}/\text{Q}^4\text{gel}$
0.8-0.0	0.20
0.95-0.0	0.16
1.20-0.0	0.1
1.40-0.0	0.05
0.8-0.05	0.65
0.95-0.05	0.60
1.20-0.05	0.54
1.40-0.05	0.50
0.8-0.1	0.74
0.95-0.1	0.54
1.20-0.1	0.77
1.40-0.1	0.75

**Summary of chapter 2:**

The structural analyses of the C-A-S-H unveil three different behaviour of Al incorporation with regard to the C/S ratio. We observed 2 Al insertion sites (Q2p, Q2b) at high C/S, 2 different Al sites at low C/S (Q3, Q2b). Following the carbonation (at very low C/S) a unique tetrahedral environment embedded in (Q3, Q4) silicates gel environment with the presence of Ca was detected. These results show an influence of both Al and Ca content on the structure of the pristine C-A-S-H, but no influence of the polymorphism. However, the degree of polymerization of the gel was strongly influenced by the Ca and Al content. The carbonation kinetics is influenced by Al content and the presence of phases such as TAH and pentahedral Al. This study evidences the requirement of further study focus on the structure of C-A-S-H and the nature of TAH and pentahedral Al species.

## **CHAPTER 3: CARBONATION IN DIFFUSIVE SYSTEM: MODEL PASTES AND INDUSTRIAL LOW ALCALINITY CEMENT**

### **Carbonation of model materials**

In the first chapter was presented the developed model pastes and their properties. Prior to carbonation the pastes were dried at 55% RH and 25°C. The cracks observed in  $C/S < 1.40$  limited the extent of data acquired. Thanks to the multi-technique approach the third chapter focuses on the link between the alkalinity especially the buffering capability, the microstructure, therefore their interplay in the materials' durability. Two of the developed pastes  $C/S = 3.0$  and  $1.4$  were carbonated and characterized; mineralogical, chemical and pores network features were obtained and correlated with the structural alteration of the C-S-Hs. The influence of the mineralogy (C-S-H + CH versus C-S-H) and the associated microstructure is highlighted.

Following, are provided a focus on model pastes and industrial LAC results, however the duration of the drying step induced a delayed launching of the carbonation experiments. The experiments are currently ongoing, which explains that only one carbonation term is discussed.

The model pastes' results in chapter 3 take the form of a manuscript in preparation for future publication

# Carbonation of model pastes: changes in mineralogy, microstructure and shrinkage

Kangni-Foli E. <sup>1,2</sup>, Poyet S. <sup>3</sup>, Le Bescop P. <sup>3</sup>, Charpentier T. <sup>4</sup>, Bernachy-Barbé F. <sup>3</sup>, Dauzères A. <sup>1</sup>, L'Hôpital E. <sup>1</sup>, d'Espinose de Lacaillerie J.-B. <sup>2</sup>

(1) IRSN, Institute of Radiation Protection and Nuclear Safety, PSE-ENV/SEDRE/ LETIS, BP 17, F-92262 Fontenay Aux Roses, France

(2) Soft Matter Science and Engineering, UMR CNRS 7615, ESPCI Paris, Université PSL, 10 rue Vauquelin, 75005 Paris, France

(3) Den-Service d'Etude du Comportement des Radionucléides (SECR), CEA, Université de Paris-Saclay, F-91191, France

(4) NIMBE, CEA, CNRS, Université Paris-Saclay, CEA Saclay, F-91191 Gif-sur-Yvette Cedex, France

**Corresponding authors:** Stéphane POYET;

- Postal address: CEA Saclay, DEN/DANS/DPC/SECR/LECBA, B158 PC25, F-91191 Gif-sur-Yvette cedex, France.
- NIMBE UMR 3685, CEA, CNRS, Université Paris-Saclay, CEA Saclay

Emails: [stephane.poyet@cea.fr](mailto:stephane.poyet@cea.fr)

## 1.1 Introduction

Atmospheric carbonation of cement corresponds to the reaction between the CO<sub>2</sub> from the atmosphere and the calcium ions (Ca<sup>2+</sup>) that are present in the poral solution [1]. As a consequence, calcium carbonate is precipitated [2,3] at the expense of Ca-bearing hydrates; among them, calcium hydroxide (portlandite, CH) and calcium silicate hydrates (C-S-H). The main consequence of carbonation is the strong reduction in pH of the poral solution that can initiate active corrosion of steel reinforcement [4,5]. Atmospheric carbonation has been studied for long, and the mechanisms are now well-known and described. This made it possible to propose models to describe the carbonation of concretes [6–11].

Nonetheless, the available models and the subsequent description of carbonation are far from being fully satisfactory and some issues remain. Although portlandite and calcium carbonate can be easily quantified using thermogravimetric analysis (TGA), the other Ca-bearing hydrates (C-S-H and sulfo-aluminates for instance) cannot. It is then difficult to obtain comprehensive and reliable experimental results such as mineralogical profiles that are needed for validating geochemists' simulations [12].

Similarly, the link between the changes in chemistry, microstructure and macroscopic properties is not clearly described up to now. For instance, the change in total porosity induced by carbonation remains uncertain. Although

the change in solid volume induced by the carbonation of portlandite is a trivial issue, that of C-S-H is not for two main reasons. Firstly, the molar volume of C-S-H remains an issue. At high C/S ratio (ca. 1.7) it was shown to be around 70-72 cm<sup>3</sup>/mol [13–15]. Sometimes, C-S-H are described as solid solutions with tobermorite and jennite as pure poles [16], the molar volume of the corresponding C-S-H is not constant and lies between 59 and 78 cm<sup>3</sup>/mol [17] or even 48 and 81 cm<sup>3</sup>/mol [18]. The second point is the molar volume of the end-product of C-S-H carbonation, namely silica gel, which also remains uncertain. Kulik proposed two distinct values: 23 cm<sup>3</sup>/mol [19] and then 29 cm<sup>3</sup>/mol [20]. Note that Wu and Ye [21] proposed the range 12-25 cm<sup>3</sup>/mol.

Another point of interest is carbonation shrinkage [22–25] and the resulting cracking [26–29] that was shown to depend on the mineralogical composition of the considered material (mainly portlandite and C-S-H) [27]. In some cases (i.e. substituted binders such CEM III, CEM V and low-alkalinity blend) a strong increase of the gas diffusion coefficient is observed in the carbonated zone [30] whereas a decrease is obtained for the corresponding OPC paste. The link between carbonation shrinkage and mineralogy remains uncertain and requires attention.

It is then the objective of this study to use two model pastes [31], the mineralogical composition of which was designed in order to be able to study separately the influence of carbonation on C-S-H. The changes in mineralogy and microstructure were probed which allowed to study the consequences of carbonation in terms of volume changes and shrinkage. The results also highlight the central role of portlandite.

### 1.1.1 Materials

The model pastes dedicated to this study were formulated in order to have the chemical, the mineralogical and the microstructural properties associated to high alkalinity and low alkalinity cementitious material (See [31] for more information about their detailed properties and formulation). The paste with the lower C/S ratio was obtained by hydration of C<sub>3</sub>S in presence of nanosilica in order to consume the nominal portlandite issued from C<sub>3</sub>S into a pozzolanic reaction with silica. The nanosilica used, the Rheomac AS 150 was provided by BASF as silica colloidal suspension (50 wt% water), with particles' D50 equal to 100 nm. The triclinic C<sub>3</sub>S was furnished by Mineral Research Processing (Meyzieu, France) with a specific area of 4600 cm<sup>2</sup>/g. The silica content was adapted to yield the required C/S (1.4; 3.0). To adjust the workability of the lower C/S paste, a superplasticizer (MasterGlenium Sky 537 from BASF) was added to the mix. Detailed compositions of the preparations are given in **Table 1**.

**Table 1: Composition of the model pastes for 1 L of paste**

C/S ratio	3.00	1.40
C <sub>3</sub> S (g)	1218.8	791.7
Colloidal silica slurry (g)	0.0	475.8
Added water (g)	609.4	379.9
w/b ratio	0.50	0.63
Superplasticiser (wt% of binder)	0.0	3.0
Batching time (min)	5	8

For each composition, two different moulds' sizes were used ( $\varnothing = 14$  mm H = 90 mm;  $\varnothing = 30$  mm H = 120 mm). The samples were kept one month in their moulds, then cured two additional months under water after unmoulding. Deionized water and calcium oxide were used to prepare C<sub>3</sub>S pastes' curing solution, for the C-S-H paste curing solution, crushed samples were added to deionized water, with the specific aim of minimizing an eventual leaching for both pastes. The samples of smaller diameter ( $\varnothing = 14$  mm) were designed for measurement of length variation induced by drying and carbonation.

The characterization of these two model pastes is fully reported in [31]. Their main properties are recalled in **Table 2**.

**Table 2: Composition and main properties of the two model pastes**

C/S atomic ratio	3.0	1.4
C/S of the C-S-H	1.7	1.4
Porosity (80°C)	38%	52%
Porosity (105°C)	41%	56%
Saturated density	1.89	1.76
C-S-H (mol/L of paste)	5.6	7.0
CH (mol/L of paste)	7.3	0.0
E (GPa)	15 ± 1	10 ± 1

The C<sub>3</sub>S paste displayed portlandite and C-S-H contents comparable to those of a fully hydrated paste despite a residual signal of anhydrous tricalcium silicate detected by x-ray diffraction (XRD) [32]. The pure C-S-H paste evidenced a higher porosity and lower saturated density compared to the paste obtained by hydration of C<sub>3</sub>S. This results from the higher w/b ratio due the requirement during fabrication to maintain a workable paste. The difference in water content resulted in a different microstructure for the two pastes, which will be detailed in the microstructural properties section.



### 1.1.2 Methods

#### Accelerated carbonation

Prior to carbonation all the samples were maintained in a desiccator (equipped with fans to avoid humidity gradients) in which the RH was fixed to 55% using a saturated solution of  $\text{Mg}(\text{NO}_3)_2$  [33]. At hygral equilibrium (when the mass variation became constant), the specimens were covered with adhesive aluminium foil to ensure unidirectional carbonation. They were then introduced into the carbonation chamber [34] where they were carbonated at  $25^\circ\text{C} \pm 0.2^\circ\text{C}$ ,  $55\% \text{ RH} \pm 1\%$  and  $3.0\% \text{ CO}_2 \pm 0.2\%$ . Carbonation was monitored for nearly one year (326 days and 316 days for the  $\text{C}_3\text{S}$  and C-S-H pastes respectively).

#### Mineralogy

XRD was used to identify the change in mineralogy induced by carbonation. The cylinders were cut orthogonally to the carbonation direction and the diffractograms were acquired on the solid surface [35], using a PANalytical X'Pert diffractometer and Cu-K $\alpha$  radiation ( $\lambda = 1.54 \text{ \AA}$ ).

The diffractograms were compared to the following ICDD reference files: portlandite (CH), 44-1481; vaterite, 01-74-1487; calcite, 05-0586; aragonite, 70-9854; triclinic tricalcium silicate ( $\text{C}_3\text{S}$ ), 31-0301. Rietveld analyses were run for quantification purpose; however, one should keep in mind the lack of crystal chemical model allowing a perfect description of the C-S-H. Besides C-S-H, the occurrence of silica gel and amorphous carbonate in partially carbonated materials increased the uncertainty on the crystalline phases' quantification. Despite this downside, combination of C-S-H models proposed by Richardson [36] lowers the unreliability on phase quantification induced by C-S-Hs' diffuse background.

TGA was performed using a Netzsch STA 409 PC Luxx apparatus. Analyses were run under a constant  $\text{N}_2$  flowrate (80 ml/min). The weight losses were recorded from  $25^\circ\text{C}$  to  $1150^\circ\text{C}$  with a heating rate of  $10^\circ\text{C}/\text{min}$  [37]. The quantification of portlandite and calcium carbonate amounts was done using the tangential method [38] considering the mass loss (between  $420$ - $900^\circ\text{C}$ ) associated to 120 mg of powdered sample.

$^{29}\text{Si}$  MAS NMR single-pulse experiment was performed on a Bruker Avance III 500 spectrometer operating at the Larmor frequency resonance of 99.3 MHz. The operation conditions were set to  $\pi/2$  pulses of 3.5  $\mu\text{s}$ , recycle delays of 20 s, spinning in 7 mm zirconia rotor at 5.5 kHz, and a minimum of 4000 scans for each spectrum. Tetramethylsilane was used as an external standard (0 ppm) to report the chemical shifts. The  $^{29}\text{Si}$  MAS NMR results were processed using the free DMfit software package [39]. The spectra were fitted using gaussio-lorentzian line shapes with chemical shifts and parameters recalled in supplementary materials section.

#### Microstructure

Microtomographic projections were acquired on a Bruker SkyScan1173 device equipped with a flat detector ( $2240 \times 2240$  pixel) using the following operating conditions: 115-130 kV and 61-69  $\mu\text{A}$ . We obtained  $360^\circ$  scans with a rotational step of  $0.3^\circ$ , exposure time of 1100 ms, a frame averaging from 8 to 10, and images with a pixel size of 16.8  $\mu\text{m}$ . A profile of grey level along the vertical axis was plotted for each slice 2 voxels deep. The carbonation front was obtained by applying a logistic function (E- 22) to the sigmoid part of the curve obtained by plotting the grey

level with respect to the position (the slices). The carbonation front was delimited as follows. Its beginning was defined as the position associated to 104% of the logistic function lower grey value (A) and its end by the position associated to the 96% of the logistic function highest value (B). In other words, the carbonation front was located between the position values associated to  $0.96*B$  and  $1.04*A$ .

$$\text{Logistic function used} = A + \frac{B}{(1 + Ce^{(-D+F)^2})} \quad \text{E- 22}$$

where **A**: sigmoid lower y-axis value, **B**: difference between the sigmoid higher y-axis value and its lower y-axis value, **C**: random factor, **D**: grey level value associated to the position fitted, **F**: sigmoid midpoint

The carbonation front was mainly followed by X- $\mu$ CT. To obtain an estimation of the carbonation depth by the usual colour indicator, phenolphthalein samples dedicated to XRD analyses were cut in half along their vertical axis and one half was sprayed with phenolphthalein. The acidification induced by the carbonation led to pH values below 9, at which pH value the colour indicator becomes colourless when it is purple at pH values around 13.

Density and total porosity of the pastes were measured using the buoyancy method and disks ( $\varnothing = 30.0$  mm H = 8 mm). Prior to the tests, the samples were re-saturated under vacuum and water. The mass loss associated to an oven drying at 80°C and 105°C allowed estimation of the total (accessible) porosity of the samples.

Some other samples were crushed in centimetric pieces, immersed in liquid nitrogen then freeze dried during 24h prior to analysis. Four samples were used for each analysis. A Micromeritics Autopore IV device was used at a maximal pressure of 414 MPa (corresponding to pores of 3 nm in diameter).

### Gas diffusion

Through diffusion experiment were implemented on three carbonated discs of each paste ( $\varnothing = 30.0$  mm H = 8 mm). For this purpose, the samples to be tested were placed between two chambers filled with synthetic air, oxygen ( $O_2$ ) and nitrogen ( $N_2$ ) at ambient temperature and 55% RH. Note that the total pressure in the two chambers was the same (atmospheric pressure, **Figure 1**). Also note that due to the presence of water vapour, the gas concentration within the two chambers was slightly lower than 100% (about 98.7%) but this was not accounted for in the assessment of the gas diffusion coefficient.

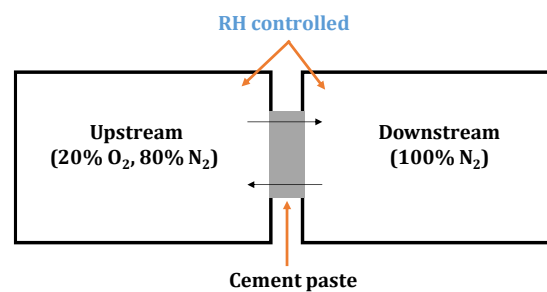


**Figure 1: Principle of the gas diffusion test**

Three fully carbonated disks ( $\emptyset 30 \times 8$  mm) were first saturated in a desiccator under water with a vacuum [40] and then equilibrated at 55% RH and ambient temperature ( $20^\circ\text{C} \pm 2^\circ\text{C}$ ). They were then sealed into position using epoxy adhesive and O-rings to avoid gas leakage during the diffusion test. The respective diffusion of oxygen and nitrogen through the disks was monitored using gas micro-chromatography and the resulting diffusion coefficients were evaluated using the 2<sup>nd</sup> Fick's law [41].

In parallel to the direct measurements, the simple model proposed by Papadakis et al. [42,43] was used to assess the diffusion coefficient of  $\text{CO}_2$  of the two carbonated pastes. The model of Papadakis creates a link between the carbonation depth  $x_c$  and the square root of time  $t$ :

$$x_c(t) = k\sqrt{t} \quad \text{with} \quad k = \sqrt{\frac{2D_{\text{CO}_2}^c [\text{CO}_2]}{[\text{Ca}]_{\text{carbo}}}} \quad \text{E- 23}$$

where  $k$  is the carbonation rate ( $\text{m/s}^{0.5}$ );  $D_{\text{CO}_2}^c$  diffusion coefficient value for  $\text{CO}_2$  through the carbonated material ( $\text{m}^2/\text{s}$ );  $[\text{CO}_2]$  concentration of  $\text{CO}_2$  ( $\text{mol}/\text{m}^3$ ) and  $[\text{Ca}]_{\text{carbo}}$  concentration of Ca that can be involved in the carbonation process ( $\text{mol}/\text{m}^3$ ).

Consequently, the value of the  $\text{CO}_2$  diffusion coefficient  $D_{\text{CO}_2}^c$  can be easily estimated if the carbonation rate  $k$  is measured experimentally:

$$D_{\text{CO}_2}^c = k^2 \left( \frac{[\text{Ca}]_{\text{carbo}}}{2[\text{CO}_2]} \right) \quad \text{E- 24}$$

More details are given in the results section.

### Shrinkage measurement

Two of the smaller cylinders ( $\emptyset 14$  mm and H80 mm) were first re-saturated under vacuum and water [40] before they were introduced in a climatic chamber where they were subjected to drying at  $25^\circ\text{C}$  and 55% RH (note that the specimens were not protected against the  $\text{CO}_2$  present in the atmosphere during that phase). After 195 days of drying they were introduced in the accelerated carbonation device where they were subjected to 3%  $\text{CO}_2$  at  $25^\circ\text{C}$  and 55% RH for 70 more days. Length change was monitored throughout the test using LVDT sensors (Solartron Metrology).

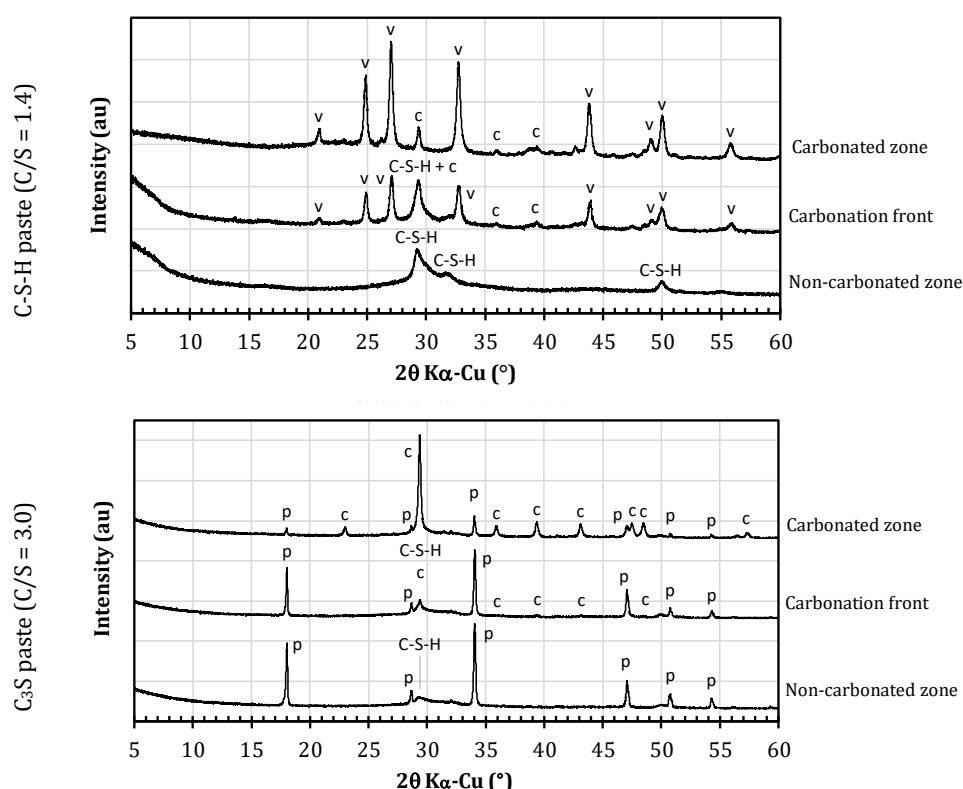
### 1.1.3 Results

#### Mineralogy

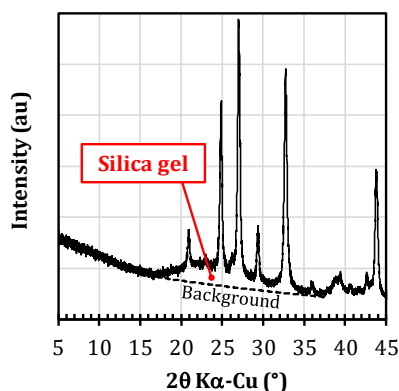
**Figure 2** presents some of the diffractograms that were obtained on the two pastes after accelerated carbonation. For the sake of clarity only three of them were selected in the non-carbonated part of the specimen, in the carbonation front and in the carbonated zone. It is plain to see that the carbonation of the C-S-H paste ( $\text{C}/\text{S} = 1.4$ ) led to the dissolution of the C-S-H and precipitation of calcium carbonate: mainly vaterite and to some extent calcite. This was consistent with the conclusion of Šauman [44] and Auroy et al. [45] that stated that the presence of vaterite was indicative of C-S-H carbonation. In the carbonation front (40.8 mm from the surface exposed to  $\text{CO}_2$ ), one can

clearly see the coexistence of calcium carbonate and C-S-H (broad peak near  $29^\circ$  [46–48]). In the carbonated zone (15.0 mm), the signal related to C-S-H has completely disappeared and a very large diffraction band can be observed between  $18^\circ$  and  $27^\circ$  that is characteristic of amorphous silica gel (**Figure 3**) [49].

The carbonation of the  $C_3S$  paste was somewhat different: portlandite was never completely dissolved (even in the carbonated zone) and calcite was the main calcium carbonate that was detected. The C-S-H was also not believed to be completely dissolved (even though it is most virtually impossible to detect them due to the presence of calcite) because of the absence of the large diffraction band discussed above.



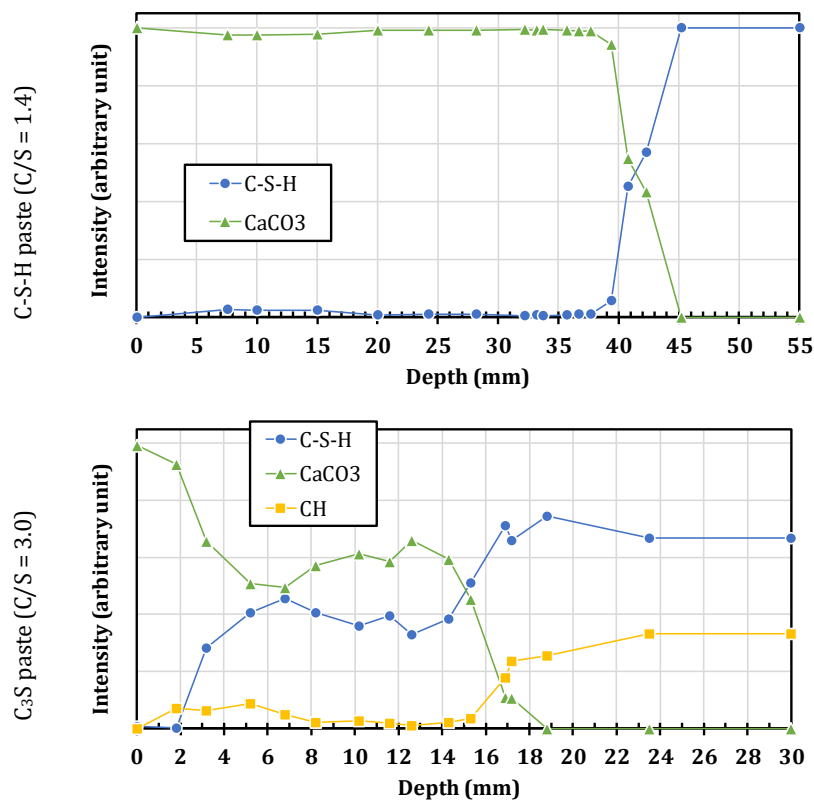
**Figure 2: Diffraction patterns of the pastes at the end of accelerated carbonation (316 and 326 days for the C-S-H and  $C_3S$  pastes respectively)**



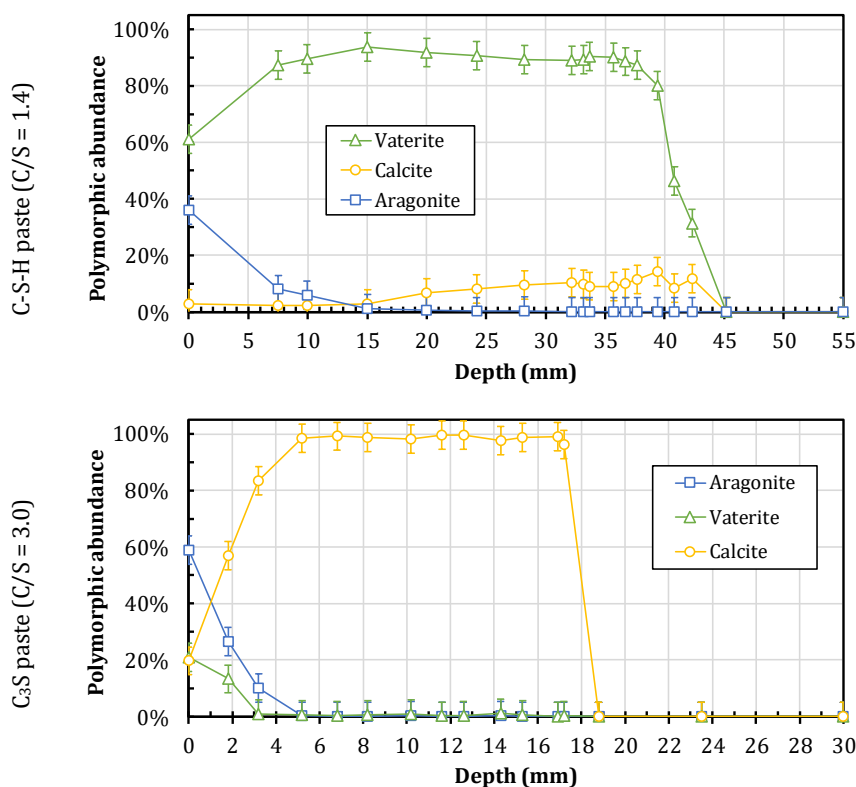
**Figure 3: Evidence of the presence of silica gel in the carbonated zone of the C-S-H paste (C/S = 1.4)**

Figure 4 presents the mineralogical assemblage obtained using XRD. Note that these results should be apprehended only in a qualitative manner. The C-S-H appeared to be completely and evenly depleted in the carbonated zone of the C-S-H paste whereas portlandite and C-S-H remained in significant amounts in the carbonated zone of the C<sub>3</sub>S paste. The latter also appeared not to be homogeneous: the first four millimetres were more carbonated than the rest of the carbonated zone in which the amount of calcium carbonate was reduced and the amounts of remaining portlandite and C-S-H increased.

Rietveld refinements were conducted to estimate the relative proportions of the three CaCO<sub>3</sub> polymorphs (vaterite, aragonite and calcite) in the carbonated zones of the two pastes. The results confirmed the observations of **Figure 2**. Vaterite was the main polymorph that was precipitated in the carbonated zone of the C-S-H paste (around 90% in weight). It must be noted though that some calcite (less than 10%) was detected throughout the carbonated zone as well as aragonite close to the surface exposed to CO<sub>2</sub>. Conversely calcite was, by far, the main polymorph that was precipitated in the carbonated zone of the C<sub>3</sub>S paste. Aragonite and vaterite were only detected close to the surface exposed to CO<sub>2</sub>. There is no clear explanation for the absence of vaterite in the depth of the carbonated zone of the C<sub>3</sub>S paste despite the carbonation of its C-S-H. Nonetheless, discrepancies in Ca-supersaturation [50–52] in pH values [53], since formation of calcite is reported at saturation index (SI) higher than vaterite's SI, or the effect of the nucleation surface [54] as disturbance of the solvated surface could decrease the energy growth barrier to the order of thermal energy, those phenomena might explained the observed behaviour.



**Figure 4: Mineralogical assemblage after accelerated carbonation (316 and 326 days for the C-S-H (top) and C<sub>3</sub>S (bottom) pastes respectively) obtained using XRD**



**Figure 5:  $\text{CaCO}_3$  polymorphic abundance (%wt) in the carbonated zone after accelerated carbonation (316 and 326 days for the C-S-H (top) and  $\text{C}_3\text{S}$  pastes (bottom) respectively) obtained using Rietveld refinement. The vertical bar stands for the uncertainty of the quantification using Rietveld refinement (evaluated to 5%).**

The  $^{29}\text{Si}$  NMR spectra (**Figure 6**) gave an insight of the influence of carbonation on C-S-H. The silicates environments are specified  $\text{Q}^n$  with  $0 \leq n \leq 4$ .  $n$  designed the number of silicate connected to a tetrahedral silicate noted  $\text{Q}$ . Similarly to tobermorite, the C-S-H natural crystalline analogous, C-S-H environments are characterized by  $n$  values comprised from 0 to 2. Three main environments are found in C-S-H, which are consistent to the literature [55,56]. The first corresponds to silicate end chain unit, namely  $\text{Q}^1$ , with resonance at about -80 ppm. The two others are  $\text{Q}^2$  sites which include,  $\text{Q}^{2b}$  and  $\text{Q}^{2p}$  environment, associated to the bridging tetrahedral silicate with resonance around -83 ppm and the pairing silicates around -85 ppm, respectively. Those environments are the three unit of the tobermorite dreierketten structure [57,58]. Silicate in C-S-H forms chain with variable length, high calcium content in C-S-H leading to a higher proportion of low coordination silicates  $\text{Q}^1$  [36] *i.e.* C-S-Hs with shorter silicates chain.

In the carbonated zone of the C-S-H paste (**Figure 6-a**), between 0 and 40 mm from the exposed surface, no signal related to C-S-H was detected, rather, large resonances ( $\text{Q}^{3_{\text{gel}}}$  and  $\text{Q}^{4_{\text{gel}}}$  100 and 110 ppm respectively) could be observed. This indicated that the C-S-H was completely degraded/dissolved and that silica chains polymerized to form an amorphous silica product (silica gel) [59]. This confirmed the observations made using XRD (**Figure 2** and **Figure 4**). In the carbonation front (around 43.8-44.6 mm), there was a decreased evidence of silica gel but the C-S-H was obviously affected by carbonation because the relative intensities of the  $\text{Q}^1$  and  $\text{Q}^2$  environments were different from those of the non-carbonated C-S-H (beyond 47.6 mm) and typical of a more polymerized

environment. This indicated that the C/S ratio of the C-S-H was decreased [60–63] and that Ca was taken from the C-S-H structure.

Once again, the results of the C<sub>3</sub>S paste were somewhat different from those of the C-S-H paste (**Figure 6-b**). The C-S-H was to be almost completely degraded very close to the surface exposed to CO<sub>2</sub> (0-2 mm) but remained in significant amounts in the carbonated zone (between 2 and 19 mm) a C/S ratio decrease is evidenced by the decrease of the relative intensities of the Q<sup>1</sup> and Q<sup>2</sup> compared to the non-carbonated part.

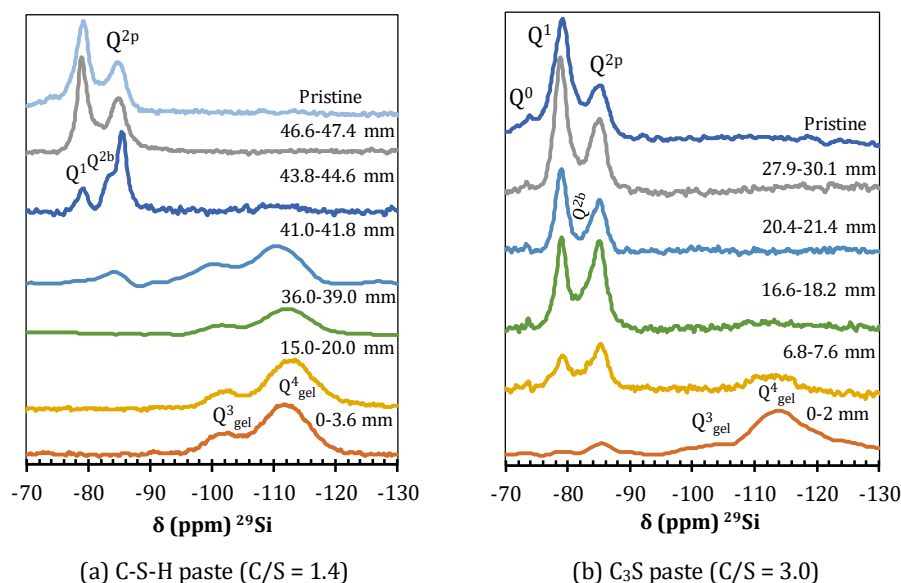


**Figure 6:** <sup>29</sup>Si NMR spectra of the C-S-H and C<sub>3</sub>S pastes after accelerated carbonation (316 and 326 days for the C-S-H and C<sub>3</sub>S pastes respectively)

The quantitative mineralogical profiles that were obtained using TGA are presented on **Figure 7**. The carbonation depth was about 40-45 mm for the C-S-H paste and the carbonation front was quite sharp (**Figure 7-a**). The CaCO<sub>3</sub> content in the carbonated zone appeared to be lower than that of the C-S-H in the non-carbonated part (**Table 2**) by about 10% in average (see remaining Ca in **Figure 7**). This did not mean that some C-S-H remained in the carbonated zone as its absence was unambiguously proven by NMR (**Figure 6**). Rather, this could be due to some discrepancy in the TGA quantification or could indicate that some Ca remained in the silica gel instead of precipitating CaCO<sub>3</sub>. In this latter case, the C/S ratio of the silica gel would not exceed 0.14.

Things were not so clear for the C<sub>3</sub>S paste: the carbonation front was not well defined and the carbonation depth was twice lower than that of the C-S-H paste, about 17-22 mm. As already shown by XRD (**Figure 2** and **Figure 4**) portlandite remained in the carbonated zone, and the residual content was estimated to 25% (wt%). As for the C-S-H paste, the CaCO<sub>3</sub> content was lower than the initial content of C-S-H: the difference between the two of them was used to evaluate the amount of residual C-S-H in the carbonated zone to about 60% (wt%, **Figure 7-b**). This result is important because it allows estimating the amount of Ca that was involved in the carbonation reaction. For the C<sub>3</sub>S paste, it was less than the total Ca content: it corresponded to 75% of CH and 40% of the C-S-H whereas it

corresponded to all the C-S-H for the C-S-H paste (**Table 3**). Despite a strong difference in their initial Ca content, the carbonation of the two pastes appeared to have yielded similar amounts of  $\text{CaCO}_3$  (9.3 versus 9.8 mol.l<sup>-1</sup>).

**Table 3: Amount of calcium involved in the carbonation reaction**

Paste	Amount of Ca that was carbonated	Value (mol/L of paste)
C <sub>3</sub> S paste	75% of [CH] + 40% of [C – S – H]	$0.75 \times 7.3 + 0.4 \times 1.7 \times 7.3 = 9.3$
C-S-H paste	100% of [C – S – H]	$1.4 \times 7.0 = 9.8$

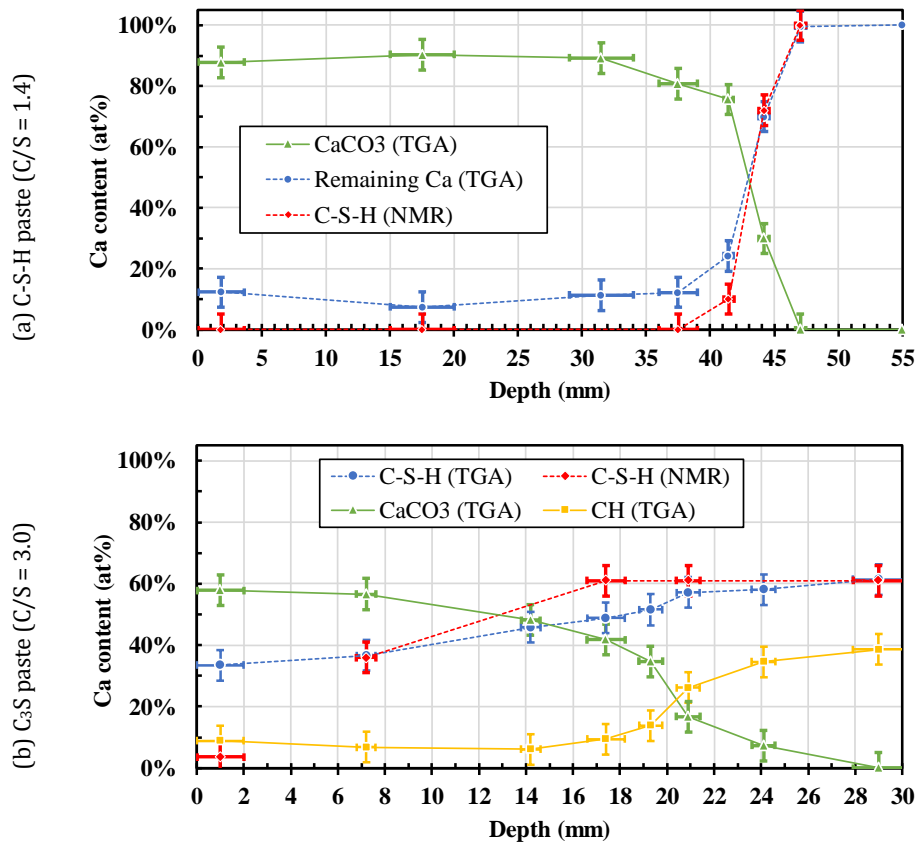


**Figure 7: Quantitative mineralogical profiles obtained using TGA after accelerated carbonation (316 and 326 days for the C-S-H and C<sub>3</sub>S pastes respectively). The horizontal bar stands for the thickness of the disk that was sampled and tested using TGA. The vertical bar stands for the uncertainty of the measurement (evaluated to 5%)**

### Microstructure/cracking

Carbonation led to a decrease in total porosity and an increase in density (**Table 4**) as commonly observed [42,64–68]. It is noteworthy that the change in dry density induced by carbonation (i.e. induced by the fixation of  $\text{CO}_2$ ) was quite similar for the two pastes. This is for sure consistent with the fact that the amounts of carbonated Ca was similar for the two pastes (9.8 and 9.3 mol/L of paste for the C-S-H and C<sub>3</sub>S pastes respectively, see **Table 3**). The fact that the porosity reduction was twice higher for the C-S-H paste was surprising. This was explained simply by



considering the phases that were present in the carbonated pastes and the corresponding volumes (see. Subsection Volume Change).

**Table 4: Porosity and density of the carbonated pastes**

	C-S-H paste (C/S = 1.4)	C3S paste (C/S = 3.0)	Unit
Density (saturated)	1.98	2.11	g/cm <sup>3</sup>
Total porosity (80°C)	35%	28%	-
Total porosity (105°C)	36%	29%	-
Density (dry – 80°C)	1.63	1.83	g/cm <sup>3</sup>
Density (dry – 105°C)	1.62	1.82	g/cm <sup>3</sup>
Change in porosity (80°C)	-20%	-10%	-
Change in dry density (80°C)	+0.39	+0.32	g/cm <sup>3</sup>

The pore size distribution was also significantly modified by carbonation (**Figure 8**). In both cases, the bimodal distribution was shifted to an almost unimodal distribution located near 10 nm [27,45], the intensity of which seemed to depend on the degree of carbonation (close to 100% for the C-S-H paste and limited for the C<sub>3</sub>S paste). In the carbonated C-S-H paste, the amount of the C-S-H pores (3 nm in diameter) was almost nil. This was consistent with the NMR results that showed that the C-S-H was depleted after carbonation. This was not the case for the carbonated C<sub>3</sub>S paste for which 60% of the C-S-H remained after carbonation. Another point of interest was the change in critical pore diameter [69][70]: the pore structure was coarsened for the C-S-H paste (the critical pore diameter was shifted from 20 nm to 150 nm by carbonation) whereas the pores were clogged for the C<sub>3</sub>S paste (the critical pore diameter was reduced from 35 nm to 20 nm by carbonation). Carbonation was then expected to increase the transport properties (and then gas diffusion) of the C-S-H paste and to reduce those of the C<sub>3</sub>S paste. Note that this divergent behaviour has already been observed for OPC and substituted binders [26] [27] [30].

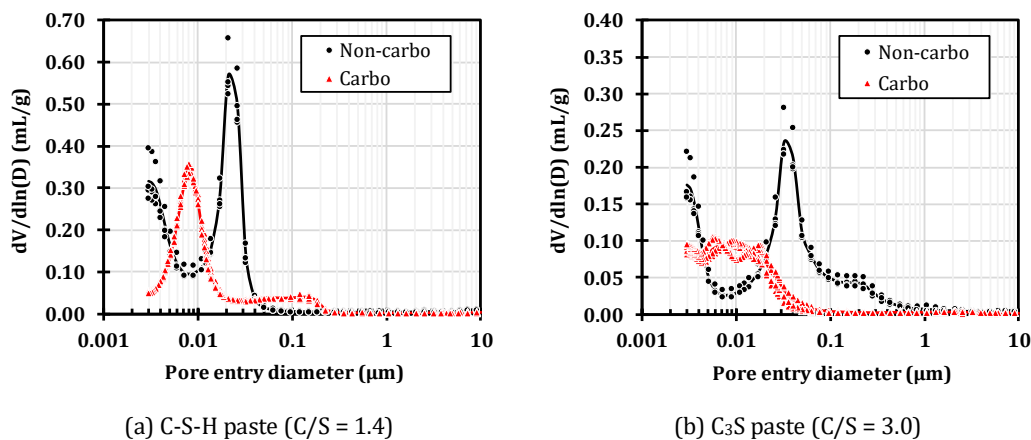


**Figure 8: Pore size distribution obtained using MIP after accelerated carbonation**

**Figure 9** presents two scans that were obtained using X- $\mu$ CT after carbonation of the two pastes. The carbonated zones are clearly visible in light grey. One can see that the carbonation is tortuous in both cases and the carbonation depth values are consistent with those obtained using XRD (**Figure 4**) and TGA (**Figure 7**). The carbonated zone of the C-S-H paste appeared to be severely cracked and especially on the first ten millimeters. Conversely the carbonated zone of the C<sub>3</sub>S paste only shows a few thinner cracks.

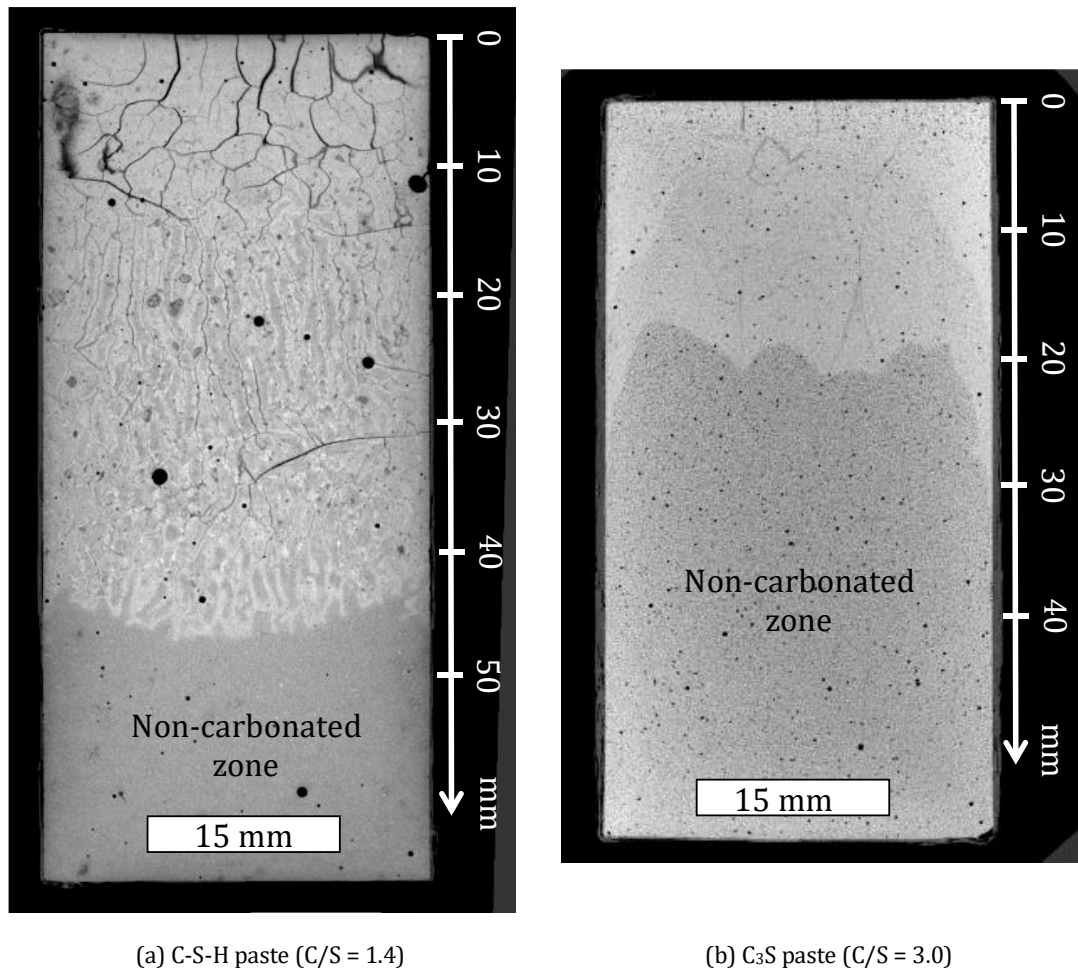


**Figure 9: Cracking pattern observed using X- $\mu$ CT after accelerated carbonation (316 and 326 days for the C-S-H and C<sub>3</sub>S pastes respectively).**

Thorough examination of the C-S-H paste scan revealed the presence of four different zones in the cylinder (**Figure 10**). The first (I) corresponded to the first ten millimetres of the carbonated zone. It was severely cracked (crazing) and the grey level was almost uniform due to complete carbonation and C-S-H decalcification. The second (II, between 10 and 40 mm) was somewhat different. The cracks were thinner than those of the first zone and almost parallel. In addition, strong heterogeneities in grey levels could be observed (**Figure 11**). Here it was assumed that cracks were generated by restrained carbonation shrinkage and that CO<sub>2</sub> was able to diffuse fast into these open cracks and helped carbonating the matrix close to the cracks. This was believed to have induced the observed

heterogeneities. It must be noted though that no significant differences were obtained between the zone I and II using XRD and NMR.

The third zone (III) corresponded to the carbonation front (between 40 and 45 mm) where the C-S-H were decalcified. The last zone (IV) corresponded to the non-carbonated zone (uniform grey level).

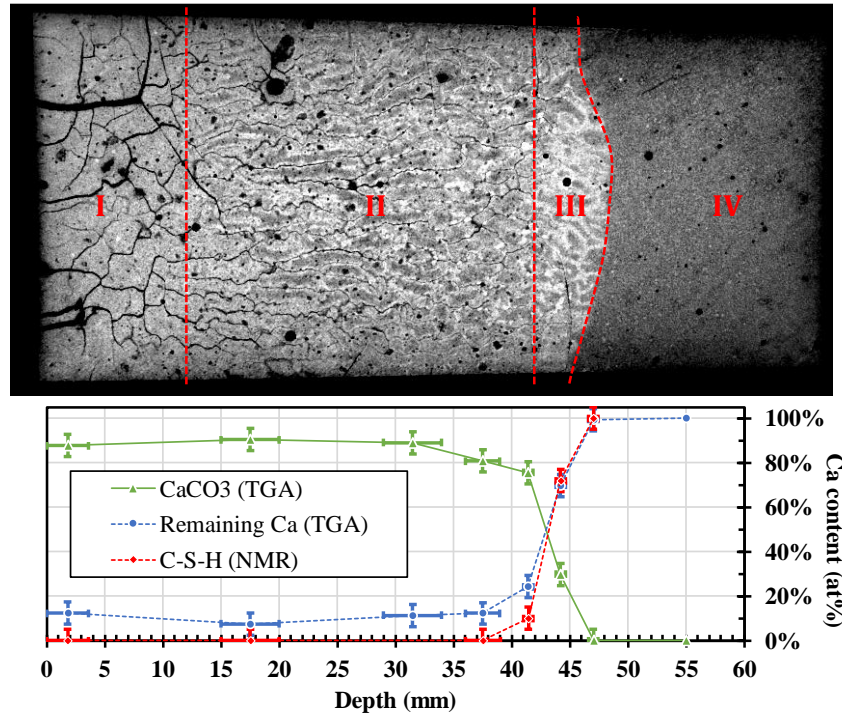


**Figure 10:** View of the four zones that were observed using X-μCT in the C-S-H paste after carbonation (316 days)

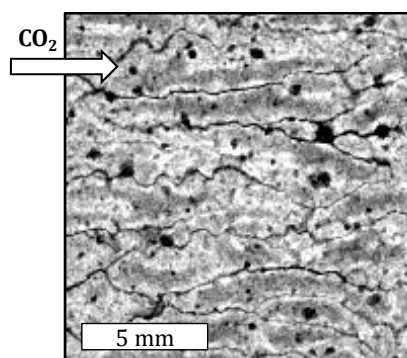


**Figure 11:** Close-up on the zone II of the C-S-H paste and view of the cracks and discrepancies in grey level

The examination of the C<sub>3</sub>S paste showed two main zones (**Figure 12**). The first (I, the first five millimetres from the surface) appeared in light grey (denser than the rest) and was then expected to be the most carbonated part of

the cylinder. This corresponded quite well with the mineralogical results that showed that the  $\text{CaCO}_3$  content was maximal. The grey level of the second zone (II, from 5 to 20 mm) was lower than that of zone I indicating that it was less carbonated. This was verified by the mineralogical results that showed that C-S-H remained in significant amount. The last zone (III) corresponded to the non-carbonated part (darker grey). The carbonation front appeared to be tortuous due to the presence of cracks that locally provides pathways for  $\text{CO}_2$  and increased the carbonation depth close to the cracks.

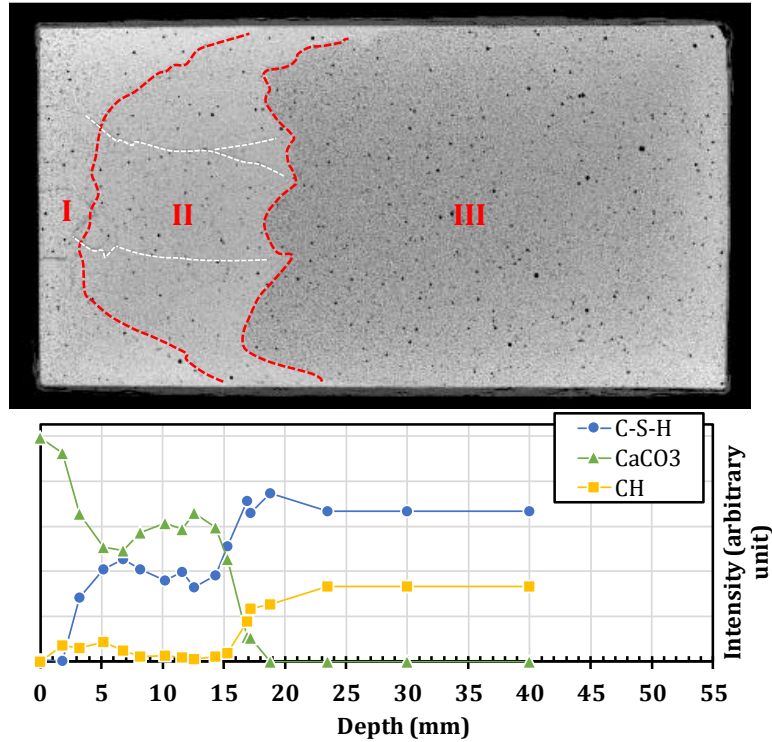


**Figure 12:** View of the three zones that were observed using X- $\mu$ CT in the  $\text{C}_3\text{S}$  paste after carbonation (326 days). The presence of some cracks was underlined using white dashed lines.

### Carbonation rate/gas diffusion

**Figure 13** shows the progress of carbonation depth with the square root of time. All the techniques used (X- $\mu$ CT, phenolphthalein and XRD) were in good agreement. As expected, the carbonation rate of the C-S-H paste was higher than that of the  $\text{C}_3\text{S}$  paste ( $2.1 \text{ mm}/\text{d}^{0.5}$  versus  $1.1 \text{ mm}/\text{d}^{0.5}$ ). Here the reduced quantity of calcium in the C-S-H paste may have played a role in increasing the carbonation rate [71–75].

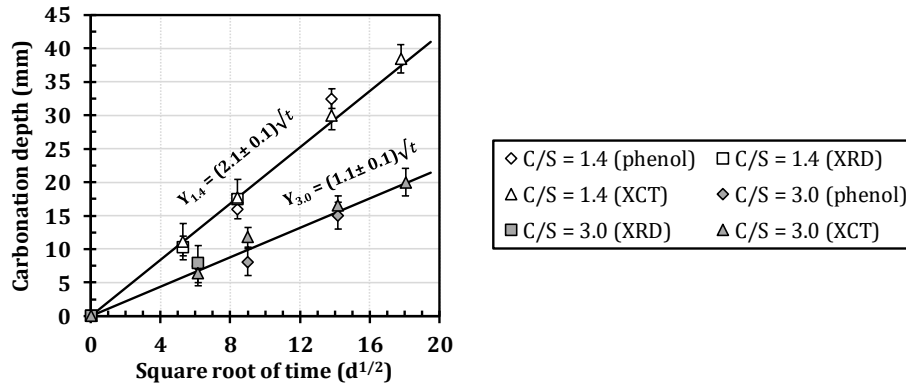


**Figure 13: Carbonation rates of the two pastes**

The results of the gas diffusion tests also gave valuable information. The value of the diffusion coefficient of the carbonated C<sub>3</sub>S paste was  $2.7 \times 10^{-8} \text{ m}^2/\text{s}$ . This value is in good agreement with the results usually observed in carbonated OPC pastes [30,65]. Because it was severely cracked (**Figure 9**), it was impossible to measure the gas diffusion coefficient of the C-S-H paste. Instead, the gas diffusion coefficient was assessed using Papadakis' model (Eq. E-3). In doing so, the experimental carbonation rate  $k$  was used as input data. Firstly and for validation purpose, the model of Papadakis was also used to evaluate the diffusion coefficient of the carbonated C<sub>3</sub>S paste. In so doing, the quantity of carbonatable calcium ( $[\text{Ca}]_{\text{carbo}}$ ) was estimated using the TGA results (**Figure 7**):

$$[\text{Ca}]_{\text{carbo}} = 75\% \text{ of } [\text{CH}] + 1.7 \times 40\% \text{ of } [\text{C} - \text{S} - \text{H}] = 9.3 \text{ mol/L of paste} \quad \text{E- 25}$$

The diffusion coefficient of the carbonated C<sub>3</sub>S paste was evaluated to  $5.2 \times 10^{-8} \text{ m}^2/\text{s}$ . This was twice the measured value ( $2.7 \times 10^{-8} \text{ m}^2/\text{s}$ ) but the order of magnitude of the diffusion coefficient estimated by Papadakis' model was correct. For the C-S-H paste, all the C-S-H was assumed to be available for carbonation, this was supported by the NMR results (**Figure 6**). Consequently, E- 24 simply became:

$$D_{\text{CO}_2}^c = \left( \frac{[\text{Ca}]_{\text{carbo}}}{2[\text{CO}_2]} \right) k^2 = 1.4k^2 \frac{[\text{C} - \text{S} - \text{H}]}{[\text{CO}_2]} \quad \text{E- 26}$$

where  $[\text{Ca}]_{\text{carbo}} = 1.4 \times [\text{C} - \text{S} - \text{H}] = 9.8 \text{ mol/L of paste}$

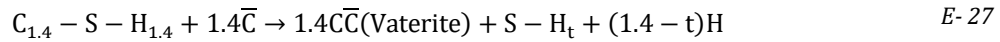
$$[\text{CO}_2] = 1.25 \times 10^{-3} \text{ mol/L (3\% CO}_2\text{)}.$$

The value of the diffusion coefficient of CO<sub>2</sub> in the carbonated C-S-H paste (C/S = 1.4) was evaluated to be  $20.0 \times 10^{-8} \text{ m}^2/\text{s}$ ; one order of magnitude greater than the value measured in the carbonated C<sub>3</sub>S paste. This strong difference was explained by two concomitant phenomena: (1) the critical pore diameter of the carbonated C-S-H paste is higher than that of the carbonated C<sub>3</sub>S paste (150 nm versus 20 nm, see **Figure 8**) and (2) the significant cracking induced by carbonation in the C-S-H paste (**Figure 9**). Because the amount of pores/voids of entry diameter of 150 nm remained limited in the carbonated C-S-H paste, cracking was believed to be the major cause for the high gas diffusion coefficient in line with the conclusions of Dutzer et al. [30]. Moreover, it must be noted that despite a strong difference in calcium quantity in the two pastes (**Table 2**), the amount of Ca that was effectively carbonated was more or less the same for the two pastes (9.8 and 9.3 mol/L of paste for the C-S-H and C<sub>3</sub>S pastes respectively).

The difference in Ca-buffer (alkaline reserve) between the two pastes then should not play any role; gas diffusion in the carbonated layer and the cracks induced by carbonation were then believed to be the main reason for the difference in carbonation rates between the two pastes. This was, once again, consistent with the conclusions of Dutzer et al. [30]. In line with the conclusions of Auroy et al. [27], these results highlight the competition between the reduction in total porosity induced by  $\text{CaCO}_3$  precipitation (leading to a reduction in transport properties) and cracking induced by carbonation shrinkage (leading to an increase in transport properties).

#### Volume change / link between mineralogy and microstructure?

All the above-mentioned results were used to evaluate the change in volume and in weight induced by carbonation. The  $\text{C/S} = 1.4$  paste was examined first because it was the simpler system. The non-carbonated paste was considered to be a porous medium made of C-S-H only (with  $\text{C/S} = 1.4$ , cf. **Figure 14**). The C-S-H carbonation reaction was assumed to be the following:



As observed using XRD, the  $\text{CaCO}_3$  resulting from the carbonation of the C-S-H was assumed to be vaterite (**Figure 5**). Without further information, the H/S ratio of the C-S-H was assumed to be 1.4 so that the C-S-H specific gravity was close to 2.604 [15] and the end product of the decalcification of the C-S-H was assumed to be an hydrated silica-gel (S-H, **Figure 6**).

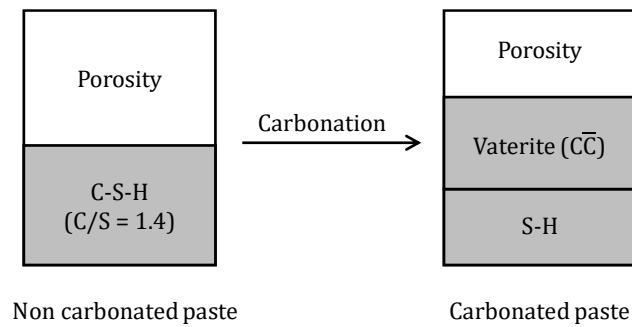


**Figure 14: Effect of the carbonation on a C-S-H paste; the hydrates are fully carbonated and replaced by silica gel and calcium carbonate.**

**Table 5** and **Table 6** detail the volume and mass calculation of the different phases present in the non-carbonated and fully carbonated paste ( $\text{C/S} = 1.4$ ).

**Table 5: Volume and mass of the different phases of the non-carbonated paste (C/S = 1.4)**

	Volume	Mass
Voids	$\emptyset_{nc}$	0
C-S-H	$(1-\emptyset_{nc})$	$\rho_d^{nc}$
Total	1	$\rho_d^{nc}$

$\emptyset_{nc}$  porosity of the non-carbonated paste

$\rho_d^{nc}$  dry density of the non-carbonated paste

**Table 6: Volume and mass of the different phases in the carbonated paste (C/S = 1.4)**

	Volume	Mass
Voids	$\emptyset_c$	0
Vaterite	$1.4[C-S-H]V_m(vat)$	$1.4[C-S-H]M_m(vat)$
S-H	$(1-\emptyset_c)-1.4[C-S-H]V_m(vat)$	$\rho_d^c-1.4[C-S-H]M_m(vat)$
Total	1	$\rho_d^c$

$\emptyset_c$  porosity of the carbonated paste

$\rho_d^c$  dry density of the carbonated paste

$[C-S-H]$  concentration of C-S-H in the non-carbonated paste

$V_m(vat)$  molar volume of vaterite (38 cm<sup>3</sup>/mol)

$M_m(vat)$  molar mass of vaterite (100.1 g/mol)

If we first consider the non-carbonated C-S-H paste (C/S = 1.4), it is easy to calculate the molar volume of the C-S-H (please note that we used here the porosity obtained by drying at 80°C):

$$V_m(C-S-H) = \frac{1-\emptyset_{nc}}{[C-S-H]} = \frac{1-0.35}{7} \approx 69 \text{ cm}^3/\text{mol} \quad E-28$$

The obtained value is close to that measured by Allen et al. [14] (72 cm<sup>3</sup>/mol) and further used by Jennings [15] (72 cm<sup>3</sup>/mol for C/S = 1.7) and the one computed using molecular dynamics by Pellenq et al. [13] (70.8 cm<sup>3</sup>/mol for C/S = 1.65).

After complete carbonation of the C-S-H paste (C/S = 1.4), the same kind of calculation was conducted to estimate the properties of the silica gel (S-H), namely molar volume  $V_m(S-H)$  and molar mass  $M_m(S-H)$ :

$$V_m(S-H) = \frac{(1-\emptyset_c)-1.4[C-S-H]V_m(vat)}{1.4[C-S-H]} \approx 40 \text{ cm}^3/\text{mol} \quad E-29$$

$$M_m(S-H) = \frac{\rho_d^c-1.4[C-S-H]M_m(vat)}{1.4[C-S-H]} \approx 93 \text{ g/mol} \quad E-30$$

The case of the C<sub>3</sub>S paste (C/S = 3.0) was more complicated than the C-S-H paste (C/S = 1.4) because the non-carbonated paste included portlandite (CH) in addition to C-S-H (**Figure 15**). Moreover, carbonation was

incomplete and then remaining hydrates (CH and C-S-H) were side by side with end-products of carbonation (silica gel and calcium carbonate) in the carbonated paste (**Figure 15**). It must be noted that we have implicitly assumed that a C-S-H with C/S lower than 1.7 could be described by an *ad-hoc* combination of silica gel and C-S-H of C/S = 1.7. Alternatively, it would have been necessary to describe the link between C/S and molar volume just like in the work of Wu & Ye [21] but this would have been much more difficult and uncertain.

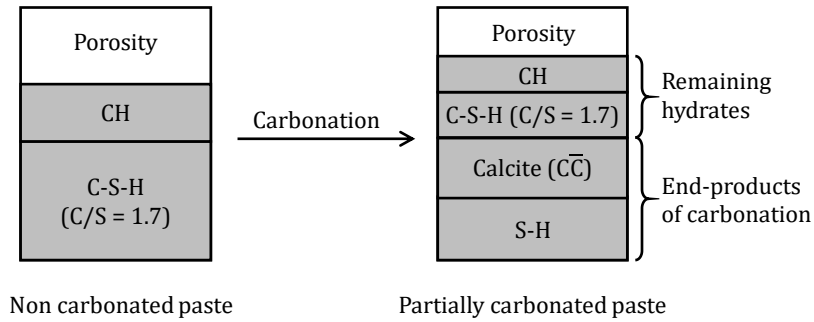


**Figure 15: Effect of the carbonation on a C-S-H + CH paste (C<sub>3</sub>S paste). The carbonation products and partially carbonated hydrated coexist**

Following the observations (XRD and <sup>29</sup>Si NMR), the carbonation of CH and C-S-H was assumed to precipitate calcite (neither aragonite nor vaterite) and silica gel (S-H); please note that the C-S-H was considered to be under the form C<sub>1.7</sub>-S-H<sub>1.8</sub> [15]:

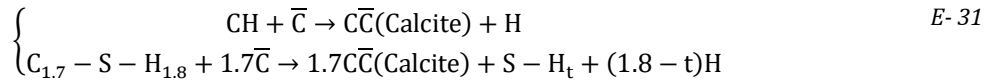


Table 7 and Table 8 detail the volume and mass calculation of all the different phases present in the non-carbonated and (partially) carbonated C<sub>3</sub>S paste (C/S = 3.0).

**Table 7: volume and mass of the different phases in the non-carbonated paste (C/S = 3.0)**

	Volume	Mass
Voids	$\emptyset_{nc}$	0
CH	$[\text{CH}]_0 V_m(\text{CH})$	$[\text{CH}]_0 M_m(\text{CH})$
C-S-H	$(1 - \emptyset_{nc}) - [\text{CH}]_0 V_m(\text{CH})$	$\rho_d^{nc} - [\text{CH}]_0 M_m(\text{CH})$
Total	1	$\rho_d^{nc}$

$[\text{CH}]_0$  concentration of portlandite in the non-carbonated paste

$V_m(\text{CH})$  molar volume of portlandite (33 cm<sup>3</sup>/mol)

$M_m(\text{CH})$  molar mass of portlandite (74.1 g/mol)

**Table 8: volume and mass of the different phases in the carbonated paste (C/S = 3.0)**

	Volume	Mass
Voids	$\emptyset_c$	0
CH	$[\text{CH}]_r V_m(\text{CH})$	$[\text{CH}]_r M_m(\text{CH})$
C-S-H	$[\text{C-S-H}]_r V_m(\text{C-S-H})$	$[\text{C-S-H}]_r M_m(\text{C-S-H})$
Calcite	$[\text{Cal}] V_m(\text{Cal})$	$[\text{Cal}] M_m(\text{Cal})$



S-H	$(1-\phi_c) \cdot V(\text{CH}) - V(\text{Cal}) - V(\text{C-S-H})$	$\rho_d^c \cdot M(\text{CH}) - M(\text{Cal}) - M(\text{C-S-H})$
Total	1	$\rho_d^c$

$[\text{CH}]_r$  concentration of the remaining portlandite in the carbonated paste

$[\text{C-S-H}]_r$  concentration of the remaining C-S-H in the carbonated paste

$[\text{Cal}]$  concentration of calcite in the carbonated paste

$V_m(\text{Cal})$  molar volume of calcite (35 cm<sup>3</sup>/mol)

$M_m(\text{Cal})$  molar mass of calcite (100.1 g/mol)

As for the C-S-H paste (C/S = 1.4), the results of the non-carbonated C<sub>3</sub>S paste were used to evaluate the molar volume of the C-S-H, according to:

$$V_m(\text{C} - \text{S} - \text{H}) = \frac{(1-\phi_{nc}) - [\text{CH}]_0 V_m(\text{CH})}{[\text{C-S-H}]} = \frac{(1-0.38) - 7.3 \times 0.033}{5.6} \approx 68 \text{ cm}^3/\text{mol} \quad E-32$$

The obtained value (68 cm<sup>3</sup>/mol) was very close to that of the C-S-H paste (69 cm<sup>3</sup>/mol). In a second step, the results of the (partially) carbonated C<sub>3</sub>S paste were used to evaluate the properties of the silica gel.

$$V_m(\text{S} - \text{H}) = \frac{(1-\phi_c) - [\text{CH}]_r V_m(\text{CH}) - [\text{Cal}] V_m(\text{Cal}) - [\text{C-S-H}]_r V_m(\text{C-S-H})}{[\text{C-S-H}]_0 - [\text{C-S-H}]_r} \approx 37 \text{ cm}^3/\text{mol} \quad E-33$$

$$M_m(\text{S} - \text{H}) = \frac{\rho_d^c - [\text{CH}]_r M_m(\text{CH}) - [\text{Cal}] M_m(\text{Cal}) - [\text{C-S-H}]_r M_m(\text{C-S-H})}{[\text{C-S-H}]_0 - [\text{C-S-H}]_r} \approx 71 \text{ g/mol}$$

The molar volume of silica gel was similar to that obtained for the C-S-H paste (37 versus 40 cm<sup>3</sup>/mol). The molar mass was however somewhat different (71 versus 93 g/mol). The reader should keep in mind that the values obtained using the results from the C<sub>3</sub>S paste were much more uncertain than those of the C-S-H paste (C/S = 1.4) mainly because of the remaining CH and C-S-H that made it difficult to estimate the volume and mass of the silica gel with accuracy.

Using the values computed above, it is easy to assess the change in volume induced by the decalcification of the C-S-H,  $\Delta V_d(\text{C} - \text{S} - \text{H})$ :

$$\Delta V_d(\text{C} - \text{S} - \text{H}) = V_m(\text{S} - \text{H}) - V_m(\text{C} - \text{S} - \text{H}) \approx 40 - 69 = -29 \text{ cm}^3/\text{mol} \quad E-34$$

Because one mol of S-H is less voluminous than one mol of C-S-H, the decalcification of the C-S-H leads to significant reduction in the solid volume (about 29 cm<sup>3</sup>/mol). This is consistent with the conclusions of Chen et al. [76]. The obtained value is also consistent with the results of Morandau et al. [68,77] who found that  $\Delta V_d(\text{C} - \text{S} - \text{H})$  was between 20 and 40 cm<sup>3</sup>/mol. Nonetheless, the precipitation of calcium carbonate also plays a significant role in volume change during the carbonation of C-S-H (E-31). It is plain to see that the reduction of solid volume generated by the decalcification of C-S-H is compensated by the precipitation of calcium carbonate (**Table 9**), resulting in the reduction of total porosity. Indeed, the change in volume depends on the calcium carbonate polymorph that is precipitated and on the C/S ratio of the C-S-H but the increase in solid volume induced by the carbonation of C-S-H

is expected to lie between 19 and 36 cm<sup>3</sup>/mol. This means that the carbonation of high C/S C-S-H (between 1.4 and 1.7) cannot be expected to generate an increase in porosity as it was observed by Wu and Ye [21] Shah et al. [78].

$$\Delta V_c(C - S - H) = V_m(S - H) + \left(\frac{C}{S}\right) V_m(\overline{CC}) - V_m(C - S - H) \quad E-35$$

**Table 9: change in solid volume (cm<sup>3</sup>/mol) induced by the carbonation of C-S-H, according to E- 15**

( $\overline{CC}$ )	Aragonite	Calcite	Vaterite	Unit
C/S = 1.4	+18.6	+20.0	+24.4	cm <sup>3</sup> /mol
C/S = 1.7	+28.8	+30.5	+35.4	cm <sup>3</sup> /mol

Lastly, considering the case of the C<sub>3</sub>S paste of this study, one can easily estimate the change in solid volume induced by the carbonation of both CH and C-S-H using (calcite was assumed to be the only calcium carbonate polymorph precipitated):

$$\begin{aligned} \Delta V_{C-S-H} &= 40\%[C - S - H]_0 \Delta V_c(C - S - H) = 0.4 \times 5.6 \times 30.5 \approx +68 \text{ cm}^3/\text{L of paste} \\ \Delta V_{CH} &= 75\%[CH]_0 (V_m(\text{Calc}) - V_m(\text{CH})) = 0.75 \times 7.3 \times 2 \approx +11 \text{ cm}^3/\text{L of paste} \end{aligned} \quad E-36$$

It could thus be concluded that the change in porosity is mostly due to C-S-H, even though the proportion of CH that was carbonated is greater than that of C-S-H. This is consistent with the conclusions of other studies [68,77,79].

### Carbonation shrinkage

**Figure 16** presents the length variation of the cylinders (Ø14 mm) that were submitted to drying and then accelerated carbonation. The drying shrinkage of the C<sub>3</sub>S paste quickly reached a stable value (0.3% = 3 mm/m) that is consistent with the results of Mindess *et al.* [80] whereas the C-S-H paste kept shrinking and was not stabilized even at 195 days. This could be due to (1) the refined pore structure of the C-S-H paste (**Figure 8**) that induced very low water transport properties and (2) to the atmospheric carbonation (0.04% CO<sub>2</sub>) of the C-S-H paste during drying that could have induced some carbonation shrinkage during the preliminary drying phase. After 195 days of drying, the specimens were submitted to 3% CO<sub>2</sub> that immediately generated additional shrinkage. Assuming that there was interaction between drying and carbonation and that drying was terminated at 195 days, carbonation shrinkage was simply estimated by subtracting the contribution of drying:  $\varepsilon^c = \varepsilon^{tot} - \varepsilon^d$ . The shrinkage of the C-S-H paste appeared to be much higher than that of the C<sub>3</sub>S paste (**Table 10**).

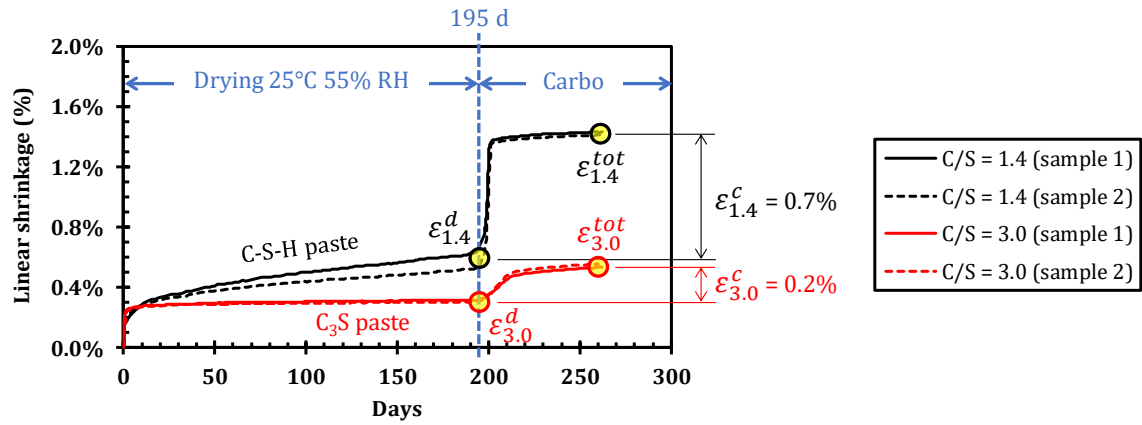


Figure 16: Length variation of the Ø14 mm cylinders exposed to drying (25°C 55% RH) and then accelerated carbonation (25°C, 55% RH and 3% CO<sub>2</sub>)

Table 10: Results of the carbonation shrinkage test

	$\varepsilon^{tot}$	$\varepsilon^d$	$\varepsilon^c$
C-S-H paste (C/S = 1.4)	1.4% (14 mm/m)	0.7% (7 mm/m)	0.7% (7 mm/m)
C <sub>3</sub> S paste (C/S = 3.0)	0.5% (5 mm/m)	0.3% (3 mm/m)	0.2% (2 mm/m)

This strongly suggests that, carbonation shrinkage is due to the C-S-H as it was already proposed by Sereda et al. [23][24]. More specifically, carbonation shrinkage is due to the decalcification of the C-S-H and the subsequent polymerization of silica chains. The measured values from **Table 10** were then compared to the results obtained by Chen et al. [76] who measured the shrinkage generated by NH<sub>4</sub>NO<sub>3</sub> decalcification of a C<sub>3</sub>S paste. It is obvious that the carbonation shrinkage values measured here are consistent with those obtained by decalcification by Chen et al. [76].

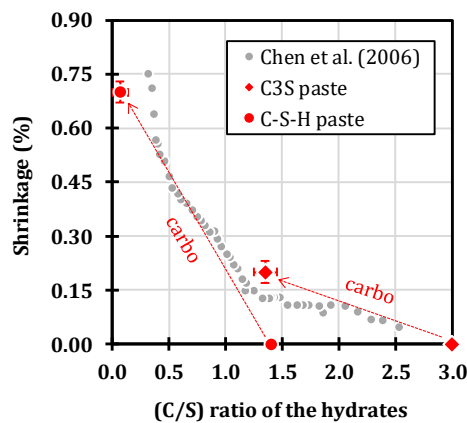


Figure 17: Comparison of the carbonation shrinkage results with the data of Chen et al. [76]

However, because of the presence of portlandite, the C/S ratio of the C<sub>3</sub>S paste cannot be compared directly to that of the C-S-H paste (free of portlandite). This shortcoming can be easily overcome by computing the change in C/S ratio of the C-S-H. Here we made the choice to characterize the decalcification level of the C-S-H using:

$$\Delta(C/S) = \frac{(C/S)(t) - (C/S)_0}{(C/S)_0} \quad E-37$$

where  $(C/S)(t)$  is the C/S ratio of the C-S-H at the time  $t$  and  $(C/S)_0$  the C/S ratio of the unaltered C-S-H.  $\Delta(C/S) = 0\%$  means that the C-S-H are unaltered whereas  $\Delta(C/S) = 100\%$  means that the C-S-H are completely degraded. The values of  $\Delta(C/S)$  could be easily computed for the tests of Chen *et al.* [76] because portlandite was completely dissolved when the C/S ratio of the solid (CH + C-S-H) reached 1.4 [see section 4.1 of [76]]. The shrinkage values were then plotted versus the decalcification level  $\Delta(C/S)$  on Figure 18. Despite some inevitable discrepancy, the results of Chen *et al.* and those from this study describe a common trend: the shrinkage increases with the decalcification level of the C-S-H. This unambiguously confirms that the shrinkage generated by carbonation is due to the decalcification of C-S-H and polymerization of the silica chains [76].

The following 2<sup>nd</sup> order polynomial was proposed to fit the data:

$$\varepsilon^c = 0.264\Delta^2(C/S) + 0.513\Delta(C/S) \quad E-38$$

This simple approach allows estimating the shrinkage generated by the decalcification of high C/S C-S-H (between 1.4 and 1.7). Please note that this function is not expected to be valid for lower C/S values. More results would be more than welcome to verify this.

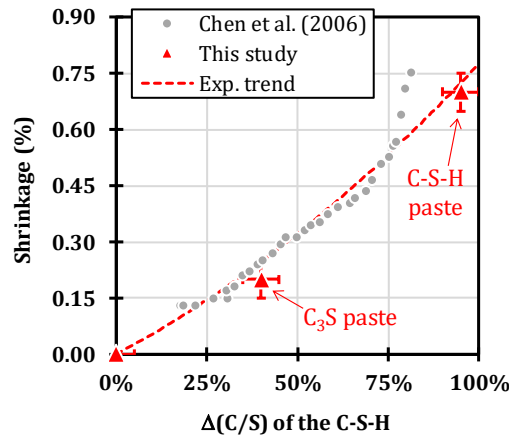


**Figure 18: Shrinkage versus decalcification level  $\Delta(C/S)$  of high C/S C-S-H**

#### 1.1.4 Discussion

The results presented here highlight the influence of the mineralogical composition on the response of cement-based materials to atmospheric carbonation. C-S-H carbonation appeared to be complete in the C-S-H paste (no

remaining C-S-H was detected in the carbonated zone). Consequently, the total porosity was strongly reduced by the precipitation of  $\text{CaCO}_3$  but the decalcification of C-S-H and the polymerization of silica chains generated shrinkage and then significant cracking. Porosity reduction and cracking have adverse effects on transport: porosity reduction is expected to decrease the transport properties whereas cracking is expected to increase them. In the case of the C-S-H paste, cracking prevailed over porosity reduction and the  $\text{CO}_2$  diffusion coefficient of the carbonated paste was high which led to high carbonation rate.

Conversely, the carbonation of the  $\text{C}_3\text{S}$  paste (including C-S-H and portlandite) was different. Portlandite was dissolved to maintain the  $\text{Ca}^{2+}$  in the poral solution but the dissolution was not complete and remaining portlandite was detected in the carbonated zone. This was already observed and is generally attributed to the formation of  $\text{CaCO}_3$  layers that hinders the dissolution of portlandite. Therefore, Ca was taken from the C-S-H to maintain equilibrium but C-S-H decalcification only remained partial oppositely to the C-S-H paste. Due to the precipitation of  $\text{CaCO}_3$  the total porosity was reduced after carbonation but less than the C-S-H paste (because C-S-H is the main contributor to porosity reduction) and only few cracks were observed. As a consequence, porosity reduction prevailed over cracking and the  $\text{CO}_2$  diffusion coefficient of the carbonated  $\text{C}_3\text{S}$  paste was low which led to low carbonation rate. The reader must keep in mind that despite a strong difference in their initial Ca content, the carbonation of the two pastes appeared to yield similar amounts of  $\text{CaCO}_3$ . So the difference in carbonation rate was expected to be mainly due to the difference in  $\text{CO}_2$  diffusion coefficient.

These results clearly showed the protective effect of portlandite: when present portlandite dissolves to maintain the  $\text{Ca}^{2+}$  concentration in the poral solution, prevents the decalcification of C-S-H and thus limits the shrinkage and cracking induced by the polymerization of silica chains. This was already discussed in [12].

Another point that deserves the reader's attention is cracking. Cracking has been known as an intrinsic consequence of carbonation [45]. Cracking is a prominent phenomenon for carbonation because it improves gas diffusion in the carbonated zone and then increases the carbonation rate. So the presence of portlandite is beneficial for the resistance to carbonation, not only because of the associated alkaline reserve but especially because it limits the decalcification of C-S-H and then cracking. Cracking not only strongly influences the carbonation rate of cement-based materials, cracking also modifies the consequences of carbonation at a lower scale:

- the presence of cracks through the carbonated zone provides pathways for  $\text{CO}_2$  that can increase the carbonation depth at the vicinity of the cracks (cf. **Figure 12**) and make the carbonation front tortuous at the centimetre scale;
- the presence of finely distributed cracks induced by the decalcification of C-S-H can also generate heterogeneities in the decalcification/carbonation level (cf. **Figure 11**) at the millimetre scale.

### 1.1.5 Conclusion

The use of two model pastes ( $C_3S$  paste and C-S-H paste with  $C/S = 1.4$ ) made it possible to investigate the mechanisms of atmospheric carbonation. The consequences of carbonation were somewhat contrasted depending on the presence/absence of portlandite. Portlandite acts as a Ca-buffer that helps protecting the C-S-H from decalcification when exposed to  $CO_2$ . In the absence of portlandite, the C-S-H are rapidly and completely decalcified and the resulting silica chains polymerize to form silica gel. This process generates shrinkage (as for Ca-leaching) and then cracking. Carbonation then generates two adverse effects: (1) the precipitation of  $CaCO_3$  leads to porosity reduction and then decreases the  $CO_2$  diffusion coefficient in the carbonated zone and (2) cracking provides pathway and then increases the  $CO_2$  diffusion coefficient. The role of portlandite is then of tantamount importance for carbonation.

The results of this study also made it possible to evaluate the volume changes induced by carbonation. The molar volume of C-S-H and silica gel (the end-product of C-S-H decalcification) were estimated, which allowed to calculate the volume change induced by the decalcification and the carbonation of C-S-H. The results showed that the decalcification of C-S-H generates an increase in porosity that is more than compensated by the precipitation of  $CaCO_3$ . The carbonation of C-S-H then generates a decrease in total porosity. Consequently, C-S-H contributes much more to porosity reduction than portlandite.

Besides, the comparison of carbonation shrinkage measurements with the  $NH_4NO_3$  leaching results of Chen *et al.* [76] confirmed that carbonation shrinkage was associated to the decalcification of C-S-H. A simple polynomial relation was proposed to estimate the shrinkage using the change in C/S ratio of the C-S-H.

### Acknowledgments

The financial support from IRSN and CEA is gratefully acknowledged.

### Literature cited

- [1] H.F.W. Taylor, Cement chemistry, Limited, Academic press, 1990.
- [2] W.F. Cole, B. Kroone, Carbonate minerals in hydrated Portland cement, *Nature*. 184 (1959) BA57.
- [3] W.F. Cole, B. Kroone, Carbon dioxide in hydrated Portland cement, *J. Am. Concr. Inst.* 56 (1960) 1275–1296.
- [4] L. Bertolini, B. Elsener, P. Pedferri, R. Polder, Corrosion of steel in concrete - prevention, diagnosis, repair, Wiley, 2004.
- [5] R. Neves, F.A. Branco, J. de Brito, A method for the use of accelerated carbonation tests in durability design, *Constr. Build. Mater.* 36 (2012) 585–591. doi:10.1016/j.conbuildmat.2012.06.028.
- [6] M. Thiery, G. Villain, P. Dangla, G. Platret, Investigation of the carbonation front shape on cementitious materials: Effects of the chemical kinetics, *Cem. Concr. Res.* 37 (2007) 1047–1058. doi:10.1016/j.cemconres.2007.04.002.

- [7] B. Bary, A. Sellier, Coupled moisture—carbon dioxide—calcium transfer model for carbonation of concrete, *Cem. Concr. Res.* 34 (2004) 1859–1872. doi:10.1016/j.cemconres.2004.01.025.
- [8] A.V. Saetta, B.A. Schrefler, R.V. Vitaliani, 2-D model for carbonation and moisture/heat flow in porous materials, *Cem. Concr. Res.* 25 (1995) 1703–1712. doi:10.1016/0008-8846(95)00166-2.
- [9] A. V. Saetta, R. V. Vitaliani, Experimental investigation and numerical modeling of carbonation process in reinforced concrete structures, *Cem. Concr. Res.* 34 (2004) 571–579. doi:10.1016/j.cemconres.2003.09.009.
- [10] M. Te Liang, W. Qu, C.H. Liang, S.M. Lin, Mathematical modeling and applications for concrete carbonation, *J. Mar. Sci. Technol.* 11 (2003) 20–33.
- [11] A. Silva, R. Neves, J. De Brito, Statistical modelling of carbonation in reinforced concrete, *Cem. Concr. Compos.* 50 (2014) 73–81. doi:10.1016/j.cemconcomp.2013.12.001.
- [12] N. Seigneur, É. Kangni-foli, V. Lagneau, A. Dauzères, S. Poyet, P. Le Bescop, E. L'Hôpital, J.B. d'Espinose de Lacaille, Understanding the effects of the atmospheric carbonation of cementitious materials using reactive transport modelling, *Submitt. to Cem. Concr. Res.* (2019).
- [13] R.J.-M. Pellenq, A. Kushima, R. Shahsavari, K.J. Van Vliet, M.J. Buehler, S. Yip, F.-J. Ulm, A realistic molecular model of cement hydrates., *Proc. Natl. Acad. Sci. U. S. A.* 106 (2009) 16102–7. doi:10.1073/pnas.0902180106.
- [14] A.J. Allen, J.J. Thomas, H.M. Jennings, Composition and density of nanoscale calcium–silicate–hydrate in cement, *Nat. Mater.* 6 (2007) 311–316. doi:10.1038/nmat1871.
- [15] H.M. Jennings, Refinements to colloid model of C-S-H in cement: CM-II, *Cem. Concr. Res.* 38 (2008) 275–289. doi:10.1016/j.cemconres.2007.10.006.
- [16] I.G. Richardson, The calcium silicate hydrates, *Cem. Concr. Res.* 38 (2008) 137–158. doi:10.1016/j.cemconres.2007.11.005.
- [17] B. Lothenbach, T. Matschei, G. Möschner, F.P. Glasser, Thermodynamic modelling of the effect of temperature on the hydration and porosity of Portland cement, *Cem. Concr. Res.* 38 (2008) 1–18. doi:10.1016/j.cemconres.2007.08.017.
- [18] B. Lothenbach, D.A. Kulik, T. Matschei, M. Balonis, L. Baquerizo, B. Dilnesa, G.D. Miron, R.J. Myers, Cemdata18: A chemical thermodynamic database for hydrated Portland cements and alkali-activated materials, *Cem. Concr. Res.* 115 (2019) 472–506. doi:10.1016/j.cemconres.2018.04.018.
- [19] D.A. Kulik, Aqueous solubility diagrams for cementitious waste stabilization systems: II, End-member stoichiometries of ideal Calcium Silicate Hydrate solid solutions, *J. Am. Ceram. Soc.* 84 (2001) 3017–3026.
- [20] D.A. Kulik, Improving the structural consistency of C-S-H solid solution thermodynamic models, *Cem. Concr. Res.* 41 (2011) 477–495. doi:10.1016/j.cemconres.2011.01.012.
- [21] B. Wu, G. Ye, Development of porosity of cement paste blended with supplementary cementitious materials after carbonation, *Constr. Build. Mater.* 145 (2017) 52–61. doi:10.1016/j.conbuildmat.2017.03.176.
- [22] G.J. Verbeck, Carbonation of hydrated portland cement, *ASTM Spec. Tech. Publ.* 205 (1958) 17–36. doi:10.1520/STP39460S.
- [23] K. Kamimura, P.J. Sereda, E.G. Swenson, Changes in weight and dimensions in the drying and carbonation of Portland cement mortars, *Mag. Concr. Res.* 17 (1965) 5–14.
- [24] E.G. Swenson, P.J. Sereda, Mechanism of the carbonation shrinkage of lime and hydrated cement, *J. Appl. Chem.* 18 (1968) 111–117.
- [25] Y.F. Houst, Carbonation Shrinkage of Hydrated Cement Paste, in: V.M. Malhotra (Ed.), 4th CANMET/ACI Int. Conf. Durab. Concr., ACI, Sydney (Australia), 1997: pp. 481–491.
- [26] P.H.R. Borges, J.O. Costa, N.B. Milestone, C.J. Lynsdale, R.E. Streatfield, Carbonation of CH and C-S-H in composite cement pastes containing high amounts of BFS, *Cem. Concr. Res.* 40 (2010) 284–292. doi:10.1016/j.cemconres.2009.10.020.

- [27] M. Auroy, S. Poyet, P. Le Bescop, J.M. Torrenti, T. Charpentier, M. Moskura, X. Bourbon, Impact of carbonation on unsaturated water transport properties of cement-based materials, *Cem. Concr. Res.* 74 (2015) 44–58. doi:10.1016/j.cemconres.2015.04.002.
- [28] J. Han, W. Sun, G. Pan, W. Caihui, Monitoring the evolution of accelerated carbonation of hardened cement pastes by X-Ray Computed Tomography, *J. Mater. Civ. Eng.* 25 (2013) 347–354.
- [29] K. Wan, eshu, Q. Xu, Y. Wang, G. Pan, 3D spatial distribution of the calcium carbonate caused by carbonation of cement paste, *Cem. Concr. Compos.* 45 (2014) 255–263. doi:10.1016/j.cemconcomp.2013.10.011.
- [30] V. Dutzer, W. Dridi, S. Poyet, P. Le Bescop, X. Bourbon, The link between gas diffusion and carbonation in hardened cement pastes, *Cem. Concr. Res.* 123 (2019) 105795. doi:10.1016/j.cemconres.2019.105795.
- [31] É. Kangni-foli, S. Poyet, P. Le Bescop, T. Charpentier, F. Bernarchy-Barbé, A. Dauzères, E. L'Hôpital, M. Neji, J.B. d'Espinose de Lacaillerie, Model synthetic pastes for low alkalinity cements, *Submitt. to Cem. Concr. Res.* (2019).
- [32] E. Kangni-foli, S. Poyet, A. Dauzères, P. Le Bescop, E. L'Hôpital, T. Charpentier, N. Mejdi, J.-B. D'Espinose, C/S ratio influence on the carbonation of cementitious material using designed model systems, proceedings of International conference on Sustainable Materials, Systems and Structures, in: *Proceedings pro 128* (Ed.), Rilem, Rovinj (Croatia), 2019.
- [33] L. Greenspan, Humidity fixed points of binary saturated aqueous solutions, *J. Res. Natl. Bur. Stand. Sect. A Phys. Chem.* 81A (1977) 89–96. doi:10.6028/jres.081A.011.
- [34] E. Drouet, S. Poyet, P. Le Bescop, J.-M. Torrenti, X. Bourbon, Carbonation of hardened cement pastes: Influence of temperature, *Cem. Concr. Res.* 115 (2019) 445–459. doi:10.1016/j.cemconres.2018.09.019.
- [35] G. Le Saoût, T. Füllmann, V. Kocaba, K.L. Scrivener, Quantitative study of cementitious materials by x-ray diffraction - Rietveld analysis using an external standard, in: J.J. Beaudoin, J.M. Makar, L. Raki (Eds.), *Proc. 12th Int. Congr. Chem. Cem., Cement Association of Canada, Montréal (Canada), 2007*: p. 12p.
- [36] I.G. Richardson, Model structures for C-(A)-S-H(I), *Acta Crystallogr. Sect. B Struct. Sci. Cryst. Eng. Mater.* 70 (2014) 903–923. doi:10.1107/S2052520614021982.
- [37] G. Villain, M. Thiery, G. Platret, Measurement methods of carbonation profiles in concrete: Thermogravimetry, chemical analysis and gammadensimetry, *Cem. Concr. Res.* 37 (2007) 1182–1192. doi:10.1016/j.cemconres.2007.04.015.
- [38] B. Lothenbach, P. Durdzinski, K. De Weerd, Thermogravimetric analysis, in: L. Scrivener, Snellings (Ed.), *A Pract. Guid. to Microstruct. Anal. Cem. Mater.*, CRC Press, Boca Raton (USA), 2016: pp. 177–211.
- [39] D. Massiot, F. Fayon, M. Capron, I. King, S. Le Calvé, B. Alonso, J.O. Durand, B. Bujoli, Z. Gan, G. Hoatson, Modelling one- and two-dimensional solid-state NMR spectra, *Magn. Reson. Chem.* 40 (2002) 70–76. doi:10.1002/mrc.984.
- [40] H. Hornain, G. Arliguie, *GranDuBé - Grandeurs associées à la durabilité des bétons* (in French), Presses des Ponts et Chaussées, 2007.
- [41] M.M.R. Williams, The mathematics of diffusion, *Ann. Nucl. Energy.* 4 (1977) 205–206. doi:10.1016/0306-4549(77)90072-X.
- [42] V.G. Papadakis, C.G. Vayenas, M.N. Fardis, Fundamental modeling and experimental investigation of concrete carbonation, *ACI Mater. J.* 88 (1991) 363–373.
- [43] V.G. Papadakis, M.N. Fardis, C.G. Vayenas, Effect of composition, environmental factors and cement-lime mortar coating on concrete carbonation, *Mater. Struct.* 25 (1992) 293–304.
- [44] Z. Šauman, Carbonization of porous concrete and its main binding components, *Cem. Concr. Res.* 1 (1971) 645–662. doi:10.1016/0008-8846(71)90019-6.
- [45] M. Auroy, S. Poyet, P. Le, J.-M. Torrenti, U. Paris-est, D. Matériaux, B. Newton, P. Le Bescop, J.-M. Torrenti, T. Charpentier, M. Moskura, X. Bourbon, Comparison between natural and accelerated carbonation (3% CO<sub>2</sub>): Impact on mineralogy, microstructure, water retention and cracking, *Cem. Concr. Res.* 109 (2018) 64–80.



doi:10.1016/j.cemconres.2018.04.012.

- [46] K. Mohan, H.F.W. Taylor, Analytical Electron Microscopy of Cement Pastes: IV,  $\beta$ -Dicalcium Silicate Pastes, *J. Am. Ceram. Soc.* 64 (1981) 717–719. doi:10.1111/j.1551-2916.1981.tb15893.x.
- [47] A. Nonat, The structure and stoichiometry of C-S-H, *Cem. Concr. Res.* 34 (2004) 1521–1528. doi:10.1016/j.cemconres.2004.04.035.
- [48] K. Garbev, G. Beuchle, M. Bornefeld, L. Black, P. Stemmermann, Cell Dimensions and Composition of Nanocrystalline Calcium Silicate Hydrate Solid Solutions. Part 1: Synchrotron-Based X-Ray Diffraction, *J. Am. Ceram. Soc.* 91 (2008) 3005–3014. doi:10.1111/j.1551-2916.2008.02484.x.
- [49] H.M. Ghodake, T.K. Goswami, A. Chakraverty, Moisture sorption isotherms, heat of sorption and vaporization of withered leaves, black and green tea, *J. Food Eng.* 78 (2007) 827–835. doi:10.1016/j.jfoodeng.2005.11.023.
- [50] T. Ogino, T. Suzuki, K. Sawada, The formation and transformation mechanism of calcium carbonate in water, *Geochim. Cosmochim. Acta.* 51 (1987) 2757–2767.
- [51] J. Kawano, N. Shimobayashi, A. Miyake, M. Kitamura, Precipitation diagram of calcium carbonate polymorphs: its construction and significance, *J. Physics. Condens. Matter.* 21 (2009) 425102. doi:10.1088/0953-8984/21/42/425102.
- [52] M. Kitamura, Strategy for control of crystallization of polymorphs, *CrystEngComm.* 11 (2009) 949–964. doi:10.1039/b809332f.
- [53] Y.S. Han, G. Hadiko, M. Fuji, M. Takahashi, Crystallization and transformation of vaterite at controlled pH, *J. Cryst. Growth.* 289 (2006) 269–274. doi:10.1016/j.jcrysgr.2005.11.011.
- [54] H. Deng, S. Wang, X. Wang, C. Du, X. Shen, Y. Wang, F. Cui, Two competitive nucleation mechanisms of calcium carbonate biomineralization in response to surface functionality in low calcium ion concentration solution, *Regen. Biomater.* 2 (2015) 187–195. doi:10.1093/rb/rbv010.
- [55] F. Brunet, P. Bertani, T. Charpentier, A. Nonat, J. Virlet, Application of 29 Si Homonuclear and 1 H-29 Si Heteronuclear NMR Correlation to Structural Studies of Calcium Silicate Hydrates, *J. Phys. Chem. B.* 108 (2004) 15494–15502. doi:10.1021/jp031174g.
- [56] I. Klur, B. Pollet, J. Virlet, A. Nonat, C-S-H Structure Evolution with Calcium Content by Multinuclear NMR, in: *Nucl. Magn. Reson. Spectrosc. Cem. Mater.*, Springer Berlin Heidelberg, Berlin, Heidelberg, 1998: pp. 119–141. doi:10.1007/978-3-642-80432-8\_8.
- [57] C. Biagioni, S. Merlino, E. Bonaccorsi, The tobermorite supergroup: a new nomenclature, *Mineral. Mag.* 79 (2015) 485–495. doi:10.1180/minmag.2015.079.2.22.
- [58] E. Bonaccorsi, S. Merlino, A.R. Kampf, The crystal structure of tobermorite 14 Å (plombierite), a C-S-H phase, *J. Am. Ceram. Soc.* 88 (2005) 505–512. doi:10.1111/j.1551-2916.2005.00116.x.
- [59] I.G. Richardson, G.W. Groves, Models for the composition and structure of calcium silicate hydrate (CSH) gel in hardened tricalcium silicate pastes, *Cem. Concr. Res.* 22 (1992) 1001–1010. doi:10.1016/0008-8846(92)90030-Y.
- [60] X. Cong, R. James Kirkpatrick, 17O and 29Si MAS NMR study of  $\beta$ -C2S hydration and the structure of calcium-silicate hydrates, *Cem. Concr. Res.* 23 (1993) 1065–1077. doi:10.1016/0008-8846(93)90166-7.
- [61] X. Cong, R.J. Kirkpatrick, 29Si MAS NMR study of the structure of calcium silicate hydrate, *Adv. Cem. Based Mater.* 3 (1996) 144–156. doi:10.1016/S1065-7355(96)90046-2.
- [62] Y. He, L. Lu, L.J. Struble, J.L. Rapp, P. Mondal, S. Hu, Effect of calcium-silicon ratio on microstructure and nanostructure of calcium silicate hydrate synthesized by reaction of fumed silica and calcium oxide at room temperature, *Mater. Struct.* 47 (2014) 311–322. doi:10.1617/s11527-013-0062-0.
- [63] M. Castellote, L. Fernandez, C. Andrade, C. Alonso, Chemical changes and phase analysis of OPC pastes carbonated at different CO<sub>2</sub> concentrations, *Mater. Struct.* 42 (2009) 515–525. doi:10.1617/s11527-008-9399-1.

- [64] S.E. Pihlajavaara, Some results of the effect of carbonation on the porosity and pore size distribution of cement paste, *Matériaux Constr.* 1 (1968) 521–527. doi:10.1007/BF02473640.
- [65] Y.F. Houst, F.H. Wittmann, Influence of porosity and water content on the diffusivity of CO<sub>2</sub> and O<sub>2</sub> through hydrated cement paste, *Cem. Concr. Res.* 24 (1994) 1165–1176. doi:10.1016/0008-8846(94)90040-X.
- [66] V.T. Ngala, C.L. Page, Effects of carbonation on pore structure and diffusional properties of hydrated cement pastes, *Cem. Concr. Res.* 27 (1997) 995–1007.
- [67] P.A. Claisse, H. El-Sayad, I.G. Shaaban, Permeability and pore volume of carbonated concrete, *ACI Mater. J.* 96 (1999) 378–381.
- [68] A. Morandea, M. Thiéry, P. Dangla, Investigation of the carbonation mechanism of CH and C-S-H in terms of kinetics, microstructure changes and moisture properties, *Cem. Concr. Res.* 56 (2014) 153–170. doi:10.1016/j.cemconres.2013.11.015.
- [69] A.J. Katz, A.H. Thompson, Quantitative prediction of permeability in porous rock, *Phys. Rev. B.* 34 (1986) 8179–8181.
- [70] A.S. El-Dieb, R.D. Hooton, Evaluation of the Katz-Thompson model for estimating the water permeability of cement-based materials from mercury intrusion porosimetry data, *Cem. Concr. Res.* 24 (1994) 443–455.
- [71] P.H.R.R. Borges, N.B. Milestone, J.O. Costa, C.J. Lynsdale, T.H. Panzera, A.L. Christophoro, Carbonation durability of blended cement pastes used for waste encapsulation, *Mater. Struct.* 45 (2012) 663–678. doi:10.1617/s11527-011-9788-8.
- [72] A. Leemann, F. Moro, Carbonation of concrete: the role of CO<sub>2</sub> concentration, relative humidity and CO<sub>2</sub> buffer capacity, *Mater. Struct.* 50 (2017) 30. doi:10.1617/s11527-016-0917-2.
- [73] J.L. Branch, D.S. Kosson, A.C. Garrabrants, P.J. He, The impact of carbonation on the microstructure and solubility of major constituents in microconcrete materials with varying alkalinities due to fly ash replacement of ordinary Portland cement, *Cem. Concr. Res.* 89 (2016) 297–309. doi:10.1016/j.cemconres.2016.08.019.
- [74] A. Leemann, P. Nygaard, J. Kaufmann, R. Loser, Relation between carbonation resistance, mix design and exposure of mortar and concrete, *Cem. Concr. Compos.* 62 (2015) 33–43. doi:10.1016/j.cemconcomp.2015.04.020.
- [75] V. Shah, S. Bishnoi, Carbonation resistance of cements containing supplementary cementitious materials and its relation to various parameters of concrete, *Constr. Build. Mater.* 178 (2018) 219–232. doi:10.1016/j.conbuildmat.2018.05.162.
- [76] J.J. Chen, J.J. Thomas, H.M. Jennings, Decalcification shrinkage of cement paste, *Cem. Concr. Res.* 36 (2006) 801–809. doi:10.1016/j.cemconres.2005.11.003.
- [77] A. Morandea, M. Thiéry, P. Dangla, Impact of accelerated carbonation on OPC cement paste blended with fly ash, *Cem. Concr. Res.* 67 (2015) 226–236. doi:10.1016/j.cemconres.2014.10.003.
- [78] V. Shah, K. Scrivener, B. Bhattacharjee, S. Bishnoi, Changes in microstructure characteristics of cement paste on carbonation, *Cem. Concr. Res.* 109 (2018) 184–197. doi:10.1016/j.cemconres.2018.04.016.
- [79] S.T. Pham, W. Prince, The carbonation of calcium-silicate-hydrate C-S-H in cement mortar studied using thermal analysis and gas pycnometer: determination of the quantity of calcium carbonate produced and the increase in molar volume, *Adv. Mater. Res.* 931–932 (2014) 411–415.
- [80] S. Mindess, J.F. Young, F.V. Lawrence, Creep and drying shrinkage of calcium silicate pastes I. Specimen preparation and mechanical properties, *Cem. Concr. Res.* 8 (1978) 591–600.

## 1.2 Appendices

### Appendix A: NMR deconvolution parameters and results.

**Table S1: Contributions of the different environments (in %) from C/S:1.4 paste decomposition**

%	0-3.6 mm	15.02-20.02 mm	36.02-39.02 mm	41.04-41.08 mm	43.8-44.6 mm	46.64-47.44 mm	Pristine
Q <sup>1</sup>	-			2	10	34	52
Q <sup>2B</sup>				3	20	22	13
Q <sup>2P</sup>				5	42	44	25
Q <sup>3gel</sup>	28	14	20	35	28		5
Q <sup>4gel</sup>	72	86	80	55			

**Table S2: Contributions of the different environments (in %) from C/S: 3.00 paste decomposition**

%	0-2 mm	6.8-7.6 mm	16.6-18.2 mm	20.4-21.4 mm	27.9-30.1 mm	Pristine
Q <sup>1</sup>	6	22	42	55	64	68
Q <sup>2B</sup>		11	18	15	12	11
Q <sup>2P</sup>		26	40	30	24	21
Q <sup>3gel</sup>	2	7				
Q <sup>4gel</sup>	92	34				

**Table S3: NMR deconvolution parameters**

	$\delta$ (ppm)		Value of x in $xG/(1-x)L$	$\overline{Width}$ (ppm)
	C/S=1.4	C/S=3.0		
Q <sup>0</sup>	-			
Q <sup>1</sup>	-78.9	-78.9	0.8	2
Q <sup>2b</sup>	-83.3	-83.5	0	2.7
Q <sup>2p</sup>	-85.5	-85.3	0.2	2.3
Q <sup>3gel</sup>	-101.6	-100.5	0	5.4
Q <sup>4gel</sup>	-112.3	-112.4	0.8	8.8
G: Gaussian L: Lorentzian				

Q<sup>0</sup> was not deconvoluted since its intensity could not confidently be distinguished from the noise.

**Table S3: Values of the carbonation depths obtained by  $\mu$ CT for the samples C/S = 3.0 at 326 days of carbonation and C/S = 1.4 at 316 days of carbonation**

Samples	Extent of the carbonation front (mm)	
	C/S = 3.0	C/S = 1.4
TGA+RMN	17.9-22.1	36.4-40.6
XRD	14.1-18.6	34.4-38.6

**Summary of the model pastes carbonation:**

A thorough characterization of carbonation's consequences from the molecular scale to the cement paste's scale was presented along with the quantification of the extent of each alteration's type. A reduced C-S-H's alteration in presence of high calcium content especially portlandite was observed. This was the expression of a buffering effect of portlandite toward C-S-H's carbonation, which tends to preserves the C-S-H. A higher extent of carbonation was exhibited by the paste with both lower alkalinity and buffering capability, and higher porosity. The C-S-H paste after carbonation was extensively cracked which highlights the ineffectiveness of the phases formed to maintain the material integrity since silica gel and calcium carbonate mechanical properties are considerably lower than C-S-H's. The carbonation affects the materials at a macroscopic level, reflected through solid volume variation. The estimated variation of the solid volume induced by the degradation of the C-S-H was found to be compensated by the silica gel and the carbonates formed, consequently contradicting previous suggestions assuming a porosity increase, this despite the observed heavy cracking by the C-S-H paste

### 1.3 Carbonation of an industrial LAC

Along with the model pastes, one of the binary formulations retained in the DOPAS FSS project (CEM I 50%+SF 50%) (section 1.1 and **Table 6**) was also fabricated. Several aims were followed namely, a better understanding of the carbonation mechanism based on the knowledge gained on model materials properties (chapter 1 in section 0), and the highlight of key durability parameters such as the calcium and aluminium content and the nature of the carbonated microstructure (chapter 2: section 0, chapter 3: section 0 ). Since this industrial material is retained in the framework of the French disposal, extensive durability understanding is required. The results detailed in the following correspond to one carbonation term (50 days) at 25°C, RH 55% and  $P_{CO_2}$ : 3%, as the experiment is still ongoing.

The typical diffractograms of the main regions of the carbonated LAC are displayed in Figure 19. The carbonated region is characterized by both a calcium carbonates signals, a diffuse contribution generated by the silica gel, and the extinction of the main C-S-H signal between 30-35°(2 $\theta$ ). The carbonation front's region is associated to the reduced calcium carbonates signals, and the predominance of the C-S-H's signal. The uncarbonated region shows mainly C-S-H signals.

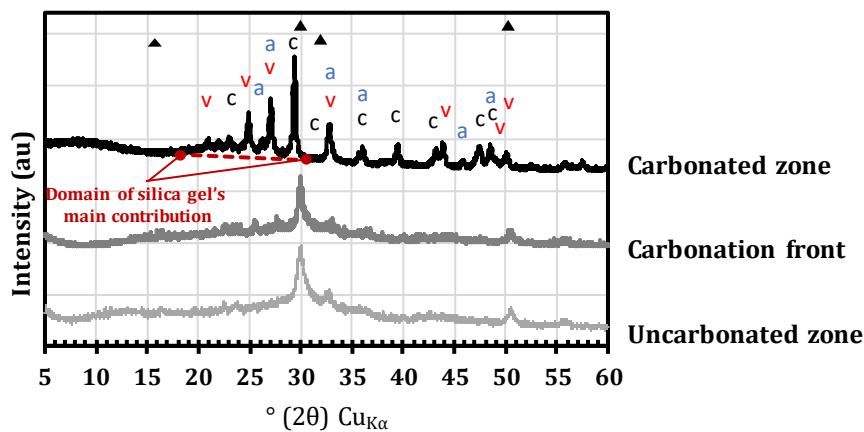


**Figure 19: Carbonated industrial LAC's XRD profiles, especially the diffractograms of uncarbonated area, carbonated front area and fully carbonated zone are showed. a: aragonite, v: vaterite, c: calcite, filled triangle: C-S-H. Carbonated zone (surface), carbonated front (15 mm), uncarbonated zone: pristine material.**

The distribution of the different phases based on Rietveld analysis is shown on Figure 20. The calcium carbonates polymorphism evidenced vaterite and calcite as the mains phases, nonetheless residual amount of aragonite was observed. The carbonation of C-A-S-H's powder (2<sup>nd</sup> chapter see section 0) mainly yielded vaterite and residual aragonite's content. Since the industrial LAC are essentially made of C-A-S-H. The effect of the microstructure which partly controls aspects such as the materials' water content, the carbonates nucleation pathways, and also the presence of foreign ions (from the cement) are believed to be responsible to the difference in polymorphic orientation observed between the LAC and the C-A-S-H powders. A system with high pH and pore solution saturated with vaterite favour the formation of calcite [1], this was one the explanation proposed for the abundant calcite formation in C<sub>3</sub>S paste. Moreover, the paste's water saturation is highly influenced by the nature of the

microstructure and high RH medium are reported to support the formation of calcite [1]. Both explanations, *i.e.* vaterite sursaturation and the water content are believed to generate calcite in the industrial LAC. One should keep in mind that due to numerous uncertainties related to the use of the Rietveld quantification in our materials, significant discrepancies are related to the estimated values yielded, nonetheless the tendencies demonstrated are thought to be reliable. Similarly to the C-S-H paste at C/S = 1.4 the carbonated zone reflects only carbonation products.

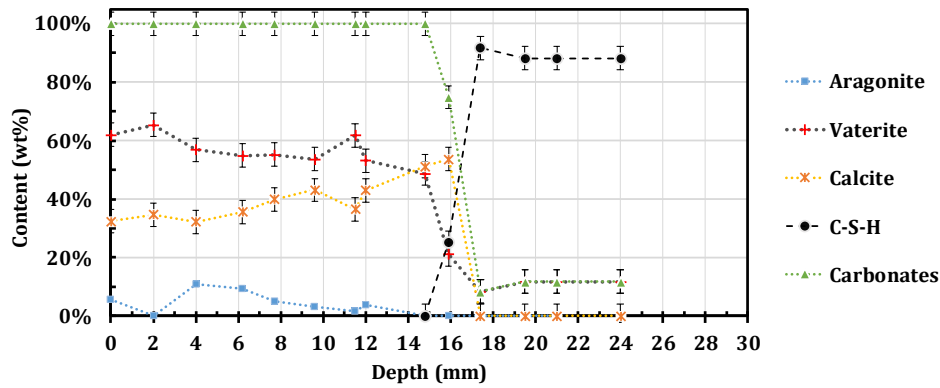


**Figure 20: Relative proportion of the different phases obtained by Rietveld analysis**

The TGA analysis of the carbonated industrial LAC is displayed in Figure 21. The maximum amount of carbonates estimated in the LAC correspond to the 60% of the carbonates demonstrated by the C/S = 1.4 paste, which is consistent with the mean C/S ratio estimated by EDS (0.84) in the pristine material (**Table 6** section 1.2.1.2). Similarly to the model C-S-H paste the industrial LAC was fully carbonated in the carbonated region this confirms the trend seen in XRD quantification shown in Figure 20.

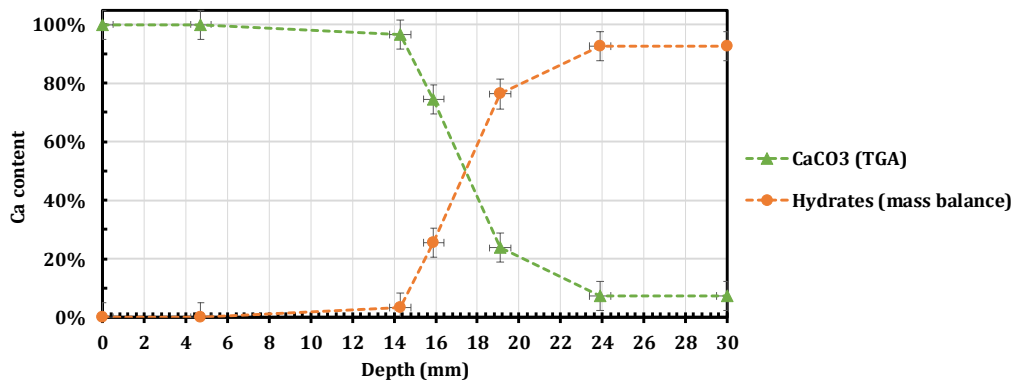


**Figure 21: Carbonation's profiles obtained by TGA analysis, the complementary to the calcium carbonates estimated by mass balance represents the hydrates of the  $\text{CaO-SiO}_2\text{-Al}_2\text{O}_3\text{-H}_2\text{O}$  quaternary system.**

The  $^{29}\text{Si}$  MAS NMR profiles of the carbonated paste is showed in Figure 22, the environment evidenced in the fully carbonated zone (0-14.6 mm) are associated to silica gel ( $\text{Q}^3$  and  $\text{Q}^4$  environment), the same observation was made

for the model C-S-H paste (chapter 2, figure 6). The presence of highly polymerized environment in the uncarbonated part of the material is consistent with both XRD and TGA analyses which showed residual content of carbonate further than the carbonation front. These carbonates could be partly explained by the amount of limestone (3% limestone and 97% clinker), a discrepancy in the distinction between C-S-H and carbonates polymorphs in XRD estimation and slight carbonation during materials preparation. Nonetheless, a broad carbonation front was observed which correlated the high proportion of silica gel environment detected between 18.6-24.4 mm compared to the pristine material. Silica gel/unreacted silica environment is also detected in the pristine material. Since the industrial LAC contains 50 wt% of added silica, it is usual to observe silica gel/unreacted silica environment in LAC after years due to incomplete reactivity.

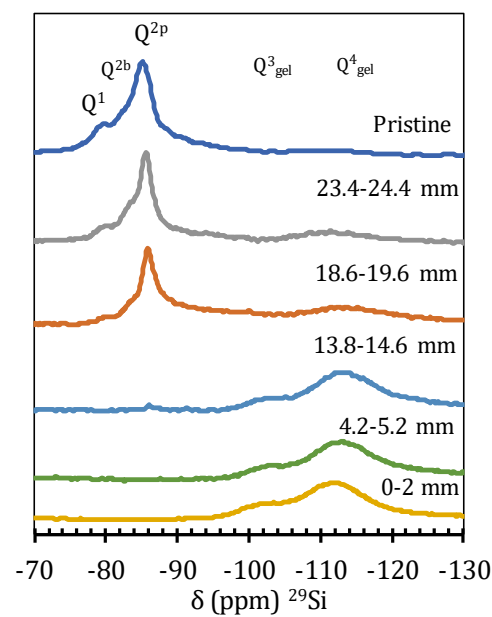


**Figure 22:  $^{29}\text{Si}$  MAS NMR profiles of the carbonated industrial LAC**

Based on the  $^{29}\text{Si}$  MAS NMR decomposition, silicates present in C-A-S-H or silica fume/silica gel environment are given in Table 11. One should keep in mind that the aluminium environments are not extracted, the spectra were poorly resolved and the pastes evidenced a small Al content  $0.04 \pm 0.03$ .

**Table 11: Distribution of  $^{29}\text{Si}$  MAS NMR between silicates environment of C-A-S-H and silicates in silica gel/silica fume, based  $^{29}\text{Si}$  MAS NMR spectra decomposition. C-A-S-H = ( $\%Q^1 + \%Q^{2b} + \%Q^{2p}$ ), Silica gel/silica fume = ( $\%Q^3_{\text{gel}} + \%Q^4_{\text{gel}}$ ).**

	0	4.2-5.2 mm	13.8-14.8 mm	18.6-19.6 mm	23.4-24.4 mm	Pristine
C-A-S-H	0%	0%	2%	55%	67%	74%
Silica gel/Silica fume	100%	100%	98%	45%	33%	26%



The details of the decomposition are given in Table 12.

**Table 12: Parameters used in the  $^{29}\text{Si}$  MAS NMR spectra decomposition**

	$Q^1$	$Q^{2b}$	$Q^{2p}$	$Q^{3\text{gel}}$	$Q^{4\text{gel}}$
$\delta$ (ppm)	-80	-83	-86	$-93 \pm 1$	-111
x in $xG/(1-x)L$	0	0.81	0	1	1
width (ppm)	$4 \pm 1$	2.2	2.3	12.5	11
G: Gaussian distribution, L: Lorentzian distribution					

The industrial LAC carbonation depth at 50 days is reported in Figure 24. Despite the fact that only one carbonation term is reported because of ongoing experiment, similar carbonation kinetics were evidenced by the model C-S-H paste  $C/S = 1.4$  and the industrial LAC. The latter demonstrated lower chemical buffering capability 40% less than the model C-S-H paste but at the same time appeared less cracked than the C-S-H paste (Figure 23). One effect compensating the other, this might explain the similar carbonation rate. This appears to be another example of the interplay between the material chemistry and its transport property.

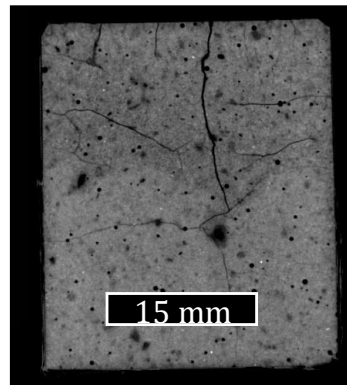


**Figure 23:  $\mu\text{CT}$  of the industrial LAC at 50 days of accelerated carbonation at  $P_{\text{CO}_2} = 3\%$**

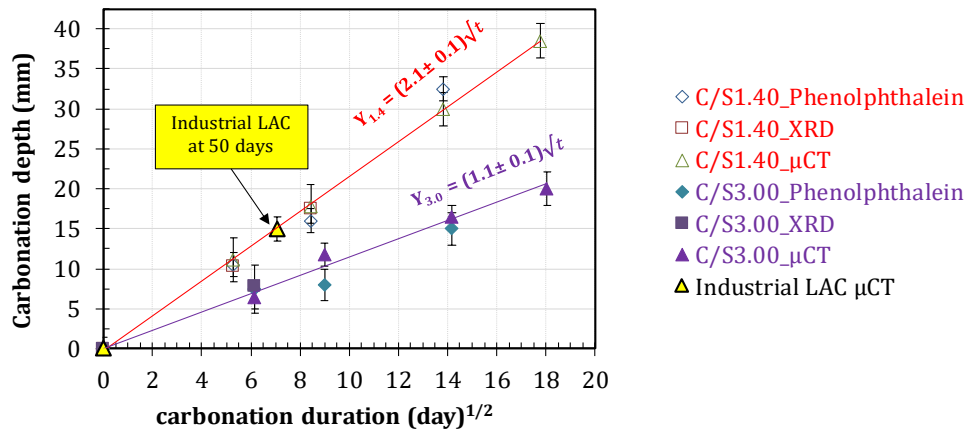


**Figure 24: Carbonation depth observed in the industrial LAC after 50 days of carbonation compared to the model pastes (C/S = 1.4 and 3.0)**

The estimation of the linear shrinkage of both the model pastes and the industrial LAC are detailed thereafter in (Figure 25), both the drying and the carbonation shrinkage were measured. A higher carbonation shrinkage is observed in the model pastes with C/S lower than 3.0 especially at C/S = 1.40 and 0.95 (Table 13). Despite the lack of extensive carbonation data for the model pastes with C/S < 1.40, we can nevertheless associate the higher carbonation shrinkage to the heavy cracking evidenced in model pastes at C/S = 1.40 and 0.95 (Figure 27). Cracks were present in the C<sub>3</sub>S paste and in the industrial LAC but at a significantly lower extent. The content on distinct partially reacted phase such as silica fume is thought to mitigate the extent of carbonation shrinkage, which might explain the similar extent of carbonation shrinkage in the C<sub>3</sub>S paste and the industrial LAC despite the higher extent of crack in the latter.

An attempt to discriminate the contributions of the carbonation shrinkage is shown in Figure 26, among the model paste of lower C/S ratio 0.95, 0.87, 0.80 it is obvious that the main contribution of the shrinkage is attributable to the C-S-H carbonated. Nonetheless the pastes tend to incorporate increasing amount of un reacted silica when decreasing the C/S ratio. This amount of unreacted silica corroborates the lesser carbonation shrinkage observed when decreasing the pastes C/S ratio 0.95, 0.87, 0.80.

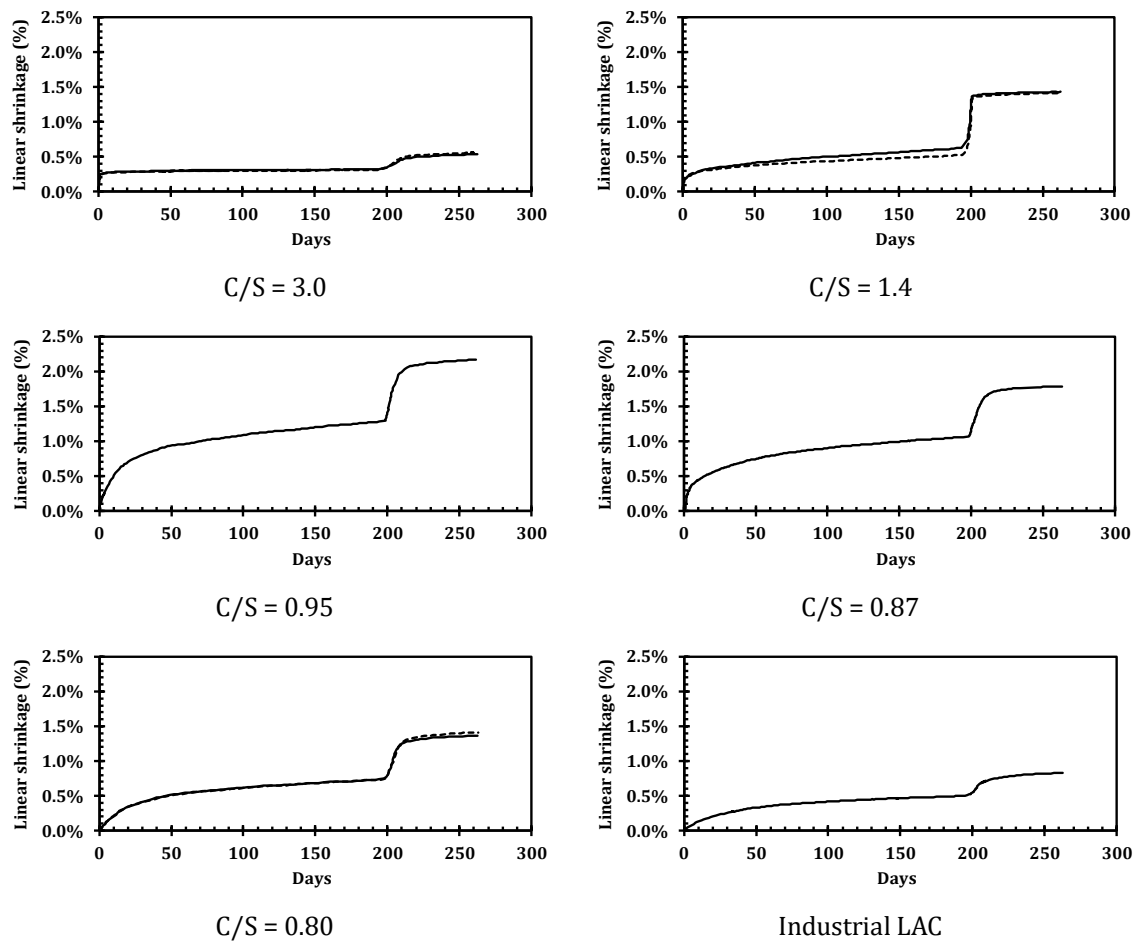


Figure 25: Individual linear shrinkage of the materials studied, from 0-195 days the drying shrinkage is acquired, then the materials were carbonated at  $P_{CO_2} = 3\%$

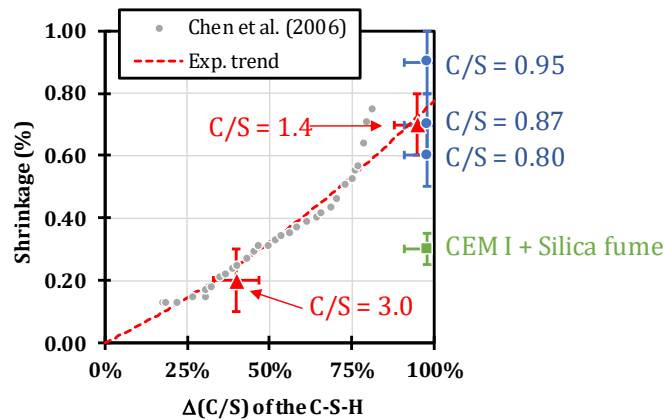


Figure 26: Extent of the carbonation shrinkage of the pastes associated to the C-S-H's C/S variation. The experimental results are compared to Chen *et al.* decalcification results [2]

**Table 13: Details of shrinkage's contribution for the model pastes and the industrial LAC**

				Relative contribution	
	Total linear shrinkage	Carbonation	Drying	Carbonation	Drying
C <sub>3</sub> S paste	0.5%	0.2%	0.3%	38.7%	61.3%
CEM I+SF	0.8%	0.3%	0.5%	36.2%	63.8%
C/S 1.40	1.4%	0.7%	0.7%	49.4%	50.6%
C/S 0.80	1.4%	0.6%	0.7%	46.5%	53.5%
C/S 0.87	1.8%	0.7%	1.1%	40.9%	59.1%
C/S 0.95	2.2%	0.9%	1.3%	40.8%	59.2%

The recourse to model materials helped question the LACs' carbonation behaviour reported in the literature. Thanks to the tailoring of the model materials, a detailed mechanistic understanding was brought based on the decoupling of carbonation's contributions. Results on aspects such as shrinkage and solid volume variation are Scarce, which justifies our contribution to the topic.

The buffering capability of the industrial LAC was therefore evidenced to be 60% of the model C-S-H (C/S = 1.4) paste. Nevertheless, similar carbonation rate was evidenced of which the heavy cracking evidenced by the C-S-H paste is believed to be the cause. Contrarily to the C-S-H paste one should keep in mind that the industrial LAC are C-A-S-H paste. They also contain unreacted silica which can contribute to the reduced linear shrinkage. However considering recent studies on C-A-S-H mechanical properties [3], the Al content might have an influence on the reduced linear shrinkage but the mechanism remains to be explained. Nevertheless, the carbonation of the industrial LAC corroborated the behaviour observed in model powder especially, *i.e.* the higher carbonation rate observed in low C/S ratio C-A-S-H. The cracks appeared to be a major carbonation consequence in both model materials and industrial material which requires further study as suggested by the results from carbonation modelling on the model pastes Seigneur N., Kangni-Foli E. *et al.* [4]

Only few carbonation results were obtained for the model pastes with C/S ratios lower than 1.4 because of the extent of cracks (see **Figure 27**) and the difficulty to handle those samples. The C/S = 0.95 was carbonated but it was not possible to extract the required chemical and microstructural information.

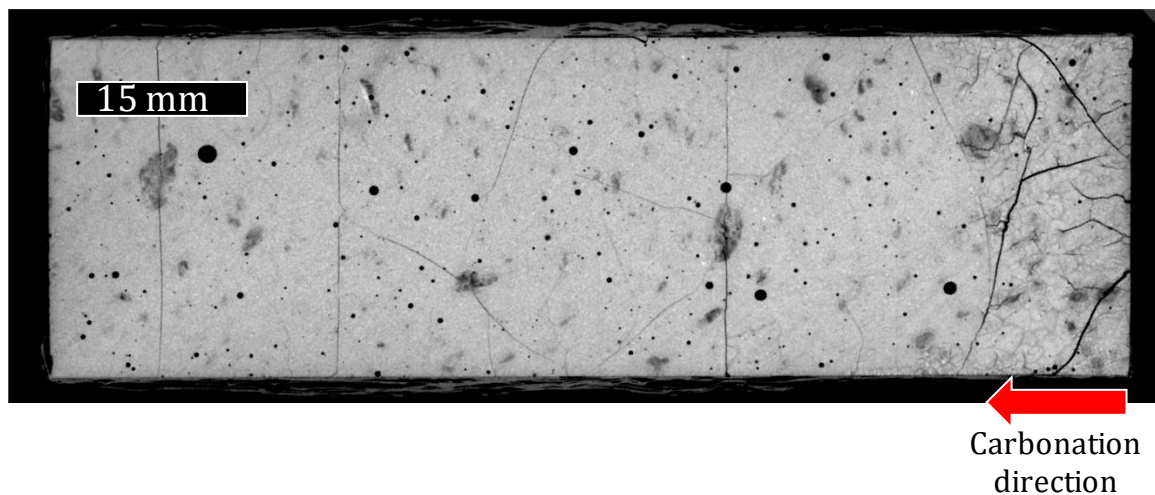


**Figure 27:  $\mu$ CT of a C/S = 0.95 sample carbonated during 50 days**

### References

- [1] C. Rodriguez-Navarro, K. Kudłacz, Ö. Cizer, E. Ruiz-Agudo, Formation of amorphous calcium carbonate and its transformation into mesostructured calcite, *CrystEngComm.* 17 (2015) 58–72. doi:10.1039/C4CE01562B.
- [2] J.J. Chen, J.J. Thomas, H.M. Jennings, Decalcification shrinkage of cement paste, *Cem. Concr. Res.* 36 (2006) 801–809. doi:10.1016/j.cemconres.2005.11.003.
- [3] G. Geng, R.J. Myers, J. Li, R. Maboudian, C. Carraro, D.A. Shapiro, P.J.M. Monteiro, Aluminum-induced dreierketten chain cross-links increase the mechanical properties of nanocrystalline calcium aluminosilicate hydrate, *Sci. Rep.* 7 (2017). doi:10.1038/srep44032.
- [4] N. Seigneur, É. Kangni-foli, V. Lagneau, A. Dautères, S. Poyet, P. Le Bescop, E. L'Hôpital, J.B. d'Espinose de Lacaille, Understanding the effects of the atmospheric carbonation of cementitious materials using reactive transport modelling, *Submitt. to Cem. Concr. Res.* (2019).

## 2. CONCLUSIONS AND PROSPECTS

Recent studies highlighted experimental evidences related to an increased sensibility of low-pH materials with regard to atmospheric carbonation. The likely recourse to low-pH materials in the framework of the French geological repository made IRSN question their durability and this question is at the origin of this thesis. Its aim was to gain a better understanding of the carbonation mechanism in low-pH materials, which is required for IRSN evaluation of the disposal facility construction's licence application. The complexity of both the carbonation mechanisms and cements composition were partly circumvented by the approach chosen: the model material approach. This approach took the form of designing a cementitious model materials based on pure phases, formulated pastes based on pozzolanic reaction of  $C_3S$  and nanosilica and also synthesized C(-A)-S-H's powders. The materials (powders and pastes) were of increasing C/S ratio ranging from 0.8 to 3.0, while the powders' Al/Si content varied from 0 to 0.1. The materials were tailored to be simplified system, nonetheless representative of cementitious materials allowing the distinction and the correlation between the contributions of the chemistry, the mineralogy and the microstructure. The effect of Ca and Al content, the evolution of the pores structures as well as the deformation related to drying and carbonation were explored.

The durability of the cementitious materials was first observed to be related to the calcium content. The materials with the higher calcium content (powders and pastes) were observed to carbonate with the slowest kinetics, this was attributed to the materials' buffering capability. The presence of aluminium was observed to affect the carbonation kinetics. The presence of phases such as TAH and pentahedral Al, generated conjointly by high Ca content and the presence of Al, correlated with a slower carbonation kinetics compared to the observed C-S-H's degradation kinetics controlled by the sole Ca content. The decrease observed in the carbonation rate (for C-A-S-H) is assumed to arise from the nature of both TAH and pentahedral Al species. They are suggested to be located at the surface and within C-A-S-H's interlayer, respectively. Therefore, at a molecular scale, those Al species are assumed to be closely related to the cementitious materials building block (C-A-S-H). We proposed a  $CO_2$  access limiting effect generated by the presence of TAH and pentahedral Al species. The Ca and Al content was observed to affect the structure of the C-S-H, the increasing Ca content induced shorten silicates chain where Al incorporation was observed to take place in both silicates' pairing and bridging position. When exposed to  $CO_2$ , the property of the products generated after carbonation, in the case of calcium carbonate polymorphs, is highly oriented by the alkalinity. Calcite was observed upon C-S-H carbonation in  $C_3S$  paste, instead of vaterite, the polymorph usually detected for C-S-H carbonation. This was explained by the presence of portlandite which dissolution is believed to induce a sursaturation of dissolved vaterite/Ca, which explains the polymorphic orientation in presence of high alkalinity toward calcite's formation. The control of silica gel polymerization's degree by the calcium and the aluminium content was also evidenced. The carbonation of C-A-S-H of high Ca and Al content evidenced increased proportion of silica gel's low polymerization unit ( $Q^3$ ). However, independently of the Ca and Al content, the same tetrahedral Al environment (distinct from pristine material Al (V) sites) is generated after carbonation. The macroscopic effect of carbonation evidenced a compensated and increased solid volume in presence of portlandite ( $C_3S$  paste) and the absence of new porosity formed. The C-S-H paste's (C/S = 1.4) solid volume estimation after

carbonation also demonstrated a solid volume increase considering the estimated molar volume difference between the C-S-H on one side and the vaterite and the silica gel on the other side. These results suggest that the carbonation of C-S-H at C/S ratio (1.4-1.7) could not be associated to a solid volume decrease. The cracking observed during carbonation is justified by the decalcification, the silicate's polymerization and the difference in mechanical properties between silica gel and the C-S-H disabling the material to withstand the mechanical strains. Moreover, the presence of unreacted silica was correlated to a lesser linear shrinkage. The study of an industrial LAC envisaged in the French disposal context correlated the observations and the understanding eased and gained from by the model materials.

The approach implemented was proven successful as the recourse to model materials allowed to segregate distinct carbonation's consequences, highlighting elemental contribution to the carbonation both at molecular and macroscopic scale. A new contribution to the carbonation mechanism was unveiled by estimation such as solid volume variation after carbonation and the influence of the joint impact of Ca and Al in the carbonation kinetics. The data gained in term of polymorphism, pore network evolution, solid volume variation, estimated hydrates and carbonation products volume, as well as the evolution of hydrates degradation are adequate both to enrich database and strengthen carbonation modelling, which was part of this work since the modelling of model materials' carbonation is the focus of a submitted publication, nonetheless further comprehension are still required.

The cracks observed in the paste at the low C/S ratio need additional study to be accurately explained. Despite the correlation between the polymerized silicates chain and the shrinkage observed, strong evidences are needed to detail the underlying mechanisms relating the silicates' polymerization, the shrinkage and the crack patterns. An experimental approach including the use of  $\mu$ CT and  $^{14}\text{C}$ -PMMA impregnation (autoradiography technique) and NMR might help to follow hydrate degradation and crack initiation and porosity evolution. A modelling approach is required to couple the evolution of local mechanical properties during atmospheric carbonation with the overall material property; this requires to take into account the microstructure, the chemistry the transport and local mechanical properties, which might also help understand mechanisms at the pore scale, since the microstructure seems to control mechanisms such as polymorphic orientation. Besides, an extended mechanical investigation (compressive strength, creep) on the pristine and the carbonated pastes are required to fully characterize the pastes developed.

A further step necessitates the formulation of a quaternary system pastes ( $\text{CaO-SiO}_2\text{-H}_2\text{O-Al}_2\text{O}_3$ ), which might be obtained by the addition of Al suspension from dissolved C<sub>3</sub>A into the fresh mix. This will allow the consideration of Al chemistry therefore a better representativity toward industrial material. An influence of the microstructure would be highlighted when confronting the results obtained on pastes (with/ without Al) and powders (C-A-S-Hs). Comparison between shrinkage in quaternary and ternary systems would also help to investigate Al contribution to linear shrinkage.

An improved understanding of the role (and the nature) of TAH and pentahedral Al species might require  $^{29}\text{Si}$  enriched materials and  $^{29}\text{Si}$ - $^{27}\text{Al}$  correlation to ease probing silicon and Al environment by NMR. Absorption spectrometry such as extended X-ray absorption fine structure (EXAFS) and XANES which are not limited by the nanocrystalline nature of the binder would inform on the atomic environment of elements and the local order.

Those methods might bring the stronger evidences needed to support the CO<sub>2</sub> access limiting effect attributed to the surface and interlayer's Al species, which would bring deeper understanding on the nature of those Al species.



## **SUMMARY IN FRENCH**

La prédiction à très long terme des propriétés de durabilité de matériaux cimentaires récents tels que les matériaux cimentaires bas-pH est désormais indispensable. Ces matériaux sont notamment proposés dans le cadre du stockage géologique de déchets HA et MAVL en France (projet CIGÉO). Des recherches complémentaires sont requises afin de répondre à ce besoin.

Durant la période d'exploitation la carbonatation représente le risque majeur d'altération de matériaux cimentaires du centre industriel de stockage géologique. Ce travail a visé à l'extension du dossier de connaissance de ces matériaux en permettant une meilleure compréhension de leurs comportements face à la carbonatation. L'approche adoptée est multi technique et inclut dans un premier temps le développement de matériaux cimentaires bas-pH modèles sous forme de pâtes (chapitre 1) et la synthèse de matériaux modèles sous formes de poudres (chapitre 2). Ces approches sont nécessaires à la compréhension d'un phénomène aussi complexe que la carbonatation, cette dernière est mise en place et traitée au chapitre 2 dans le cas des poudres et au chapitre 3 dans le cas de systèmes diffusifs tels que les pâtes durcies.

Le premier chapitre met en lumière, la méthodologie mise en œuvre afin d'obtenir des matériaux cimentaires modèles sous forme de pâtes durcies, à différents rapports C/S, ayant une chimie et une minéralogie contrôlée. Ce premier chapitre propose également une discussion des propriétés physico-chimiques des pâtes développées, comparées à celles des matériaux cimentaires bas-pH. Dans un souci de représentativité, nous avons opté pour l'obtention de matériaux cimentaires modèles avec une réactivité basée sur la réaction pouzzolanique à l'image des matériaux cimentaires usuels. Nous avons eu recours à du silicate tricalcique, de la silice colloïdale en suspension, de l'eau et du superplastifiant. Nous avons fabriqué des matériaux couvrant une large gamme de rapports C/S variant de 0,80 à 3,0, comprenant ainsi le domaine d'alcalinité des matériaux cimentaires usuels et ceux des matériaux cimentaires bas-pH. Les teneurs importantes en silice de faible granulométrie (diamètre médian D50 = 100 nm) dans les pâtes à faibles rapports C/S ont été à l'origine de difficultés de mise en œuvre. L'obtention de ces matériaux a nécessité entre autres un travail de formulation et de contrôle de la mise en œuvre. Ont également été fabriquées une pâte de ciment de Portland, et un mélange ternaire à base de CEM I, de cendre volante et de fumée de silice, ces dernières servant de références en tant que matériaux cimentaires usuels et matériaux bas pH respectivement. La pâte durcie de C<sub>3</sub>S au

C/S = 3,0 est constituée de C-S-H et de portlandite (DRX, ATG), les pâtes modèles durcies aux  $C/S \leq 1,40$  sont essentiellement constituées de C-S-H et démontrent une faible dispersion de leurs rapports C/S (MEB-EDS) nous assurant ainsi du contrôle de la chimie et de la minéralogie escompté pour les matériaux fabriqués. L'estimation de la teneur en C-S-H montre une teneur plus élevée de C-S-H dans les pâtes à plus bas pH en comparaison à la pâte de ciment de Portland. Les pâtes modèles ont démontré avec l'abaissement du C/S, une gamme similaire de porosité et un raffinement de la porosité sondée attribuée au C-S-H (porosité par intrusion de mercure) similaire à celle des matériaux bas-pH. Cette observation est attribuée au comblement de la porosité générée par les teneurs plus élevées en C-S-H. A l'échelle nanométrique les propriétés des C-S-Hs formés sont similaires à celles répertoriées par la littérature. Le recours à la RMN du noyau  $^{29}\text{Si}$  a permis de mettre en évidence des propriétés structurales (distribution d'environnement  $^{29}\text{Si}$ , taille moyenne des chaînes de silicates) au sein des pâtes synthétiques modèles similaires aux matériaux industriels et les matériaux détaillés dans la littérature.

Des points de faiblesses nous sont apparus, spécialement sur les matériaux aux plus bas rapports C/S, cela comprend la présence de fissures à bas rapports C/S. Nous avons proposé comme explication à la présence de ces fissures, la réactivité donnant lieu aux C-S-Hs à bas rapports C/S et les propriétés physicochimiques de ces mêmes C-S-Hs. Nous avons eu recours à des doses de superplastifiant supérieures aux doses habituelles afin de permettre la mise en œuvres des pâtes ce qui représente également une des faiblesses de ces matériaux. Ces derniers aspects représentent des pistes d'amélioration de ces matériaux.

Au vu des caractéristiques observées, les matériaux modèles ont démontré des propriétés permettant l'acquisition d'un spectre large de connaissances touchant notamment aux propriétés intrinsèques des C-S-Hs de l'état sain à l'état carbonaté, aux conséquences liées à d'autres pathologies de matériaux cimentaires, ou encore aux dynamiques de transports réactifs au sein de ces matériaux.

Le second chapitre traite du lien entre propriétés structurales à l'échelle nanométrique et réactivité. Dans cette partie les matériaux utilisés sont des poudres de C(-A)-S-Hs, des silicates de calciums hydratés à teneurs variables en aluminium. Les matériaux à bas-pH incorporent souvent de l'aluminium issu des ajouts et de l'aluminium issu des minerais à l'origine du clinker. L'aluminium est connu pour modifier le motif dreierketten, structure de base du liant. La question du lien entre cette modification structurale et son impact sur la réactivité du matériau

cimentaire reste une question ouverte. Nous avons donc synthétisé des C-A-S-Hs aux rapports C/S compris entre 0,80 et 1,40 et aux rapports Al/Si suivants 0,0 ; 0,05 et 0,10 pour chacun des C/S synthétisés.

Les résultats obtenus s'appuient sur une approche multitechnique (DRX, ATG, RMN). La RMN a été la méthode de choix adoptée pour sonder les structures nanocrystallines des C-A-S-Hs. Nous avons fait appel à de la RMN des noyaux  $^{29}\text{Si}$  et  $^{27}\text{Al}$  en impulsion unique et quanta multiple ainsi qu'à de la simulation de résonances magnétiques afin d'extraire des propriétés structurales.

Les résultats obtenus ont mis en évidence les différents environnements attendus que ce soit en RMN du noyau  $^{29}\text{Si}$  ou  $^{27}\text{Al}$ . L'incorporation d'aluminium s'est révélé par un désordre plus important dans les environnements  $^{29}\text{Si}$ , traduit par une plus grande distribution des environnements  $^{29}\text{Si}$ . Les analyses  $^{27}\text{Al}$  MQMAS ont confirmé un environnement pour l'Al tétraédrique distordu à bas C/S (0,80) avec une substitution de silicates par de l'aluminium, ceci en position pontant et en position dite  $Q^3$  (correspondant à de l'Al en position pontant dans une double chaîne de silicate) et deux environnements tétraédriques à hauts C/S. Ces résultats supportent l'incorporation d'Al à la fois en position pontant et en position dimérique du motif dreierketten à haut C/S. L'augmentation du rapport C/S et de la teneur en Al génèrent la formation de deux espèces d'intérêt, la première nommée TAH (third aluminate hydrate) formée d'Al en coordinence octaédrique, la seconde espèce constituée d'Al en coordinence pentaédrique. Nous avons observé en suivi de carbonatation ( $P_{\text{CO}_2} = 3\%$ , HR = 55%, 25°C) une dégradation des matériaux sains donnant le même produit de carbonatation quelle que soit la structure initiale du matériau. Un gel de silicate ou d'aluminosilicate et des carbonates de calcium sont formés lors de la carbonatation. Les résultats mettent en évidence une résistance plus élevée à la carbonatation des C-A-S-Hs à hautes teneurs en calcium et en aluminium. Ces derniers ont une vitesse de dégradation plus faible. Nous avons mis en avant une implication des espèces Al (V) et Al (VI) (les TAH), ces aluminates sont intimement associés aux C-S-Hs et sont proposés ici comme des structures écrantant l'accès au Ca du C-S-H pour le  $\text{CO}_2$ .

Ces études ont mis en lumière un rôle structural fort de l'Al dans les C-A-S-Hs en fonction du rapport C/S et du rôle couplé du Ca et de l'Al dans la préservation du liant lors de la carbonatation.

La troisième partie du manuscrit traite du comportement de pâtes modèles décrites dans le premier chapitre face à la carbonatation avec une approche multitechnique (DRX, ATG, RMN  $^{29}\text{Si}$ ,

$\mu$ CT, diffusion de gaz, mesure de retrait). Ces matériaux permettent la prise en compte de la contribution de la diffusion dans la carbonatation puisque ces derniers possèdent une microstructure (contrairement aux poudres, objets du chapitre 2). Cette troisième partie apporte des réponses sur des volets tels que la contribution du pouvoir tampon du matériau lors de la carbonatation, les évolutions microstructurales et le couplage entre les deux phénomènes précédemment cités. La carbonatation de deux matériaux modèles ( $C/S = 3,0$  et  $1,40$ ) sont traités et comparés à celle d'un matériau bas-pH formulé à partir d'un mélange à 50% de CEM I et à 50% de fumée de silice.

Une carbonatation complète a été observée dans la pâte faite de C-S-H ( $C/S = 1,40$ ) le signal propre au C-S-H n'était plus détecté (DRX, RMN), mais dans le cas de la pâte au  $C/S = 3,0$  servant de modèle de matériaux cimentaires usuels type OPC, seule une carbonatation partielle a été vue. Ce résultat met en évidence entre autre le rôle de la portlandite dans le matériau à plus haut  $C/S$ . Du point de vue de la microstructure, la porosité totale du matériau diminue du fait de la précipitation de carbonate de calcium mais la décalcification des C-S-Hs et leur polymérisation est source de retrait et de fissuration. Bien que la réduction de porosité et la fissuration ont deux effets opposés sur le transport, dans le cas de la pâte de C-S-H l'effet de la fissuration prévaut sur celle de réduction de la porosité ce qui corrèle avec la valeur élevée du coefficient de diffusion du  $CO_2$  de la pâte carbonatée. Ces conditions amènent à un taux de carbonatation élevé. La dissolution de la portlandite contenue dans la pâte de  $C/S = 3,0$  n'est pas complète dans la région carbonatée. La présence d'un réservoir de Ca en excès tel que la portlandite limite la dissolution du C-S-H. Il est à noter que peu de fissures sont observées dans cette pâte. Les résultats obtenus comparés à la littérature mettent en évidence la décalcification des C-S-Hs comme moteur du retrait. Une loi polynomiale a été proposée pour corrélérer le retrait développé par le matériau et la variation du rapport  $C/S$  de son liant.

La comparaison entre le matériau modèle au rapport  $C/S = 1,40$  et le matériau industriel bas pH fabriqué fait ressortir un comportement similaire en terme de profil de dégradation des C-S-Hs. Cela comprend une carbonatation totale des C-S-Hs dans la zone carbonatée, mettant en évidence ici l'absence d'effet tampon d'une source de Ca telle que la portlandite qui serait présente en excès et qui amènerait à la préservation du liant. Le pouvoir tampon de la pâte industrielle est estimée à 60% de celle de la pâte au rapport  $C/S = 1,40$ . Une cinétique similaire de dégradation est observée dans les deux pâtes, expliquée par la prédominance de fissures issues de la dégradation avancée des C-S-Hs.

Ces travaux mettent l'accent sur le rôle de la teneur élevée en calcium dans les matériaux cimentaires et du rôle conjoint d'une teneur élevée en calcium et en aluminium dans la préservation de l'intégrité du liant face à la carbonatation.

## RÉSUMÉ

---

Le projet CIGÉO initié par l'Andra vise au stockage de déchets radioactifs en site géologique profond. L'Andra envisage le stockage des déchets MAVL (Moyenne Activité Vie Longue) dans des alvéoles souterraines scellées par un noyau d'argile gonflante en appui sur deux massifs en béton bas-pH, ceci dans le but d'éviter l'éventuelle inhibition des propriétés de gonflement due à la forte alcalinité des matériaux cimentaires usuels. Les bétons bas-pH ont donc été développés en conséquence.

L'IRSN (à travers cette thèse) questionne la durabilité des éléments bas-pH, puisque des études récentes montrent suite à la carbonatation de matériaux bas-pH, une augmentation des propriétés de perméabilité corrélée à une plus grande distribution des tailles de pores et une fissuration plus importante au sein de ces matériaux. Cette carbonatation serait induite par la réaction entre le CO<sub>2</sub> contenu dans l'air (utilisé pour ventiler les alvéoles durant leur phase d'exploitation) et le calcium contenu dans les différentes phases constitutives du matériau cimentaire.

Cette thèse a permis de séparer et d'identifier différentes contributions propres à la carbonatation. D'une part, à travers le développement de matériaux modèles, la mise en évidence du rôle sur la vitesse de carbonatation, d'une teneur élevée de portlandite constituant un réservoir de calcium dont la présence et la consommation induisent une réduction du taux de dégradation des C-S-Hs. D'autre part, de souligner le rôle des aluminates de calcium hydratés tels que les TAH et les aluminates pentaédriques formés en présence d'aluminium et d'une teneur élevée en calcium, sur la vitesse de dégradation des C-A-S-Hs significativement plus faible que pour des C-S-Hs à teneur équivalente en calcium. Les évolutions microstructurales et volumique à l'échelle macroscopique, telles que les fissures et le retrait de carbonatation corrélées à la chimie et à la minéralogie ont mis en évidence aussi bien dans les matériaux modèles que le matériau bas-pH industriel un couplage entre la chimie et le transport dont la cinétique est en défaveur du matériau bas-pH.

## MOTS CLÉS

---

Cigéo, matériaux cimentaires bas-pH, carbonatation, stockage géologique, pâtes cimentaires modèles, C-A-S-H, C-S-H, C/S, Al/Si, microstructure, minéralogie, chimie, retrait

## ABSTRACT

---

Andra, the agency in charge of the radioactive waste management in France, is responsible for the design and the conception of the future deep geological disposal facility purposed to host among others the intermediate level long lived wastes (ILW-LL). The design proposed envisaged the sealing of the disposal ILW-LL wastes' cells by a swelling clay and two Low-pH concrete plugs. Those Low-pH cementitious materials are obtained by massive incorporation of siliceous bearing materials in usual cements, which aimed to lower the materials' alkalinity (pH). The recourse to commonly used cementitious materials for the sealing would lead to an inhibition of the swelling properties of the clays due to the cements' high alkalinity.

Recent studies have highlighted for Low-pH materials an increased permeability, cracking and pore size distribution upon carbonation. IRSN as a French nuclear safety expert raised the question (through this study) of the durability of Low-pH materials in the framework of the carbonation. The carbonation is defined in cementitious materials as the reaction of calcium (Ca) from Ca-bearing phases with the dissolved CO<sub>2</sub> in the pore structure, initially present in the atmosphere. A model material approach was adopted in order to unveil the chemical changes and to allow mass balances after carbonation. The results obtained evidenced the role of the calcium content and the aluminium content. Materials with high Ca content evidenced the slower carbonation kinetic. In presence of aluminium and high calcium content TAH and pentahedral Al species were formed, their presence and reactivity correlated with a decreased rate of C-A-S-H's degradation compared to the one induced by the sole high ca content in C-S-H. The microstructural evolutions and the changes in volumes and the shrinkage were quantified, the coupling between the chemistry and the transport properties was demonstrated comparing the model materials and the industrial low-pH material.

## KEYWORDS

---

Cigéo, Low-pH cementitious materials, carbonation, microstructure, geological disposal, C-A-S-H, C-S-H, C/S, Al/Si, mineralogy, chemistry, shrinkage, model cement pastes, shrinkage